ASTROCYTE METABOLIC NETWORKS IN NEURODEGENERATION

By

Melissa Cooper

Dissertation
Submitted to the Faculty of the
Graduate School of Vanderbilt University
in partial fulfillment of the requirements
for the degree of

DOCTOR OF PHILOSOPHY
In
NEUROSCIENCE

August 9, 2019
Nashville, Tennessee

Approved:

Professor David J. Calkins, Ph.D.

Professor Rebecca M. Sappington, Ph.D.

Professor Bruce D. Carter, Ph.D.

Professor Rebecca A. Ihrie, Ph.D.

This work is dedicated to my mother, Karen Cooper, for her constant support of my independence and creativity; my father, Richard Cooper, for his persistent confidence in my ability to conquer anything I set my mind to; and my brother, Matthew Cooper, who inspires me every day to be the amazing person he has always insisted I am. I would not be the person I am today if it were not for my grandmother, Arlene Kaszovitz, the remarkable woman who first inspired me to love science. I would also like to thank Stephen Davis, my wonderful, dedicated partner who provided the unceasing love, strength, and pancakes I needed to pursue my dreams.

ACKNOWLEDGEMENTS

This journey would not have been possible without the help of my thesis advisor, Dr. David Calkins. His boundless energy, enthusiasm, and passion for science inspired me to take risks and execute experiments I never would have imagined otherwise. I appreciate his trust and confidence in my abilities that gave me the freedom I needed to explore the frontier of neuroscience. The training and support I received from him have been instrumental in my growth and development as a scientist. I would also like to thank the members of my committee. Dr. Rebecca Sappington, who chaired my committee, strengthened this work through her constructive probing of each possible mechanism. She always provided great advice and knowledge regarding the visual system, glaucoma, and glia. Dr. Bruce Carter and Dr. Rebecca Ihrie asked insightful questions that led me to consider new aspects of astrocyte remodeling, coupling, and metabolism. I appreciate my committee's constant support and availability as they guided me through all aspects of graduate school and beyond.

I also benefitted tremendously from the support of a wonderful team of researchers in the Calkins Lab. Dr. Silvia Pasini was always available to listen, help me troubleshoot techniques, and brainstorm new ideas and approaches. Her scientific knowledge and patience made me confident in my experiments and their results, giving me the freedom to be creative as I navigated my project. Dr. Wendi Lambert provided technical expertise, support, and guidance without which this project would have been impossible. Dr. Carl Weitlauf was a much needed source of support in the early days of this project, for which I will always be indebted.

Dr. Michael Risner provided a great deal of help with the electrophysiology, and Brian Carlson made sure I had the reagents and supplies I needed. Vincent Yao and Karis D’Allessandro were instrumental in helping me maintain my colony of knockout mice and were both wonderful colleagues. Victoria Vest was exceptionally helpful in data analysis and coding. I am fortunate to have worked with so many incredible people.

I am also grateful to the Neuroscience Program for their strong training paradigms and the Vision Research Training Grant for helping fund my research. I am especially grateful to Robin Schafer, Randy Gollovan, Jean Paul Noel, Katherine Swett, and Corey Roach for their friendship, help, and support. Part of my training is also attributed to the Vanderbilt Eye Institute, and I appreciate the support from Vanessa Alderson, Jill Brott, and Susan Kelton. I am also grateful to the Cell Imaging Shared Resource and Small Animal Imaging cores at Vanderbilt.

I am forever grateful to all the friends, coworkers, and family that made Nashville home for the last five years. I will fondly remember my graduate school career for the rest of my life.

Table of Contents

Page

Chapter

LIST OF FIGURES

Figure Page

LIST OF TABLES

Table Page

CHAPTER 1

BACKGROUND AND INTRODUCTION

1.1 ASTROCYTE STRUCTURE AND FUNCTION

> *A towel, [The Hitchhiker's Guide to the Galaxy] says, is about the most massively useful thing an interstellar hitchhiker can have. Partly it has great practical value. You can wrap it around you for warmth as you bound across the cold moons of Jaglan Beta; you can lie on it on the brilliant marble-sanded beaches of Santraginus V, inhaling the heady sea vapors; you can sleep under it beneath the stars which shine so redly on the desert world of Kakrafoon; use it to sail a miniraft down the slow heavy River Moth; wet it for use in hand-to-hand-combat; wrap it round your head to ward off noxious fumes or avoid the gaze of the Ravenous Bugblatter Beast of Traal (such a mind-boggingly stupid animal, it assumes that if you can't see it, it can't see you); you can wave your towel in emergencies as a distress signal, and of course dry yourself off with it if it still seems to be clean enough.*
>
> *Douglas Adams*

1.1.1 ASTROCYTE CHARACTERIZATION

The defining characteristic of a neuron is the ability to generate and propagate an action potential. All cells that lack this property, the majority of cells within the brain[2], are characterized as glia. Glia are sorted into five subcategories based upon their origin, morphology, and function: microglia, ependymal cells, oligodendrocytes, polydendrocytes (NG2 cells), and astrocytes. Microglial cells, representing approximately 10% of glia, are derived from mesoderm and represent the resident immune cells of the nervous system[3,4]. Ependymal cells line ventricles in the brain and central canal of the spinal cord and are involved in the production of cerebrospinal fluid. Oligodendrocytes provide insulating myelin to the neuronal axons propagating action potentials through white matter, and likely supply (or transmit) a small amount of metabolites to these axons as well[5-7]. Polydendrocytes are defined by the expression of the proteoglycan NG2, and are distributed through grey and white matter[8]. *In vitro* they differentiate into oligodendrocytes, and thus have often been equated with oligodendrocyte precursor cells, but new evidence demonstrates polydendrocytes can differentiate into neurons and astrocytes as well[8]. Astrocytes are the most abundant glial cell type in the central nervous system in each number, surface area, and volume[9]. They are distinguished by their stellate morphology and exist in distinct, non-overlapping domains[10]. Astrocytes exhibit vast morphological and functional heterogeneity, resulting in no singular cellular marker (although GFAP is most often used) or physiological characteristic. New functions and subclassifications of astrocytes are still only now being discovered, and thus many questions still remain.

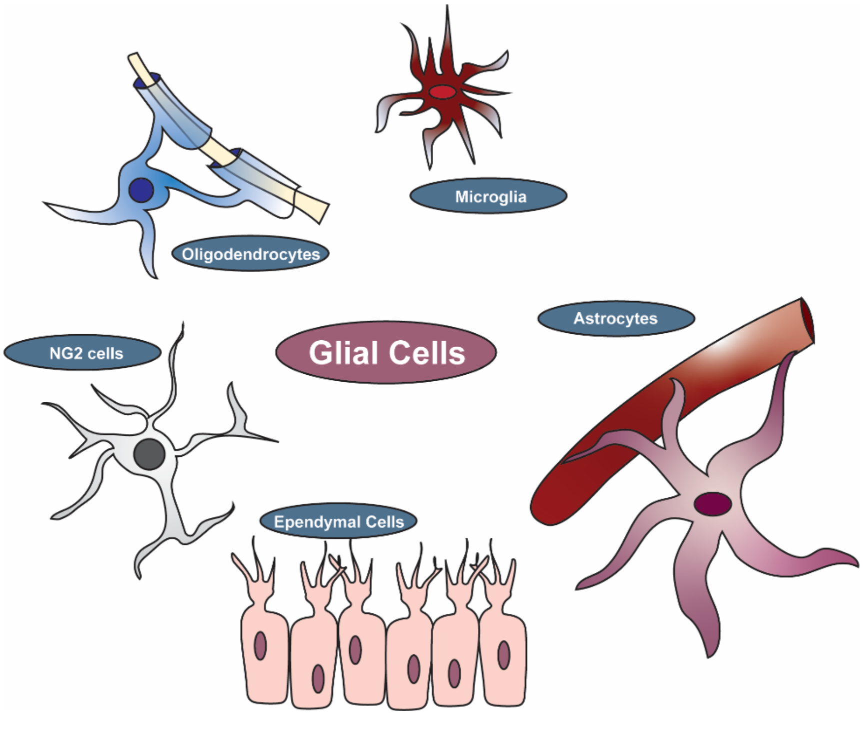

Figure 1.1 Glial cell types.

Glia are sorted into four categories based upon their origin, morphology, and function. Oligodendrocytes insulate axons between Nodes of Ranvier. Microglial cells are the resident immune cells of the nervous system. Astrocytes are the most abundant glial cells and exhibit vast functional heterogeneity, but are often associated with the blood brain barrier and support of signaling axons. Ependymal cells line ventricles and produce cerebrospinal fluid. NG2 cells (polydendrocytes) are thought to be precursor cells to many cell types.

Astrocytes are broadly divided into two groups (Figure 1.2). Protoplasmic astrocytes are found in the brain's grey matter, and fibrous astrocytes in white matter. Protoplasmic astrocytes, with their many fine processes, are associated with neuronal cell bodies and synapses[11]. At these synapses they maintain function by quickly removing and recycling neurotransmitters for more precise, efficient signaling[12-14]. Some reside adjacent to blood vessels, with longer processes that can distribute glucose and other metabolites to neuronal cell bodies while removing the byproducts of their consumption[15]. Fibrous astrocytes have longer processes and surround bundles of axons, into which they extend fine processes to monitor signaling patterns and extracellular conditions[16]. Astrocytes appear to adapt a protoplasmic or fibrous morphology according to their location rather than internal drivers, although the factors that drive this morphological development are largely unknown[14].

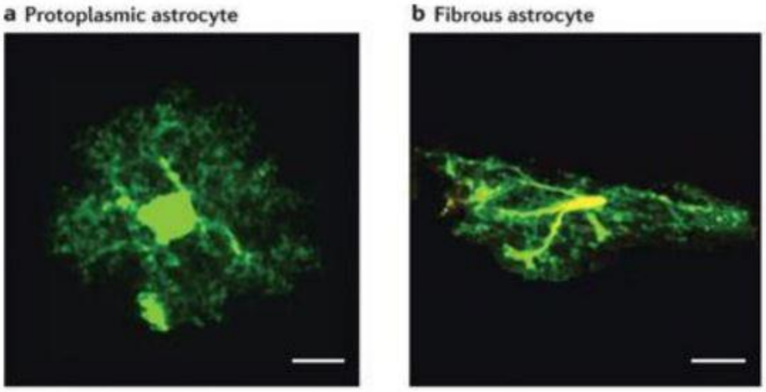

Figure 1.2 General astrocyte subtypes.

Astrocytes are broadly classified as protoplasmic or fibrous. Here, astrocytes in normal CNS tissue are visualized with green fluorescent protein under the control of an astrocyte-specific promoter. Protoplasmic astrocytes are found in grey matter and possess finer, more branched processes than fibrous astrocytes in white matter, which typically exhibit an oblong morphology. Scale: 10 µm.

Figure from Robel et al., 2011b and used in accordance with Copyright Clearance Center's RightsLink service.

The proportion of astrocytes to neurons varies according both to the size of the animal and the complexity of its brain[2]. Astrocytes themselves become much more complex as the cognitive ability of an organism increases, even distinguishing the human brain from that of other mammals[13]. The human neocortex harbors several anatomically unique subclasses of astrocytes not represented in other mammals, while neurons appear quite similar between mammals[17]. Despite their importance, astrocytes have little been studied compared to neurons, leaving an exciting opportunity for novel discoveries.

1.1.2 ASTROCYTE FUNCTION

Traditionally, scientists have operated under the assumption that astrocytes support neurons and occupy a somewhat passive niche themselves. Astrocytes additionally exhibit tremendous heterogeneity, which makes both their classification and study difficult[15]. However, astrocytes are vital in maintaining the homeostasis and general function of the nervous system. It is only recently that astrocytes have been increasingly recognized to have much broader and more active functionality, spanning from modulating synaptic activity, actively processing signals themselves, and directly influencing neurodegeneration[2].

This active role manifests in many ways (Figure 1.3). When a region is stimulated and signals more rapidly, astrocytes mobilize glycogen stores to provide neurons with additional glucose in support of the increased activity[18]. Astrocytes additionally mediate the energy supply within the brain via a direct physical link between blood vessels and neurons[19]. Astrocyte endfeet contact endothelial cells surrounding blood vessels, while their processes extend to envelop neurons and contact other astrocytes within their network[20]. Astrocytes actively signal through ‘gliotransmitters’, many of which are merely neurotransmitters released by glia, to alter the signaling patterns of neurons and act upon vascular smooth muscle[21]. In fact, astrocyte-mediated vascular contraction and expansion are the basis of the BOLD fMRI signal widely studied as a proxy for neuronal signaling[22]. Further, astrocytes propagate calcium ions through their networks in little-understood waves that may constitute an extraneuronal signaling system in the CNS[23]. Intriguingly, elevated intracellular calcium concentration within astrocytes in turn induces an elevation of neuronal calcium[24].

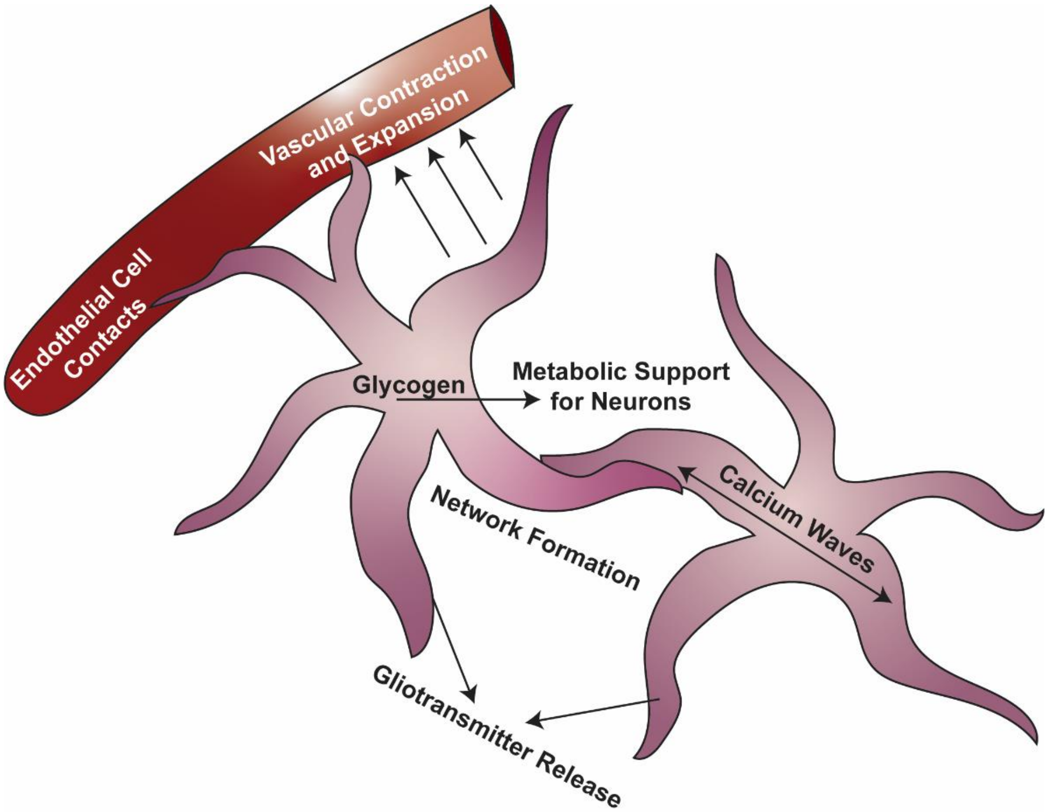

Figure 1.3 The many functions of astrocytes.

Astrocytes both support neuronal function and actively signal through many mechanisms. Astrocytes mobilize their stored glycogen when neurons need metabolic support. They form a direct link with blood vessels through their endothelial cell contacts and are a crucial component of the blood brain barrier. Astrocyte processes extend to form a network spanning the brain through which they share cytoplasm with one another and signal through calcium waves. Astrocytes additionally signal through ‘gliotransmitters’ to alter the signaling patterns of neurons and contract or expand vascular smooth muscle.

Calcium-evoked release of messengers from astrocytes regulate the energy supply to the brain in three ways. First, the release of arachidonic acid derived messengers from astrocytes modifies the contraction state of vascular smooth muscle within the brain, directing blood flow to those regions which are most active[19,23]. Second, glutamate-evoked elevation in astrocyte calcium triggers the insertion of more glucose transporters into the cell membrane, facilitating glucose uptake from the blood[25]. Third, regulation of oxygen supply to the entire body involves acidification of brainstem astrocytes by CO_2, which leads to a calcium increase and ATP release that in turn increases breathing rate[26]. These discoveries led to the idea that astrocytes constitute a network of cells that process information and regulate brain energy supply in parallel with neurons. In fact, hominid astrocytes, with their increased complexity and functionality, propagate calcium waves four times as fast as rodent astrocytes[17,27]. This may lead to the synaptic plasticity and learning ability unique to humans – but also, perhaps, to our unique neurological diseases.

Astrocytes directly mediate the physical structure of neurons, as well. Transcriptome profiling indicates astrocytes express proteins involved in phagocytosis[28]. MEGF10 and MERTK, two such proteins, allow astrocytes to prune both synapses and portions of the neuronal dendritic arbor[29]. Physical alterations to the connectome of each neuron changes the signals that can evoke a response, refining the capacity of each cell to signal and evoke other responses. Deletion of MEGF10 and MERTK during development results in a failure to refine signaling pathways and results in an excess of functional synapses[29]. Astrocytes continuously engulf both excitatory and inhibitory synapses, constantly pruning and refining the neuronal architecture[29,30] and thus altering the networks that compose the brain.

1.1.3 ASTROCYTE STRESS RESPONSE

Alterations in astrocyte signaling, protein expression, and morphology have been implicated in many diseases including epilepsy[31], inflammation[32], Alzheimer's disease[33], Huntington's disease[34], and even HIV infection[35]. In each instance astrocytes are attributed with diverse functions both compensatory and pathogenic. This obviously complicates the study of astrocyte reactivity. Typically, early neuropathology is associated with protective glial responses[36-38] while late neurodegeneration is associated with glia spreading inflammatory factors and degrading damaged tissue[39-41]. However, the extensive heterogeneity of astrocyte functions renders even this assumption often false.

For example, following neuronal injury astrocytes form a glial scar, a structure characterized as an extreme form of reactive astrogliosis that occurs around an injury site (Figure 1.4)[42]. The process involves expansion of astrocyte processes and deposition of inhibitory chondroitin sulfate proteoglycans[43]. In addition to these glial components, a fibrotic portion of the scar is formed as fibroblasts derived from perivascular and meningeal cells invade the region and deposit a collagen matrix[44]. Glial scarring acts as a barrier to regeneration of damaged CNS regions, and the process has served as one of the major barriers to recovery after spinal cord injury[45]. However, this glial scar may also serve to isolate damaged or degenerating regions from healthy ones, protecting the function of nearby neurons[38]. Glial scars are associated with an extensive acute injury or a protracted chronic one, rather than a mild to moderate injury as used in the models herein. However, the simultaneous protective and pathological components of glial responses are reported even in the earliest stages of neuropathology.

Recently, reactive astrocytes were further characterized into A1 and A2 subtypes[46]. A1 astrocytes upregulate many destructive protein cascades, while A2 astrocytes upregulate neurotrophic factors. It appears these two classifications of reactive astrocytes are induced through different pathologies. A1 astrocytes require reactive microglia, as the phenotype is induced through a combination of microglia-derived Il1α, TNF and C1q. A2 astrocytes, a much less studied subtype, appear to be induced by ischaemia, but may additionally be induced through other mechanisms[47]. The A2 subtype appears to be involved in many protective cascades, but the full extent of this protection is largely unknown.

A characteristic of several neurodegenerative diseases is aggregates of the microtubule-associated protein tau. In Alzheimer's disease, accumulation and dysfunction of tau is strongly correlated with the appearance of dementia[48,49]. Although astrocytes in mouse models of Alzheimer's disease do not express tau themselves, these astrocytes demonstrate the earliest

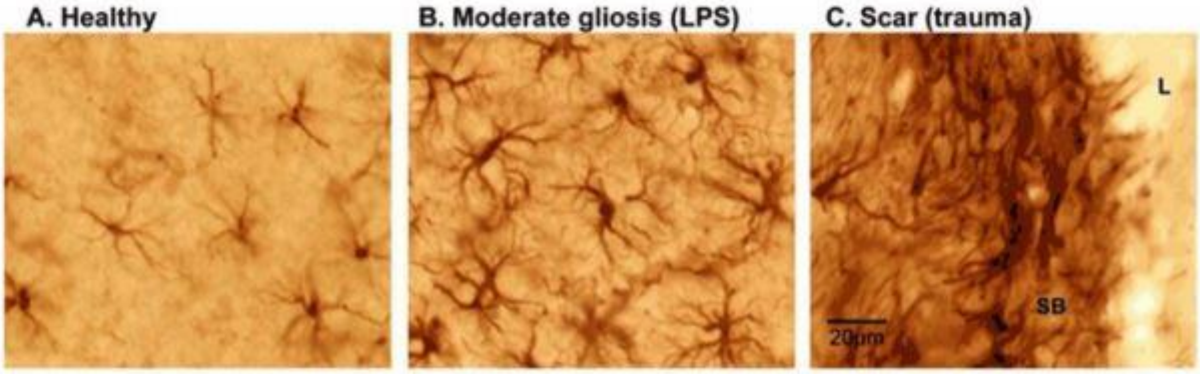

Figure 1.4 Grades of astrocyte reactivity following injury.

A. Healthy astrocytes distribute relatively evenly throughout nervous tissue, tiling such that each astrocyte has a distinct region of tissue for which it is responsible. **B.** Moderate gliosis induced by lipopolysaccharide results in hypertrophy. Astrocytes no longer occupy isolated regions of tissue, and processes become larger. **C.** More severe trauma can lead to the formation of a glial scar, an extreme form of reactive gliosis. Glial scars act as a barrier (SB: scar border) between damaged (L: lesion) and healthy tissue. Scale bar: 20 µm.

Figure from Verkhratsky et al., 2012, and used in accordance with Copyright Clearance Center's RightsLink service.

morphological changes and functional deficits[50]. These alterations likely result in neurological pathology, as transplantation of neural precursor cells that differentiate into astrocytes can rescue the neuronal death associated with this model[51]. However, astrocytes alter their metabolic profile early in models of Alzheimer's to compensate for diminished energetic availability, sustaining neuronal functionality and implying a multifaceted response to this stressor[52].

As in many neurodegenerative diseases, glial pathology precedes symptoms of Parkinson's disease as well[53,54]. Intriguingly, some studies describe the substantia nigra (SN) as particularly deficient in astrocytes compared to other regions of the brain, and indicate that this deficiency causes a particular vulnerability in SN neurons[4,55]. Early in Parkinson's disease progression, astrocyte energy-sensing and signaling pathways become dysregulated as the brain begins to use alternative sources of energy[56,57]. Although these alternative sources of energy (especially ketones) do maintain neuronal function, that function comes at a cost. Ketogenic metabolism causes significantly more metabolic stress than oxidative glucose metabolism and can stress the neurons beyond repair when it is chronically utilized[58]. Alterations in the metabolic profile of the brain are often associated with neuropathology, and are explored in greater detail in subsequent chapters.

1.1.4 ASTROCYTE GAP JUNCTIONS AND CHEMICAL SYNAPSES

Gap junctions provide the unique modality of a direct pathway for information distribution. This communication occurs through the direct exchange of cytoplasm between cells through a pore connecting the two cell membranes. This allows both for electrical coupling and rapid distribution of small molecules. In the brain, glia constitute the major population of cells coupled by gap junctions, forming a network of closely linked communicating cells[59]. Expression of connexins persists throughout the lifespan with a few differences between glial classes. Each glial cell type expresses a specific connexin or set of connexins, but no connexin is solely specific to glia[60-63].

The most extensive, and most extensively studied, glial network is that of astrocytes. Astrocytes primarily express connexin 43 (cx43)[61,64,65]. Astrocytes do also express connexins 30 and 26 to a much lesser extent than cx43, but generally use each in heteromers with cx43 subunits[62,66,67]. Intriguingly, the astrocyte network appears to extend both to oligodendrocytes and neurons, most often noted *in vitro* or during development but occasionally noted in select brain regions[68-73]. How this network alters through disease is largely unknown; however, connexin 43 expression increases during chronic stress[64]. Alterations in phosphorylation state and expression pattern have been briefly explored, but are largely unknown and likely depend largely on the stressor a particular region is exposed to[74].

1.2 NEURON/ASTROCYTE METABOLIC INTERACTIONS

Listen, strange women lying in ponds distributing swords is no basis for a system of government!

Monty Python

1.2.1 GLUCOSE DISTRIBUTION AND UPTAKE

The brain has disproportionately high energy requirements compared to the periphery. Despite representing only 2% of a human's adult body mass, the brain accounts for 30-50% of the resting rate of energy consumption[75]. This energetic discrepancy is further compounded by the fact that the brain is almost entirely oxitative; glucose is often termed the 'obligatory energy substrate' of the adult brain[76,77]. Glucose is a logical choice for the brain's purposes. When metabolized, it produces a minimal level of damaging reactive oxygen species (ROS) and is, for the most part, readily available within the blood stream. Under particular circumstances the brain has the capacity to use other blood-derived energy substrates, such as ketone bodies, glutamate, and glutamine during development and starvation[78-80] or lactate during periods of intense physical activity[81], but these instances are limited and generally produce metabolites more damaging to the brain than those generated by glucose.

The rate at which glucose is transported from the blood stream to the brain depends largely on the activity within any particular region. There is strong *in vitro* and *in vivo* evidence that astrocytes, mainly through neuron-to-astrocyte glutamate signaling, are essential contributors to vasomotor responses to neuronal activity[82,83]. Vasoconstriction and vasodilation involve different but parallel signaling cascades within astrocytes. To cause vasodilation, Ca^{2+}

transients within astrocytes resulting from mGluR stimulation trigger the formation of arachidonic acid, which is then converted into vasodilating agents such as epoxyeicosatrienoic acids and prostaglandin E2[19,82]. Alternatively, arachidonic acid can diffuse into smooth muscle cells where it is converted into 20-hydroxyeicosatetraenoic acid, a vasoconstricting agent[23]. Vasoconstriction and vasodilation allow for precise control of the energy supply directed to any particular region of the brain. Due to the limited nature of the brain's energy reserves, neurons are highly dependent on the uninterrupted supply of energy substrates from the circulation.

Glucose is transported by aptly named glucose transporters, or GLUTs, and is phosphorylated by hexokinase to produce glucose-6-phosphate. Glucose-6-phosphate can be processed via different metabolic pathways depending on immediate need (Figure 1.5). The three main pathways are 1) glycolysis, which

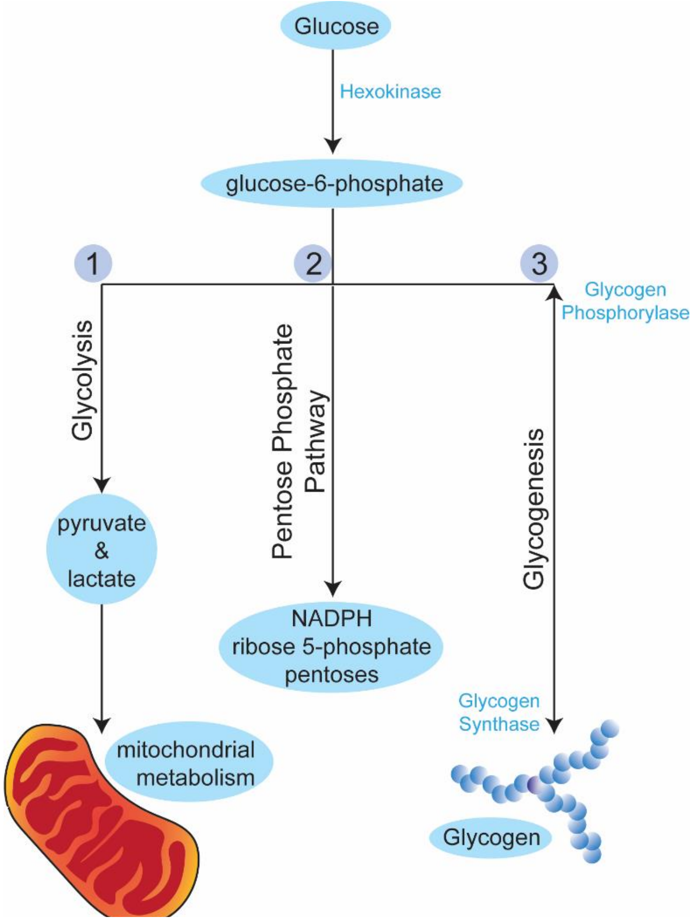

Figure 1.5 Glucose processing pathways.

Glucose is phosphorylated by hexokinase to produce glucose-6-phosphate, which can be processed through multiple pathways dependent on the cell type and current demand. The most common is glycolysis, which produces pyruvate and/or lactate which can then be used by mitochondria for oxidative phosphorylation. The pentose phosphate pathway produces the precursors for nucleotide synthesis, particularly ribose-5-phosphate, and NADPH. Glycogenesis is a method by which glucose is stored in glycogen granules; chains within these granules are built up by glycogen synthase and glucose is mobilized by glycogen phosphorylase.

leads to pyruvate/lactate production and mitochondrial metabolism, 2) the pentose phosphate pathway, which produces the precursors for nucleotide synthesis and NADPH which maintains the cellular antioxidant potential, and 3) glycogenesis, the method by which astrocytes store glucose. As evidenced by the multiple routes glucose can follow, each individual cell does not necessarily fully metabolize glucose to CO_2 and water. Rather, a wide range of metabolic intermediates, along with glucose itself, can be rapidly distributed and later oxidized for energy production[80].

In addition to the well-defined calcium waves astrocytes use to propagate signals through their network, there is some evidence that electrical or mechanical stimulation triggers "metabolic waves" as well[84]. Metabolic waves are mediated by the Ca^{2+}-dependent release of glutamate. Astrocyte uptake of glutamate is Na^+ dependent, generating a Na^+ wave that propagates through gap junctions to their network. The propagating Na^+ signal is spatially and temporally correlated with increased glucose uptake[84]. Such metabolic waves could mediate the propagation of the metabolic response to regions distant from the activated neurons, allowing astrocytes to metabolically couple across portions of the brain.

1.2.2 GLYCOGEN

Glycogen is the biological repository for stored glucose and is found in most tissues. However, its main deposits reside in liver and skeletal muscle, so it is from these two tissues that the majority of our understanding of glycogen dynamics is derived. In the adult brain, glycogen is the primary energy reserve and is stored almost exclusively in astrocytes[85]. It is an advantageous form of energy storage; glycogen can be rapidly metabolized without ATP and, unlike lipids, can yield ATP under both aerobic and anaerobic conditions[86]. Despite the brain's low glycogen concentration compared to that of liver or muscle, this source of energy can extend axon function for over 20 additional minutes[85,87,88]. During periods of intense neuronal activity when energy demand exceeds neuronal capabilities, astrocyte glycogen is degraded to lactate, much of which is transferred to neurons for fuel[7,18,89]. Oddly, neurons do express glycogen synthase but, as with some enzymes specific to glycolysis, continuously degrade glycogen synthase through proteasomal-dependant mechanisms[85,90]. Manipulations that drive the expression of glycogen synthase in cultured neurons cause apoptosis, highlighting the uniquely astrocytic mechanism for its production in the brain[90].

When glycogen's localization to astrocytes was first discovered, many scientists raised an obvious question: why is glycogen stored exclusively in astrocytes when neurons are the most energy-demanding cell type in the brain? We know that astrocytes do not have the capability to modulate blood glucose levels with their glycogen stores; brain glycogen levels of 6 - 12 µmol[91] are insignificant compared to those in liver (100 - 500 µmol) and muscle (300 – 350 µmol)[92]. Thus, astrocyte glycogen stores must be utilized by the brain itself. This led to some of the earliest discoveries regarding astrocyte/neuron metabolic interactions. Electron microscopy in the 1970s demonstrated that astrocyte glycogen stores are greatest in brain areas with the highest synaptic density[93], implying a role in the energy-dependent process of synaptic transmission. In the early 1980s, this role was further evidenced when Magistretti et al. discovered that a restricted set of neurotransmitters could drive glycogenolysis in cortical slices and primary astrocyte cultures[94,95]. Later studies demonstrated that increasing glycogen stores

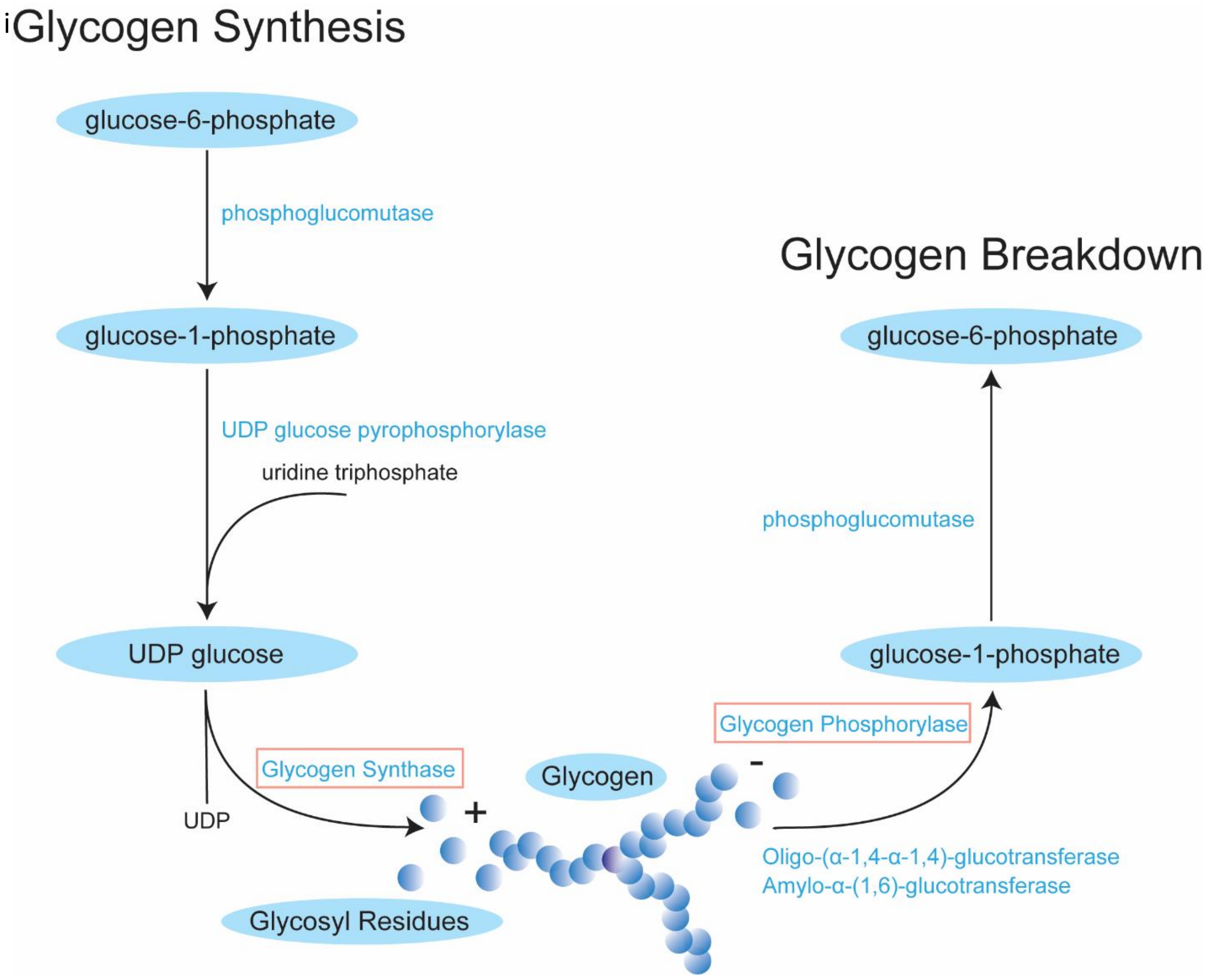

Figure 1.6 Glycogen synthesis and breakdown.

Glycogen formation involves a few key enzymes. First, glucose-6-phosphate is converted to glucose-1-phosphate by phosphoglucomutase. Next, UDP glucose pyrophosphorylase catalyzes a reaction that combines glucose-1-phosphate with uridine triphosphate to form UDP glucose. This reaction is the source of the glycosyl residues that donate to the glycogen molecule. Glycosyl units attach to glycogenin, glycogen's protein core, via their hydroxyl group on a tyrosine side chain of the protein in a reaction catalyzed by glycogen initiator synthase. Additional glycosyl units attach to those bound to the core through the formation of an α-1,4-glycosidic bond catalyzed by glycogen synthase. After about 8-10 glycosyl units, amylo-(α-1,4-α-1,6)-transglycosylase catalyzes the formation of a branch by forming an α-1.6-glycosidic bond. This increases the number of nonreducing ends to which a glycosyl unit can attach, and allows simultaneous release of multiple glycosyl residues[1]. Glycogen metabolism occurs independently from formation, involving a completely different set of enzymes. Glycogen phosphorylase cleaves the α-1,4 bond between glycosyl residues, releasing glucose-1-phosphate until four glycosyl units remain before a branch point. The branches are removed by two cooperating enzymes. Oligo-(α-1,4-α-1,4)-glucantransferase removes the three outermost glycosyl units and attaches them to an unrelated nonreducing end of the molecule. The remaining glycosyl unit attached by an α-1,6 bond is removed by amylo-α-(1,6)-glucosidase, which releases that unit as glucose. Glycogen sysnthesis and degradation can occur simultaneously, but the appropriate reaction is favored based upon the surrounding glucose concentration[1].

are depleted[1,85,96].

In addition to its role as an energy reserve, there is compelling evidence for glycogen's role in normal brain function. Decreased neuronal activity, as observed during sleep and anesthesia, correlates with increased levels of brain glycogen[85,91,93], just as increased activity results in diminished glycogen levels[18,89,96]. More interestingly, pharmacological inhibition of glycogenolysis in astrocytes interrupts memory consolidation, long-term memory formation, and maintenance of long-term potentiation of synaptic strength[97-99]. Glycogen synthesis and degradation can occur simultaneously, but the appropriate reaction is favored based upon the surrounding glucose concentration[1].

Although the only source of glycogen in the brain is that within astrocytes, lactate derived from skeletal muscle glycogen stores circulates through the blood stream and can be utilized by neurons[81,100]. This is a potential mechanism for the positive impact of exercise on neurodegenerative progression; exercise opens another potential 'pool' of glycogen for the brain's utilization.

1.2.3 CANONICAL GLUCOSE METABOLISM: GLYCOLYSIS AND MITOCHONDRIAL OXIDATIVE PHOSPHORYLATION

From an organ level, the nervous system's metabolism is almost fully oxidative. Elegant studies pioneered in the 1940s by Schmitt and Kety[76] and later by Sokoloff[77] demonstrate that glucose is the obligatory physiological energy substrate of the brain. When metabolized fully, glucose produces CO_2 and water to yield 32-36 ATP molecules per molecule of oxidized glucose.

The past 20 years have added cellular resolution to these organ studies, demonstrating that glial cells predominantly process glucose glycolytically while neurons are mainly oxidative[87,101].

To be metabolized, glucose first must go through a series of events together termed glycolysis. Glycolysis is an anaerobic process resulting in a net output of two NADH, two ATP, and two pyruvate molecules. ATP is immediately useful and pyruvate can be shuttled to mitochondria for further oxidation. NADH is useful as well – it serves as an electron donor within the mitochondrial electron transport chain. To produce two additional ATP molecules, pyruvate can be further reduced to lactate by lactate dehydrogenase. This lactate can then be transported through monocarboxylate transporters (MCTs) into the extracellular space, where, in the nervous system amongst other tissues, cells shuttle it to mitochondria expressing a specialized mitochondrial lactate oxidation complex. This complex allows lactate entry and conversion back into pyruvate for oxidative phosphorylation[101].

Oxidative phosphorylation is a process that forms ATP due to electron transfer from NADH or $FADH_2$ to O_2 through a series of electron carriers. The process generates 26 of the 30 ATP molecules formed as glucose is completely oxidized, meaning it is the major source of energy in aerobic organisms. As electrons flow from NADH or $FADH_2$ across the mitochondrial inner membrane protons are pumped out of the mitochondrial matrix. The resulting uneven distribution of protons results in a pH gradient and a transmembrane electrical potential, generating a proton-motive force. As protons flow back into the mitochondrial matrix through various enzyme complexes ATP is synthesized. Thus, the proton gradient and double membrane structure of mitochondria are critical for cellular respiration. As discussed later, mitochondrial damage and structural alterations are some of the earliest signs of neuropathology[102,103].

1.2.4 LACTATE SHUTTLE

Among the metabolic substrates the brain processes, lactate has been the center of much attention in recent years. Lactate is present in the extracellular space in concentrations similar to those of glucose (between 0.5 and 1.5 mM) [104]. While it has long been considered the dead end of anaerobic processes, this view has drastically changed in light of growing evidence indicating that it represents another important energy source for the brain[105-107]. In many emerging models, lactate is even regarded as the product of glycolysis rather than pyruvate[108]. The main evidence for this is the discovery of a mitochondrial lactate oxidation complex, reported in neurons among many other cell types, which would allow lactate entry and oxidation in the mitochondria itself[101]. This complex, and the metabolic cooperation it implies between neurons and astrocytes, has been evolutionarily conserved from *Drosophila melanogaster* through the mammalian brain[101,109,110].

Both astrocytes and neurons have the capacity to fully oxidize glucose and/or lactate, and both contain roughly equivalent numbers of mitochondria across various regions of the brain[11,80,111]. However, neurons and astrocytes preferentially utilize different metabolic pathways under physiological conditions and have different cell type-specific expression patterns of key genes regulating energy metabolism[11,90,112] (Figure 1.5). Consistent with their higher energy requirements, neurons sustain oxidative metabolism at an elevated rate compared to glia[113-115]. Intriguingly, neurons efficiently use lactate as an energy substrate and will preferentially utilize it over glucose when both substrates are present[81,115,116]. Conversely, astrocytes preferentially metabolize glucose due to their elevated expression and maintenance of the enzyme 6-phosphofructose-2-kinase/fructose-2,6-bisphosphatase-3 (Pfkfb3), which, oddly, is subjugated to constant proteasomal degradation after its production in neurons[112,117]. The enzyme is a potent activator of the key glycolytic enzyme phosphofructokinase-1 (PFK), and is responsible for upregulating glycolytic rate during periods of metabolic stress[117]. Additionally, astrocytes and neurons differentially group their mitochondrial respiratory chain (MRC) complexes. In astrocytes most complex I is uncoupled from supercomplexes, resulting in less efficient mitochondrial respiration, while neurons embed most of their complex I into their

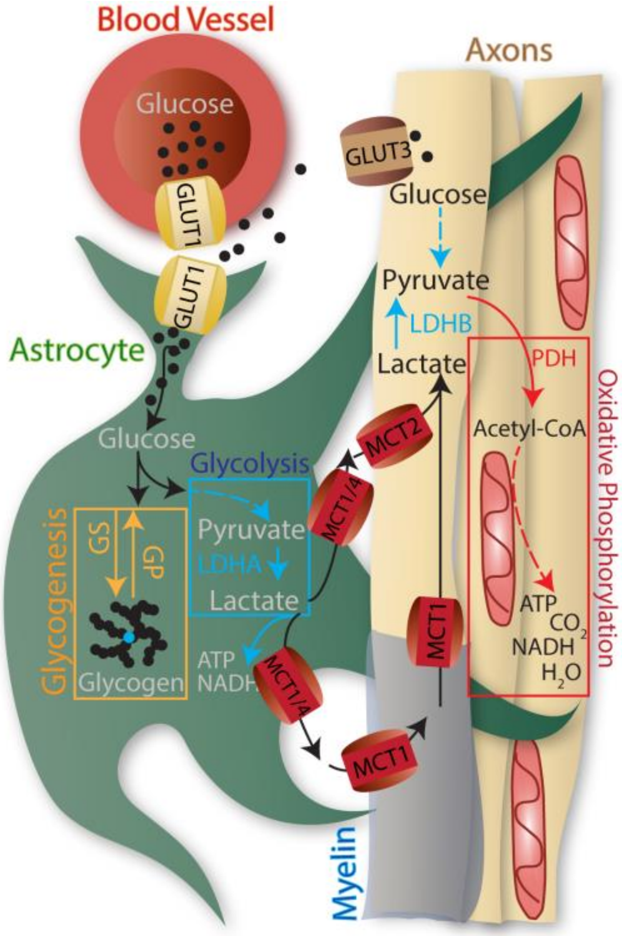

Figure 1.7: Key astrocyte/axon metabolic components.

Glucose is transported from vessels via GLUT1 transporter, then uptaken by astrocytes via GLUT1 and, to a lesser degree, axons via GLUT3. Astrocytes form glucose into glycogen stores via glycogen synthase (GS) and mobilize it by glycogen phosphorylase (GP). Via glycolysis, glucose is metabolized into pyruvate, which is metabolized by lactate dehoydrogenase A (LDHA) into lactate, making ATP and NADH. Monocarboxylate transporters 1 and 4 (MCT1/4) transport lactate into the extracellular space, where it is uptaken by axonal MCT2. Lactate is then converted back into pyruvate by lactate dehydrogenase B (LDHB). Pyruvate is metabolized in mitochondria, producing large sums of ATP along with CO2, NADH, and H2O.

supercomplexes for increased efficiency[118]. As a result, neurons and astrocytes function as a compartmentalized metabolic unit, cooperating to distribute energy in an efficient manner.

Due to these different metabolic profiles, astrocytes uptake far more glucose than they fully reduce. It is estimated that astrocytes account for only 5-15% of the brain's energy expenditure[119], but are responsible for approximately half of glucose uptake and even increase that proportionally with activity[120-122]. A central point of the astrocyte-neuron lactate shuttle hypothesis provides a simple explanation for this discrepancy: astrocytes transfer energy substrates to neurons to compensate for their high activity levels[123]. The model states that neuronal activity increases extracellular glutamate, which is taken up by Na^+-dependent mechanism by glial glutamate transporters. The resulting increase in Na^+ activates the Na^+/K^+ ATPase, thereby increasing ATP consumption, glucose uptake, and glycolysis in astrocytes. This leads to a large increase in lactate production, which is released into the extracellular space and subsequently taken up by neurons for use in oxidative phosphorylation. Through this mechanism, neurons are able to sustain their elevated rates of energy consumption without dependence on glycolysis itself.

Astrocyte support of neuronal function is further supported by recent studies demonstrating that mice presenting a haploinsufficiency of the neuron-specific glucose transporter GLUT3 do not present any neurological or brain energy metabolism abnormalities. Further, their brain glucose utilization does not differ from that of wild-type animals[124,125]. In contrast, haploinsufficiency for GLUT1, which is absent in neurons but highly expressed in astrocytes, results in a severe neurological phenotype[126]. Certainly, there is abundant evidence for a net transfer of energy from astrocytes to neurons; the astrocyte-neuron lactate shuttle is the most widely accepted model for this energy transfer.

In white matter, the astrocyte-neuron lactate shuttle involves a third cell type: oligodendrocytes. Much of an axon's surface is covered by oligodendrocytes and their myelin, limiting the capacity for astrocytes to transfer metabolites through the extracellular space. To compensate, oligodendrocytes function as an intermediary by shuttling lactate from the extracellular space through monocarboxylate transporter 1 (MCT1)[127]. The oligodendrocytes themselves do not utilize the lactate – inhibiting cytochrome C oxidase, a key component of mitochondrial oxidative phosphorylation, does not influence oligodendrocyte survival after development[128]. Rather, the lactate is again shuttled into the periaxonal space through MCT1, where neuronal MCT2 transporters then shuttle it into axons[5]. How the intermediary oligodendrocytes alter their metabolic support through neuropathology, however, remains unknown.

1.2.5 ALTERATIONS DURING DISEASE

Oxidative injury is a unifying feature of many neuropathological conditions such as stroke[129], traumatic brain injury[130], and neurodegeneration[103,131-133]. The brain's particular susceptibility to oxidative injury exists due to several factors, including its high rate of oxidative energy metabolism (a process inevitably generating reactive oxygen species, or ROS), its high unsaturated fatty acid content (a substrate particularly prone to lipid peroxidation), and its relatively low antioxidant capacity[132,134]. Further, this antioxidant capacity is housed in a paradoxical manner. Despite the fact that the greater part of the brain's oxidative metabolism occurs in neurons, neurons contain extraordinarily limited defense mechanisms against oxidative stress. Nearby astrocytes contain large, readily available stores of various antioxidant molecules and ROS-detoxifying enzymes including glutathione, heme-oxygenase 1, glutathione peroxidase, glutathione S-transferase, catalase, and thioredoxin reductase[132,135-137]. Astrocyte cultures are significantly more resistant to oxidative stress than neuronal cultures and will even protect neighboring neurons in co-culture systems[138,139]. This suggests that neurons are highly dependent on astrocytes not only for for metabolic substrates, but also for defense against the oxidative stress those substrates generate.

The dependence of neurons upon astrocytes for normal function only increases during neuropathology. Early stages of neurodegeneration typically involve increased metabolic activity, further compounding metabolic and oxidative stress[131,140]. Aging, another key feature of most neurodegenerative diseases, additionally involves reduced neuronal metabolic capacity[113,141]. The most instrumental and abundant antioxidant in the brain is glutathione (GSH), which can act directly as a ROS scavenger or be used as a substrate for glutathione S-transferase or glutathione peroxidase[142]. Both neurons and astrocytes can synthesize the GSH tripeptide; however, neurons are highly dependent on astrocytes for the supply of precursor amino acids, especially cysteine, for their own GSH synthesis[135,142]. The differential antioxidant response of neurons and astrocytes is partially explained by the preferential astrocytic expression and activation of nuclear factor erythroid-2-related factor 2 (Nrf2), a redox-sensitive transcription factor that plays a key role in a cell's sensitivity to ROS and orchestrates the antioxidant response[139]. It is further compounded by the antioxidant potential's reliance upon NADPH as an electron donor to regenerate GSH; as NADPH is generated through glycolysis and the pentose phosphate pathway, astrocytes have a more abundant supply and thus greater antioxidant potential[143].

Astrocytes play many active roles in neurodegeneration in addition to conferring resistance against the oxidative stress associated with neuropathology. Astrocytes exposed to amyloid-beta (Aβ), a peptide long associated with Alzheimer's disease, demonstrate profound alterations in their metabolic phenotype. Following Aβ exposure, astrocytes increase glucose uptake along with its metabolism and incorporation into glycogen[144]. These astrocytes then reduce their support of neurons they are co-cultured with, causing impaired neuronal viability[144]. This relates to studies demonstrating that when mitochondrial respiration in neurons is inhibited with NO, astrocytic glycolysis plays a critical role in preventing the collapse of mitochondrial membrane potential and thus cell death[138]. In a model of glaucoma, a neurodegenerative disease primarily impacting the optic nerve, if astrocytes are prevented from remodeling degeneration progresses much more rapidly[36]. The same is true in models of ischemia[37,38]. Thus, rather than considering each cell type independently, scientists studying neurodegeneration must consider neurons and astrocytes as a cohesive unit, together establishing the function of the brain.

1.3 NEURONAL ALTERATIONS IN EARLY NEURODEGENERATION

I cannot imagine any condition which would cause a ship to founder…
Modern shipbuilding has gone beyond that.

Capt. E. J. Smith, RMS Titanic

1.3.1 TRANSPORT DEFICITS

As neurons degenerate, one of the earliest noted functional deficits involves axonal structure and function. Despite heterogeneous etiology, models and human case studies of Alzheimer's Disease[145,146], familial amyotrophic lateral sclerosis (ALS)[147-149], Parkinson's Disease[150,151], Huntington's Disease[152], and glaucoma[153] demonstrate that early disease states commonly involve accumulation of abnormal neurofilaments within the axon. Neurofilaments act as molecular highways for motor proteins as axonal cargoes are propelled to and from presynaptic terminals. Thus, disruptions in their structure result in transport failure for critical cargo produced in the soma, or waste that needs to be moved away from the synaptic terminal and degraded. This causes abnormal accumulation of proteins and organelles, as well as starves distal regions of neurons of necessary resources, such as mitochondria and neurotransmitters[154].

Axonal transport function involves two major components: molecular motors (kinesin and dynein) and the microtubules these motors use to 'walk' to different cellular compartments. Microtubules are polarized, containing a fast growing plus end and a slower growing minus end. In axons, microtubule organization is nearly uniform, with the plus ends oriented toward the distal synapse and the minus end toward the proximal cell body. Most molecular motors of the kinesin family unidirectionally move toward the microtubule plus end, and so are classified as anterograde transporters in neurons. In contrast, dynein family members move toward the minus end and thus mediate retrograde transport.

Disruptions in axonal transport can occur through many mechanisms. Mutations that inhibit molecular motor activity have been implicated in some familial forms of ALS[155] and Charcot-Marie-Tooth disease[156]. The microtubules themselves can be destabilized, inhibiting motor protein binding, a well-published function of mutant huntingtin protein[157]. Interactions between motor proteins and their cargos can be impeded, such as when p28 and/or cdk5/p35 kinases hyperphosphorylate newly synthesized neurofilament components, preventing their attachment to motor proteins and thus their transport to growing ends[158]. Damage to mitochondria, too, has been linked to a reduction in their anterograde transport[159]. Inhibition of anterograde mitochondrial transport leads to a net increase in their retrograde transport, resulting in depletion of mitochondria from axons. Axonal transport is an energy-demanding process, and diminished ATP levels would impede movement[160]. Microtubule maintenance, too, requires ATP[161]. Any damage to mitochondria or related alterations in their distribution can have a profound effect on axonal transport and thus maintenance of distal portions of a neuron.

1.3.2 MITOCHONDRIAL CHANGES

Mitochondrial alterations during neurodegenerative disease encompass even more than simply the loss of ATP and diminishment in their number at distal regions of a neuron. Mitochondria are critical regulators of cell death and play a key role in multiple apoptotic pathways[162,163]. Mutations in mitochondrial DNA and increased oxidative stress are both linked to aging, a unifying element and risk factor for most neurodegenerative diseases[113]. Further, many neurodegenerative disease-specific proteins interact with mitochondria, including APP[164], PS2[165], Parkin[166], α-synuclein[167], and huntingtin[157,168].

Because mitochondria have their own generational and reproductive cycle, they accumulate mutations at a different rate than their host cell[169]; additionally, because adult neurons do not canonically reproduce except in particular regions of the brain, mitochondrial DNA is a critical weak point for mutations[170,171]. Although most mitochondrial proteins are encoded by the nuclear genome, human mitochondria retain a circular molecule encoding 13 components of the respiratory chains as well as the rRNAs and tRNAs necessary to support intramitochondrial protein synthesis[172]. Mutations in mtDNA cause a variety of diseases, the majority of which impact the brain and muscles[173] – the tissues with the highest energy requirements[75]. The point mutations that accumulate at a relatively high rate in other tissues occur at much lower levels in the brain, where mitochondria are likely under greater selection pressure due to high demand[174,175]. This is supported by the fact that noncoding regions of mtDNA in the brain accumulate between twice and four times as many mutations as coding regions[176].

Mitochondrial health directly influences both the development of neurodegenerative disease and longevity itself in otherwise healthy individuals. Mitochondrial DNA replication is carried out by mtDNA polymerase-γ (POLG), which in addition to its 5’-to-3’ polymerase activity exhibits 3’-to-5’ exonuclease (proofreading) activity. Humans with POLG mutations, who invariably accumulate more mtDNA mutations, exhibit Parkinsonism, ophthalmolegia, seizures, and myopathy[177,178]. The ROS generated through mitochondrial processes, too, impact aging; in fact, increasing mitochondrial antioxidant capacity has been shown to increase median and maximal lifespan in an already long-lived mouse strain by 20%, even delaying cardiac pathology, arteriosclerosis, and cataract development[179].

This correlates with human findings demonstrating oxidative damage plays a major role in the cognitive decline that accompanies aging[180]. Genes downregulated with age relate particularly to synaptic plasticity, vesicular transport, and mitochondrial function. These genes suffer markedly increased oxidative DNA damage compared with age-stable or –upregulated genes. To investigate whether impaired mitochondrial function could predispose these age-downregulated genes to DNA damage, these same scientists used siRNAs to reduce SH-SY5Y cellular mitochondrial function in a manner approximating the reduction seen in the aged human cortex[180]. This resulted in increased DNA damage in the same age-downregulated genes, and was partially reversed by the antioxidant vitamin E. This partial rescue is likely due to the complexity of mitochondrial ROS metabolism; interventions involving administration of one or few antioxidants are likely too simplistic.

1.3.3 MORPHOLOGICAL ALTERATIONS

Morphological alterations to neurons during neurodegenerative disease occur primarily in the dendritic and axonal compartments; intriguingly, the cell body can remain long after both compartments have failed[153]. Prior to complete failure, both the dendritic and axonal compartments undergo more subtle alterations.

Dendritic spines, specialized structures on which excitatory synaptic contacts form, have been studied in detail in Alzheimer's disease. A commonality between many Alzheimer's disease models, and a pathology noted in the human disease, is the gradual dysfunction and eventual loss of dendritic spines[181]. Many diverse mechanisms have been proposed to cause this pathology, from amyloid beta accumulation to tau hyperphosphorylation and microglia activation; the true etiology is likely complex and involves components of each mechanism.

Intriguingly, microglia have been implicated in dendritic remodeling involved in other neurodegenerative diseases as well. During glaucomatous optic neuropathy, retinal ganglion cells exhibit extensive pruning of their dendritic arbors in both the off[182] and on[183] substrata. The complement component C1q localizes to dendrites prior to microglial engulfment, and inhibition of C1 production is sufficient to preserve dendritic and synaptic architecture[184]. However, the complement pathway plays multiple roles in homeostasis through aging[185], so more study is needed before determining the correct complement-modulating therapeutics that could play a role in preserving dendritic architecture from disease-related, but not homeostatic, pruning.

Within the axonal compartment, early alterations involve changes in the relationship between oligodendrocytes and neurons. The distance between nodes of Ranvier lengthens as the electrically resistive seal between the myelin and the axon at the paranode fails, exposing the voltage-gated Na^+ and K^+ channels in the juxtaparanode[186]. Each of these alterations have been observed in a wide range of diseases, including stroke, spinal cord injury, glaucomatous optic neuropathy, and multiple sclerosis[187,188]. These alterations are not only common, but also among the earliest changes noted in neuropathology.

Intriguingly, the axonal compartment exhibits alterations during normal aging. With age, axon caliber and neurofilament density increase without corresponding changes in myelin thickness, otherwise known as increasing the g-ratio[189]. Further, the axonal mitochondrial capacity within axons diminishes by up to 30% during aging[113]. This loss of energetic capacity may be accelerated by neurodegeneration, or it may accelerate neurodegeneration[190]; the causality is yet to be determined.

1.4 OPTIC NEUROPATHIES

The only thing worse than being blind is having sight but no vision.

Hellen Keler

1.4.1 THE VISUAL SYSTEM

The majority of the central nervous system is enclosed within the skull or spinal cord. Such protective structures help minimize trauma to the central nervous system but are a hindrance to experimental manipulation and longitudinal monitoring. The unique accessibility of the retina renders it a particularly useful structure for visualizing and monitoring alterations throughout disease. Additionally, visual stimulus evokes distinct and repeatable behaviors, meaning the ultimate effects of manipulation can be easily monitored.

The retina originates as an outgrowth of diencephalon, the embryonic structure also responsible for the thalamus, hypothalamus, epithalamus, and subthalamus. Retinal progenitor cells are competent to produce all types of retinal neurons and remain as Muller glia once development is complete[191]. Early progenitor divisions produce ganglion cells, until eventual lateral inhibition signals the start of horizontal cell production – then cones, amacrine cells, rods, bipolar cells, and finally Muller glia[192]. Each cell type serves a distinct purpose in deciphering the visual scene, deconstructing it into distinct signals that are transmitted through the optic nerve to the brain.

In the mammalian retina, light passes through each cell type until it reaches the outer segments of photoreceptors at the back of the eye (Figure 1.8). These outer segments contain a protein complex called rhodopsin (rods) or photopsin (cones), which change their conformation in response to light and begin a chain of events that result in the conversion of a photon to a neuronal impulse. Photoreceptors communicate in graded impulses to bipolar cells, releasing glutamate in darkness and reducing that signal relative to the number of photons encountered. Bipolar cells provide a graded signal to retinal ganglion cells (RGCs), who then translate that signal into action potentials transmitted through the optic nerve to multiple regions of the brain.

There are three distinct varieties of glial cell in the mammalian retina. The first and most predominant are Müller glia, which extend vertically through the retina from the distal margin of the outer nuclear layer to the inner margin of the retina. Müller cell nuclei are usually found in the middle of the inner nuclear layer. Retinal astrocytes are found along the inner margin of the retina, amongst the nerve fiber layer and forming connections with the retinal vasculature. Microglia typically have a minimal presence in the retina, but migrate through the retina as

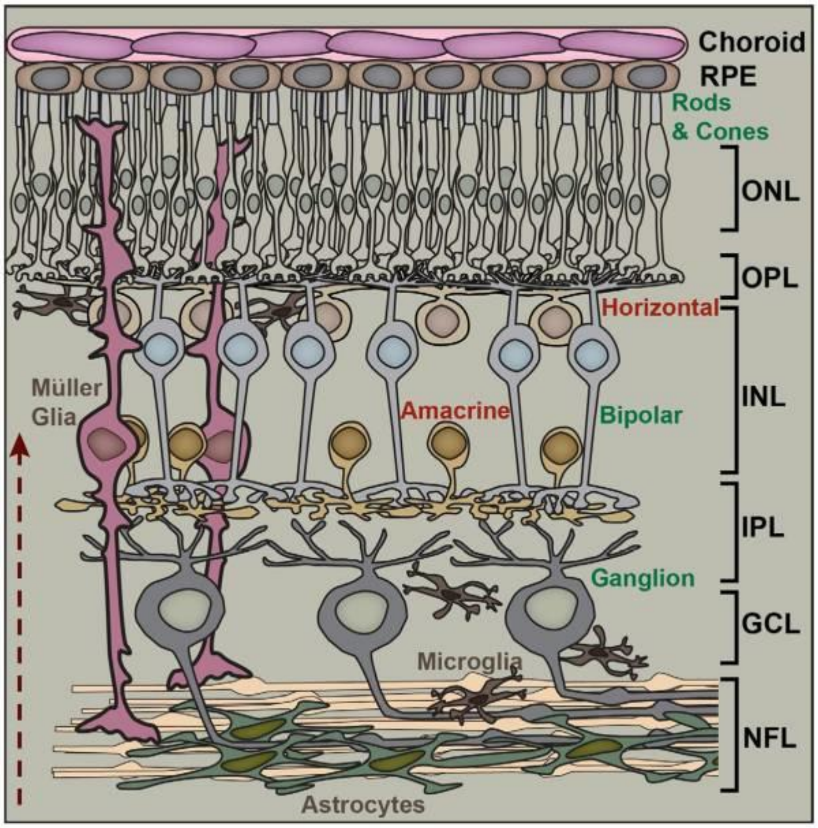

Figure 1.8 **Basic retinal circuitry.**

The fundamental retinal circuit includes rod and cone photoreceptors, bipolar cells, and retinal ganglion cells (RGCS), each of which are excitatory (glutamatergic). Synaptic transmission between photoreceptors and bipolar cells is modulated by inhibitory (GABAergic) horizontal cells in the outer plexiform layer (OPL), while amacrine cells modulate signaling between bipolar cells and RGCs in the inner plexiform layer (IPL). Müller cell bodies reside in the inner nuclear layer (INL) with bipolar, amacrine, and horizontal cell bodies. Astrocytes form a dense network over RGC axons in the nerve fiber layer (NFL), while microglia distribute dependent on retinal conditions. Red arrow indicates the path of light.

Figure from Calkins, 2012 and used in accordance with Copyright Clearance Center's RightsLink service.

they become reactive during disease[193]. In fact, each glial cell type becomes reactive during retinal disease and are often the initial signal of distress. Despite their limited occupation of the retina, astrocytes are plentiful throughout the optic nerve and brain, so play a major role in overall visual system health. RGCs extend their axons through the optic nerve, each of which projects to one or multiple regions within the brain responsible for interpreting different aspects of visual input. The percentage of optic nerve axons that synapse at each neuronal target varies between mammalian species. In primates, the majority (~85%) of RGC axons project to the lateral geniculate nucleus (LGN) of the thalamus[194-196], the central relay between the retina and primary visual cortex[197]. In rodents (Figure 1.9) only about 25% of RGC axons project to the LGN[198], approximately 80% of which also innervate the superior colliculus (SC)[199]. The SC is the main neuronal target for RGCs in rodents and is innervated by approximately 88%

of RGC axons, while in humans only about 10% of RGCs project to this location[198,199]. The differing targets between mammals reflects the different demands rodents and primates have for their visual systems; cortical vision is critical for humans, while rodents rely upon the rapid reflexes and eye movements coordinated by the superior colliculus.

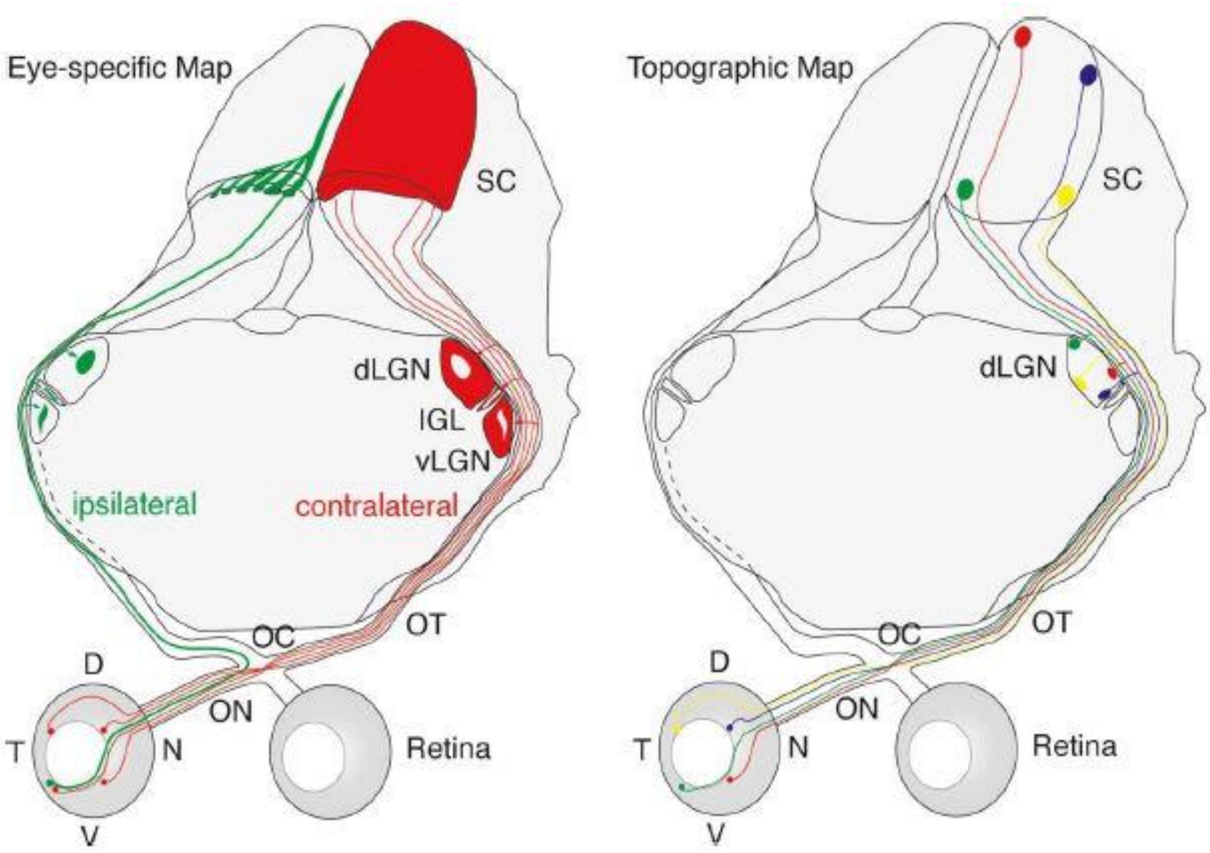

Figure 1.9 Murine optic projections.

Left: Upon entering the brain, murine RGCs project primarily to contralateral (red) visual processing areas including the lateral geniculate nucleus (LGN) and the superior colliculus (SC). A small population of RGCs connects ipsilaterally to these same regions. **Right:** RGCs project to the LGN and SC in a topographic manner, meaning the orientation of information in space is preserved from the retina as it is represented by each region of the brain.

Figure from Assali et al., 2014 and used in accordance with Copyright Clearance Center's RightsLink service.

1.4.2 LINKS BETWEEN OPTIC NEUROPATHIES AND OTHER NEURODEGENERATIVE DISEASES

Although very specialized for the visual system, retinal ganglion cells (RGCs) exhibit similarities to other CNS neurons as they respond to injury. Like neurons in other regions of the nervous system, RGCs have a very limited potential for axonal regeneration subsequent to injury[200]. In fact, extensive manipulation is necessary for any significant regeneration to occur, and such regeneration allows for limited visual ability at best[201,202]. The difficulties in optic nerve regeneration after injury are strikingly similar to those in the spinal cord[43,203], and findings in one field are often applied to the other.

Further links between retinal and brain diseases abound in neurodegenerative disease. In Alzheimer's disease, accumulations of β-amyloid and phosphorylated tau are associated with onset of symptoms[146,204]. Intriguingly, these accumulations exist in the retinas of both Alzheimer's disease patients and in transgenic mouse models of the disease[205,206]. Additionally, Alzheimer's disease patients exhibit a reduction in RGC numbers and optic nerve degeneration beyond that of normal aging[207,208]. In multiple sclerosis many patients are diagnosed with optic neuritis, in which RGC degeneration and demyelination is observed[209]. Many studies additionally demonstrate hypometabolism and oxidative stress are a common factor of most neurodegenerative disease[130,131,144].

As a whole, this evidence demonstrates RGCs are adversely affected by neurodegenerative diseases in much the same manner as other CNS neurons. It is, therefore, reasonable to believe that studies of RGC degeneration could likewise inform research related to all neurodegeneration.

1.5 GLAUCOMA PATHOGENESIS AND STUDY

"Sometimes I think a man could wander across the disc all his life and not see everything there is to see,' said Twoflower. 'And now is seems there are lots of other worlds as well. When I think I might die without seeing a hundredth of all there is to see it makes me feel,' he paused, then added, 'well, humble, I suppose. And very angry, of course."

Terry Pratchett

1.5.1 CLINICAL PRESENTATION OF GLAUCOMA

Glaucomatous optic neuropathy (glaucoma) is the world's leading cause of irreversible blindness, projected to impact 80 million people by the year 2020 and 112 million by the year 2040[210,211]. Glaucoma has two main risk factors: age, a common factor of many neurodegenerative diseases, and sensitivity to intraocular pressure (IOP)[212]. Of these, IOP is the only modifiable risk factor and as such is the target of clinical treatment. However, glaucoma is actually a family of diseases, each of which has a unique etymology.

The two most often cited subtypes of glaucoma are open angle and closed angle glaucoma. The 'angle' refers to the portion of the anterior chamber between the iris and cornea, where aqueous humor exits the eye through the trabecular meshwork into Schlemm's canal and finally to the episcleral veins (Figure 1.10). Constant production of aqueous humor by the ciliary body and its eventual removal through the trabecular meshwork is critical for generating a constant flow, refreshing the avascular tissue it surrounds. In humans, the fluid is typically 15 mmHg above atmospheric pressure (normal IOP). Elevation or loss of pressure indicates a disruption in aqueous fluid flow. In open angle glaucoma, this disruption involves the degradation and obstruction of the trabecular meshwork that leads to a decrease in outflow facility at the angle and increased IOP[213]. Closed angle glaucoma arises when the iris presses against the cornea, physically obstructing the angle to prevent outflow[214]. Patients with closed angle glaucoma typically exhibit exceptionally high IOP, which can create ocular pain, while patients with open angle glaucoma typically never feel any alterations[215]. Because both closed and open angle glaucoma are associated with increases in IOP, measurement of IOP by tonometry is a common component of eye health exams.

Intriguingly, many patients exhibit disease progression despite having normal IOP, a condition deemed normotensive glaucoma[216,217]. Even more interesting, these patients do often, but not always, benefit from IOP-lowering regimens[218-220]. Further, there are many individuals with elevated IOP that do not exhibit symptoms of glaucoma[221]. Therefore, glaucoma is not as simple a disease as one of IOP disturbances; IOP is certainly important, but

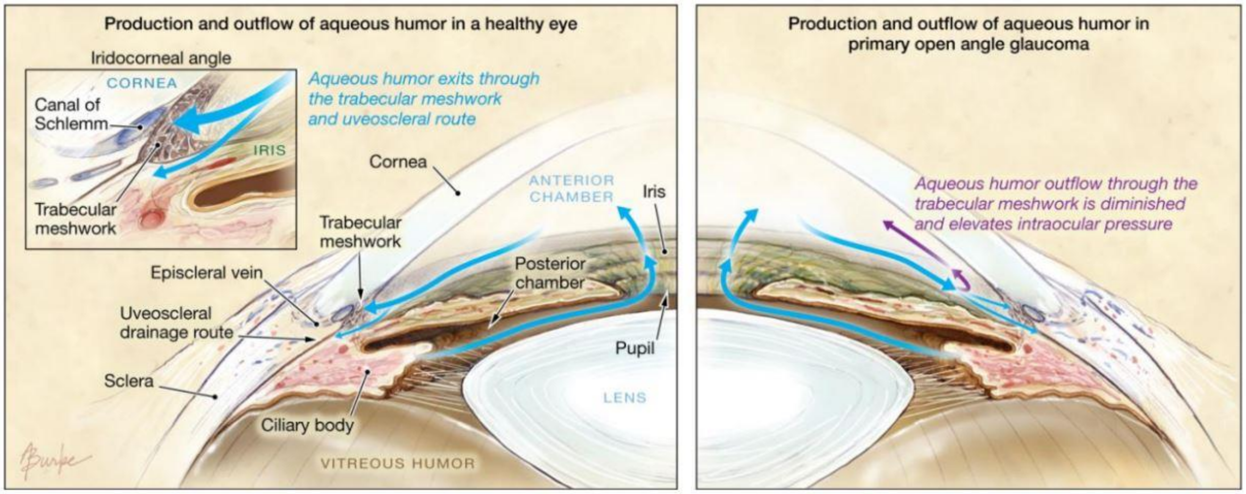

Figure 1.10 Production and outflow of aqueous humor in the eye.

Aqueous humor is continually produced by the ciliary body to nourish the avascular tissue of the anterior chamber as well as maintain intraocular pressure (IOP). In the healthy eye (left), aqueous humor flows between the lens and the iris through the pupil and exits the eye through drainage structures at the iridocorneal angle (see inset, left). Production of aqueous humor is balanced with outflow in the healthy eye to maintain IOP within a normal range (in humans, typically considered ≤21 mmHg). In primary open angle glaucoma (right), aqueous humor outflow is diminished or obstructed in some way. The resulting buildup of fluid in the anterior eye results in increased IOP.

Figure from Hollands et al., 2013 and used in accordance with Copyright Clearance Center’s RightsLink service.

more recent theories of the disease include cerebrospinal pressure as a component[222,223]. This model then involves trans-lamina cribrosa pressure, where IOP in the eye is balanced by cerebrospinal fluid pressure to regulate the structure of the optic nerve head; disturbances in either pressure, therefore, would result in glaucomatous progression[224].

There are a number of characteristics associated with clinical glaucoma presentation. Primary among these are deficits in the visual field and thinning of the retinal nerve fiber layer (RNFL), the portion of the retina in which RGC axons reside. Visual field loss is typically assessed by perimetry, in which the examiner maps the patient's field of vision to determine the location of scotomas, or areas of visual field loss. The most common scotoma exhibited in glaucoma is termed an arcuate scotoma, which forms an arc beginning temporally near the region of the optic disc, curving around into either the superior or inferior field, and ceasing toward the nasal end of the horizontal axis[225]. Many patients do not perceive scotomas until they have progressed significantly, both because peripheral vision is often affected first and because much of the visual system compensates for deficits in retinal vision. Intriguingly, there is a very strong tendency for optimizing the binocular visual field as scotomas appear, meaning that scotomas in both eyes do not occur randomly and even defy simple anatomic symmetry considerations[226,227]. This provides strong evidence that the two eyes degenerate neither independently from each other nor from the brain itself.

The clinically observed structural correlate of visual field loss is thinning of the RNFL, caused by loss of RGC axons. This is additionally associated with an increased "cupping" at the optic disc observed in clinical ophthalmoscopic exams (Figure 1.11). Optic nerve cupping is the key diagnostic factor for glaucoma, and is generally associated with axonal loss[228]. However, optic disc cupping can be a consequence of multiple disorders, not only glaucoma, meaning that up to 20% of patients may be misdiagnosed and treated for glaucoma due to misinterpretation of optic disc cupping[229]. Therefore, a glaucoma diagnosis involves optical coherence tomography, patient history, and examination of the retinal vasculature to rule out diseases that closely resemble glaucoma.

1.5.2 RGCS AND THEIR SUSCEPTIBILITY TO GLAUCOMATOUS NEURODEGENERATION

RGCs have a unique structure that accommodates the retina's need for transparency; until their axons exit the optic nerve head each remains unmyelinated. As myelin is opaque and photoreceptors reside below RGCs, this is necessary to maintain visual acuity. However, it also results in a unique susceptibility of RGCs to metabolic stress. Without myelin, RGCs must fire without energy-saving saltatory conduction for much of their initial length, including the optic nerve head that receives the primary glaucomatous stressors[230,231]. Additionally, RGC axons are particularly thin, especially when considering the distance they extend[111]. This further limits the energetic efficiency at which RGCs can signal. This susceptibility means that RGCs are particularly useful in modeling metabolic stressors during neurodegeneration, but also renders them easily damaged during disease. Likely, this susceptibility is what causes the NFL thinning noted in early stages of glaucoma.

RGC degeneration occurs first in the axon, with the cell body and axon terminals both remaining after the axon has disassembled (Figure 1.12)[153]. The mechanism of this disassembly, however, is still largely unknown. The two main theories hypothesize either a Wallerian-style neurodegeneration or a dying-back mechanism[212]. Insertion of the Wallerian degeneration slow allele (*Wld*^{S}) slows axonal loss in both the DBA[232] and an inducible rat model[233], although the mechanism this protein works within is currently unknown. RGC somas with intact axons remain in these models, but each show signs of early apoptotic injury[232]. Scientists additionally

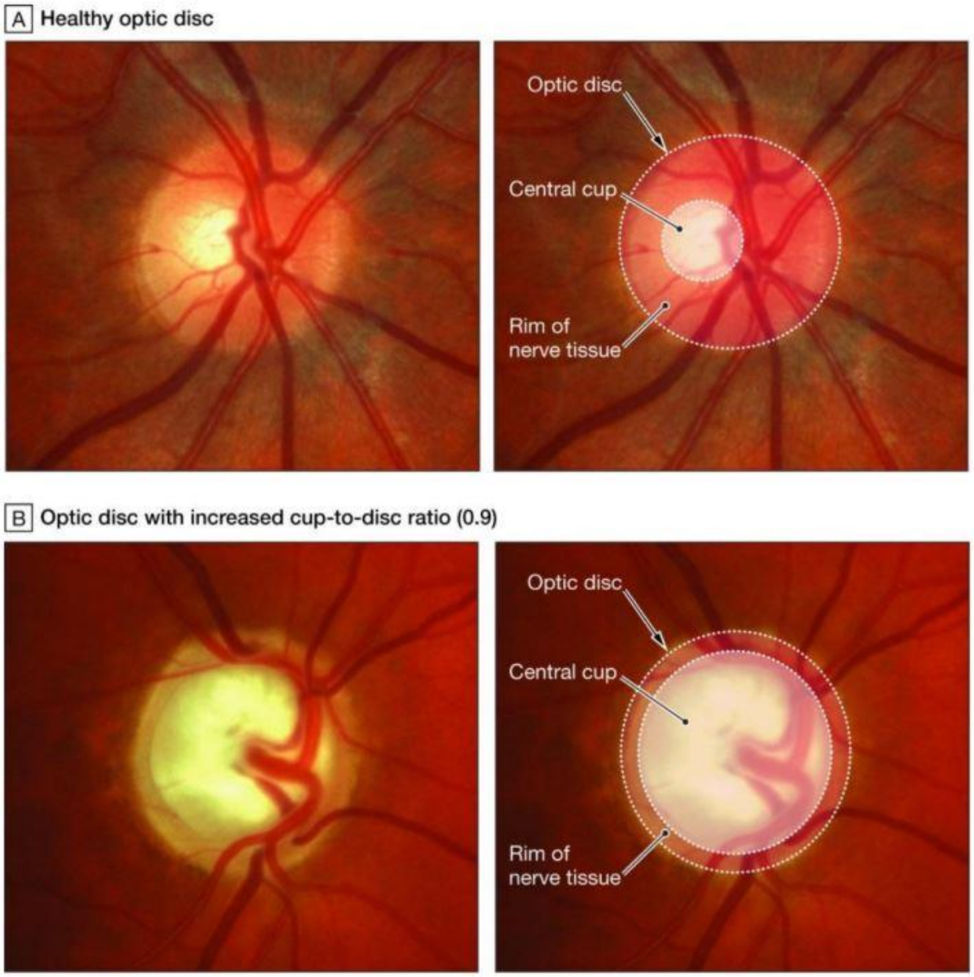

Figure 1.11 Optic disc cupping in human glaucoma patients.

The optic disc, where RGC axons leave the eye to form the optic nerve, is the anatomical location of the visual blind spot. **A.** A healthy optic nerve typically exhibits a slightly cupped shape (inner circle, central cup), where the RGC axons come together while leaving the retina. **B.** As glaucoma progresses, RGC axonal loss results in thinning of the retinal nerve fiber layer and expansion of the central cup. Clinicians examining the eye often speak of glaucoma patients exhibiting a high cup-to-disc ratio, meaning that the size of the central cup is large with respect to the size of the entire optic disc structure.

Figure from Hollands et al, 2013, and used in accordance with Copyright Clearance Center's RightsLink service.

note a distal-to-proximal depletion of tracer transport in the optic nerve and fewer axons in the distal nerve than in the proximal nerve after onset of pathology[153,232]. Together, these data suggest that RGC axons are susceptible to either degenerative paradigm, and exhibit aspects of both.

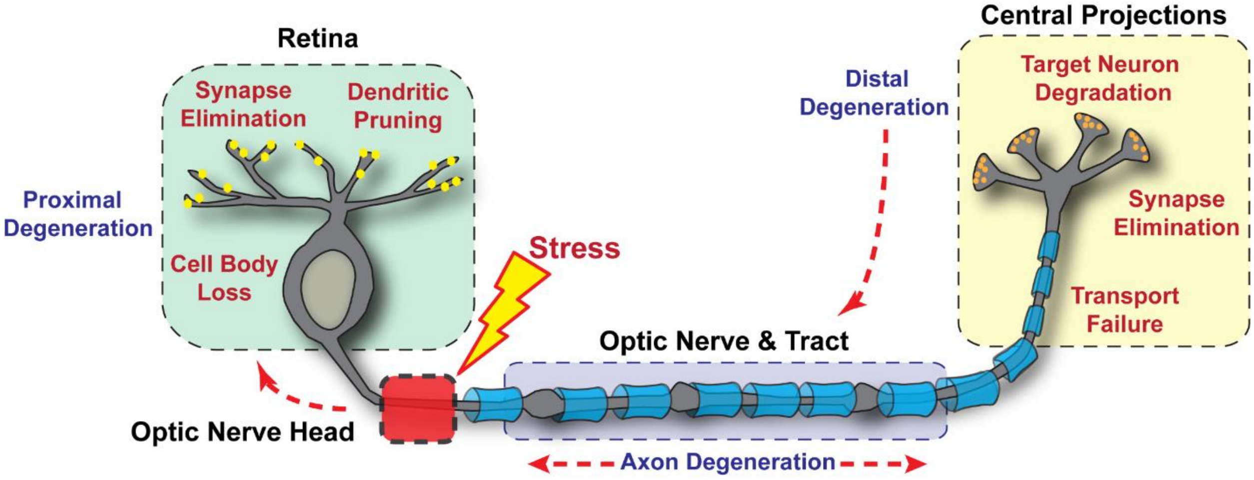

Figure 1.12 Key events in RGC glaucomatous progression.

The events defining RGC degeneration in glaucoma span four critical regions: retina, optic nerve head, optic nerve and tract, and the central projection to the brain. Stress originates at the optic nerve head and induces a program of distal axonopathy. First, intra-axonal transport begins to fail as RGC synapses and dendrites are pruned. Eventually, axon terminals in central projection sites are lost and the target neurons degenerate. Most pathological features of glaucoma follow a distal-to-proximal progression but Wallerian patterns of degeneration occur as well, including axonal dystrophies and more acute axon disassembly beginning distal to the nerve head. Proximal degeneration in the retina is marked by dendritic pruning and eventual somatic loss.

Modified from Calkins, 2012, and used in accordance with Copyright Clearance Center’s RightsLink service.

1.5.3 MODELING GLAUCOMA IN RODENTS

Models of glaucoma involve either a gradual, chronic onset that progresses over the animal’s lifetime or an acute onset of elevated IOP that can be closely monitored as pathology progresses over the span of weeks. The most commonly used chronic model of glaucoma is the

DBA/2J mouse, which develops a form of pigmentary glaucoma involving pigment dispersion and iris stromal atrophy. Pathology results from mutations in the glycosylated protein nmb (*Gpnmb*) and tyrosinase-related protein 1 (*Tyrp1b*) genes, which are related to iris health, pigment production, and pigment dispersion[234]. DBA/2J mice exhibit pigment dispersion from the iris, which collects at the iridocorneal angle to elevate IOP. IOP increases with age in most, but not all, DBA/2J mice, resulting in a population of mice with a distribution of pathologies even when age-matched[235]. Intriguingly, the disease process is not always uniform even in both eyes from the same mouse[236]. Most mice exhibit elevated IOP by 9 months of age, and optic nerve atrophy and optic nerve cupping is present in the majority of mice by 22 months[236]. The model exhibits many characteristics of human glaucoma, but not consistently[237]. This is useful for modeling a potential human population, but renders any experimentation beyond mere correlations with likely pathological onset nearly impossible.

Acute models are useful because they can be applied to any rodent, providing the opportunity to induce elevated intraocular pressure in any genetically manipulated or naïve rodent. The four most commonly used models all involve altering aqueous fluid dynamics in the anterior segment, and result in varied elevations and different periods of time for which the elevation is sustained.

The first model, episcleral vein injection of hypertonic saline, elevates IOP by altering aqueous outflow through sclerosis[238]. One injection elevates IOP from 7 up to 28 mm Hg (46 – 186% above average baseline)[238]. Although the authors assert retinal vasculature remains perfused, elevations of this extreme magnitude may cause transient ischemic events that do not typically occur in the retinas of glaucoma patients. This elevation persists as long as 200 days, but varies dramatically in both longevity and magnitude between animals. Additionally, only about half of rats injected sustain a pressure elevation following one injection; this model is not regularly used in mice, limiting the applicability of this model to genetically manipulated animals. This model does preserve the structure of the cornea, but displays deepening of the anterior chamber and reduction in size of the ciliary body within 5 to 6 weeks[239].

The second model, laser photocoagulation, is applied either to the trabecular meshwork alone or in addition to the episcleral veins. In this model IOP is elevated for far shorter durations; the elevation occurs for less than 21 days in rats[240,241] and up to 6 weeks in mice[242,243], with repeated laser treatments required to maintain elevations. This model, like the hypertonic saline model, is quite variable in both success rate and degree of elevation. It also results in significant levels of RGC death, a phenomenon not noted in human glaucoma until the disease has progressed for many years; the human RNFL diminishes in size while the ganglion cell layer (GCL) does not alter greatly in early glaucomatous progression[244]. In the laser photocoagulation model, thickness of every retinal layer decreases and electroretinographic analysis indicates a massive reduction in the a-wave and b-wave amplitudes as well as a complete loss of oscillatory potentials, confirming retinal neurons other than RGCs are injured[245]. This indicates the laser photocoagulation model produces a large, acute injury that may be quite different from human glaucoma.

The third model involves cauterization of two or three episcleral veins alone, and elevates IOP by reducing venous outflow[246,247]. This elevates IOP by approximately 1.6-fold, is relatively consistent between animals, and persists for 6 months without re-treatment[247]. This procedure induces RGC apoptosis, NFL thinning, optic disc cupping, and optic nerve degeneration; additionally, the pathology progresses much more slowly than the previous two models, indicating a chronic injury rather that an acute insult[248-250]. However, the potential for ocular ischemia and neovascularization can confound the interpretation of this model[251]. This neovascularization is theorized to result in the transient nature of this model, as it provides new routes for aqueous fluid to be removed from the anterior chamber[249]. Further, this model has been primarily applied to rats, as the surgery is difficult to accomplish in mice; this limits the ability of applying the stressor to an animal with a targeted mutation.

The final model, and the model utilized in this work, is the microbead occlusion model. In this model, a small volume of polystyrene microbeads is injected into the anterior chamber where they move with the aqueous humor to the trabecular meshwork[252]. These beads then occlude outflow to elevate IOP. This model has been applied in primates[253], rats[254], rabbits[255], and, as done herein, mice[252]. Although the presence of beads impedes study of the trabecular meshwork, this minimally invasive model consistently induces an IOP elevation about 33-50% above baseline, similar to that of glaucoma patients[213,256]. Typically, this model is utilized with one eye receiving an injection of microbeads while the contralateral eye receives an equivalent injection of saline as internal control[252]. This internal control is useful for many studies, but the data detailed herein demonstrates some limitations to its use. Some labs have modified this model, replacing polystyrene microbeads with magnetic; in this model, the beads can be drawn to the iridocorneal angle immediately upon injection[257]. This ensures that beads are not in the reflux as the needle is withdrawn, but may induce more damage to the trabecular meshwork and results in a higher IOP elevation. Both variations, however, result in an elevation that lasts two months in mice before reinjection is necessary, and so the results are fairly comparable between them.

1.5.4 INTER-ORBITAL INTERACTIONS

Interactions in disease progression between the two eyes is noted on as large a scale as human visual fields, and as small a scale as protein expression. Humans with glaucoma present with a strong tendency for maintaining the binocular visual field, preserving regions in one eye where the corresponding visual field in the contralateral eye is damaged[227]. As this effect relates to visual field placement and not necessary location on the retina or within the optic nerve, they hypothesize that it is largely driven by neurons. In support of this, many regions of the brain alter their structure through the course of human glaucoma[258]. However, a molecular mechanism has not yet been proposed.

In rodents with unilateral IOP elevations, glial morphology has been repeatedly determined to alter bilaterally. Microglia in the contralateral mouse retina exhibit multiple signs of activation, including amoeboid morphology, process retraction and reorientation, soma displacement, and upregulation of proteins associated with an inflammatory response[259]. Astrocytes in the contralateral retina, too, express significantly more GFAP and occupy a larger portion of the retina[260,261]. Unilateral optic nerve transection in rats additionally induces a reactive microglial response in the contralateral retina[262]. These bilateral alterations after unilateral insult are not limited to morphological changes; amyloid precursor protein and amyloid β distribution and expression patterns are altered in both the hypertensive and contralateral eye[263]. These data highlight the extensive interconnectivity between visual streams; additionally, researchers must keep these alterations in mind when determining whether an internal control is appropriate for their paradigm.

1.6 CONNEXIN 43 AND NEURODEGENERATION

Divide and rule, a sound motto. Unite and lead, a better one.

- Johann Wolfgang von Goethe

1.6.1 CONNEXINS

Gap junctions are a unique modality of specialized synapses that form a direct pathway for cell-to-cell communication between cytoplasm. These chemical synapses link many different classes of cells to share electrical signals (as in photoreceptors detecting polarized light), inhibit signals across tissue in concordance (as in amacrine cells expressing signals related to circadian rhythm), or maintain patterns of signaling across tissue (as in the heart). Each gap junction is composed of two hemichannels, or connexons, which are composed of arrays of six connexin protein subunits each with four transmembrane segments. A connexon in one plasma membrane either docks with another in a closely opposed cell or, in specific cell types, remains open to the intracellular space.

Connexins are encoded by a gene family with roughly 20 members in mammals[264], commonly named by their predicted molecular mass to the nearest kDa. The family exhibits many conserved sequences and exhibit a common membrane topology – meaning different connexin proteins can often dock to one another. Such heterotypic junctions are rarer than homomeric junctions but allow different cell types to connect and communicate with one another. Additionally, different connexins form junctions that differ in single channel conductance, gating, and permeability, so many cells express multiple connexins and vary their expression patterns to compensate for different conditions[265,266], although the prevalence and stoichiometry of heterotypic junctions are still poorly understood as they may vary on a cell-to-cell basis.

The life cycle of gap junctions, however, is well characterized. Most connexins are cotranslationally inserted into the ER membrane, the exception being the smallest connexin, Cx36, which is transported to the membrane by a microtubule-based system and inserted into membranes posttranslationally. Cx43, one of the most widely studied and utilized connexins, is assembled into hexamers in a trans-Golgi compartment[267] from which vesicles are transported to the cell surface by a microtubule-independent system where they fuse with the cell membrane. These hemichannels then diffuse laterally until they dock with a hemichannel in an opposed membrane to form a gap junction between cells[268].

Gap junctions are degraded after both junctional membranes are internalized into one of the adjoining cells[269]. Because this internalization involves a double-membrane, the internalized structure has been given a unique name: the connexosome. Connexosomes likely include many other molecules, as several connexin binding proteins have been identified. There is still debate as to whether the connexosome is the only mechanism through which gap junctions are internalized; there is some evidence for a clatherin-mediated[270] or lipid-raft dependent[271] pathway under particular circumstances.

Connexins generally exist transiently, with a half-life between 1 and 5 hours[268,272,273]. The transient nature of Cx43 especially has been repeatedly determined in both the heart[272,273] and within astrocytes[70,274]. The extraordinary transience of connexins makes them a prime candidate for remodeling during early compensation for stressors. Because connexins serve as the pathway through which these stressors might be communicated to nearby regions, they are often an early site of protein modification during stress as well. Adenosine monophosphate-activated protein kinase (AMPK), for example, is the main sensor of cellular energy status and functions to promote context-appropriate responses to changes in metabolic state. It is activated by ATP depletion (increased AMP/ATP ratio), and while in this state it phosphorylates Cx43 at S373. When Cx43 is phosphorylated at this site it no longer interacts with zona occludens-1 (ZO-1), which allows it to enlarge[275]. In this state more, and larger, molecules can be transmitted through the channel. There are more than 20 currently known sites at which Cx43 can be phosphorylated, and the downstream consequences of each manipulated site are largely unknown. As more functions of gap junctions and their responses to various injuries are still being discovered, new experiments revealing the consequences of their behavior are extraordinarily important to understanding the brain and the methods through which different cells and regions communicate.

1.6.2 METABOLITE TRANSFER THROUGH GAP JUNCTIONS

Gap junctions allow the passive intercellular diffusion of small molecules indiscriminately, dependent on the size of the pore they create. In its native state, connexin 43 is permeable to molecules up to 1-1.2 KDa[276]. This allows each of the metabolic resources primarily utilized by the brain to flow freely through these synapses; glucose (180 Da), pyruvate

(88 Da), and lactate (90 Da) all flow down their concentration gradients through connexins. As both pyruvate and lactate are polar, they may additionally be pushed through gap junctions by calcium waves; however, the dynamics of calcium waves during various stressors is still a topic of intense debate.

One of the most well-observed stressors within the nervous system is oxidative stress. Oxidative stress is a result of the imbalance between the reactive oxygen species (ROS) produced due to energy consumption and the antioxidant activity meant to minimize their impact. Astrocytes are the center of the brain's defense mechanism against oxidative stress; they maintain antioxidant levels and provide energy, largely through the utilization of glycogen, to those neurons utilizing energy at a rate outpacing their supply [96,132]. Knockdown of cx43 in cortical astrocytes is reported to increase cell death induced by the ROS hydrogen peroxide (H_2O_2)[277]. Additionally, H_2O_2 generated by hypoxia and reoxygenation is correlated with differential regulation of cx43 phosphorylation and spatial distribution [274]. Some studies associate this remodeling with protection, while others associate it with injury [278-281]. Likely, whether gap junction remodeling is protective or detrimental depends on the severity of the stressor and the length of time a cell is subjected to it.

1.6.3 CONNEXIN EXPRESSION IN THE NERVOUS SYSTEM

In the CNS, glia are the major cells coupled through gap junctions; neuronal gap junction expression typically involves Cx36, and is generally limited to particular subpopulations of neurons in localized regions of the brain. Each glial cell type expresses its own set of connexins, none of which are limited to glia. These sets of connexins dictate the strength of coupling. The level of connexin expression depends on the glial cell type[282].

Oligodendrocytes express Cx29, Cx30, Cx32, Cx45, and Cx47, but primarily utilize connexins Cx32 and Cx47[6,283-285]. Intriguingly, oligodendrocytes typically do not couple with one another and gap junctions have not been found between layers of myelin[286,287]. Rather, oligodendrocytes and astrocytes exhibit panglial coupling by forming heterotypic junctions with astrocytes, where the astrocytes contribute mainly Cx43 and to a smaller extent Cx30. If Cx47 is ablated coupling of oligodendrocytes to astrocytes is very nearly abolished, resulting in much smaller oligodendrocyte networks[288]; as Cx43 is the main connexin in astrocytes and Cx47 is the main oligodendrocyte connexin, the Cx47:Cx43 O:A coupling is the primary mediator of this network. A main function of this network is the transport of lactate between astrocytes and the neuronal axons oligodendrocytes surround[6]. This transport can additionally occur actively through MCT transporters, but as oligodendrocytes minimally store metabolites themselves they largely appear to serve as a conduit between astrocytes and axons, at least in terms of energetics.

A number of studies have identified microglial connexins and have reported that these connexins are functional *in vitro*[289-291]. However, the functionality of these connexins *in vivo*, even after neuronal injury, has yet to be shown[292]. A prevailing hypothesis states that microglial connexins largely serve as a connection with extracellular space through which microglia can monitor the prevailing conditions of the region they reside within. As such, these connexins may not be directly relevant to the data presented herein.

In astrocytes, intercellular communication is mediated primarily by Cx43, although Cx26, Cx40, Cx45, and Cx46 expression has also been identified[60,61,293]. Astrocytes isolated from Cx43 knockout mice demonstrate coupling reduced a dramatic 95% from control[60]. However, the expression and coupling efficiency of astrocyte connexins varies dependent on the brain region they reside within. For example, connexin expression is relatively low in rat striatal astrocytes and high in hippocampal astrocytes[294]. As with most astrocyte-related functions, their study is complicated by their adaptability and heterogeneity. Astrocyte connexin expression varies throughout development, as well as the cells astrocytes connect to[66,67,295,296]. Thus, the studies performed herein utilized knockouts only after mice had aged 8 weeks.

1.7 HYPOTHESIS AND SPECIFIC AIMS

1.7.1 CENTRAL HYPOTHESIS

We propose that early in neurodegeneration, astrocytes increase connectivity through cx43 to endogenously protect neuronal function by utilizing network-wide energy stores.

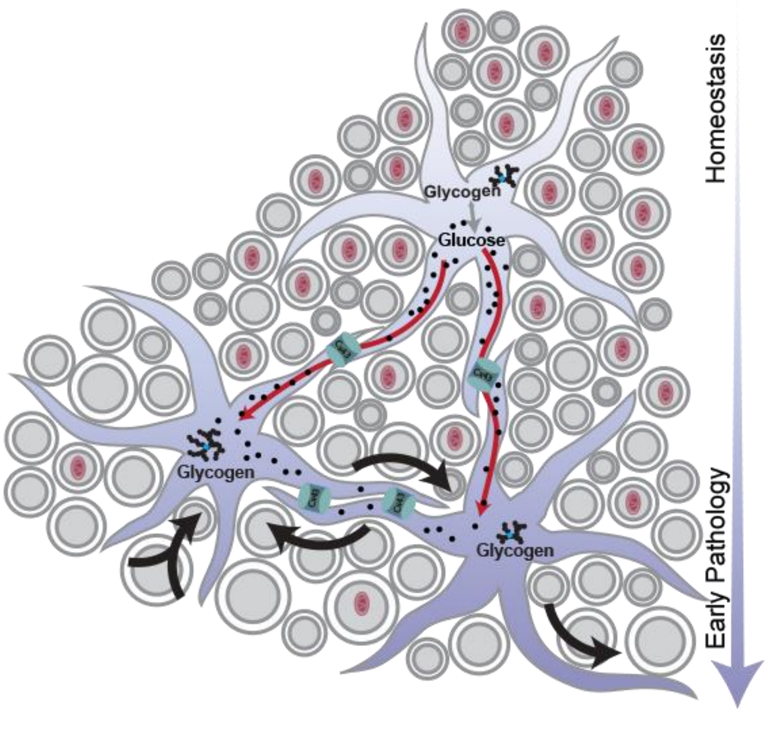

Figure 1.13 A potentially neuroprotective astrocyte function during early neurodegeneration.

Early in pathology, axons (grey) expand and mitochondrial density in the optic nerve diminishes (red). Concurrently, astrocytic glycogen content in nearby healthy tissue diminishes (black structures) and astrocytes remodel (black arrows). We hypothesize that astrocytes redistribute glycogen-derived glucose (red arrows) through cx43 gap junctions (blue) in an endogenously protective mechanism that maintains the function of stressed axons.

1.7.2 AIMS

AIM 1: CHARACTERIZE MORPHOLOGICAL AND METABOLIC ASTROCYTE REMODELING EARLY IN GLAUCOMATOUS PROGRESSION.

As the brain ages, it becomes depleted of mitochondria and energetic resources. This is accelerated during chronic neurodegenerative stress. One such stressor, elevated IOP, results in depletion of astrocytic energy stores. Further, as anterograde transport in retinal ganglion cells is lost, the distal optic nerve degenerates more quickly as mitochondrial transport from the soma is slowed. Here, we aimed to quantify both the alterations in global astrocyte morphology and the diminishment of mitochondrial density to test the working hypothesis that *astrocytes remodel early in neurodegeneration as energetic capacity is depleted.*

AIM 2: DETERMINE THE MECHANISM FOR METABOLITE REDISTRIBUTION DURING EARLY CHRONIC STRESS.

Astrocytes form local networks of coupled cells through gap junctions formed by connexins (cx43). Through gap junctions, astrocytes can communicate both electrically and chemically, rapidly conducting signals to their network. Chronic stressors, such as elevated IOP in glaucoma, result in depletion of astrocytic energy stores. During early chronic stress, this depletion occurs in neighboring tissues as well as the stressed region. Here we aim to apply real-time, in vivo measures of glucose gradients to examine this redistribution and evaluate the relationship between these gradients and optic nerve glycogen content. We utilized nerve transection and conditional cx43-/- mice to determine the mechanism through which metabolites are shuttled to stressed regions to test the working hypothesis that *during early chronic stress astrocytes redistribute metabolites through cx43 gap junctions*.

AIM 3: ASSESS THE IMPACT OF METABOLITE REDISTRIBUTION ON AXONAL STRUCTURE AND FUNCTION IN BOTH VISUAL STREAMS.

During early phases of neurodegeneration, neurons increase their rate of energy consumption. This is not only true in animal models, but also in pre-degenerative forms of neurodegenerative disease in humans. Neurons primarily utilize glucose as an energy substrate, which depletes quickly during periods of stress or high demand. To maintain normal function, neurons must rely upon astrocyte-derived energy stores. Astrocyte-derived resources increase neuronal survival, but the extent to which the redistribution of resources from healthy to degenerating tissue can influence the brain's ability to resist neurodegenerative stress is unknown. To examine this, we tested the working hypothesis that *glucose redistribution through the optic projection endogenously protects stressed axons but renders donating tissue vulnerable to additional stress.*

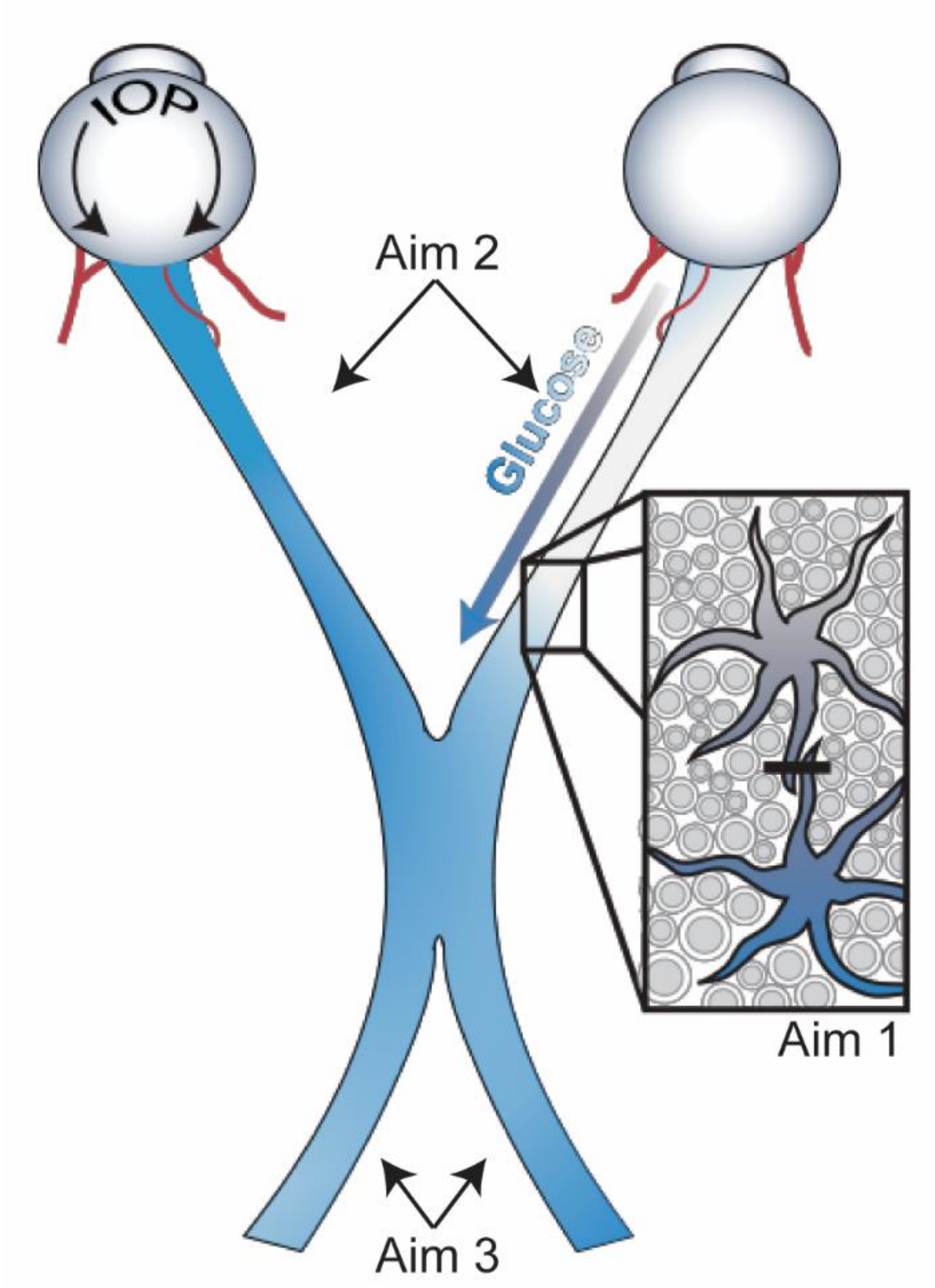

Figure 1.14 Summary of Aims.

We propose that early in neurodegeneration, astrocytes increase connectivity through cx43 to endogenously protect neuronal function by utilizing network-wide energy stores. We have tested this through three experimental aims. In Aim 1, we characterized morphological and metabolic astrocyte remodeling early in glaucomatous progression. Through the experiments in Aim 2, we determined necessary components of the mechanism for metabolite redistribution during early chronic stress. In Aim 3, we assessed the impact of metabolite redistribution on axonal structure and function in both visual streams.

CHAPTER 2

ASTROCYTES REMODEL EARLY IN DEGENERATION AS ENERGETIC EAPACITY IS DEPLETED

To err is human, but to really foul thighs up you need a computer.

Paul R. Ehrlich

2.1 INTRODUCTION[1]

Astrocytes serve myriad functions in the mammalian central nervous system; aside from providing structural support, they additionally maintain the extracellular environment, optimize neuronal signaling, and release neurotransmitters themselves[19,276]. Astrocytes are especially critical in white matter tracts, where axons propagate energy demanding action potentials great distances from their nuclei[42,297]. Due to this relationship, astrocyte-axon interactions are increasingly recognized as important both in neural homeostasis and in pathology. Astrocytes exhibit multiple phases of remodeling due to neurodegenerative stress, demonstrating nuanced responsiveness and providing depth to a previously binary 'reactive or quiescent' classification

---

[1] Portions of this chapter have been published in the following papers:

1. **Cooper, M. L.**, Crish, S. D., Inman, D. M., Horner, P. J., and Calkins, D. J. 2016. Early astrocyte redistribution in the optic nerve precedes axonopathy in the DBA/2J mouse model of glaucoma. *Exp Eye Res.* 150:22-23. Doi: 10.1016/j.exer.2015.11.016.
2. **Cooper, M. L.**, Collyer, J. W., and Calkins, D. J. 2018. Astrocyte remodeling without gliosis precedes optic nerve axonopathy. *Acta Neuropath Comm.* 6(1): 38. Doi: 10.1186/s40478-018-0542-0.

system[298-300]. Intriguingly, early astrocyte responses to neurodegeneration are often highly beneficial to injured neurons[36,38,52,301]. In the optic nerve, astrocytes provide biochemical support and maintain extracellular ion balance for retinal ganglion cell (RGC) axons, which transmit retinal signals to visual structures in the brain[7,138]. Glaucomatous optic neuropathy (or simply glaucoma), a neurodegenerative disease projected to affect some 11 million people by 2020[[37]], selectively targets RGCs and their axons. Although age is the greatest risk factor, intraocular pressure (IOP) remains the only modifiable risk factor[213,302]. However, many patients continue to lose RGC axons despite IOP-lowering treatments[220]. RGC axons and the glia that support them are particularly sensitive to age-related stressors, such as deficits in metabolism and loss of anterograde axonal transport, both of which are common aspects of age-related neurodegenerative disease[113,224,303-306]. Recent work has focused on early phases of axonal pathology in order to abate axon susceptibility prior to overt loss[134,307].

In neurodegenerative disease, a glial scar generally fills volume previously occupied by axons[42]. Such reactive gliosis contributes to remodeling within the optic nerve during glaucomatous progression, as in the DBA/2J mouse model of hereditary glaucoma[12,193,308-311]. However, earlier components of astrocyte remodeling presage overt axonal degeneration[74,190]. Early RGC axonopathy in animal models of glaucoma is characterized by enlargement of the optic nerve concurrent with expansion of individual axons, accumulation of hyperphosphorylated neurofilaments, and loss of anterograde transport from the retina to central brain targets[153,190,312]. Early morphological remodeling may be reversible without leading to discernible axonal damage[298,300]. Thus, understanding how astrocyte remodeling progresses early and its relationship to axonopathy may present novel therapeutic opportunities.

Astrocyte remodeling at early stages of neurodegeneration is closely linked to both changes in metabolic capacity and energy reserves. In addition to applying a novel method to quantify global alterations in optic nerve astrocyte morphology, here we examine the components of metabolism that relate to astrocytes and how they are altered during early stages of neurodegeneration. Intriguingly, and counterintuitively, metabolic alterations occur throughout the nervous system in a much broader scope than the initial injury would suggest.

2.2 MATERIALS AND METHODS

2.2.1 ANIMALS

The Vanderbilt University Medical Center Institutional Animal Care and Use Committee approved all animal work and experimental procedures. We obtained DBA/2J and DBA/2J-*Gpnmb⁺/SjJ* ('D2 control') mice from Jackson Laboratories (Bar Harbor, ME). A subset of DBA/2J mice were bred in a pathogen-free facility and regularly backcrossed with fresh founders obtained from Jackson Laboratories to minimize genetic drift, as previously described[235,313]. As described[190], 48 DBA/2J optic nerves were used in the cross-sectional analyses within this study (**Table 1**). An additional 10 DBA/2J mice and 8 D2 control mice were utilized in the immunolabeling portion of this study, all of which were harvested at 10 months. All mice were maintained on a 12 h light-dark cycle with standard rodent chow available *ad libitum*. We measured IOP monthly in a subset of these DBA/2J mice representing 20 eyes using TonoPen

XL rebound tonometry as previously described [190,235]. Briefly, prior to measurement, the mice were anesthetized (Avertin, 1.3% tribromoethanol, 0.8% tert-amyl alcohol) and proparacaine ophthalmic solution (0.5% proparacaine hydrochloride, Bausch&Lomb, Tampa, FL) was applied topically to the eye. Monthly IOP for each eye was taken as the average of 25–30 Tono-Pen measurements recorded during a session.

2.2.2 TISSUE PREPARATION AND IMAGING

All mice were transcardially perfused with PBS followed by 4% paraformaldehyde in PBS. A 1-3 mm section of optic nerve proximal to the globe was isolated and post-fixed for 1 hour in 4% paraformaldehyde. Nerves were prepared for embedding in Epon resin and semi-thin (1–2 µm) cross-sectioning as described previously[190,235,252,314-316]. Cross-sections were imaged using an Olympus Provis AX70 microscope equipped with a motorized X-Y-Z stage, a digital video camera, and 100x oil-immersion, differential interference contrast optics. Photomicrographs were obtained *en montage* to represent the entire cross-section.

A subset of eyes and optic nerves from DBA/2J and D2 control mice were enucleated and dissected from the optic chiasm for longitudinal sectioning and immunohistochemical staining. Tissue was cryoprotected in a sequence of 10, 20, and 30% sucrose/PBS overnight and subsequently embedded and frozen in Tissue-Plus O.C.T. Compound (Fisher Healthcare, Houston, TX). We labeled 10 µm cryosections with the following antibodies: anti-glial fibrillary acidic protein (GFAP; EMD Millipore, Billerica, MA, 1:500), and anti-Connexin-43 (Cx43; Alomone Labs, Jerusalem, Israel, 1:250). Immunolabeling was visualized using appropriate DyLight-conjugated secondary antibodies (Jackson Immunoresearch, West Grove, PA 1:200). Fluorescent montages were captured using an Olympus Provis AX70 microscope as described above. Confocal images were captured using an Olympus FV-1000 inverted microscope. Settings were kept constant for all sections so that comparisons in label intensity could be made.

2.2.3 NERVE AND AXON QUANTIFICATION

We measured cross-sectional nerve area in a total of 110 DBA/2J optic nerves and axon density (axons/mm^2) in a subset of 46 DBA/2J optic nerves as described previously[235,308,313]. Briefly, we randomly selected 25-30 non-overlapping frames representing a known area of nerve. Previously developed routines were used to identify and count each axon for which a single, intact myelin sheath could be identified. Nerves with pathology so severe that intact myelin sheaths were difficult for the program to detect were excluded. The mean axon density relationship for all frames was taken as the representative axon density for the nerve. In these same 46 nerves, we additionally determined the cross-sectional area for each identified axon within a myelin sheath. A range of 6,000-40,000 measurements was used to calculate mean axon area (in um^2). We calculated correlation coefficients from best-fitting regression via Pearson’s coefficient.

2.2.4 QUANTIFICATION OF GLIAL AREA AND PROCESS ORGANIZATION

To measure the fraction of each nerve area covered by glia, montages were filtered using a suite of MATLAB routines (MathWorks, Natick, MA) that highlighted glial processes separate from axons. These routines detected glial boundaries in contrast-enhanced binary images of each nerve by edge enhancement and size filtering to exclude axons. Noise from small axons was eliminated from this image based on a roundness and size filter. We calculated the percentage of the nerve occupied by glial processes by summing the area of all identified processes. Finally, the outer boundary of the nerve was outlined from the original montage and eroded to exclude pia and dura mater. Each binary image was segmented into 20 concentric divisions that each represented an interval of 5% of the total nerve area from the outer boundary of the nerve (division 1) to the center (division 20). This was achieved using a structuring element that reduced the area within the outline of the nerve by 5% with each subsequent iteration. This accounted for any irregularities in the shape of the outer boundary of the nerve to produce a consistent area for each division. The percent glial area for each division was calculated to produce a distribution from edge to center. The center of mass (CoM) was obtained by dividing the binary image into 20 concentric rings from the edge to the center of the nerve, measuring the percent glial area within each, and determining which division delineated 50% of total glial area on either side. Thus, a nerve with an even distribution of glial area between edge and center has a CoM of 10; nerves with glial area biased towards the edge have a lower CoM, while nerves with glial area biased towards the center have a higher CoM.

Binary images were additionally used to quantify glial organization by measuring the overall parallelism of the cells' processes. The outer 20% of each nerve's area was first eroded in order to remove the disorganized glia along the nerve edge. This erosion maximized the signal-to-noise ratio and thus the robustness of the final organization parameter. Next, the eroded image was skeletonized and pruned, reducing each binary object to a one-pixel wide collection of segments. The length of each segment was determined as the maximum with constant orientation between corners, with each corner defining a branch point to a different orientation. The branch points between segments were then removed in order to calculate a vector for each segment. The magnitude (*M*) and the directional angle (***θ***) of each organizational vector were computed using **Eqns. 1-2**. These values were then used to calculate the horizontal (x) and vertical (y) components of each vector (**Eqns. 3–4**). This process was repeated as the eroded image was rotated one degree at a time until the sum of all vertical components reached an absolute minimum, indicating the orientation of maximal horizontal orientation of glial processes in the nerve. After finding this optimal rotational angle, the final organizational parameter was derived using **Eqn. 5**. A parallelism percentage of 100% corresponds to a theoretical nerve that is perfectly organized, while 0% describes a nerve that is perfectly disorganized. Parallelism percentages above 50% were rarely observed because glial cell bodies typically have a rounded shape, and thus the vectors derived from their skeletons are not oriented parallel to one another.

EQUATIONS 1-5:

$$(\mathbf{1})\ \ M = \sqrt{(y_2 - y_1)^2 + (x_2 - x_1)^2}$$

$$(\mathbf{2})\ \ \theta = \left|\arctan\left(\frac{y_2 - y_1}{x_2 - x_1}\right)\right|, \qquad \text{for branch endpoints } (x_1, y_1), (x_2, y_2)$$

$$(\mathbf{3})\ \ x\_comp = M\cos\theta$$

$$(\mathbf{4})\ y\_comp = M\sin\theta\,, \ \ \text{where } \theta \in [0, 90]$$

$$(\mathbf{5})\ \ Parallelism = \left(1 - \frac{\min \sum_{i=1}^{n} y\_comp_i}{\max \sum_{i=1}^{n} x\_comp_i}\right) \times 100$$

2.2.5 TRACING ANTEROGRADE AXONAL TRANSPORT

Forty-eight hours prior to perfusion, a subset of animals were anesthetized with 2.5% isoflurane and bilaterally injected intravitreally with 2µl of 0.5mg cholera toxin subunit B (CTB) conjugated to Alexa Fluor 488 (Invitrogen) as previously described[153,315]. Two days post-injection, animals were transcardially perfused with PBS followed by 4% paraformaldehyde in PBS. Each retina was checked to ensure a quality injection, and any retina without detectable CTB excluded the corresponding projection from the study. Brains were cryoprotected in 30% sucrose/PBS overnight, and 50µm coronal midbrain sections were cut on a freezing sliding microtome. Serial superior colliculus sections were imaged using a Nikon Eclipse TI microscope (Nikon Instruments) and the intensity of the fluorescent CTB signal was quantified using ImagePro custom routines (Media Cybernetics) as previously described[153,256]. CTB signal was normalized to background and alternating sections were analyzed for intensity. Intensity from each section was calculated to reconstruct a retinotopic map of intact anterograde transport across the superior colliculus. Intact transport for each map was defined as any region with an intensity ≥70% of the maximum CTB signal for that tissue.

2.2.6 STATISTICAL ANALYSIS

Data for IOP and glial area analysis are presented as mean ± standard error of the mean (SEM) for each treatment. Statistical analysis and p-values for comparing means were obtained using Kruskal-Wallis one-way ANOVA or two-sided t-tests, and all data met criteria for normality as confirmed using the Shapiro-Wilk normality test; all datasets compared passed with $p \geq 0.22$. Correlations were calculated using the two-tailed Pearson product moment test and verified by linear regression analysis. Statistical tests were considered significant if $p < 0.05$. All statistical tests were performed with SigmaPlot 12.5 (Systat Software Inc., San Jose, CA). Numbers of samples and measurements along with actual *p* values of significance are indicated where appropriate in the text or figure legends.

2.3 RESULTS

2.3.1 OPTIC NERVE AND AXON EXPANSION PRECEDE AXON LOSS

The electron micrographs below show a 4 month nerve side-by-side with a 9 month nerve that was 32% larger (Figure 2.1A,B). The 9 month nerve also had a 39% larger mean axon area, 0.40 vs. 0.31 μm^2, which is quite evident in the micrographs. Even so, axon density in the 9 month nerve was among the highest in our sample, 6.2×10^5 axons/mm^2, comparable to density in the 4 month nerve (5.6×10^5 axons/mm^2). Similarly, for two 9 month nerves (Figure 2.1C,D), axon density was quite high for each, 6.2 vs. 6.0×10^5 axons/mm^2, though the nerve in Figure 2.1D was larger (.095 mm^2 vs. 0.08 mm^2) with expanded axons (0.40 μm^2 vs. 0.35 μm^2). At higher magnifications, the axoplasm in the larger nerve appeared highly disordered with poorly articulated microtubules and neurofilaments, compared to axons in the smaller nerve (Figure 2.1E,F). Also, the axolemma that normally separates the axoplasm from the myelin sheath, quite evident in the smaller 9 month nerve (Figure 2.1E), was nearly indistinguishable in the larger nerve (Figure 2.1E). This change suggests that increased axon area prior to loss involves distended axoplasmic volume.

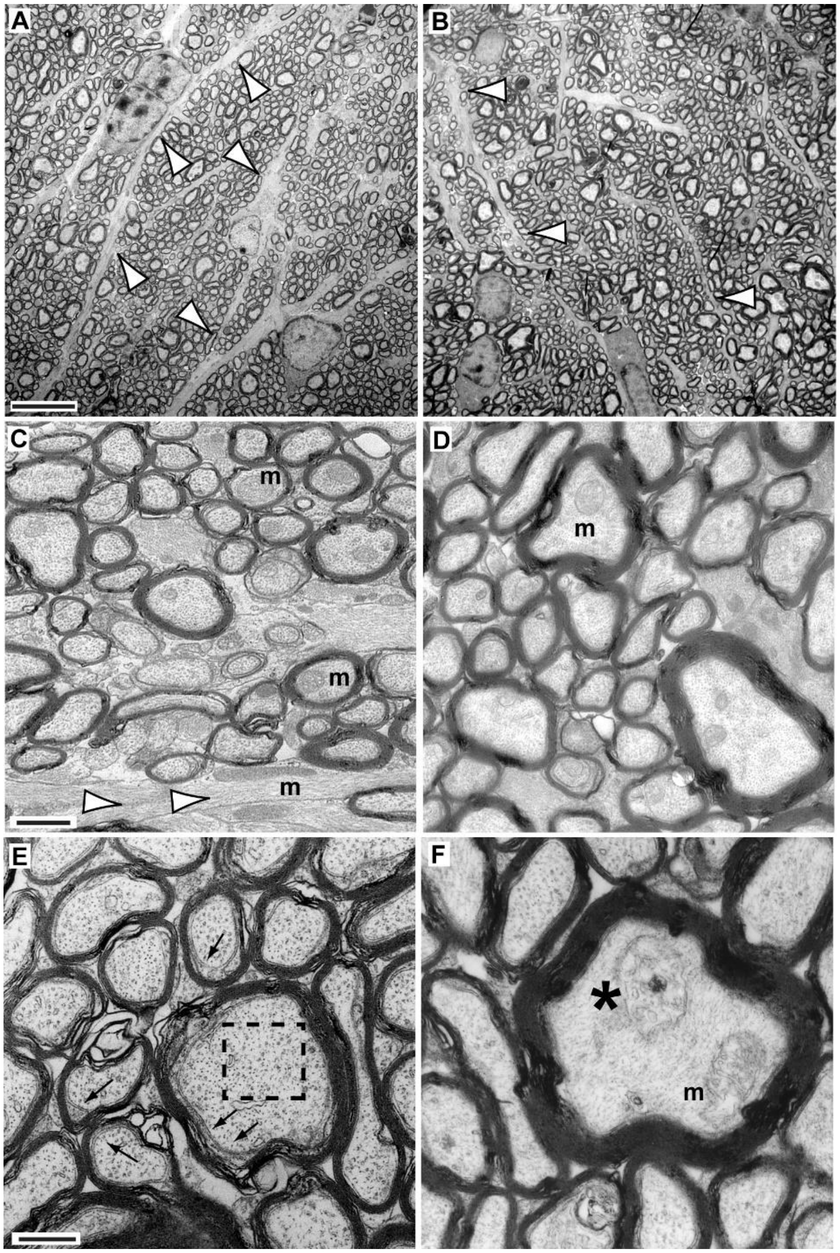

Figure 2.1 Axons enlarge prior to degeneration.

A. Low magnification electron micrograph of 4 month nerve with tight axonal packing (5.6 x 10^5 axons/mm^2), nerve area of 0.069 mm^2, and mean axon area of 0.31 μm^2. Arrowheads indicate ramifying astrocyte processes. **B**. Larger 9 month nerve (0.091 mm^2) has larger mean axon area (0.40 μm^2) but comparable density (6.0 x 10^5 axons/mm^2). **C.** Higher magnification electron micrograph of a small 9 month nerve (0.08 mm^2) and mean axon area of 0.35 μm^2. Axon density was 6.2 x 10^5 axons/mm^2. Mitochondria in axons and astrocyte processes (arrowheads) are indicated (m). **D.** Larger 9 month nerve (0.095 mm^2) has expanded mean axon area of 0.41 μm^2 but comparable axon density (6.0 x 10^5 axons/mm^2). **E**. High power image of nerve in **C** demonstrates well-ordered packing of neurofilaments and microtubules in axoplasm (dashed square) and prominent axolemma separating the axoplasm and myelin sheath (arrows). **F**. Enlarged axon from nerve in **D** shows disordered axoplasm, phagocytic vacuole (*) and little or no distinguishable axolemma. Scale = 5 μm (A, B), 0.5 μm (C, D) and 0.25 μm (E, F).

The comparisons of equal-density nerves in Figure 2.1 suggest that axonal and nerve enlargement are pre-degenerative, in that expansion can occur without frank loss of axons. To determine the critical threshold at which axon enlargement is associated with axon loss, we ranked the nerves in our sample from highest to lowest axon density. We then compared density with mean cross-sectional axon area for increasingly inclusive density ranges (Figure 2.2). For the top 20th percentile in density (5.6 – 6.2 x 10^5 axons/mm^2), the span of mean axon areas was modest (0.28-0.40 μm^2) and the slope of the best-fitting regression line did not differ from zero (p=0.45). This indicates density did not change with axon size over this range. For the top 40% nerves, the range of axon areas increased to 0.45 μm^2, but the slope of the regression line still did not differ from zero (p=0.74). For the 60th percentile group, the range of axon areas increased to nearly 0.50 μm^2,

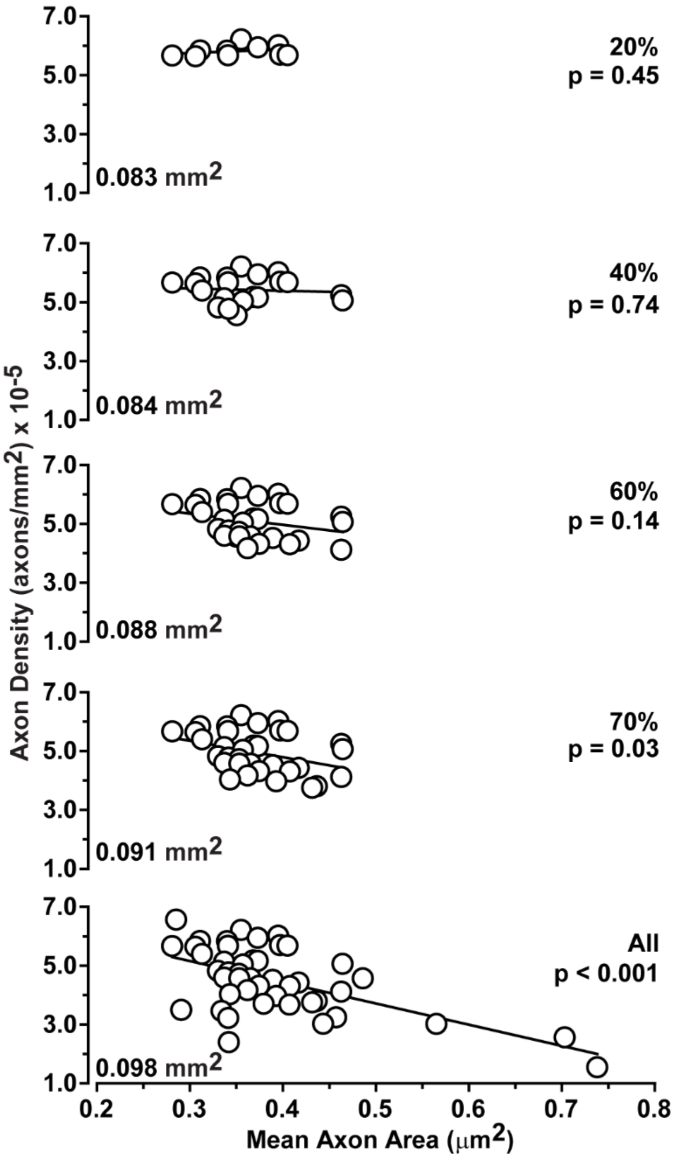

Figure 2.2 Axon expansion eventually leads to loss.

Axon density vs. mean axon area for nerves ranging from the highest density group (top 20th percentile) to the entire sample. Best-fitting linear regression is included for each group. Density and axon area become negatively correlated by the 70th percentile (r = -0.36, p=0.03). For each ranking, the average cross-sectional nerve area for the group is given.

and axon density approached a negative correlation with axon area (r = -0.28, p=0.14). By the 70th percentile, axon density and area were negatively correlated (r = -0.36, p=0.03). For the entire sample, axon area ranged to almost 0.75 μm^2, and the decrease in axon density with increasing axon size was highly significant (r = -0.60, p<0.001). Thus, axon density can remain high and relatively invariant with increasing axon area up to a certain threshold of approximately 0.50 μm^2. This is just about twice the size of the smallest mean axon area in our sample. Figure 2.2 also shows that as the density range became more inclusive of lower values and the range of axon sizes increased, the average nerve size also increased.

2.3.2 RETRACTION OF ASTROCYTE PROCESSES WITH EARLY AXON EXPANSION

The micrographs in Figure 2.1 hint at another feature of axon expansion prior to outright loss. We noticed that for high axon density nerves, increased nerve and axon size was accompanied by apparent reduction in astrocyte processes within the extra-axonal and inter-fascicular space (e.g., Figure 2.1A,B). This trend is illustrated more clearly below for two young DBA/2J nerves with comparable axon density: 5.2 x 10^5 axons/mm^2 (Figure 2.3A) and 5.1 x 10^5 axons/mm^2 (Figure 2.3B). Compared to the smaller nerve (0.075 mm^2; Figure 2.3A), mean axon size in the larger nerve (0.10 mm^2; Figure 2.3B) was increased: 0.46 μm^2 vs. 0.37 μm^2. This expansion in axon size was accompanied by diminished ramification of astrocyte processes with less separation between axon bundles. This change was evident also in the next comparison. Figure 2.3C shows an electron micrograph of a small 9 month nerve (0.076 mm^2) with axon density of 5.7 x 10^5 axons/mm^2 and mean axonal area of 0.28 μm^2. An adjacent section through the same nerve demonstrated modest levels of phosphorylated neurofilament in axons highlighted by typical ramification of GFAP-labeled astrocyte processes (Figure 2.3D). Another 9 month nerve that was larger (0.11 mm^2) had the same axon density but significantly expanded axons (0.41 μm^2) with increased levels of phosphorylated neurofilament and greatly reduced ramification of GFAP-labeled astrocytes (Figure 2.3E,F). Thus, it appears that axon expansion prior to frank loss of axon density is accompanied by a reduction in glial ramification.

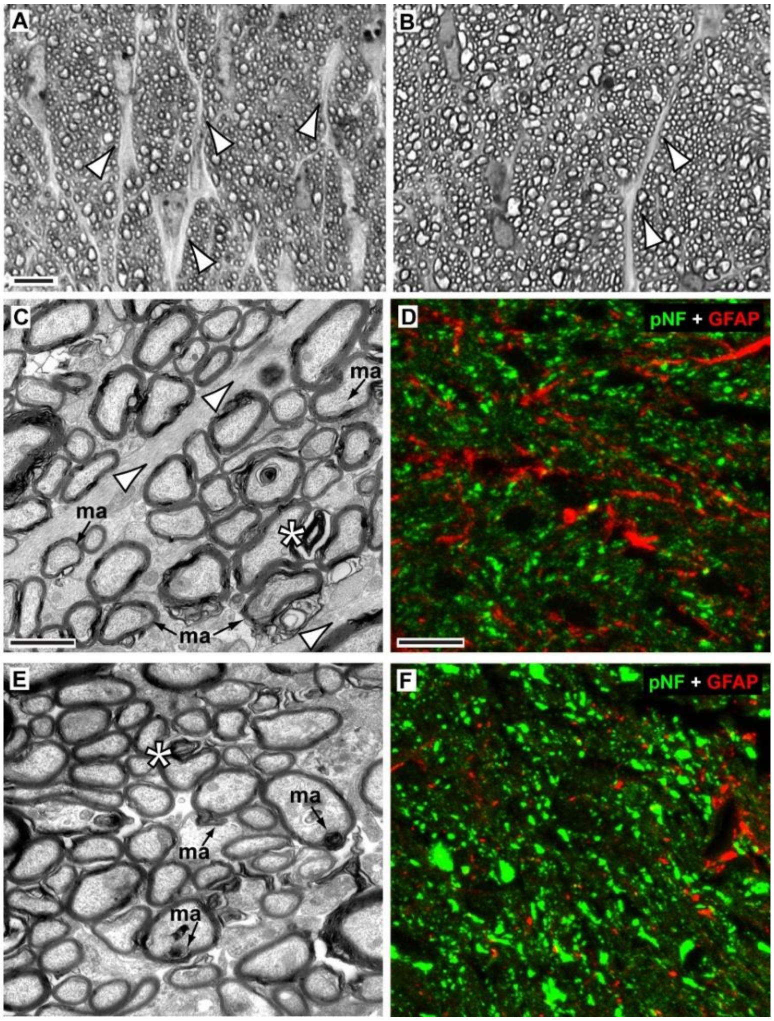

Figure 2.3 Increased axon size is accompanied by astrocyte withdrawal.

A. Light micrograph of cross-section through young (1.5 mo) DBA/2J optic nerve demonstrates tight packing of axons (5.2 x 10^5 axons/mm^2) separated by glial processes (arrowheads). Nerve area is 0.075 mm^2 and mean axon area is 0.37 μm^2. **B**. A 5 month nerve has similar axon density (5.1 x 10^5 axons/mm^2) but is larger (0.10 mm^2) with increased axon area (0.46 μm^2) and diminished astrocyte ramification (arrowheads). **C.** Electron micrograph of a small 9 month nerve (0.076 mm^2) with axon density of 5.7 x 10^5 axons/mm^2 interspersed with glial processes (arrowheads). Mean cross-sectional area of axons was 0.28 μm^2. **D.** Cross-section through same nerve as **C** with astrocyte processes labeled with antibodies against GFAP (red) and axons labeled for phosphorylated neurofilaments (pNF, green). **E**. A 9 month nerve with same axon density was larger (0.11 mm^2) and had significantly expanded axon area (0.41 μm^2) with less inter-axonal space. **F.** Immunolabeling of same nerve demonstrates increased phosphorylated neurofilaments in axons and greatly reduced ramification of GFAP-labeled astrocytes. Scale = 5 µm (A, B), 1 µm (C, E) and 10 µm (D, F).

To investigate this phenomenon further, we devised an algorithm to characterize the degree and pattern of glial ramification in a subset of nerves. This algorithm applies a series of sequential filters to separate ramifying glial processes from axons in an outline of each nerve. We then superimposed on the resulting binary image 20 concentric divisions, each representing 5% of the total nerve area. Figure 2.4 shows two examples: an 11-month nerve with glial processes that distribute about evenly across divisions (Figure 2.4A) and a 6-month nerve with a higher concentration of ramification near the edge (Figure 2.4B). Accordingly, for the first nerve, each division has about 20% of its area covered by glia (Figure 2.4C), while for the other nerve, divisions near the edge have increasingly greater glial

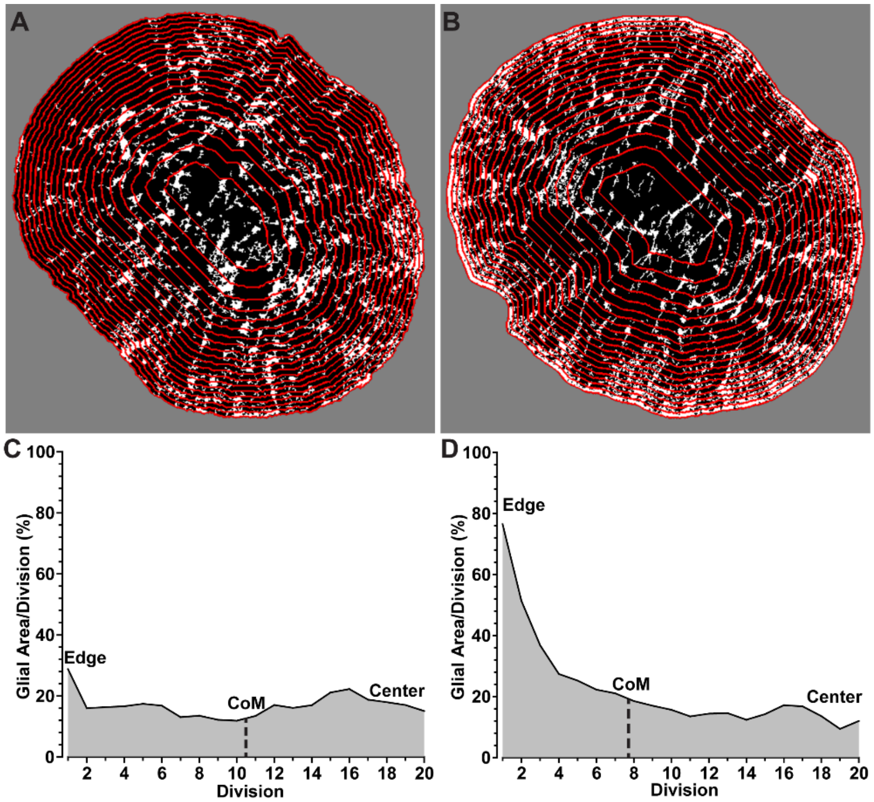

Figure 2.4 Method to quantify changes in glial distribution.

A. Outline of an 11 month DBA/2J nerve (black) with high axon density and small axons (0.29 μm^2) with glial processes highlighted (white). Twenty concentric divisions (red) from the outer edge to the center each delineate an area representing 5% of the nerve. Glial coverage appears nearly uniform from division to division. **B.** A 6 month DBA/2J nerve with larger mean axon size (0.33μm^2) has a higher concentration of glial processes near the edge. **C.** For the nerve in **A**, distribution shows the fraction of each division covered by glia from the outer edge (division 1) to the center of the nerve (division 20). Dashed line shows the center of mass (CoM) for the distribution, which represents the location at which glial area is equivalent on either side. **D.** For the nerve in **B**, the CoM lies closer to the edge of the nerve, where more glial processes ramify and a greater fraction of each division's area is covered.

coverage, rising to over 60% for the first few divisions (Figure 2.4D). This difference is reflected in the center of mass (CoM) for each distribution, which divides the distribution of glial area per division into halves. While the CoM for the nerve in Figure 2.4A lies near the 10th division, indicating equivalent glial area between the center and edge of the nerve, the CoM for the other nerve is closer to 8, indicating a shift towards the edge (Figure 2.4D).

Next, we calculated the CoM of the glial distribution for nerves with mean axon areas below 0.50 μm^2 (Figure 2.5, left panel). We chose this value because it represents the approximate threshold above which axon density diminishes (see Figure 2.2). For nerves with

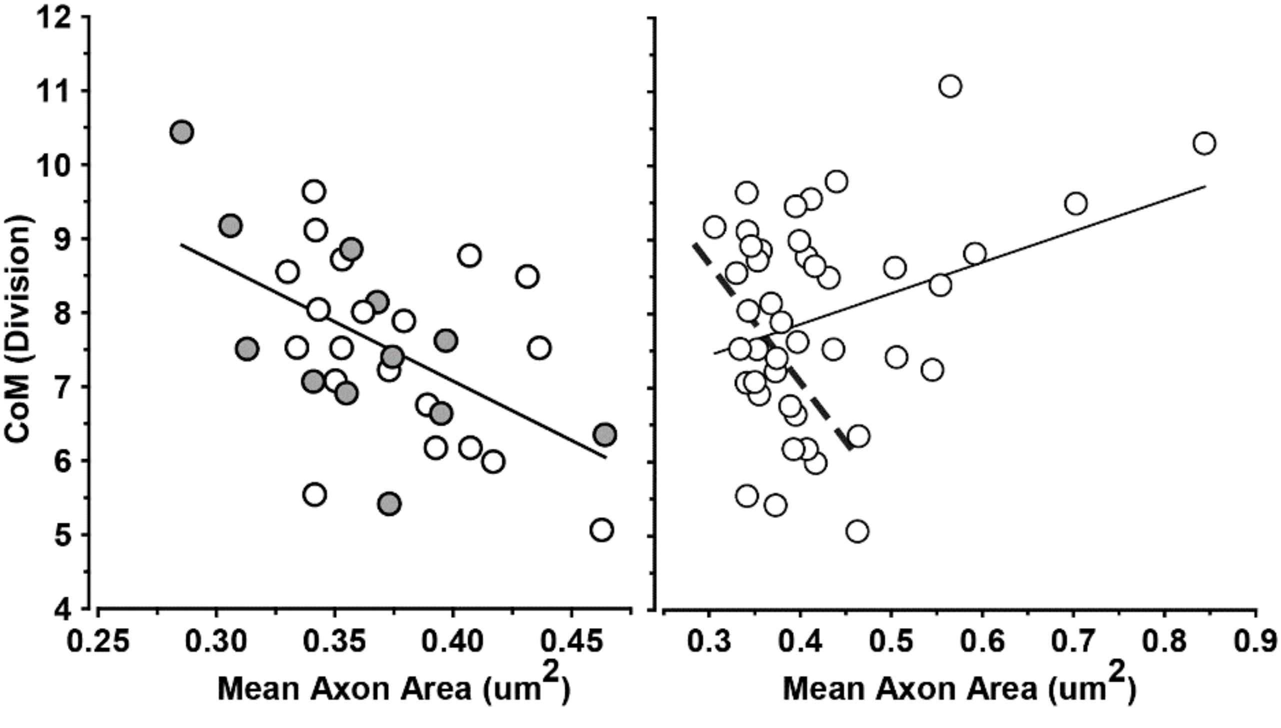

Figure 2.5 Distribution of glial ramification as axons expand.

Left: CoM (center of mass) for a subset of nerves with mean axon area below 0.50 μm^2 (open symbols) decreases as axon size increases (r = -0.535, p = 0.002). The linear regression was similar for the subset of nerves with axon density > 5.0 x 10^5 axons/mm^2 (filled symbols; p = 0.32). Right: for the complete set of nerves with glial quantification, CoM increases with axon expansion (r = 0.32, p = 0.036). Regression line for nerves with axon area below 0.50 μm^2 is repeated from the left panel for comparison (dashed line).

the smallest mean axon size, the CoM is near 10 – indicating an even distribution of glial coverage from center to edge. As axon size increases in this subset of nerves, CoM diminishes. This is consistent with movement of glial processes out of the center and towards the edge of the nerve, as shown for the nerve in Figure 2.4B. We repeated this analysis for a larger population of DBA/2J nerves, including those with much larger mean axon size (Figure 2.5, right panel). With increasing axon size, the CoM returns to higher values, though never exceeding 10 or 11. This indicates that as axons continue to expand glial ramification once again covers the nerve about evenly.

2.3.3 OPTIC NERVE REMODELING INVOLVES DIMINISHED ASTROCYTE ORGANIZATION

Astrocyte processes retract from axon bundles prior to frank loss of axons in the myelinated segment of the DBA/2J optic nerve[190]. Using the same cohort of nerves, here we report another interesting characteristic of astrocyte organization and orientation. Figure 2.6A (left) shows a healthy nerve with high axon density (6.2×10^5 axons/mm^2) and a low fraction of its area covered by glia (11.4%). For this nerve, astrocyte processes appear to follow a parallel pattern of distribution (Figure 2.6B**)**. This pattern is consistent with astrocyte distribution in cross-section of healthy white matter tracts[317,318]. However, a glaucomatous nerve with substantial loss of axons (2.4×10^5 axons/mm^2) and increased glial coverage (45.19%) demonstrates clear disorganization of astrocyte processes (Figure 2.6A, right), with less apparent parallel orientation (Figure 2.6C).

To quantify loss of parallelism in our cross-sections of proximal DBA/2J optic nerve, we devised an algorithm that decomposes glial processes into horizontal and vertical vector components. First, each nerve was rotated to maximize the orientation of glial processes along the horizontal axis (Figure 2.7A,B). This normalizes images for nerve orientation. Following rotation (Figure 2.7C), each process was skeletonized to simplify decomposition into

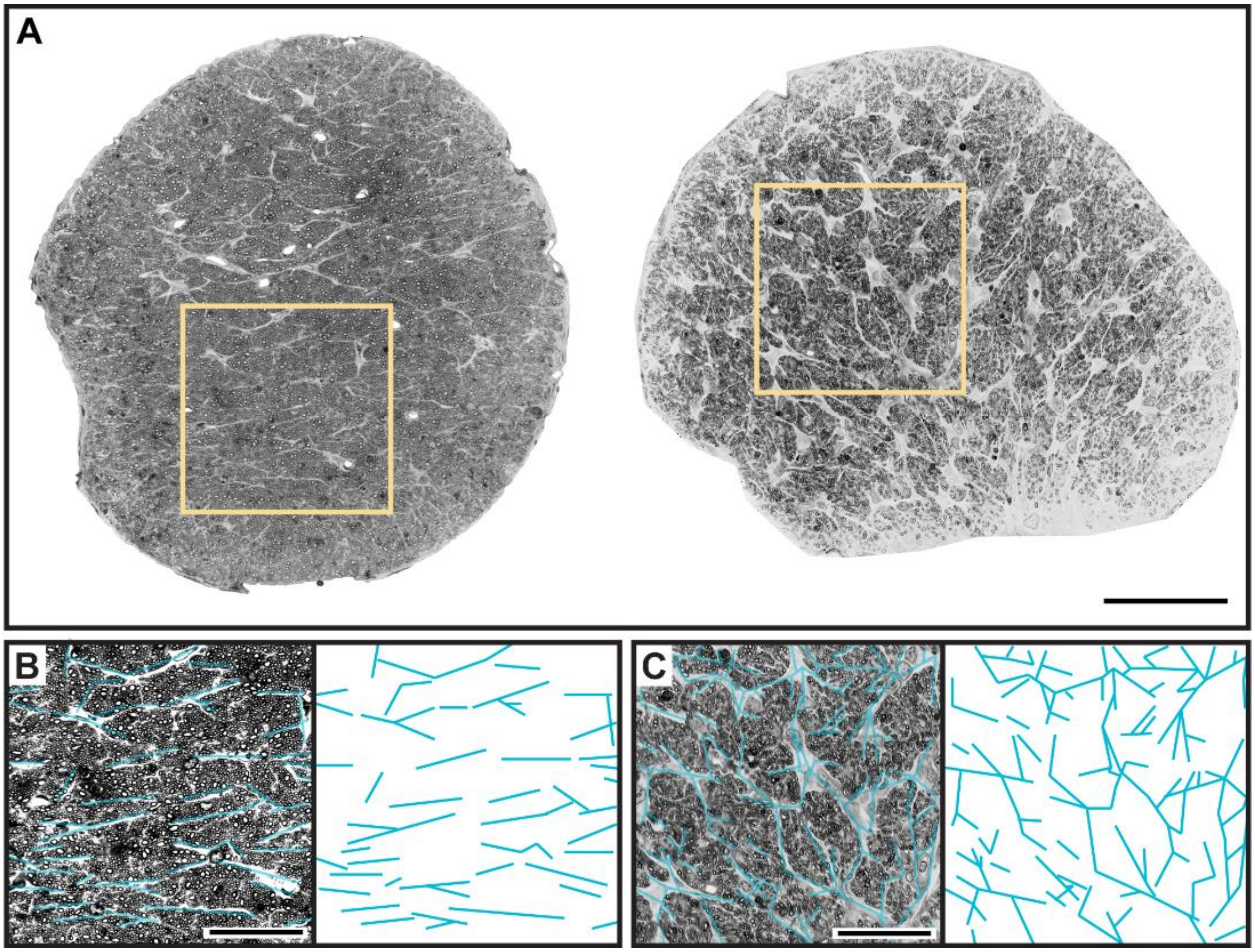

Figure 2.6 Pathology alters glial orientation in the optic nerve.

A. Left: cross-section through DBA/2J optic nerve prior to progression. Nerve has high axon packing density (6.2×10^5 axons/mm^2) and low glial coverage area (11.4% of total nerve area). Right: during progression axons are lost (2.4×10^5 axons/mm^2) and glial coverage increases (45.19%). **B.** Higher magnification of inset from healthy nerve in **A** with highlighted glial processes demonstrating parallel orientation. **C.** Inset from glaucomatous nerve in **A** with glial processes similarly highlighted. In this nerve, processes appear disordered, or oriented without a discernable pattern. Scale = 100 µm (A), 10 µm (B,C).

vectors (Figure 2.7D). Skeletons were decomposed by removing branch points, resulting in a population of vectors representing the orientation of each segment of astrocyte processes (Figure 2.7E).

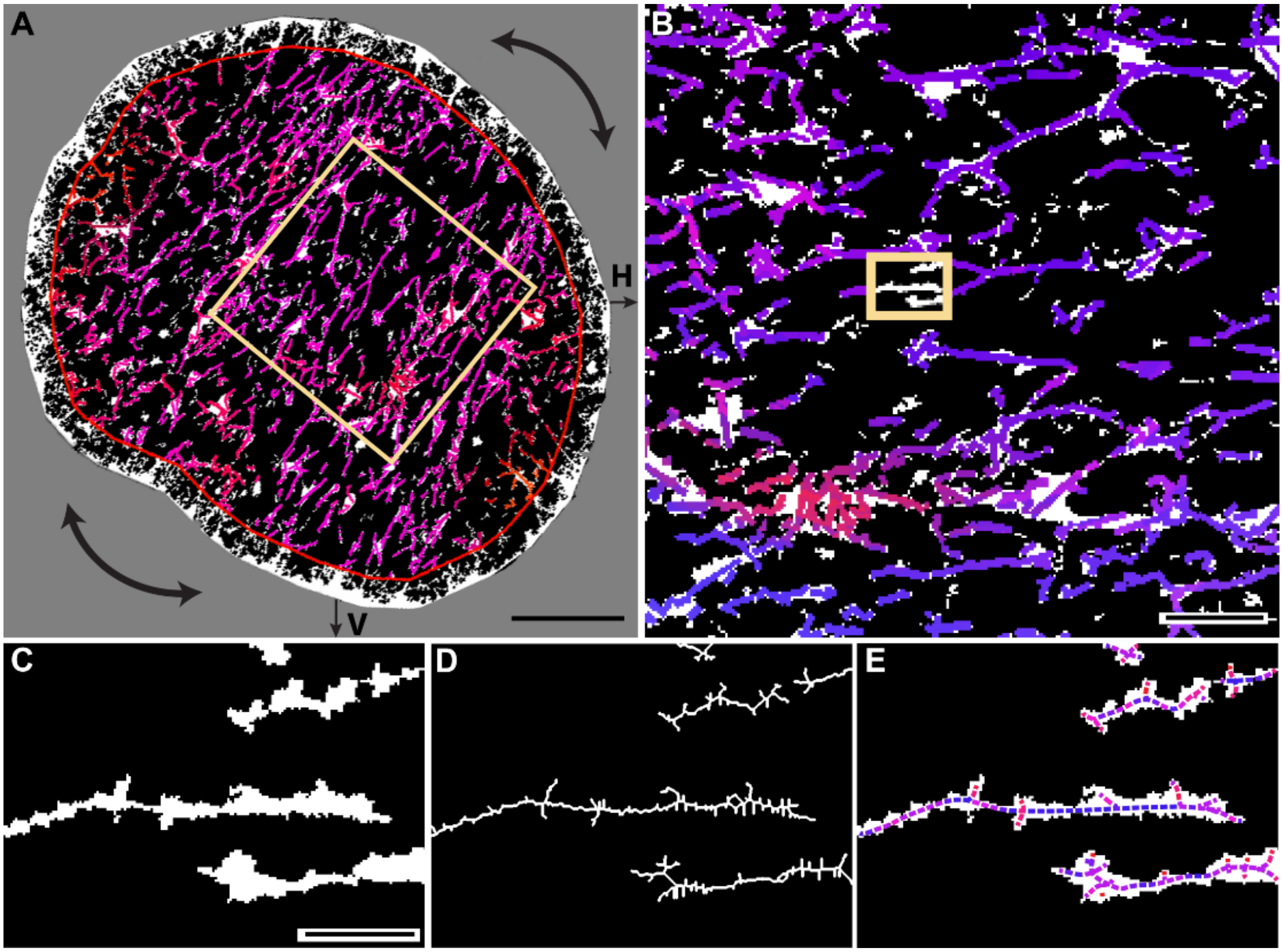

Figure 2.7 Deconstruction of astrocyte processes into representative vectors.

A. Binary representation of an 8-month DBA/2J nerve with glial processes highlighted to indicate coverage (white; 19.35% of nerve area). Colored overlay demonstrates result of algorithm to calculate vectors, with degree of orientation along the vertical axis (V) indicated by red tint and degree of orientation along the horizontal axis (H) indicated with blue tint. Our algorithm excludes the outer 20% of nerve area to minimize edge effects and rotates the image to maximize orientation along the horizontal axis, shown by the inset magnified in panel **B. C.** Inset from **B** in higher magnification shows glial processes in binary image. **D.** Same glial processes skeletonized for assigning vectors to segments of constant orientation. **E.** Representative resultant vectors for each segment calculated from skeletonized image overlaid on original binary representation of glial processes. The length of each vector represents the pixel distance of each segment between branch points in the skeletonized image. Scale = 100 µm (A), 10 µm (B), 2 µm (C, D, E).

By collecting all such segments across the nerve, we generated a single representative value of astrocyte parallelism. For the collection of vectors (Figure 2.8A), we summed the pixel length of all horizontal and vertical components (Figure 2.8B). This summation defined a resultant vector representing the orientation and length of all vectors across the cross section (Figure 3C). We defined the percent parallelism in each nerve using the ratio of summed horizontal and vertical components such that that a value of 100 indicates perfectly parallel orientation (i.e., no vertical component), while a value of 0 indicates random orientation due to

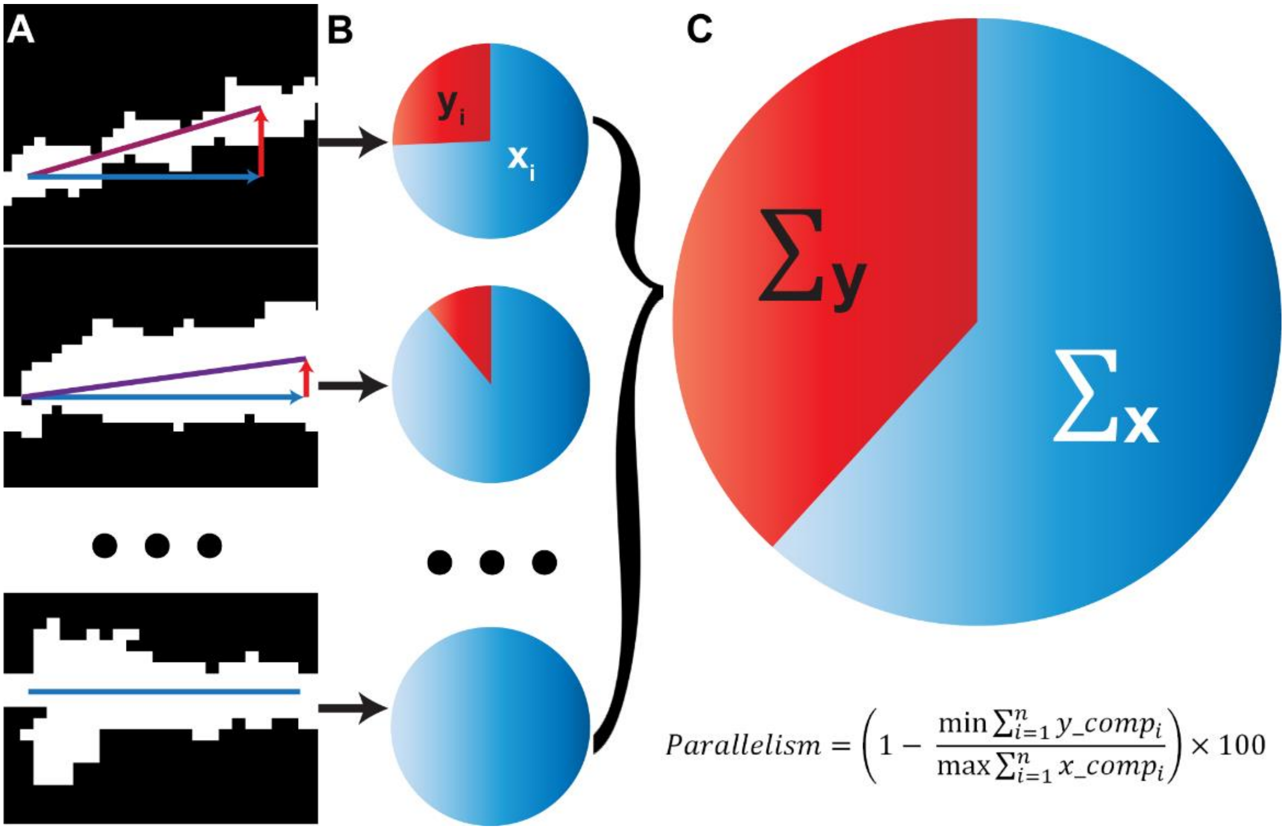

$$Parallelism = \left(1 - \frac{\min \sum_{i=1}^{n} y\_comp_i}{\max \sum_{i=1}^{n} x\_comp_i}\right) \times 100$$

Figure 2.8 Method to quantify overall parallelism of glial processes.

A. Binary high-mag of glial processes with increasing horizontal vector components (blue) compared to vertical (red). Resultant vector is the sum of these components (purple). **B.** Individual pie charts depict the ratio of the length of the horizontal (blue, x_i) and vertical (red, y_i) components for each resultant vector. **C.** The sum of the horizontal (x) and vertical (y) components for each nerve represents the degree of parallelism. The percent parallelism for each nerve is calculated from the ratio of the summed components following rotation to minimize vertical and maximize horizontal orientation. 100% corresponds to perfect parallelism and 0% corresponds to random orientation.

equivalent vertical and horizontal components. This single value represents the organization across an entire nerve, providing a mechanism to analyze process organization in relation to other outcome measures.

Astrocyte processes in the DBA/2J optic nerve redistribute spatially during progression, showing a tendency to retreat towards the edge prior to frank axon degeneration[190]. With progression, astrocyte processes once again fill in across the nerve. In Cooper et al, 2016, we quantified this trend by defining a center of mass (CoM) based on division of the nerve into concentric rings, with values near 10 indicating an even distribution and values < 10 indicating

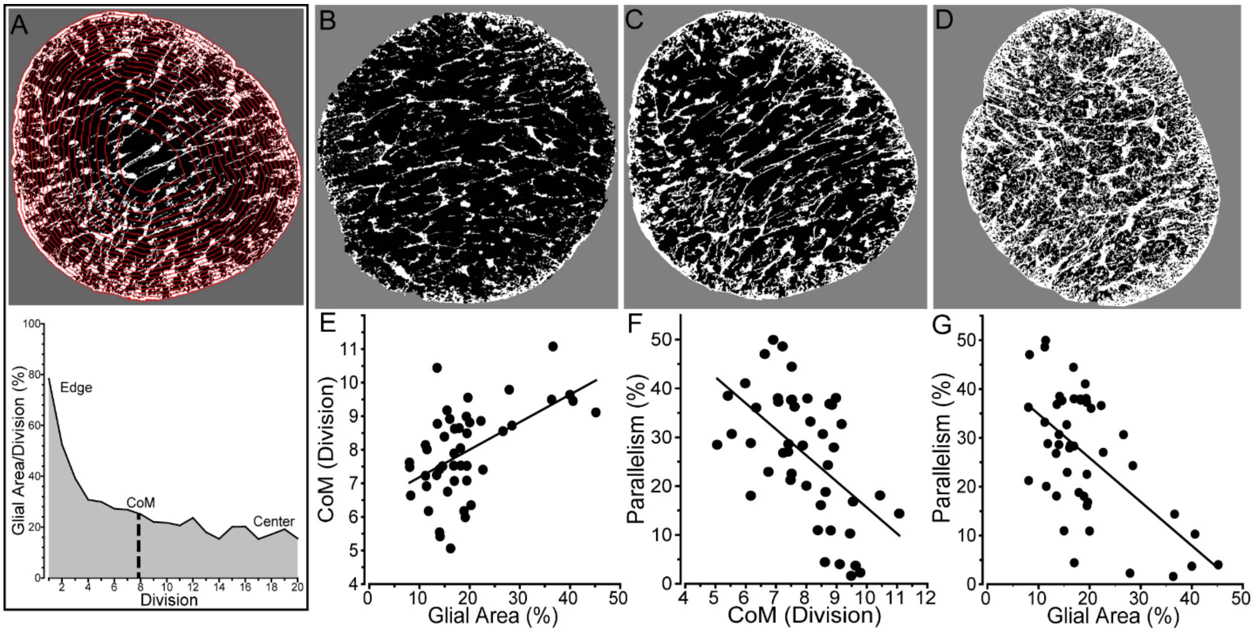

Figure 2.9 Measuring the spatial distribution of astrocyte processes.

A. Center of Mass (CoM) was calculated using a series of concentric circles (red) each delineating 5% of nerve area. From the first division at the edge of the nerve to the twentieth division at the center (graph below), the CoM represents the division at which half of the glial area resides on each side. **B.** Cross-section through a young (1.5 month) DBA/2J optic nerve shows slight bias of astrocyte center of mass (CoM) towards edge (CoM = 7.22), low coverage (11.2%), and high parallelism (48.6%). **C.** A 3 month DBA/2J nerve with higher CoM (8.55) and coverage (26.7%) shows less parallelism (30.6%). **D.** A 5 month nerve with expansive glial coverage (40.6%) shows even astrocyte distribution (CoM = 9.44) and loss of parallelism (10.3%). **E.** CoM increases significantly with glial area (modified from Cooper et al., 2016; r = 0.529 , $p < 0.001$). **F,G.** Parallelism decreases with both increasing CoM (r = -0.55, $p < 0.001$) and expanding glial area (r = -0.60 , $p < 0.001$). Scale = 100 µm (A-C).

bias towards the edge of the nerve (Figure 2.9A). As glial area increases, the pattern of process distribution alters (Figure 2.9B,C,D). We found that nerves with lower glial area tended to have an edge-distributed CoM (about 7), while nerves with higher glial area have a relatively even glial distribution (about 10; Figure 2.9E). As CoM increased and glial coverage expanded, parallelism diminished as well (Figure 2.9F,G).

2.3.4. PARALLELISM REFLECTS EARLY AXONAL CHANGES

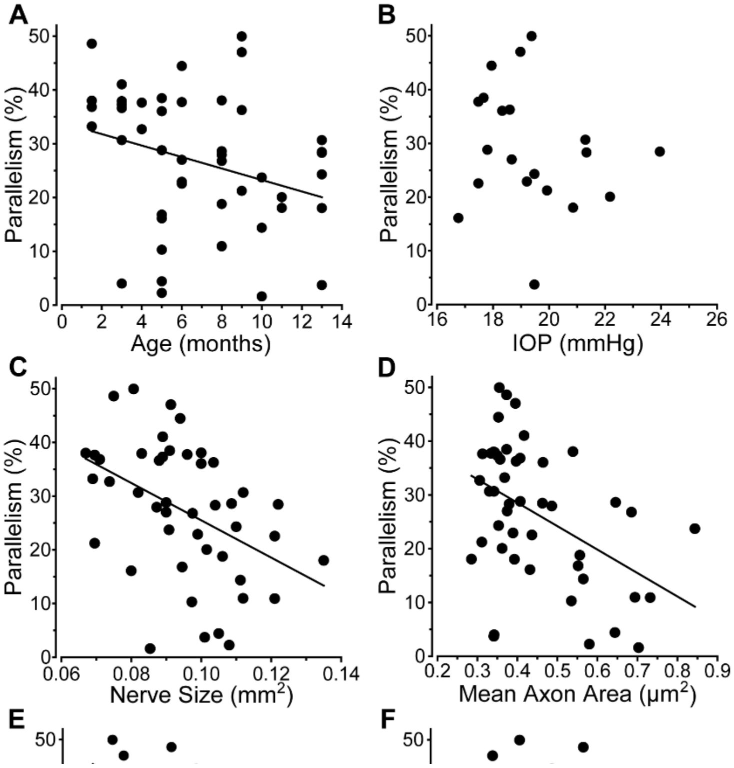

Figure 2.10 Parallelism diminishes with markers of axon degeneration.

A. Parallelism decreases moderately as DBA/2J mice age (r = -0.293, *p* = 0.046); there is no correlation with the mean lifetime IOP (**B**; r = -0.193, *p* = 0.415). **C.** Parallelism rapidly diminishes with enlargement of the nerve (r = -0.435, *p* = 0.003). **D.** Increased mean axon area is also correlated with decreased parallelism (r = -0.457, *p* = 0.001). **E.** Parallelism demonstrates a tight correlation with diminished axon density (r = -0.628, *p* < 0.001). **F.** As the total number of axons decreases, parallelism decreases (r = -0.427, *p* = 0.005).

Next we examined how redistribution of astrocyte processes in the nerve is influenced by other predictors and indices of glaucomatous progression in the DBA/2J nerves. Across our sample of optic nerves, we found that parallelism diminished only modestly with age (Figure 2.10A); the relationship with IOP was even weaker (Figure 2.10B). Cross-sectional nerve area (measured in mm^2) increases with age in the DBA/2J mouse; this is linked eventually to axon loss and significant enlargement of cross-sectional area of surviving axons[190]. Here, we found that as the nerve enlarges, parallelism decreases significantly (Figure 2.10C). Accordingly, since nerve expansion predicts both axon loss and axonal enlargement[190], increased axon size (Figure 2.10D), diminished axon density (Figure 2.10E), and loss of total number of axons all correlated with decreased parallelism (Figure 2.10F). There is, however, a caveat to this conclusion.

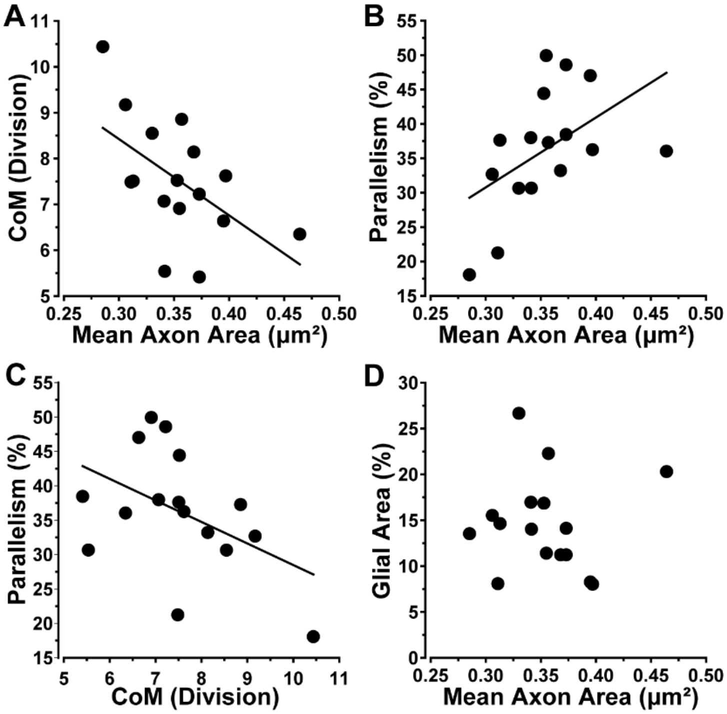

Figure 2.11 Astrocytes become more parallel as axons expand early prior to loss.

A. CoM decreases significantly as axons expand early in the DBA/2J nerve prior to overt loss of axons ($r = 0.55$, $p < 0.001$). **B.** As axons expand prior to outright loss, parallelism increases ($r = 0.50$, $p = 0.05$). **C**. Parallelism tends to increase with decreasing CoM for the same set of nerves ($r = 0.47$; $p = 0.071$). **D.** Glial coverage of the nerve does not change as axons expand prior to loss ($r=0.006$, $p=0.98$). All data collected from subset of nerves with highest axon sampling density below the threshold of axon size for which loss occurs ($4.8\text{-}6.5 \times 10^5$ axons/mm^2).

While axons expand in area continuously from early to late progression in the DBA/2J optic nerve, expansion is not associated with axon loss up to a critical threshold of about 0.50 µm^2 [190]. This early axon expansion is coincident with retraction of astrocyte processes towards the nerve edge and a temporary decrease in CoM (Figure 2.11A). For these same pre-degenerative nerves, we then examined parallelism. As axons expanded and astrocyte processes retracted towards the edge, parallelism increased (Figure 2.11B). Intriguingly, these nerves at early stages of pathology exhibit glial distributions opposite that of the sample of nerves across all stages of degeneration (Figure 2.11D). Moreover, the dependence of parallelism on CoM was slightly weaker for these pre-degenerative nerves than for the entire sample (*p* = 0.071; Figure 2.11C**,** compare to Figure 2.10E). For this subset of nerves, glial coverage did not change with axon size (Figure 2.11D) or with parallelism (data not shown; r = 0.0942; p = 0.0729). These data indicate that while parallelism diminishes as axons degenerate later (Figure 2.10E), early changes in the nerve prior to overt axon loss are associated with increased parallelism without a change in overall glial coverage.

2.3.5 ASTROCYTE CYTOSKELETAL REORGANIZATION DEPENDS ON LOCATION IN THE NERVE

To determine how astrocyte reorganization reflects cytoskeletal changes, we measured the distribution of GFAP in discrete intervals along longitudinal sections through the aged (10 month) DBA/2J optic nerve, spanning proximal to the nerve head (< 1 mm) and to more distal (> 4 mm; Figure 2.12A insets 1 and 2). We then compared this distribution to CoM and parallelism redefined for immuno-labeling in longitudinal sections. On average, DBA/2J nerves exhibited increased total nerve GFAP compared to the age-matched D2 control strain (*p* < 0.001; Figure 2.12B). While at discrete points along the nerve GFAP in DBA/2J was systematically higher, this trend did not translate to a significant difference within any one interval (Figure 2.12C). The CoM for GFAP was significantly elevated in DBA/2J compared to D2 nerves, indicating a more central distribution of astrocytes (*p* < 0.001; Figure 2.12D). Moreover, unlike GFAP levels, CoM did significantly depend on location in the nerve (Figure 2.12E), with GFAP-labeled processes

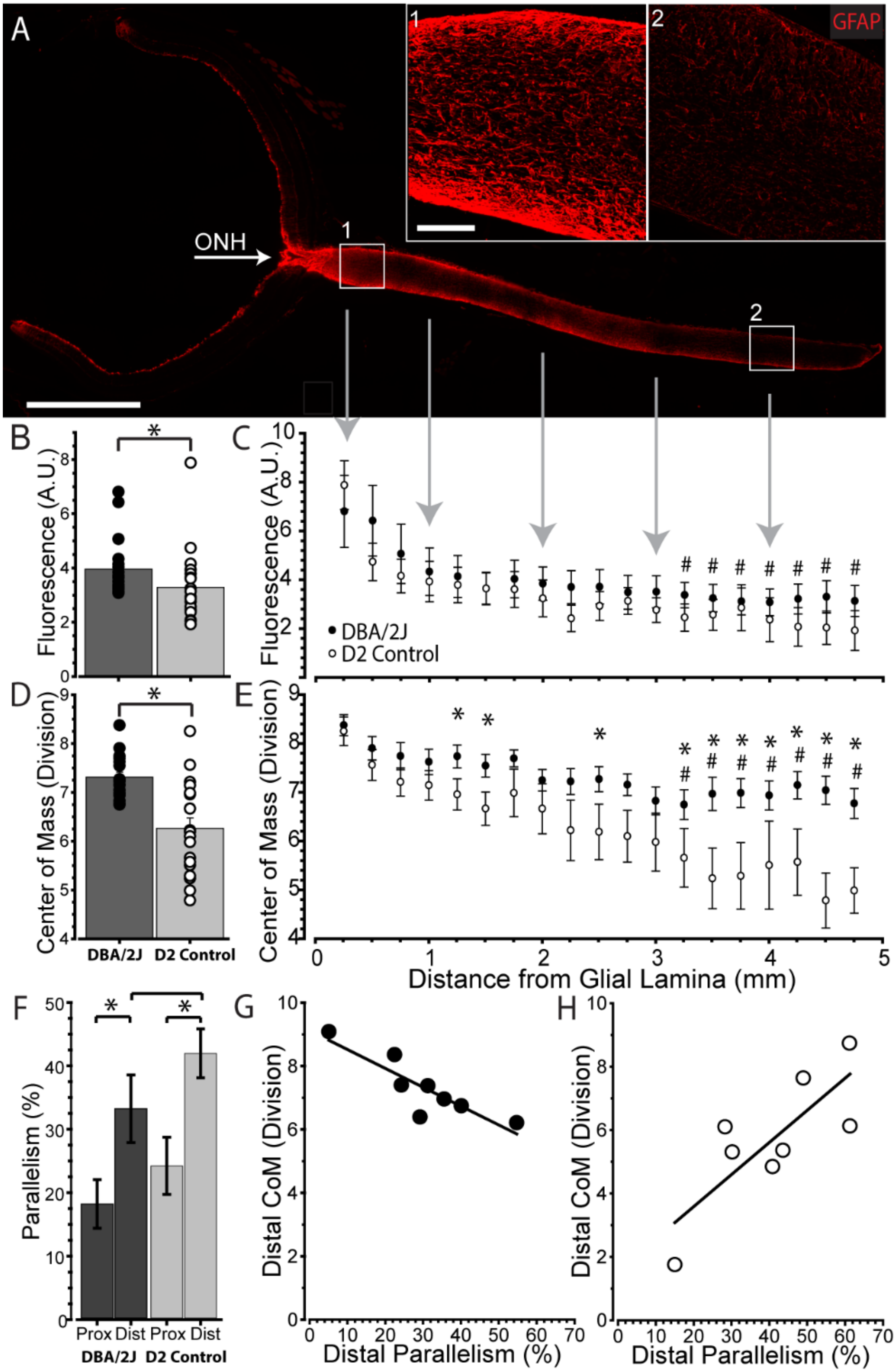
A
ONH
1
2
GFAP
B
Fluorescence (A.U.)
DBA/2J
D2 Control
C
DBA/2J
D2 Control
D
Center of Mass (Division)
E
Distance from Glial Lamina (mm)
F
Parallelism (%)
Prox
Dist
G
Distal CoM (Division)
Distal Parallelism (%)
H
Distal CoM (Division)
Distal Parallelism (%)

Figure 2.12 Astrocyte GFAP redistributes throughout the optic nerve.

A. Longitudinal section through 10-month DBA/2J retina and optic nerve shows astrocytes labeled for GFAP (red). GFAP expression is highest at the optic nerve head (ONH), proximal optic nerve (1), and at the edges of the distal nerve (2). **B.** GFAP is significantly elevated in DBA/2J nerves compared to D2 control nerves ($p < 0.001$). **C.** When analyzed in 0.25 mm segments, no one segment of DBA/2J nerve contains significantly elevated GFAP compared to the same D2 control segment; however, the most proximal segment (0.25 mm) in both DBA/2J and D2 control nerves contains significantly more GFAP than distal segments (#; $p < 0.001$). **D.** The CoM of GFAP within DBA/2J nerves is significantly greater than D2 control nerves ($p < 0.001$). **E.** DBA/2J nerves contain significantly altered GFAP CoM from D2 control nerves, and these differences occur most often within distal nerve segments (*; $p < 0.029$). **F.** GFAP parallelism is significantly greater in the distal compared to the proximal nerve in both the DBA/2J ($p = 0.015$) and D2 control ($p = 0.003$). Additionally, GFAP within distal DBA/2J nerves trends toward less parallelism than the equivalent segment of D2 control nerves ($p = 0.09$). **G.** DBA/2J distal nerves tend to have a more edge-distributed center of mass when parallelism is greater ($p = 0.005$), indicating parallelism and center of mass are related. **H.** This relationship is trending toward the reverse in distal D2 control nerves ($p = 0.07$). Scale: 1 mm (A), 100 µm (A insets).

distributing more towards the nerve center at distal locations compared to D2 nerves. This is a later hallmark of progression[190]. Additionally, we found that GFAP parallelism is elevated in the distal nerve of both DBA/2J (p = 0.015) and D2 control compared to proximal nerve (p = 0.003; Figure 2.12F). Finally, the CoM for distal segments of DBA/2J nerve indicated edge-distributed astrocytes with increased parallelism (p = 0.005), while CoM in D2 nerves showed the opposite trend (Figure 2.12G), though not significant (p = 0.07).

2.3.6 PARALLELISM REFLECTS BOTH ASTROCYTE CONNECTIVITY AND RGC AXONAL FUNCTION

Loss of anterograde axonal transport of cholera toxin B (CTB) from retina to superior colliculus (SC) is an early hallmark of axonopathy in the DBA/2J and other models[10,45,153,256,300,316]. Consistent with this pattern, while SC from D2 animals demonstrated mostly intact transport (75% intact), DBA/2J SC exhibited severe deficits (Figure 2.13A), with intact transport averaging only about 20% (22.784 ± 5.493), a highly significant difference (p = 0.0015, Figure 2.13B). Astrocytes couple to one another through gap junctions to form a dense network that is tightly modulated by axonal function and neuronal activity[319]. In these same animals, we examined levels of connexin 43 (Cx43), a marker for gap junctions between astrocytes[62]. Consistent with this role, both proximal and distal segments of DBA/2J and D2 optic nerve show strong Cx43 colocalization with GFAP (Figure 2.13C). Additionally, there are significantly more Cx43 puncta in proximal vs. distal segments in the DBA/2J nerve (p = 0.043; Figure 2.13D), similar to the distribution of GFAP (Figure 2.12C). Additionally, Cx43 puncta are increased in DBA/2J nerve compared to D2, though this is only significant for proximal segments (p = 0.032; Figure 2.13D).

Higher Cx43 in the proximal segment predicted a greater degree of parallelism for GFAP-labeled astrocyte processes (*p* = 0.04; Figure 2.14A, left). This was not so for the distal segment (*p* = 0.77; Fig. 2.14A, right), though overall parallelism was higher in this location (Figure 2.14F). These differences may have functional significance for axons. Earlier we demonstrated that anterograde transport from retina to the SC in the DBA/2J degrades in a distal (brain) to proximal (retina) pattern[153]. Here, while Cx43 in the proximal segment did not correlate with

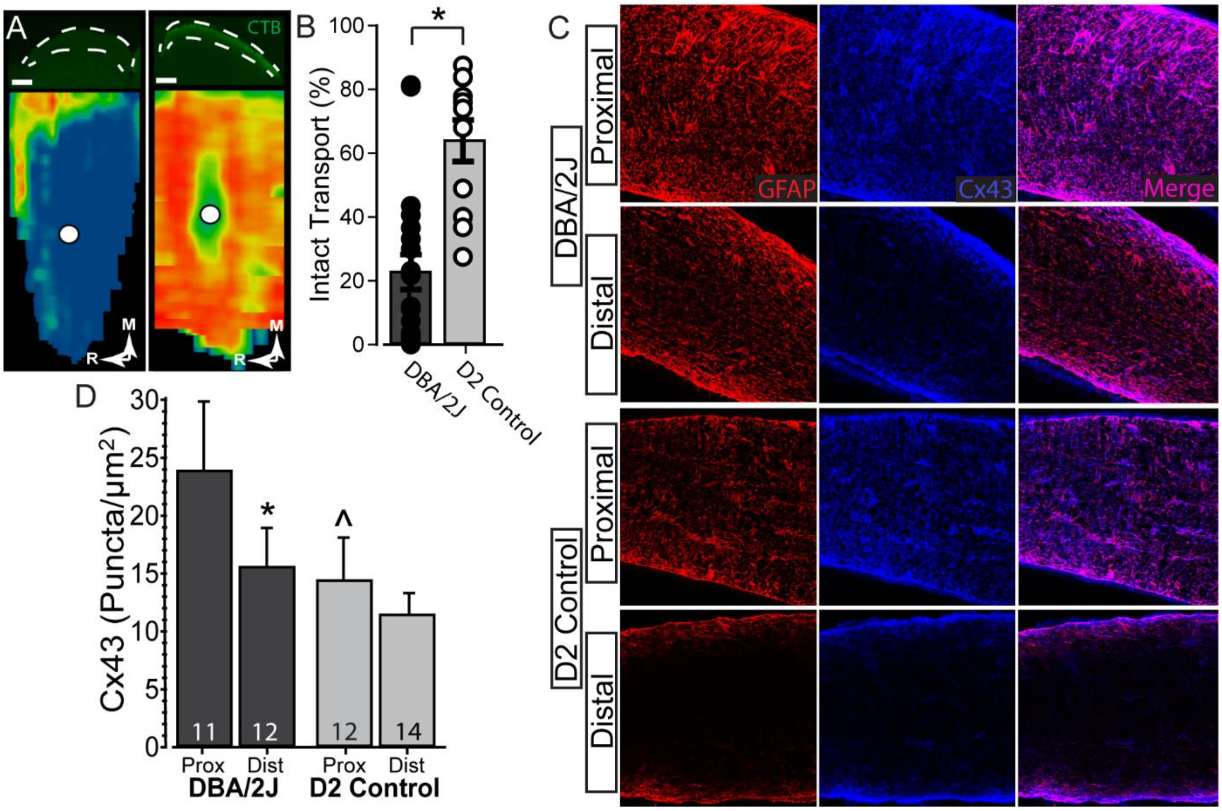

Figure 2.13 Diminished anterograde transport in a sample of DBA/2J nerves.

A. Top Left: Coronal section through superior colliculus of DBA/2J mouse (between dashed white lines) following intravitreal injection of CTB (green). Bottom Left: Corresponding retinotopic map shows nearly depleted anterograde transport of CTB. Top Right: Coronal section through superior colliculus of D2 control mouse prepared as on left. Bottom Right: Corresponding retinotopic map shows a full complement of anterogradely transported CTB. **B.** Transport of CTB from DBA/2J eyes was near 20% (22.8 ± 5.5), significantly reduced from D2 control which is near 75% (74.896 ± 4.328) (*p* = 0.0015). **C.** Confocal micrographs of proximal (left) and distal (right) DBA/2J (top) and D2 control (bottom) optic nerves. Connexin 43 (Cx43, blue) and GFAP (red) colocalize, and both are elevated in proximal optic nerve. **D.** Density of Cx43 (puncta/µm²) in proximal segment of DBA/2J nerves is significantly elevated compared to both distal DBA/2J (*; *p* = 0.043) and proximal D2 nerves (#; *p* = 0.032).

levels of intact axonal anterograde transport (Figure 2.14B, left), increased Cx43 in the distal segment strongly correlated with this measure of axonal function ($p < 0.001$; Figure 2.14B, right).

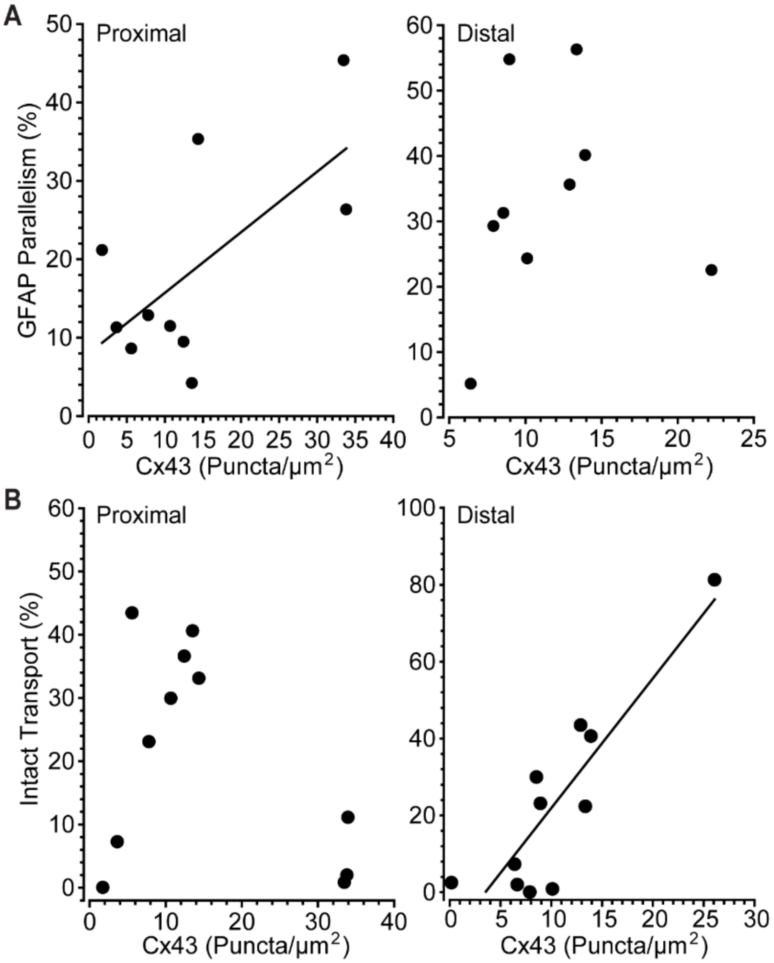

Figure 2.14 RGC axon functional deficits are associated with astrocyte connectivity in DBA/2J optic nerve.

A. Confocal micrographs of proximal (left) and distal (right) DBA/2J (top) and D2 control (bottom) optic nerves. Connexin 43 (Cx43, blue) and GFAP (red) colocalize, and both are elevated in proximal optic nerve. **B.** Density of Cx43 (puncta/μm²) in proximal segment of DBA/2J nerves is significantly elevated compared to both distal DBA/2J (*; $p = 0.043$) and proximal D2 nerves (#; $p = 0.032$). **C.** Higher levels of Cx43 are associated with a greater degree of parallelism of GFAP-labeled astrocyte processes in proximal segments of DBA/2J nerve (left, R = 0.66; $p = 0.04$) but not distal (right, R = 0.11; $p = 0.77$). **D.** Intact anterograde transport to the superior colliculus is well-predicted by levels of Cx43 in the distal optic nerve (right, R = 0.88; $p < 0.001$), but not proximal (left, R= 0.39; $p = 0.23$). Scale: 100 μm (A).

2.3.7 EARLY AXON EXPANSION INVOLVES DIMINISHED MITOCHONDRIAL DENSITY

Our micrographs show another feature of associated with early axon expansion. We found that for nerves with axon density among the highest in our sample, as mean cross-sectional axon area increased along with nerve size, the number of discernible mitochondria in

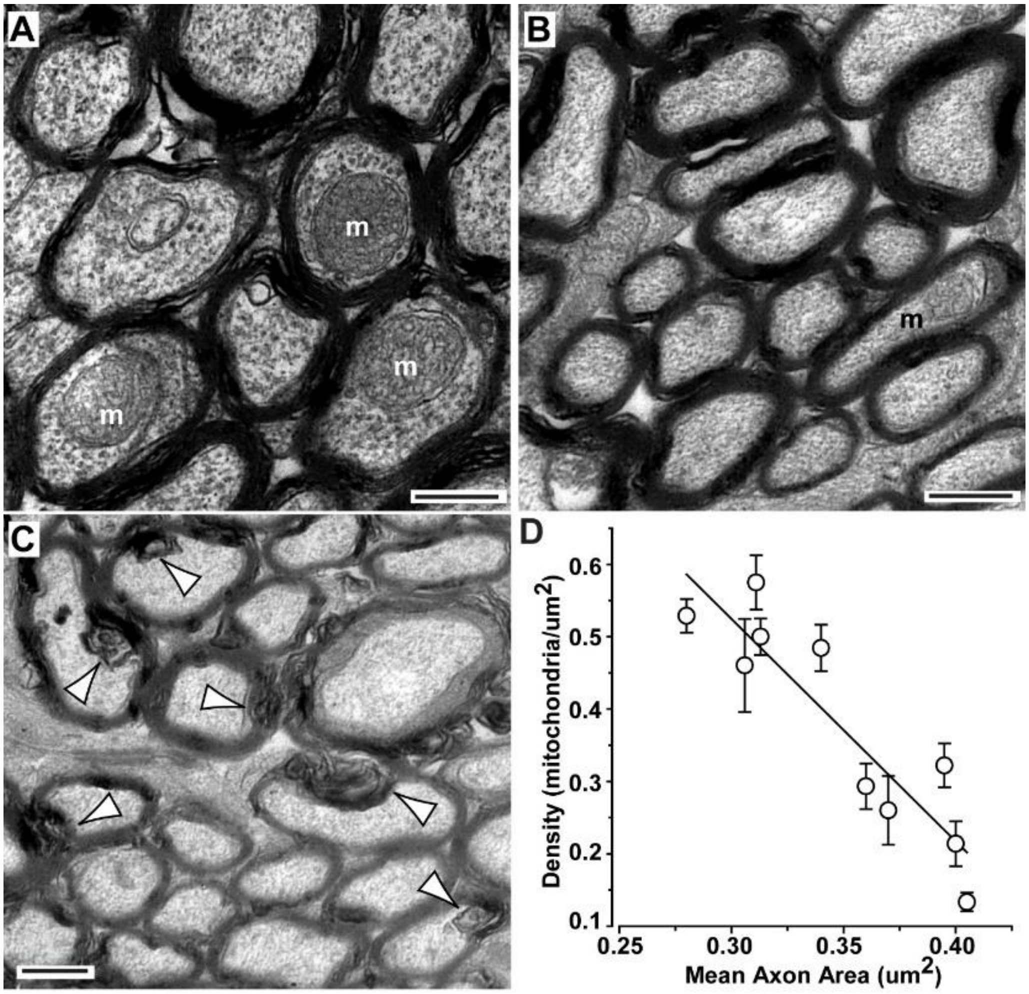

Figure 2.15 Mitochondrial density decreases as mean axon area increases.

A. Electron micrograph of a small 4 month nerve (0.074 mm^2) with axon density of 5.6 x 10^5 axons/mm^2. Note well-ordered cytoskeleton and multiple mitochondria (m). Mean axon area is small (0.31 μm^2). **B.** A 9 month nerve also has high axon density (6.0 x 10^5 axons/mm^2) but increased mean axon area (0.40 μm^2) and nerve size (0.091 mm^2). Micrograph shows fewer mitochondria. **C.** A larger 9 month nerve (0.10 mm^2) with high axon density (5.6 x 10^5 axons/mm^2) has disordered axoplasm, few mitochondria, and distended mesaxons in several axons (arrowheads). Mean axon area is 0.40 μm^2. **D.** In a sample of high-density nerves (5.2 – 6.2 x 10^5 axons/mm^2), mitochondrial density decreases as mean axon area increases (r = -0.831, p=0.003). Scale = 0.5 μm.

our electron micrographs seemed to diminish. For example, a small 4-month nerve with small axon size had mitochondria distributed throughout both axons and glial processes within the inter-axonal space (Figure 2.15A). In contrast, an older, larger nerve with expanded axons had far fewer mitochondria (Figure 2.15B). Similar nerves showed other signs of axon pathology, including disorganized axoplasm and swelling of the internal mesaxon in many axons (Figure 2.15C). When quantified from multiple electron micrographs of nerves with high axon density, we found that axon expansion was strongly associated with decreased density of mitochondria (Figure 2.15D).

2.3 DISCUSSION

Intrinsic variability in optic nerve pathology is a signature feature of the DBA/2J mouse model of glaucoma [235,320-323]. A DBA/2J nerve unaffected by disease will demonstrate a mean axon packing density of 5.0 – 6.0 x 105 axons/mm^2. When multiplied by the cross-sectional nerve area delineated within the layers of pia and dura mater, this leads to an estimated total number of axons of 50,000 – 60,000, comparable to that in C57/B6 nerve[323,324]. Nerves with the worst pathology often demonstrate a packing density less than about 100,000 axons/mm^2. Here, nerves with pathology so severe that identification of intact myelin sheaths was too ambiguous to quantify were excluded, since we are interested in early changes associated with progression.

We find that with age, the cross-sectional area of the myelinated segment of the DBA/2J optic nerve tends to increase[190]. Nerve size ranges from about 0.06 mm^2 at 2 months of age to as high as 0.16 mm^2 at 10-12 months. Expansion of the nerve generally is associated with increased pathology, including diminished axon packing density and increased incidence of degenerating profiles[190]. The mean cross-sectional area of surviving axons, too, increases as nerves expand (Figure 2.1). Intriguingly, many nerves retain a high packing density (> 5.0 x 10^5 axons/mm^2) even as nerve area initially increases (Figure 2.2). Axon density remains relatively invariant up to a mean axon area of 0.45-0.50 μm^2 (Figure 2.2). Thus, modest axonal enlargement with nerve expansion presages degeneration; once this threshold is reached, axon density decreases rapidly with increasing mean axon size up to an average size of 0.7-0.8 μm^2 (Figure2.2).

Even so, expanding axons show signs of early axonopathy. These features include disorganized and expanded axoplasm, poorly articulated microtubules and neurofilaments, deformation of the mesaxon and axolemma, and increased accumulation of hyperphosphorylated neurofilaments (Figures 2.1, 2.3). The latter is indicative of challenged axonal transport, which relies upon cytoskeletal integrity to efficiently move cargo[325,326]. Deficiencies in anterograde axon transport are one of the earliest pathogenic events in DBA/2J glaucoma[153,212] which we again replicate here (Figure 2.13). Thus, axon expansion and diminished anterograde transport likely directly relate to accumulation of phosphorylated neurofilaments and disordered axoplasm[232,309,327].

Hypertrophy of glial process in the optic nerve, particularly of astrocyte processes, is a prominent characteristic of a nerve experiencing substantial axon loss in glaucoma[328] and in the DBA/2J model[193,308,309]. We utilized cross-sections of DBA/2J optic nerve to examine the spatial distribution of astrocytes among the full complement of axons residing within the proximal optic nerve. This allows for more reliable comparison between peripheral and central astrocytes, but restricts our analysis to the locations we section. Our results demonstrate that as axons expand early prior to frank loss, the ramification of astrocyte processes in the inter-axonal space actually diminishes (Figures 2.1, 2.3). This finding is consistent with two previous studies, both involving acute elevations in IOP. In the first, short-term elevations in IOP (7 days) in a rat model reduced GFAP label in the optic nerve head concurrent with axonal enlargement and increased levels of phosphorylated neurofilaments; significant axon loss occurred later[329]. In another acute model, an early phase of reactive astrocyte gliosis involves retraction of processes from the center of the nerve prior to re-extension[300]. In the DBA/2J, we found that with early axon expansion, the center of mass for glial ramification changed from an even distribution across the nerve to one skewed towards the edge of the nerve (Figures 2.4, 2.5). As axons continued to expand beyond the threshold for overt loss, the center of mass returned to an even distribution (Figure 2.5, right panel). This result stands in contrast to those from another inducible model in which astrocyte processes in the optic nerve head actually appear to detach from the edge of the nerve[330].

Further, cross-sections of healthy DBA/2J optic nerve demonstrate organization along a common axis (Figure 2.6, left panel), exhibiting a high degree of parallelism as indicated by our metric (Figures 2.7, 2.8). As axon pathology increases with a commensurate increase in glial coverage of the nerve, parallelism diminishes and astrocytes distribute more evenly across the nerve (Figure 2.9). Accordingly, axon density, total number of axons, and axon expansion all predict changes in astrocyte parallelism more accurately than independent measures of glaucoma progression in the DBA/2J (i.e., IOP and age; Figure 2.10). As the mean axon area increases toward the threshold for loss, astrocyte parallelism increases without a change in overall glial coverage of the nerve (Figure 2.11). Once axon loss begins and density diminishes, parallelism decreases in kind (Figure 2.9E), presumably as astrocyte processes re-invade axon bundles. In total, these results from the DBA/2J model indicate that astrocytes remodel biphasically. During early axon expansion prior to axonal loss, astrocyte processes increase in parallelism as CoM diminishes *independent from gliosis* (Figure 2.11). Once axons are lost, gliosis involves diminished parallelism and uniform astrocyte distribution across the nerve (Figure 2.9). This coincides with the time points other groups have noted microglial invasion of the optic nerve, which may contribute to the rapid, dynamic response astrocytes exhibit[48].

In longitudinal sections of nerve, we found that both GFAP and Cx43 are higher in proximal vs distal segments (Figures 2.12C, 2.13D). This is consistent with a more even distribution of astrocytes, as indicated by the higher CoM in the proximal vs the distal segment (Figure 2.12E). Previous work has demonstrated anterograde axonal transport from retina to brain is an early harbinger of axon pathology in the DBA/2J and degrades in distal-to-proximal fashion[153]. Here, we found that parallelism of GFAP-labeled astrocyte processes was higher in distal segments of our 10-month old DBA/2J nerves. (Figure 2.12F). As parallelism increased in the distal segment, astrocytes redistributed towards the nerve edge, as indicated by a lower CoM (Figure 2.12G). This pattern of remodeling reflects that seen in early stages of axonal pathology, indicating that astrocytes in the distal nerve may be reacting to pathology prior to those in the proximal nerve.

In the distal segment, nerves containing elevated Cx43 also demonstrated higher levels of intact transport but did not show a relationship with parallelism (Figure 2.14B). In contrast, levels of Cx43 in the proximal segment predicted parallelism with no clear relationship to transport (Figure 2.14A). Thus, these results indicate that in the distal segment, where axonopathy has already begun, Cx43 in astrocytes better reflects axon function that astrocyte organization. This is consistent with findings demonstrating gap-junction coupling of the astrocyte network is tightly modulated by axonal function and neuronal activity[319]. Similarly, increased parallelism in the distal vs proximal segment is reminiscent of our results from cross-sections of proximal nerve, where increased parallelism correlated with early expansion of axons prior to overt loss (Figure 2.11B). Through gap-junction coupling, astrocytes may be able to more evenly distribute resources to those axons undergoing the highest degree of stress[230,231,312,331].

Our results suggest that early progression in the optic nerve involves remodeling of astrocyte processes, first to a higher state of organization with increased parallelism (Figure 2.11) and gap-junction coupling (Figure 2.14), then to gradual deterioration of organization as coverage increases and axons are lost (Figures 2.9, 2.10). Perhaps well-organized astrocyte processes lend structural stability to the nerve. In the optic nerve head, astrocytes form a continuously remodeling network that adapts to IOP exposure [332], with astrocyte actin and tubulin filaments gradually re-orienting as IOP increases[333]. With short exposures to elevated IOP, astrocyte processes retract towards the cell body[300]; astrocyte processes also may also fortify the edge of the nerve, as coverage in the center diminishes (Figure 3 of Sun et al., 2013). As astrocyte processes re-invade the nerve center with longer IOP exposure, their organization diminishes[300]. With acute injury (nerve crush), astrocyte processes appear to detach from the edge[16], but this likely reflects the more severe nature of the injury. Similar to our results in the myelinated nerve, astrocyte remodeling following induced short-term elevations in pressure is most extensive distal from the sclera[334]. Portions of the optic nerve beyond the sclera itself are unlikely to be impacted directly by elevated IOP, and secondary changes could involve different structural mechanisms. This may be why we did not note a simple linear relationship between IOP and loss of parallelism (Figure 2.10B), but did find strong correlations between measures of axonal degeneration and loss of parallelism (Figures 2.10, 2.11).

Perhaps the most important question is whether early astrocyte remodeling is protective or pathogenic. Cx43 is elevated in the optic nerve head and the retina in human glaucomatous tissue[64], and here we find that astrocyte remodeling is associated with increased Cx43 (Figure 2.14). Intriguingly, we additionally find that elevated Cx43 is also associated with intact axonal anterograde transport (Figure 2.14D). This suggest that the early phases of astrocyte remodeling involving increased connectivity may be a component of an endogenously protective mechanism, wherein these alterations within astrocytes positively influence the health of axons within the optic nerve. In late stages of neurodegeneration Cx43-mediated coupling helps disperse inflammatory cytokines through gap junctions[278,335]. The data presented herein leads us to believe that Cx43 exhibits a multitude of functions, like astrocytes themselves. In these early stages of pathology, gap junctions allow astrocytes to couple with neighboring cells and share signals that may contribute to the redistribution of resources to those regions most at risk.

Concurrently, the degenerating optic nerve undergoes significant diminishment in its mitochondrial capacity. These two findings are not as disparate as they initially appear. Astrocytes are directly responsible for the mitochondrial health of the optic nerve; as mitochondria age and begin to degenerate themselves, they are shuttled from axons into nearby astrocytes that degrade them[336]. This maintains the structural stability of axons, whose neurofilaments are particularly susceptible to the increased reactive oxygen species produced by aging mitochondria[118,167]. We found that nerves exhibiting axon expansion prior to frank loss demonstrated diminished numbers of mitochondria per unit area of tissue with increasing axon size (Figure 2.15). If axons are not transporting fresh mitochondria to distal regions of the nerve, those mitochondria that are degraded as they age will not be replaced. As anterograde transport fails more and more proximally, this phenotype will become more severe. This renders axons increasingly reliant on astrocytes and their energy stores (Figure 2.16). Astrocytes depleting their resources then increase their connectivity – perhaps to obtain resources from nearby regions. This, however, may drastically influence the functionality of the system as a whole.

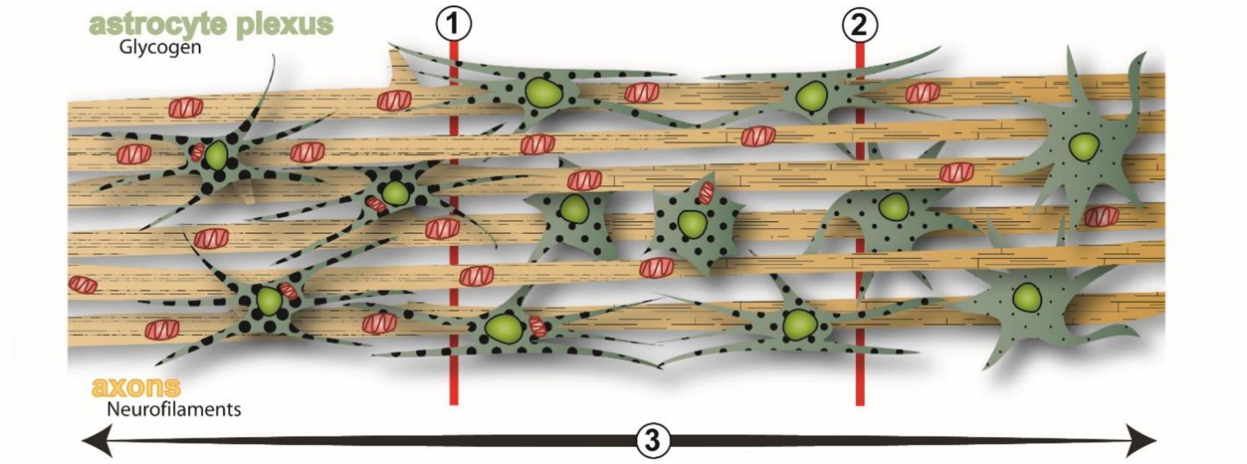

Figure 2.16 Astrocytes and the energetic environment of the myelinated optic nerve through pathology.

As pathology progresses (left to right), astrocytes (green) lose process organization and become hypertrophic, while axons (yellow) lose mitochondrial density (red) and neurofilaments become hyperphosphorylated (black lines), impeding axonal transport. During initial pathology (1), astrocytes distribute their process density toward the edge and those processes orient increasingly in parallel, while during late pathology (2) they expand evenly across the nerve. Astrocytes likely utilize energy stores (glycogen, black dots) to support axons through pathology (3), increasing their connectivity in an attempt to draw upon additional resources and meet excess demand.

CHAPTER 3

ASTROCYTES REDISTRIBUTE METABOLITES FROM HEALTHY TO DEGENERATING TISSUE THROUGH GAP JUNCTIONS

Invincibility lies in the defense; the possibility of victory in the attack.

Sun Tzu

3.1 INTRODUCTION

The brain is a disproportionately metabolically demanding organ. Despite comprising only 2% of body mass, the brain accounts for roughly 30% of all energy consumption[52,104,337]. Neurons rely primarily on glucose as an energy substrate, which is depleted quickly during periods of stress or high demand[18,96]. To maintain normal function, neurons rely upon astrocyte glia that create and store glycogen, which serves as the brain's largest energy reserve and a safeguard against periods of stress[7,96,338]. This metabolic collaboration between neurons and astrocytes is exceptionally important during neurodegenerative disease, which taxes normal energy utilization and increases reliance on alternative sources[131,141]. As the brain ages, metabolism becomes less efficient, rendering the nervous system more susceptible to metabolic stressors[113]. In preclinical neurodegeneration, hypometabolism and oxidative stress become increasingly apparent[102,131,338]. At this early stage of pathology astrocytes remodel and utilize glycogen stores, likely preserving axonal function through chronic stress[190,224,300]. This endogenous protection occurs through multiple mechanisms, but many alterations astrocytes undergo at this stage of neurodegeneration occur due to a deficiency of metabolic resources[303,338]. What these mechanisms involve, however, is still unknown – and this information could elucidate new protective therapies for those individuals in the early stages of pathology, or perhaps even render a preventative measure.

Astrocyte-axon interactions are uniquely critical in glaucomatous optic neuropathy (or simply glaucoma), the world's leading cause of irreversible blindness. Glaucoma is projected to impact 80 million people by the year 2020[211]. Retinal ganglion cell (RGC) axons contain an energetically demanding unmyelinated segment that travels through the retina and optic nerve head. This means that RGC axons must fire without energy-saving saltatory conduction for much of their initial length. Additionally, the optic nerve head is the location likely impacted most by sensitivity to intraocular pressure (IOP), one of the key risk factors of glaucoma[224,312,330]. However, despite IOP being a risk factor, glaucoma itself is diagnosed through measures of optic nerve health, where deficits are first noted during the disease. Functional and structural deficits emerge within the optic nerve early in progression, even as the cell body and axon segment in the retina persist. Prior to axonal changes, astrocytes redistribute their processes near those axons that likely receive the most stress[190,230,231,331,332]. Therefore, not only is the optic nerve a prime model for studying the interactions between astrocytes and axons in response to stress, but it is also the key target for protective therapies in glaucoma.

Astrocytes form plastic networks of interconnected cells through the retina, optic nerve, and brain, allowing them the unique ability to quickly redistribute resources to those areas most in need through gap junctions. Gap junctions are a unique modality of specialized synapses that form a direct pathway for cell-to-cell communication between cytoplasm.

Astrocytes utilize gap junctions, primarily composed of connexin 43 (cx43), to couple with neighboring cells and share signals pertaining to the health of their domain as well as redistribute resources[61]. Cx43 is permeable to molecules up to 1-1.2 KDa, much larger than the metabolic resources primarily utilized by the brain: glucose (180 Da), pyruvate (88 Da), and lactate (90 Da) [61,89,339]. The lifetime of connexins is only about 2 hours, meaning the networks they form can be quickly modulated[61]. Intriguingly, cx43 is elevated in human glaucomatous optic nerve head[64]. However, the majority of studies on cx43 in neurodegeneration pertain to the late stages of disease, where inflammatory cytokines are dispersed through these membrane pores. These cytokines may directly relate to pathology[278,335], but this represents an exceptionally narrow view of the complicated and nuanced system of constantly reforming and reorganizing astrocyte networks. Here, we are interested in the early stages of glaucomatous neurodegeneration, where astrocytic gap junctions may modulate an endogenously protective mechanism wherein they redistribute resources from healthy regions of the brain to areas actively undergoing stress.

3.2 MATERIALS AND METHODS

3.2.1 GENERATING *GFAP-CRE-ER*^{T2} *X CX43*$^{FLOX/FLOX}$ MICE

The *Gja1* gene encodes cx43, a protein abundant in astrocytes that forms the majority of their gap junctions. However, cx43 is not only expressed by astrocytes; it is essential for a synchronous heartbeat[63] and proper embryonic development[340] amongst many other functions. Cx43 knockout mice die at birth, as well. To avoid the issues inherent with a universal knockout, we generated a temporally and locally controlled knockout using the *cre/lox* system.

In this system, the target gene is encapsulated within two small 34 base pair (bp) *loxP* sites that are carefully placed in locations that do not impede normal function; only when the protein Cre is both present and functional will the gene be excised. Thus, here we utilized a *GFAP-Cre-ER*^{t2} mouse, which is hemizygous for a tamoxifen-controlled Cre under the GFAP promoter[341], and through a sequence of generations bred it with a mouse homozygous for *flox* sites surrounding exon 2 of the *Gja1* gene[342,343]. In the absence of Cx43, astrocytes have very few remaining gap junctions, profoundly reducing their functional connectivity. The Jackson Laboratory (Bar Harbor, ME) supplies all mice expressing a *Cre-ER*^{T2} as hemizygotes, meaning the gene is present on one chromosome and absent on the other (as opposed to heterozygous, where two different alleles are present). Dependent both on the location of initial gene insertion when the model is generated and the promoter used for the *Cre-ER*^{T2}, there have been reports of mice that do not survive homozygosity. However, in our model we did not see any marked differences between mice that were hemi- or homozygous for *GFAP* promoted *Cre-ER*^{T2}, including rates of gene excision. For this reason, we kept all mice that had any expression of *cre* in experimental groups, and later genotyped for gene excision in every mouse in target tissue to confirm the knockout.

The initial cross utilized six mice, one male and two females each of mice hemizygous for *GFAP-Cre-ER*^{t2} or homozygous for *cx43*$^{flox/flox}$. A male of one genotype was caged in a harem with two females of the opposing genotype to maximize efficiency and minimize cost at this early stage. Crosses resulted in a 1 in 2 chance of the desired genotype, which at this stage is a mouse hemizygous for a *GFAP-Cre-ER*^{t2} and heterozygous for *Cx43*^{flox} (Figure 3.1).

For the second cross, we utilized two strategies to maximize the number of usable mice in our colony and increase output of potentially useful offspring (Figure 3.2). For both of these crosses, we are targeting mice positive for *cre* (whether hemi- or homozygous) and homozygous for our *floxed* gene. We only need *cre* to be present to achieve our knockout; however, the *Gja1* genes on both alleles must be floxed to eliminate the presence of Cx43 protein. The first strategy involved crossing two unrelated offspring from cross 1, both of which are positive for *cre* and heterozygous for *floxed* Cx43. This cross resulted in three of 16 offspring with our target genotype. The second strategy utilized parent 2 from cross 1, a mouse without *cre* but homozygous for *floxed* Cx43, and an unrelated mouse positive for *cre* and heterozygous for *floxed* Cx43. This cross resulted in one of four offspring with our target genotype, and increased the number of breeder cages to provide more potential unrelated mice for future crosses.

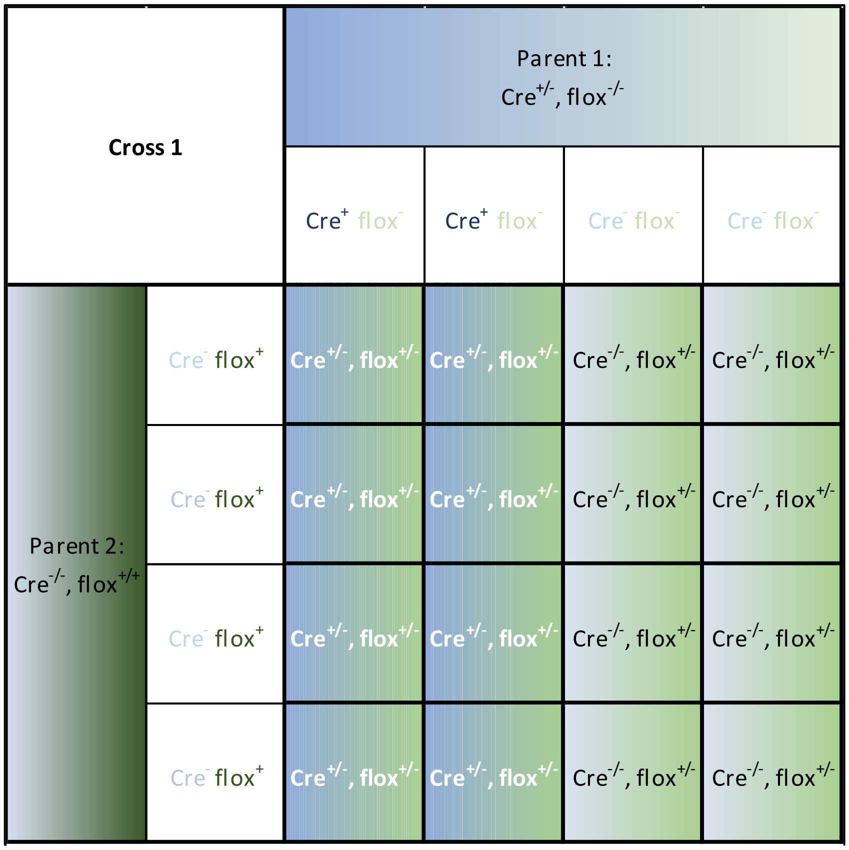

Cross 1		Parent 1: Cre$^{+/-}$, flox$^{-/-}$			
		Cre^{+} flox^{-}	Cre^{+} flox^{-}	Cre^{-} flox^{-}	Cre^{-} flox^{-}
Parent 2: Cre$^{-/-}$, flox$^{+/+}$	Cre^{-} flox^{+}	**Cre$^{+/-}$, flox$^{+/-}$**	**Cre$^{+/-}$, flox$^{+/-}$**	Cre$^{-/-}$, flox$^{+/-}$	Cre$^{-/-}$, flox$^{+/-}$
	Cre^{-} flox^{+}	**Cre$^{+/-}$, flox$^{+/-}$**	**Cre$^{+/-}$, flox$^{+/-}$**	Cre$^{-/-}$, flox$^{+/-}$	Cre$^{-/-}$, flox$^{+/-}$
	Cre^{-} flox^{+}	**Cre$^{+/-}$, flox$^{+/-}$**	**Cre$^{+/-}$, flox$^{+/-}$**	Cre$^{-/-}$, flox$^{+/-}$	Cre$^{-/-}$, flox$^{+/-}$
	Cre^{-} flox^{+}	**Cre$^{+/-}$, flox$^{+/-}$**	**Cre$^{+/-}$, flox$^{+/-}$**	Cre$^{-/-}$, flox$^{+/-}$	Cre$^{-/-}$, flox$^{+/-}$

Figure 3.1 Generating *GFAP-Cre-ER^{t2}* x *Cx43$^{flox/flox}$* mice, cross 1.

In our initial cross, we utilized a mouse hemizygous for *GFAP-Cre-ER^{t2}* (parent 1) and crossed with a mouse homozygous for *Cx43^{flox}*. The half of offspring positive for *cre* and heterozygous for *floxed* Cx43 were utilized in cross 2 (bold, white offspring).

Once we obtained an unrelated male and female with our target genotype from cross 2 we began cross 3, the final cross in our sequence and the cross resulting in our experimental mice. Because our target genotype from cross 2 involves mice positive for *GFAP-Cre-ER*^{t2}, whether homo- or hemizygous, and our genotyping method (detailed in section 3.2.2) only reveals the presence of *GFAP-Cre-ER*^{t2} and not its zygosity, crosses here had variable results dependent on the true genotype of both parents. In all cases offspring were now homozygous for *Cx43*^{flox}, as we were breeding two mice homozygous for this gene. If both parents were hemizygous for *GFAP-Cre-ER*^{t2}, half of offspring were positive for *GFAP-Cre-ER*^{t2} while the other half were *cre* negative; these *cre* negative mice were then utilized as littermate controls for

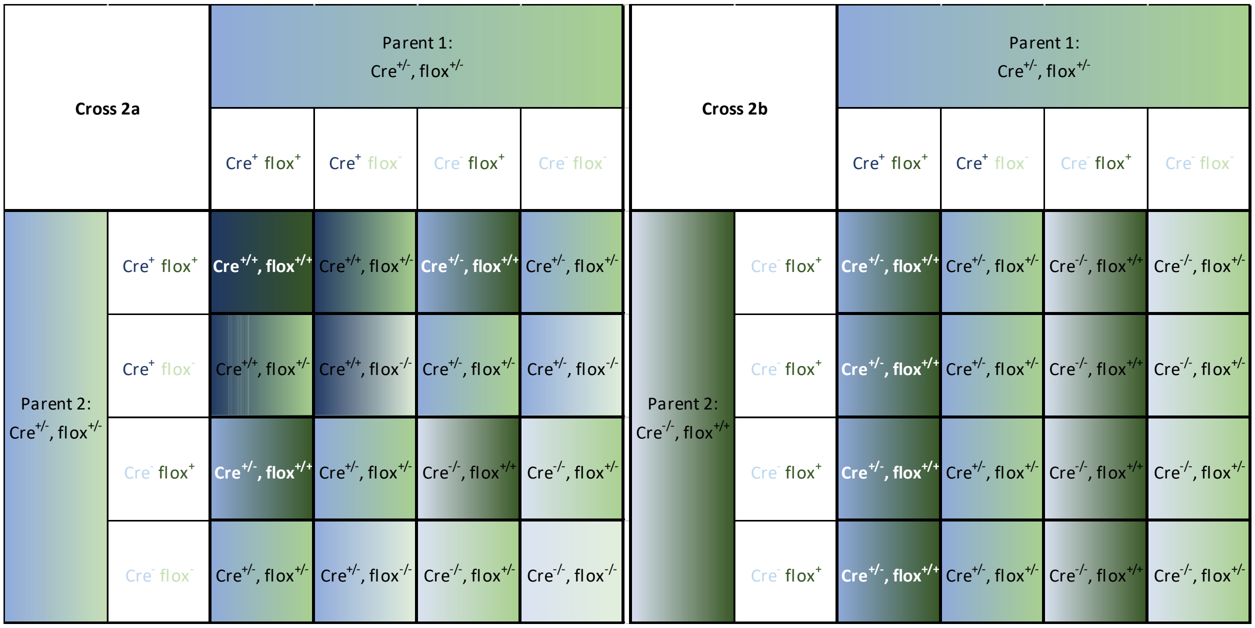

Cross 2a		Parent 1: Cre$^{+/-}$, flox$^{+/-}$			
		Cre^{+} flox^{+}	Cre^{+} flox^{-}	Cre^{-} flox^{+}	Cre^{-} flox^{-}
Parent 2: Cre$^{+/-}$, flox$^{+/-}$	Cre^{+} flox^{+}	**Cre$^{+/+}$, flox$^{+/+}$**	Cre$^{+/+}$, flox$^{+/-}$	**Cre$^{+/-}$, flox$^{+/+}$**	Cre$^{+/-}$, flox$^{+/-}$
	Cre^{+} flox^{-}	Cre$^{+/+}$, flox$^{+/-}$	Cre$^{+/+}$, flox$^{-/-}$	Cre$^{+/-}$, flox$^{+/-}$	Cre$^{+/-}$, flox$^{-/-}$
	Cre^{-} flox^{+}	**Cre$^{+/-}$, flox$^{+/+}$**	Cre$^{+/-}$, flox$^{+/-}$	Cre$^{-/-}$, flox$^{+/+}$	Cre$^{-/-}$, flox$^{+/-}$
	Cre^{-} flox^{-}	Cre$^{+/-}$, flox$^{+/-}$	Cre$^{+/-}$, flox$^{-/-}$	Cre$^{-/-}$, flox$^{+/-}$	Cre$^{-/-}$, flox$^{-/-}$

Cross 2b		Parent 1: Cre$^{+/-}$, flox$^{+/-}$			
		Cre^{+} flox^{+}	Cre^{+} flox^{-}	Cre^{-} flox^{+}	Cre^{-} flox^{-}
Parent 2: Cre$^{-/-}$, flox$^{+/+}$	Cre^{-} flox^{+}	**Cre$^{+/-}$, flox$^{+/+}$**	Cre$^{+/-}$, flox$^{+/-}$	Cre$^{-/-}$, flox$^{+/+}$	Cre$^{-/-}$, flox$^{+/-}$
	Cre^{-} flox^{+}	**Cre$^{+/-}$, flox$^{+/+}$**	Cre$^{+/-}$, flox$^{+/-}$	Cre$^{-/-}$, flox$^{+/+}$	Cre$^{-/-}$, flox$^{+/-}$
	Cre^{-} flox^{+}	**Cre$^{+/-}$, flox$^{+/+}$**	Cre$^{+/-}$, flox$^{+/-}$	Cre$^{-/-}$, flox$^{+/+}$	Cre$^{-/-}$, flox$^{+/-}$
	Cre^{-} flox^{+}	**Cre$^{+/-}$, flox$^{+/+}$**	Cre$^{+/-}$, flox$^{+/-}$	Cre$^{-/-}$, flox$^{+/+}$	Cre$^{-/-}$, flox$^{+/-}$

Figure 3.2 Generating *GFAP-Cre-ER*^{t2} *x Cx43*$^{flox/flox}$ mice, crosses 2a and 2b.

In our second cross, we utilized two strategies to optimize the number of available target offspring, mice positive for *cre* (whether hemi- or homozygous) and homozygous for *Cx43*^{flox} (bold, white offspring). In cross 2a (left), both mice are unrelated offspring from cross 1, positive for *cre* and heterozygous for *floxed* Cx43. This cross resulted in 3 of 16 mice with our target genotype. Cross 2b involved one offspring from cross 1 (Parent 1) and an unrelated mouse without *cre* but homozygous for *Cx43*^{flox} (Parent 2), resulting in 1 of 4 offspring with the target genotype.

tamoxifen induction and genetic manipulation. If either parent was homozygous for *GFAP-Cre-ER^{t2}* all offspring were *cre* positive and were viable for experimental cohorts.

All mice detailed herein were generated on a C57BL/6 (C57) background, so C57 mice (Jackson Labs, Bar Harbor, ME) were always used as a wild-type control.

3.2.2 GENOTYPING *GFAP-CRE-ER^{T2} X CX43$^{FLOX/FLOX}$* MICE

All pups were genotyped after day 14 but prior to weaning to allow the mother to care for pups after tail snips were taken and ear clips were administered. Each pup was anesthetized with isoflurane (Minrad Inc., Bethlehem, PA) and efficacy of anesthesia was evaluated by gentle pinching of the tail and paw. A razor blade washed in 100% EtOH was used to collect a 3-5mm section of tissue from the end of the tail. The tissue was immediately placed in a tube containing a solution of 250µl DirectPCR Lysis Reagent (Mouse Tail) and 50µl Proteinase K solution (supplied at 20mg/ml), both from Viagen Biotech (Los Angeles, CA). Each tube was incubated at 55-60°C for 6 hours to overnight, until tissue was completely lysed. After complete lysis, tubes were incubated for 45 minutes at 85°C to denature the protease. Tubes were then placed on ice and 1.5µl of crude lysate from each sample was immediately used in each genotyping reaction, then the remaining stock was stored at -20°C.

Table 0.1 Primers	
1. *GFAP-Cre-ER^{T2}* Forward	GCCAGTCTAGCCCACTCCTT
2. GFAP-Cre-ERT2 Reverse	TCCCTGAACATGTCCATCAG
3. Internal Positive Control Forward	CTAGGCCACAGAATTGAAAGATCT
4. Internal Positive Control Reverse	GTAGGTGGAAATTCTAGCATCATCC
5. *Cx43^{flox}* Forward	CTTTGACTCTGATTACAGAGCTTAA
6. *Cx43^{flox}* Reverse	GTCTCACTGTTACTTAACAGCTTGA
7. *Cx43^{flox}* Knockout Forward	GCTACTTCTTGCTTTGACTCTGATTA
8. *Cx43^{flox}* Knockout Reverse	GCTCACTTGATAGTCCACTCTAAGC

For initial genotyping, we used primers 1 through 6 in Table 3.1, for which the sequences were obtained from Jackson Labs (Bar Harbor, ME) and the primers themselves from Integrated DNA Technologies (Coralville, IA). For initial genotyping, two separate reactions were required. The first reveals the presence of *GFAP-Cre-ER*^{t2} (not its zygosity) through a reaction involving the first four primers in Table 3.1. The first two primers produce a 200 bp product in the presence of *GFAP-Cre-ER*^{t2} and no product when it is not present; thus, a second set of primers are added to the reaction as an internal positive control (Primers 3 and 4, Table 3.1). These primers contain a similar C-G percentage to the primers for the *GFAP-Cre-ER*^{t2} reaction and produce a 324 bp product when the PCR has run successfully. This reaction requires 23.5µl of *GFAP-Cre-ER*^{t2} master mix (Table 3.2) and 1.5µl crude lysate.

Table 3.2: *GFAP-Cre-ER*^{T2} Master Mix

	Volume per reaction (µl)	Final Concentration
Promega Green GoTaq® Flexi Buffer (5X)	5	1X
Promega PCR Nucleotide Mix	0.5	0.2 mM
MgCl$_2$	2	2 mM
GoTaq® Hot Start Polymerase	0.1	1 unit
***GFAP-Cre-ER*^{T2} Forward**	0.5	0.2 µM
GFAP-Cre-ERT2 Reverse	0.5	0.2 µM
Internal Positive Control Forward	0.5	0.2 µM
Internal Positive Control Reverse	0.5	0.2 µM
Water	13.9	
Crude DNA lysate	1.5	

Table 3.3: *Cx43*^{flox} Master Mix

	Volume per reaction (µl)	Final Concentration
Promega Green GoTaq® Flexi Buffer (5X)	5	1X
Promega PCR Nucleotide Mix	0.5	0.2 mM
MgCl$_2$	2	2 mM
GoTaq® Hot Start Polymerase	0.1	1 unit
***Cx43*^{flox} Forward**	0.5	0.2 µM
***Cx43*^{flox} Reverse**	0.5	0.2 µM
Water	14.9	
Crude DNA lysate	1.5	

The second reaction for initial genotyping reveals the zygosity of *Cx43*^{flox} through two potential products produced using the same set of primers (Primers 5 and 6, Table 3.1). In the presence of mutant *Cx43*^{flox} a 580 bp reaction product is produced, while wild type *Cx43* will reveal a 490 bp reaction product. A heterozygote will produce both reaction products. This reaction requires 23.5µl of *Cx43*^{flox} master mix (Table 3.3) and 1.5µl crude lysate.

PCR reactions were carried out using a Mastercycler gradient thermocycler (Eppendorf, AG, Hamburg, Germany) using the steps in Table 3.4. Products contained dye in the buffer, so 20µl of each product was loaded into a 3% agarose gel (3 g agarose in 100 ml 1X TAE) along with a 100 bp DNA ladder (New England BioLabs, Ipswich, MA). Products were loaded alternating *GFAP-Cre-ER*^{t2} and *Cx43*^{flox} lanes so both products could be imaged for the same animal together. Products were separated at 100

Table 3.4: PCR Reaction Program

	Temperature (°C)	Time (min:sec)
1. Initial Denaturing	94	2:00
2. Denaturing	94	0:40
3. Annealing	65, -0.5 per cycle	0:40
4. Elongation	68	1:30
5. Repeat steps 2-4 10x		
6. Denaturing	94	0:40
7. Annealing	60	0:30
8. Elongation	72	1:30
9. Repeat steps 6-8 28x		
10. Final Elongation	72	2:00
11. Finish	10	Hold

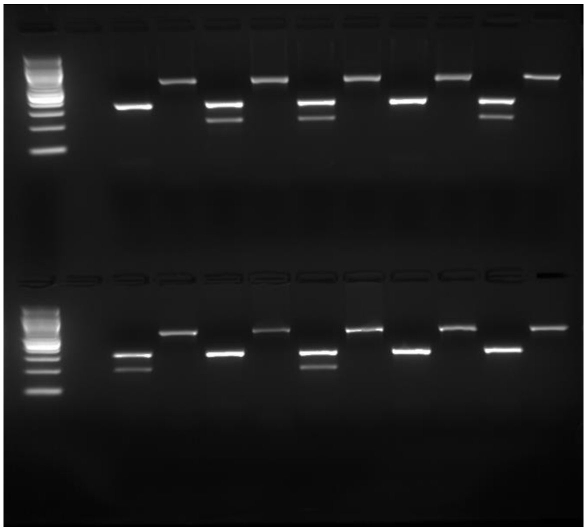

Figure 3.3 Genotyping *GFAP-Cre-ER*^{t2} *x Cx43*$^{flox/flox}$ mice, final products.

Final gels are imaged with a 100 bp ladder (left) and products from the same individual are imaged together. All experimental mice are homozygous for *Cx43*^{flox} (higher MW bands). The first mouse on the left is *cre* negative while the second is *cre* positive

V for 80 min or until the leading edge was near the bottom of the gel. Gels were digitally imaged on a Gel Doc XR+ (Bio-Rad, Hercules, CA) gel reader to determine the final genotype.

3.2.3 INDUCING AND CONFIRMING CX43 EXCISION IN *GFAP-CRE-ER*^{T2} *X CX43*$^{FLOX/FLOX}$ MICE

Upon the conclusion of each experiment, each mouse was additionally genotyped for the excision of the *floxed* region of *Cx43*. Initially, we used multiple methods of tamoxifen administration in an attempt to determine which would be most efficient; however, no method had 100% efficacy. We utilized a tamoxifen diet (500mg tamoxifen/kg chow) for two and four weeks, which resulted in excision in about half of mice, but many mice had an unacceptable reduction in weight (roughly 10-20% of body weight that was never regained) and began fighting, so had to be individually housed. Intraperitoneal injection never induced recombination in our cohort, likely because tamoxifen must be digested into 4-hydroxy tamoxifen through the liver before it is in a state that will bind *ER*^{T2}. Gavage had the highest efficacy rate, with between 60-80% of mice in each cohort exhibiting excision after three consecutive days of gavage of tamoxifen in corn oil at 20 mg/ml, fed at 10µl per gram of mouse. Combinations of gavage and food were not successful in inducing a higher rate of excision and still resulted in unacceptable weight loss, so for all experiments we utilized three consecutive days of gavage with a week between the final gavage and any experimental manipulation. Control animals were gavaged with vehicle corn oil at 10µl per gram of mouse.

Because tamoxifen did not excise the gene in every mouse, we continued genotyping each mouse on the conclusion of every experiment. For each mouse, we used a sample of cerebellum in addition to either a sample of frontal cortex or optic nerve depending on experimental outcomes. Our excision genotyping protocol involved extracting DNA using the DNeasy Blood and Tissue Kit (Qiagen, MD) following the Bench Protocol: Animal Tissues (Spin Column) protocol. This extracts a more pure, concentrated DNA solution, rather than the simple crude lysate used in section 3.2.2. DNA concentration was determined using a NanoDrop 8000 (Thermo Scientific, Wilmington, DE) and was stored at -20°C prior to running PCR reactions.

Table 3.5: *Cx43*^{flox} Excision Master Mix

	Volume per reaction (µl)	Final Concentration
Promega Green GoTaq® Flexi Buffer (5X)	5	1X
Promega PCR Nucleotide Mix	0.5	0.2 mM
$MgCl_2$	2	2 mM
GoTaq® Hot Start Polymerase	0.1	1 unit
***Cx43*^{flox} Knockout Forward**	0.5	0.2 µM
***Cx43*^{flox} Knockout Reverse**	0.5	0.2 µM
DNA solution	200 ng	
Water	14.9 - DNA volume	

Each PCR reaction was 25µl in volume, but the volume of DNA added was dependent on the concentration obtained from the kit. For each reaction, we added 200 ng of extracted DNA template, and subtracted that volume from the required amount of molecular water. Full

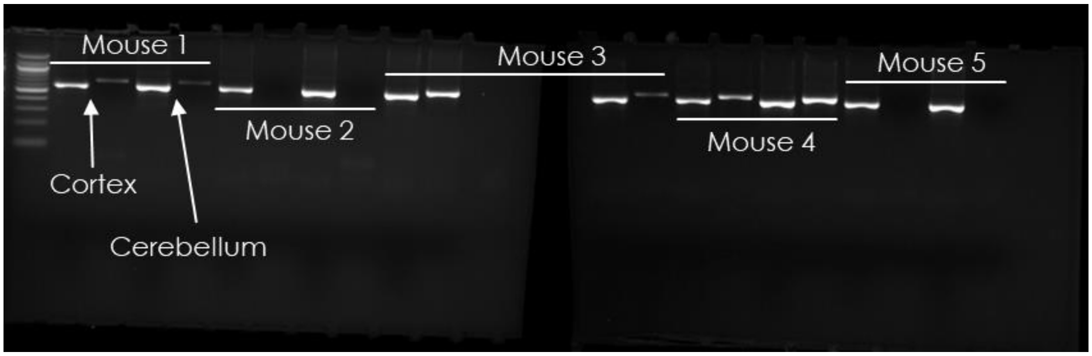

Figure 3.4 Genotyping *GFAP-Cre-ER*^{t2} x *Cx43*$^{flox/flox}$ mice for excision, final products.

Final gels are imaged with a 100 bp ladder (left) and products from the same sample and then the same individual are imaged together. Lanes alternate between *Cx43*^{flox} (positive control) and *Cx43*^{flox} *KO* bands. Not all mice exhibit excision; for example, mouse 1 shows the knockout in both cortex and cerebellum, where mouse 2 does not exhibit either.

details on master mix composition for this reaction are in Table 3.5, and the primers utilized are Primers 7 and 8[343] from Table 3.1. Reaction products are separated as detailed in section 3.2.2.

3.2.4 IMMUNOHISTOCHEMISTRY IN RETINAL WHOLEMOUNT TISSUE

Retinal wholemount tissue was retrieved by dissecting perfused eyes under a dissecting scope. Using microdissection scissors, the eye was cut in a circular fashion above the ora serrata and #5 forceps were used to gently separate the retina from the ora serrata. The sclera was gently cut and peeled back to reveal the underside of the retina. The optic disc was cut using microdissection scissors, freeing the retina from the sclera completely. To flatten the retina in preparation for imaging, four relief cuts were made to create a cross shape that was then flattened against a slide. To improve antibody penetration and imaging of the tissue, vitreous was manually removed using forceps and paintbrushes.

Whole retinal tissue was immersed 10, 20, or 30% sucrose in PBS solutions. Tissue was moved to higher sucrose concentrations once it sank to the bottom of the solution it was currently in. Once in 30% sucrose, retinas were incubated overnight at 4°C. Following overnight incubation, the majority of the sucrose solution was removed and retinas were freeze-thawed at -80°C three times. Retinas were then washed three times in PBS for 5 minutes each. Tissue was blocked in a solution of 5% normal donkey serum plus 0.1% Triton-X 100 diluted in PBS overnight at 4°C.

Retinas were immunolabeled against GFAP (goat 1:500, Abcam, Cambridge, UK), Cx43 (rabbit 1:200, Cell Signaling Technology, Danvers, MA), and Cre (mouse 1:200, Millipore, Burlington, MA) in a primary antibody solution diluted in 3% normal donkey serum plus 0.1%

Triton-X 100 in PBS for 4 days at 4°C with gentle shaking. Retinas were then rinsed in PBS and washed 3 times in PBS for 10 minutes each at room temperature. Tissue was then placed in a solution of donkey anti-mouse Cy3, donkey anti-rabbit 647, and donkey anti-goat 405 antibodies (1:200, Jackson), 1% normal donkey serum, and 0.1% Triton-X 100 diluted in PBS. Plates were protected from light and incubated overnight at 4°C with shaking. Retinas were rinsed in PBS and washed 3 times in PBS for 10 minutes each at room temperature. Each retina was mounted RGC side up on a slide under a dissecting microscope using aqueous mounting media (Fluoro-mount). Slides were coverslipped, protected from light, and dried overnight at room temperature. Images were captured at 100x on an Olympus FV-1000 inverted confocal microscope.

3.2.5 IMMUNOHISTOCHEMISTRY OF RETINAL AND OPTIC NERVE CRYOSECTIONS

A subset of eyes and optic nerves were enucleated and dissected from the optic chiasm for longitudinal sectioning and immunohistochemical staining. Tissue was cryoprotected in a sequence of 10, 20, and 30% sucrose/PBS overnight and subsequently embedded and frozen in Tissue-Plus O.C.T. Compound (Fisher Healthcare, Houston, TX). We labeled 10 µm cryosections with the following antibodies: anti-glial fibrillary acidic protein (GFAP; EMD Millipore, Billerica, MA, 1:500), anti-phosphorylated neurofilament H (NF-H, SMI 34; BioLegend, San Diego, CA, 1:500), and anti-platelet endothelial cell adhesion molecule (CD31; Abcam, Cambridge, UK, 1:50). Immunolabeling was visualized using appropriate DyLight-conjugated secondary antibodies (Jackson Immunoresearch, West Grove, PA 1:200). Fluorescent montages were captured using an Olympus Provis AX70 microscope as described above. Confocal images were captured using an Olympus FV-1000 inverted microscope. Montages were captured using a Nikon Ti2-E inverted microscope equipped with an Andor sCMOS super high-resolution camera.

3.2.6 INDUCTION OF OCULAR HYPERTENSION BY MICROBEAD OCCLUSION

Intraocular pressure was acutely elevated[252] in 2-month-old C57, *GFAP-Cre-ER*^{t2} *x Cx43*$^{flox/flox}$, and *Cx43*$^{flox/flox}$ mice as dictated by experimental need. Prior to injections, mice were anesthetized with isoflurane (Minrad Inc., Bethlehem, PA) and efficacy of anesthesia was evaluated by gentle pinching of the tail and paw. Eyedrops containing 1% tropicamide were applied to dilate the iris, and eyedrops containing 0.5% proparacaine were applied as a local anesthetic. The proparacaine drops were applied as necessary to maintain eye moisture and provide pre- and post-operative analgesia. Drops of antibiotic tobramycin ophthalmic solution (0.3%, Akorn) were also applied after the injection to counter infection.

Microbeads were injected using a standard microinjection setup (World Precision Instruments) consisting of a microsyringe pump and micromanipulator. A borosilicate microneedle pulled to a final diameter of 100µm was attached to a syringe filled with mineral oil to prevent backflow of injected solution. The needle tip was sterilized with 100% EtOH before drawing PBS through the needle and finally a solution of PBS containing inert polystyrene microbeads (15µm diameter, 1×10^6 microbeads/ml solution; Life Technologies, Carlsbad, CA). Microbeads were injected unilaterally into the anterior chamber of one eye. If experimentally necessary, the contralateral eye was injected with an equivalent volume of PBS containing no microbeads. Following the procedure, additional numbing drops containing 0.5% proparacaine were applied.

IOP was measured in anesthetized (2.5% isoflurane) mice at least twice weekly using TonoPen XL (Medtronic Solan, Jacksonville, FL) rebound tonometry as previously described[235,252]. An IOP measurement was determined as the mean of 15 readings. IOPs were measured for 2 days prior to microbead procedures to determine a baseline value and twice weekly until the experimental endpoint.

3.2.7 GLYCOGEN ASSAY

To determine glycogen content, we modified an assay developed by Abcam (ab65620). Unanesthetized mice were sacrificed via cervical dislocation and beheading. Both optic nerves were dissected within one minute of sacrifice, alternating the nerve dissected first to control for postmortem metabolism. Tissues were immediately placed in 5 ml tubes containing a solution of ice-cold 85% ethanol/15% 30mM HCl[87] to halt metabolism. The nerves in the ethanol/HCl solution were gradually warmed to room temperature and the tissue was agitated gently for several hours to permit egress of all glucose (glucose is soluble in this solution, but glycogen is not). Nerves were then washed in 1X PBS 3 times for 5 minutes each. Using a paintbrush, nerves were then carefully transferred into 150 µl molecular grade water in a 1.5 ml microcentrifuge tube and placed on ice. Each sample was then ground using a pestle and immediately placed in an 95°C dry bath for 10 minutes to denature any remaining functional enzymes, then transferred immediately back to ice.

Using a NanoDrop 8000 (Thermo Scientific, Wilmington, DE) an A280 protein analysis was performed 3x on each sample, and the average value was determined to normalize results to the amount of nerve protein obtained. From this point, Abcam’s fluorescent protocol was utilized. Briefly, samples and a standard curve were pipetted into a 96 well plate. A hydrolysis enzyme mix (mainly glucoamylases) was added to each well apart from glucose background control wells, and the plate was incubated with gentle agitation for 30 minutes at room temperature. A reaction mix containing the OxiRed probe and a development enzyme mix was added to each well and the plate was incubated again with gentle agitation for 30 minutes at room temperature while protected from light. The plate was immediately analyzed using a SpectraMax M2 Microplate Reader (Molecular Devices, San Jose, CA) to determine fluorescence (Ex 535/ Em 587) to detect the amount of hydrolyzed glycogen. The assay detects glycogen 0.0004 – 2 mg/ml, which is sensitive enough to assay a single mouse optic nerve in duplicate.

3.2.8 POSITRON EMISSION TOMOGRAPHY

To determine the capacity for metabolite redistribution between optic nerves, we utilized a Siemens Inveon PET scanner (Siemens Preclinical, Knoxville, TN), a NanoSPECT/CT (Bioscan, Washington DC), and the radioactive glucose analogue ^{18}F-FDG[58,344,345]. Mice were briefly anesthetized with 2.5% isoflurane and unilaterally intravitreally injected with 1.4 – 4.2 MBq/0.002 mL of ^{18}F-FDG using a Hamilton syringe and 33 gauge, 0.375 inch needles. Injections occurred contralateral to the microbead injected eye, if applicable. Animals were then returned to their cages and fed ad libitum for 60 minutes to allow for ^{18}F-FDG uptake and transport in an awake, functioning brain.

Animals were again anesthetized with 2% isoflurane and imaged for 40 minutes in the Inveon microPET in static mode. All data sets were reconstructed using the MAP algorithm into 128 x 128 x 95 slices with a voxel size of 0.095 x 0.095 x 0.08 cm^3 at a beta value of 0.01. To obtain CT anatomical images, immediately following the PET scans the mice were imaged in NanoSPECT/CT at an X-ray beam intensity of 90 mAs and an X-ray tube voltage of 45 kVp. The images were reconstructed into 170 x 170 x 170 slices with a voxel size of 0.4 x 0.4 x 0.4 mm^3.

The PET and CT images were uploaded in the medical imaging tool Amide (www.sourceforge.amide.com). The PET images were normalized to the injected radioactive dose of ^{18}F-FDG. Regions-of-interest (ROIs) were drawn around the optic nerve contralateral to the ^{18}F-FDG injected eye as defined in the CT scan, and mean radiotracer concentrations within these ROIs were measured in units of percent injected dose per unit volume (%ID/g).

3.2.9 OPTIC NERVE TRANSECTION

Optic nerve transection has been utilized and documented in rats[346,347]; here, we adapt the procedure to mice. Mice were anesthetized with ketamine and xylazine and eyedrops containing 0.5% proparacaine were applied as a local anesthetic and a preemptive measure against discomfort. A 2-3 mm lateral canthotomy was performed on one eye per mouse to allow access to the posterior globe and optic nerve. The conjunctiva was then incised to allow gentle outward retraction of the globe using fine forceps. While carefully avoiding the ocular muscles and blood supply to the eye, the optic nerve was exposed and transected with iridectomy scissors 2-3 mm from the globe.

The site of canthotomy was not sutured after transection as this region heals well without suturing[348] and sutures could increase IOP thus confounding results. For each mouse that received a transection injury, a sham procedure was performed involving the same procedure as the transection but omitting the actual transection in a single eye of another mouse. Upon waking, all animals were assessed for signs of distress or pain. Analgesic ophthalmic drops were applied to the eye as necessary to relieve any discomfort.

3.2.10 COMPOUND ACTION POTENTIAL

To determine optic nerve functional conductance, we measured the compound action potential (CAP) of the whole optic nerve, from the beginning of the myelinated region to the optic chiasm. Unanesthetized mice were sacrificed via cervical dislocation and beheading. Both optic nerves are dissected within one minute of sacrifice, alternating the nerve dissected first to control for postmortem metabolism. Nerves were placed in vials of bubbling ice cold artificial cerebrospinal fluid (aCSF) that contained (in mM): 126 nACl, 3 KCl, 2 $MgSO_4$, 26 $NaHCO_3$, 1.25 NaH_2PO_4, 2 $CaCl_2$, and 10 D-glucose[7]. The aCSF was bubbled with a 5% CO_2-containing gas mixture (95% O_2, 5% CO_2) to maintain pH at 7.45. Thirty minutes prior to recording, the vial was removed from ice and allowed to gradually equilibrate to room temperature. Nerves were counterbalanced between left and right by day of recording. Suction electrodes filled with aCSF were attached to the nerve for stimulation and recording the CAP after nerves had been equilibrated for at least 60 minutes in aCSF.

Initially, CAPs were evoked every 30 seconds and stimulus strength was adjusted to evoke the maximal-amplitude CAP and then increased another 25% to ensure that stimulus strength was always supramaximal[349]. Maintaining this stimulus strength, all subsequent CAPs were evoked every 5 minutes over a period of 1 hour and 45 minutes. For 15 minutes a maximal baseline was established as the highest of three measurements, which then represented 100% of the normalized signal. For the next hour, the bath solution was replaced with aCSF with L-glucose replacing D-glucose. This maintains the same osmolarity, but L-glucose cannot be metabolized and the nerve must then rely upon its astrocytic glycogen to maintain function[7,96]. Following this glucose deprivation, the bath solution is again replaced with normal aCSF containing D-glucose. The nerve's ability to recover from glucose derivation is measured for the following 30 minutes.

Signals were amplified (DAM60, World Precision Instruments, Sarasota, FL) and digitized at a sampling rate of 5 Hz (Digidata 1200, Molecular Devices). Data were acquired with proprietary software (Clampex 10, Axon Instruments). CAP area was calculated in Clampfit (Axon Instruments).

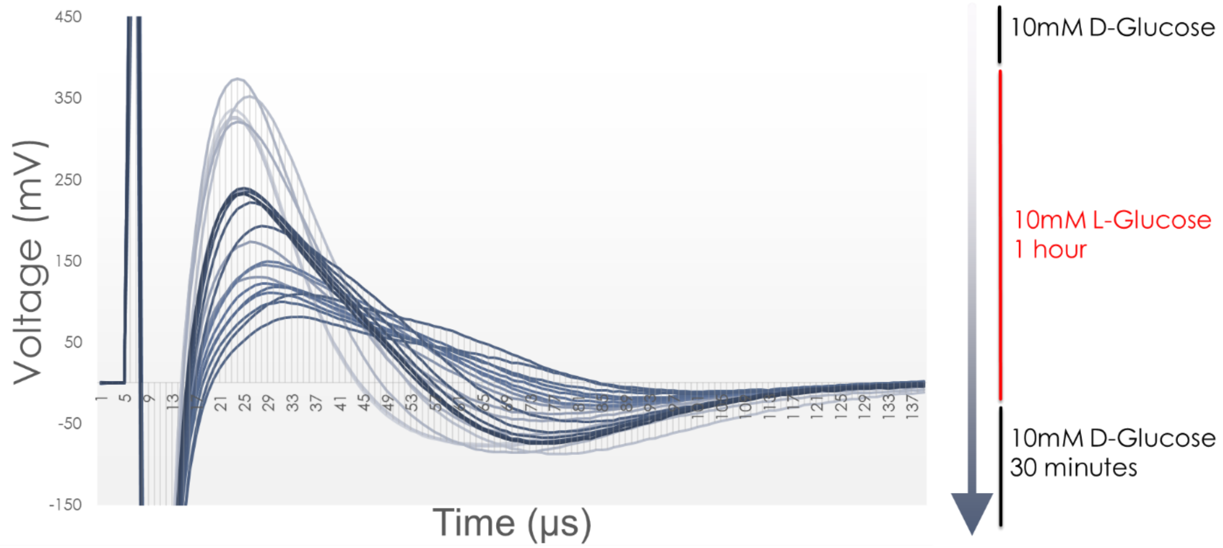

Figure 3.5 Measuring optic nerve compound action potential during glucose deprivation and recovery.

CAPs were evoked every 5 minutes over a period of 1 hour and 45 minutes (blue lines, darker as experiment progresses). For 15 minutes a maximal baseline was established with an aCSF solution containing D-glucose (light blue). Over the next hour, CAP voltage depleted during glucose deprivation in a bath of aCSF containing L-glucose. For the final 30 minutes (dark blue), the nerve's ability to recover was determined in a bath again containing aCSF with D-glucose.

3.2.11 STATISTICAL ANALYSIS

Data for are presented as mean ± standard error of the mean (SEM) for each treatment. Statistical analysis and p-values for comparing means were obtained using Kruskal-Wallis one-way ANOVA or two-sided t-tests for all data that met criteria for normality as confirmed using the Shapiro-Wilk normality test. For data that did not pass Shapiro-Wilk normality, non-parametric Mann-Whitney Rank Sum tests were used. Statistical tests were considered significant if $p < 0.05$. All statistical tests were performed with SigmaPlot 12.5 (Systat Software Inc., San Jose, CA). Numbers of samples and measurements along with actual *p* values of significance are indicated where appropriate in the text or figure legends.

3.3 RESULTS

3.3.1 TAMOXIFEN INDUCES CX43 KNOCKOUT IN *GFAP-CRE-ER^{T2} X CX43$^{FLOX/FLOX}$* MICE

In each experiment, mice were aged 2 month prior to tamoxifen gavage. After one week to allow for maximal protein turnover, tamoxifen action, and complete digestion and removal of both corn oil and drug, IOP was elevated as necessary per experiment (Figure 3.6 A). In *GFAP-Cre-ER^{t2} x Cx43$^{flox/flox}$* mice, tamoxifen administration did not alter GFAP expression or density, but greatly reduced Cx43 expression as expected (Figure 3.6 B). Cx43 is not completely removed; this is expected, as it may still be expressed by astrocytes that do not express GFAP, endothelial cells, or, in the retina, Müller glia. The few puncta that remain could also be attributed to the imperfection of the model itself. Cre-ER^{T2} induction often produces a mosaic of cells exhibiting the knockout. A majority of cells exhibiting excision is considered a successful induction. However, the imperfections of this model should be considered in the context of our results. The properties of this model will render results less significant than could be expected by a complete, perfect knockout.

Tamoxifen administration additionally altered the pattern of Cre localization as expected (Figure 3.6 B). Without tamoxifen induction, Cre expression is diffuse. After tamoxifen is administered, Cre localizes to astrocyte cell bodies, indicative of tamoxifen bound to ER^{T2}, liberating Cre and allowing it to enter nuclear pores[350]. Cre expression after tamoxifen

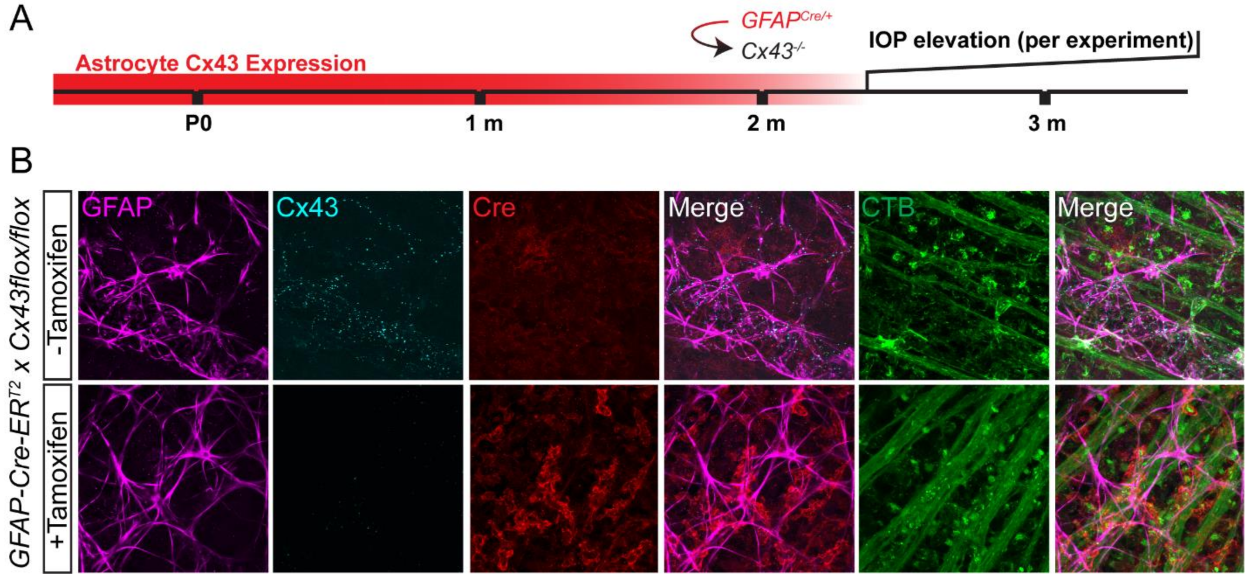

Figure 3.6 Tamoxifen administration in *GFAP-Cre-ER*^{t2} *x Cx43*$^{flox/flox}$ mice reduces Cx43 expression and alters Cre localization.

A. In each subsequent experiment, mice were aged 2 months before tamoxifen administration. One week after the final tamoxifen gavage, IOP was elevated as required per experiment. **B.** All images were obtained from in *GFAP-Cre-ER*^{t2} *x Cx43*$^{flox/flox}$ mice. The top row contains representative images from control mice (no tamoxifen), while the bottom row contains images from a mouse that both received tamoxifen and exhibited genetic excision. GFAP appears similarly distributed in astrocytes of both mice, while Cx43 expression is greatly reduced (while not completely eliminated) in knockout mice. Cre expression appears distributed in control mice, while it is localized mainly to cell bodies in knockout mice. Cre expression follows astrocyte cell bodies, and not neuronal cell bodies or axons (CTB).

induction follows the pattern of astrocyte GFAP expression and cell body localization rather than nuclear cell bodies or axons (Figure 3.6 B).

3.3.2 GLYCOGEN STORES DIMINISH BILATERALLY AFTER UNILATERAL IOP ELEVATION

In our initial experiments, we aimed to determine how glycogen is altered after microbead occlusion, both ipsilaterally and contralaterally to the unilateral elevation, and how this alteration relates to glycogen levels in naïve optic nerve. To establish a timecourse of energetic alterations, we elevated IOP for periods of 4 days, 1 week, 2 weeks, and 4 weeks and compared each cohort to naïve optic nerves. IOP was significantly elevated unilaterally in all conditions (Figure 3.7 A, $p<0.001$). After 4 days of unilateral IOP elevation, glycogen distribution exhibits the expected pattern; in the nerve impacted by the stress of elevated IOP, glycogen is significantly diminished compared both to the contralateral nerve ($p=0.046$) and naïve nerves ($p=0.005$). The nerve contralateral to IOP elevation did not exhibit any alterations in glycogen content.

Counterintuitively, this pattern did not continue for the remainder of the timecourse. After 1 week of unilateral IOP elevation, glycogen content diminishes in both the ipsi- and contralateral optic nerves compared to naïve levels ($p=0.001$, $p<0.001$). Further, the microbead nerve contains significantly *more* glycogen than the contralateral, theoretically unstressed, nerve ($p=0.007$). This pattern is repeated after 2 weeks of IOP elevation ($p<0.001$, $p<0.001$, $p=0.004$). After 4 weeks of IOP elevation, the nerves both ipsi- and contralateral to IOP elevation exhibit diminished glycogen content compared to naïve nerves ($p<0.001$, $p<0.001$) but are no longer significantly different from one another (Figure 3.7 B).

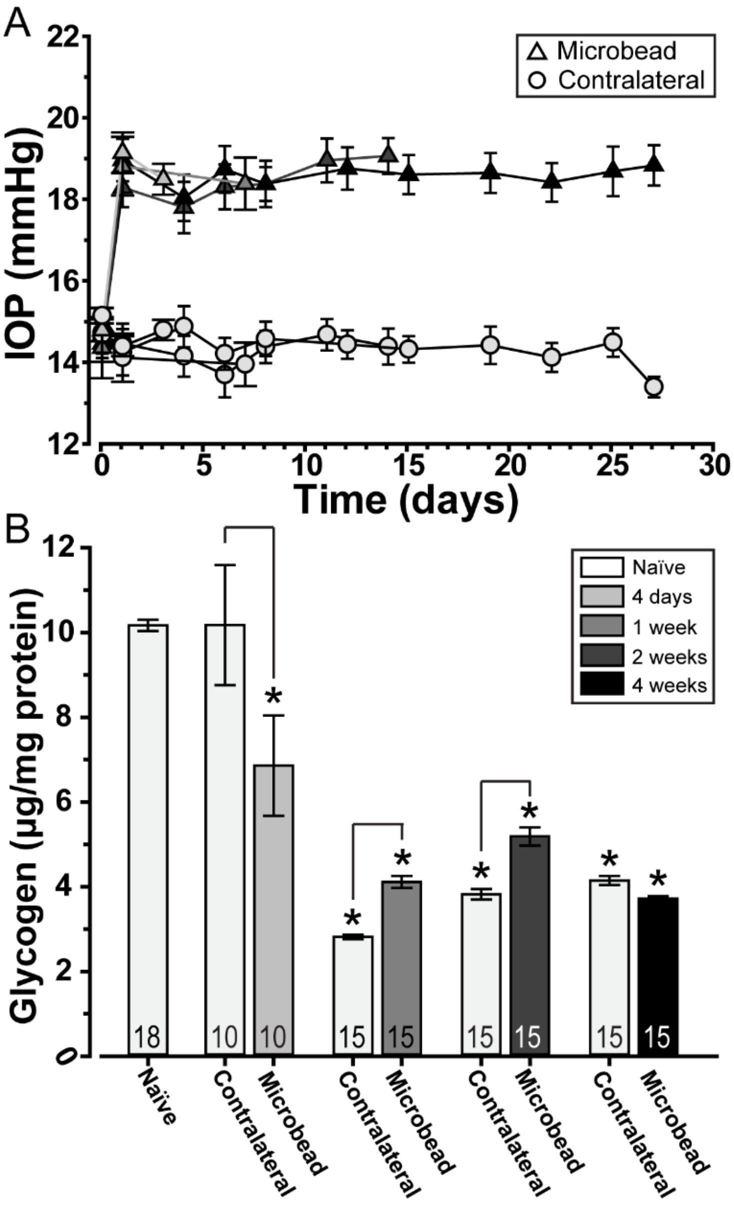

Figure 3.7 Glycogen stores diminish bilaterally after unilateral IOP elevation.

A. IOP was significantly elevated unilaterally in microbead (Δ) compared to contralateral (o) eyes ($p<0.001$). **B.** Four days of unilateral IOP elevation result in diminished glycogen stores (µg/mg nerve protein) in microbead compared both to contralateral and naïve nerves ($p=0.046$, $p=0.005$). 1 and 2 weeks of unilateral IOP elevation cause diminished glycogen stores compared to naïve nerves both ipsi- ($p=0.001$, $p<0.001$) and contralateral ($p<0.001$, $p<0.001$) to the microbead eye. Further, contralateral nerves contain significantly less glycogen than their microbead counterparts ($p=0.007$, $p=0.005$). 4 weeks of IOP elevation result in diminished glycogen in both nerves compared to naïve ($p<0.001$ $p<0.001$), but nerves are no longer significantly different from one another.

3.3.3 ASTROCYTE-SPECIFIC CX43 KO REVERSES GLYCOGEN DISTRIBUTION PATTERN AFTER CHRONIC UNILATERAL IOP ELEVATION

We next repeated this experiment in *GFAP-Cre-ER*^{t2} *x Cx43*$^{flox/flox}$ mice with *Cx43*$^{flox/flox}$ mice serving as control. Both groups were given three tamoxifen gavages one week prior to IOP elevation. IOP was elevated for either 4 days or 1 week, the timepoints our experiments in C57 mice demonstrated as nearest the tipping point for contralateral glycogen depletion (Figure 3.7). IOP was significantly elevated in all microbead groups compared to contralateral eyes, and IOP elevation was similar to that achieved in wild type mice ($p<0.001$; Figure 3.8 A, right). Control mice exhibit a pattern of glycogen distribution similar to that of wild type mice both 4 days and 1 week after unilateral IOP elevation (Figure 3.8 B, right, grey bars); 4 days of elevation causes glycogen to diminish in the ipsilateral optic nerve ($p=0.013$) while 1 week of elevation causes glycogen to diminish in both nerves compared to control values ($p<0.001$, $p<0.001$) and the contralateral nerve to exhibit diminished glycogen compared to the ipsilateral nerve ($p=0.024$). Cx43 knockout and 4 days of unilaterally elevated IOP resulted in significantly diminished glycogen in the microbead nerve compared to contralateral ($p<0.001$) and naïve ($p=0.015$) nerves, similar both to wild type and control results. However, the pattern of glycogen distribution is reversed after 1 week of unilateral IOP elevation. Although glycogen levels are diminished in both microbead and contralateral nerves ($p<0.001$, $p<0.001$), glycogen is significantly lower in the microbead nerve compared to the contralateral nerve ($p<0.001$). Cx43, therefore, is a component of the normal energetic redistribution that occurs after localized neurodegenerative stress.

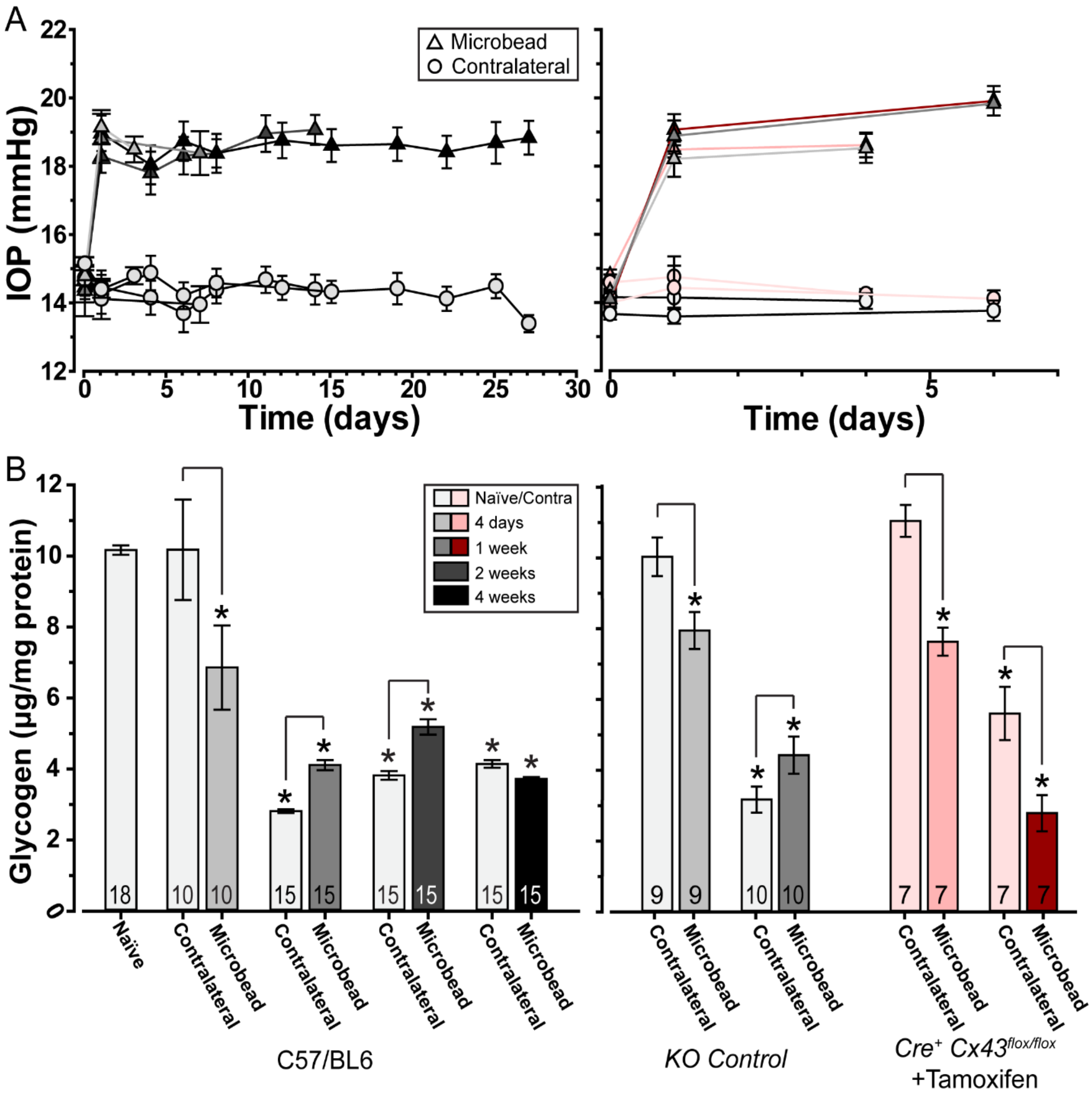

Figure 3.8 Cx43 is a component of energetic redistribution after localized neurodegenerative stress.

A. IOP was significantly elevated unilaterally in microbead (Δ) compared to contralateral (o) eyes in all conditions ($p<0.001$). **B.** Left: repeated from figure 3.7 for comparison. Right: KO control nerves (grey) exhibit a pattern of glycogen distribution similar to that of wild type mice. After 4 days of unilateral IOP elevation, glycogen is diminished in the microbead nerve compared both to naïve ($p=0.007$) and contralateral ($p=0.013$) nerves; 1 week of unilateral IOP elevation causes diminished glycogen in both nerves compared to naïve ($p<0.001$), and contralateral nerves contain less glycogen than their microbead counterparts ($p<0.001$). In KO nerves, 4 days of unilateral IOP elevation result in the same pattern; glycogen diminishes in the microbead nerve compared both to naïve ($p=0.015$) and contralateral nerves ($p<0.001$). However, although 1 week of unilateral IOP elevation causes glycogen content to significantly diminish in both microbead and contralateral nerves compared to naïve ($p<0.001$, $p<0.001$),microbead nerves now contain significantly less glycogen than their contralateral counterparts ($p<0.001$).

3.3.4 UNILATERAL IOP ELEVATION RESULTS IN ENERGY TRANSFER BETWEEN NORMAL AND GLAUCOMATOUS OPTIC PROJECTIONS

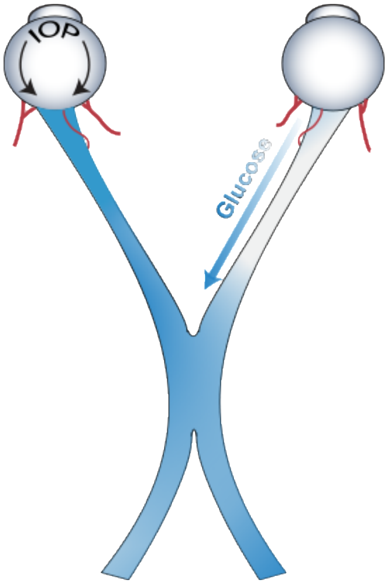

Figure 3.9 Hypothesis: glucose is redistributed from healthy to chronically stressed tissue.

We hypothesize that when the CNS experiences a local, chronic stressor such as unilaterally elevated IOP (left eye), glycogen stores are mobilized in nearby regions. The mobilized glucose is then drawn to the stressed region to maintain function.

Our experiments demonstrated that glycogen diminishes bilaterally after a chronic unilateral stressor, meaning that glycogen was being mobilized into glucose in both visual streams. We hypothesized that these energy reserves were not merely utilized locally; rather, that glucose was drawn from the healthy projection to the actively stressed projection to help maintain RGC function (Figure 3.9). To test this, we devised an experiment where we elevated IOP unilaterally for one week and then injected ^{18}F-FDG, a radioactive glucose analogue, into the contralateral eye. After the mice were awake for one hour to allow for uptake, we imaged for 40 minutes in a PET scanner in static mode. The cumulative amount of radiation detected in the stressed optic nerve, ipsilateral to IOP elevation and contralateral to ^{18}F-FDG injection, was measured and compared between naïve and microbead-injected animals.

In naïve mice intravitreally injected with ^{18}F-FDG, 0.614 ± 0.070% of the injected dose is transferred to the contralateral visual stream (Figure 3.10). However, if that contralateral visual stream has been stressed through elevated IOP for 1 week, 1.023 ± 0.088% of the injected dose is transferred, a statistically significant increase of a remarkable 41% (p = 0.001). These data demonstrate the brain's capability to transport glucose between optic projections in a remarkably short period of time, as well as the impact a chronic stressor has on this transport.

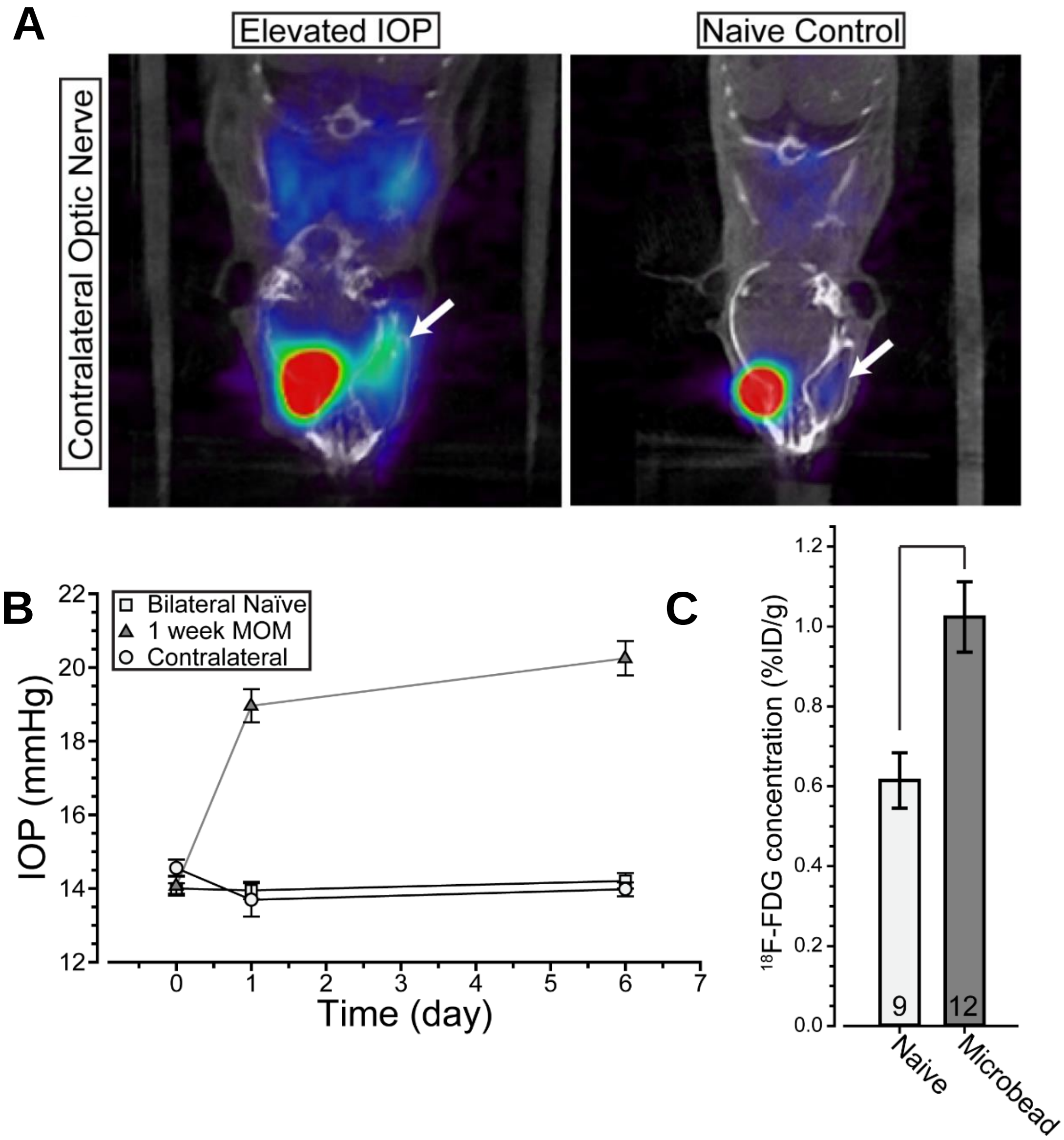

Figure 3.10 Unilaterally elevated IOP causes neuroenergetic redistribution between optic projections.

A. PET scan (color) overlaid onto CT scan (black and white) from a mouse with 1 week unilaterally elevated IOP (left) and a naïve control mouse (right). ^{18}F-FDG injected in to the right eye (left of each image, large red object) moves into the contralateral optic nerve (right arrows) 1 hour after IVT injection. This occurs to a much greater extent in the contralateral projection has been stressed by IOP elevation (left). **B.** IOP elevation in 1 week MOM eyes resulted in significantly greater IOP than both bilateral naïve and contralateral values ($p < 0.001$). **C.** Contralateral nerves in naïve mice received 0.614 ± 0.070% of the injected dose, while contralateral microbead-stressed nerves received 1.023 ± 0.088%, a 41% increase in glucose transfer ($p = 0.001$).

3.3.5 ENERGY TRANSFER BETWEEN NORMAL AND GLAUCOMATOUS OPTIC PROJECTIONS OCCURS THROUGH THE OPTIC NERVE PROPER

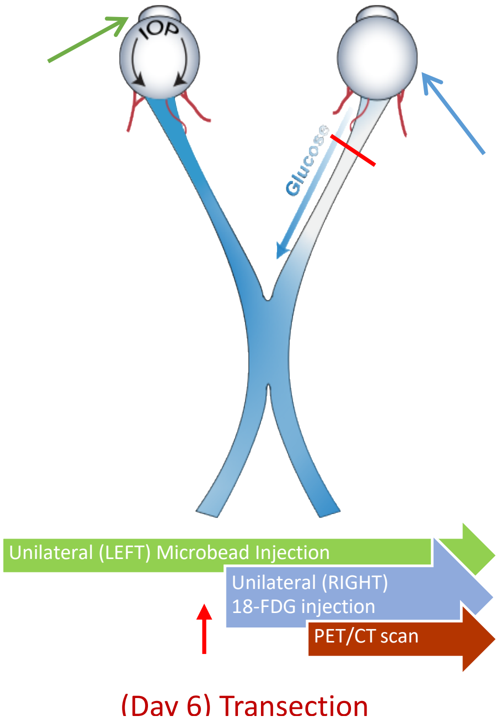

Figure 3.11 Determining the route metabolites use through optic nerve transection.

To assess whether glucose traverses the optic nerve proper, we utilized the same experimental paradigm as in section 3.3.4 but implemented an optic nerve transection the day prior to PET scanning. The eye corresponding to the transected or sham nerve was injected with ^{18}F-FDG. The amount of radioactivity in the contralateral IOP-stressed projection corresponds with the amount of glucose that has moved from one projection to the other.

To determine whether glucose transfer was occurring through the optic nerve proper itself or the bloodstream supplying the retina, we next performed PET experiments on mice that each underwent a unilateral microbead injection to elevate IOP 7 days prior. The day before PET scans occurred, three mice underwent a unilateral optic nerve transection in the projection contralateral to IOP elevation (Figure 3.11). Three additional mice underwent sham procedures as a control. To ensure the retina was still alive and receiving an intact blood supply, the day following PET scans each transected or sham eye was injected intravitreally with CTB.

Transection, sham, and control mice exhibited significant IOP elevation compared to bilateral naïve and contralateral eyes (Figure 3.12A). As expected, microbead/sham mice exhibited glucose transfer comparable to mice that underwent microbead injection alone (1.04 ± 0.21% vs 1.02 ± 0.09%; $p = 0.467$; Figure 3.12C). Transection, however, resulted in a statistically significant 61% loss over sham mice (0.43 ± 0.05% vs 1.04 ± 0.21%; $p = 0.023$). Additionally, the bladder exhibited a strong radioactive signal in each mouse; from this, we know that the ^{18}F-FDG was metabolized and absorbed into the blood (Figure 3.12B).

Transected mice additionally exhibited intact transport of CTB to the site of transection, beyond which there was no signal (Figure 3.13). Additionally, the transection site was about 2mm from the sclera, while the central retinal artery and vein invade the murine optic nerve less than 0.25mm from the sclera[351]. From these data, we infer that glucose transfer must have necessitated the optic nerve proper.

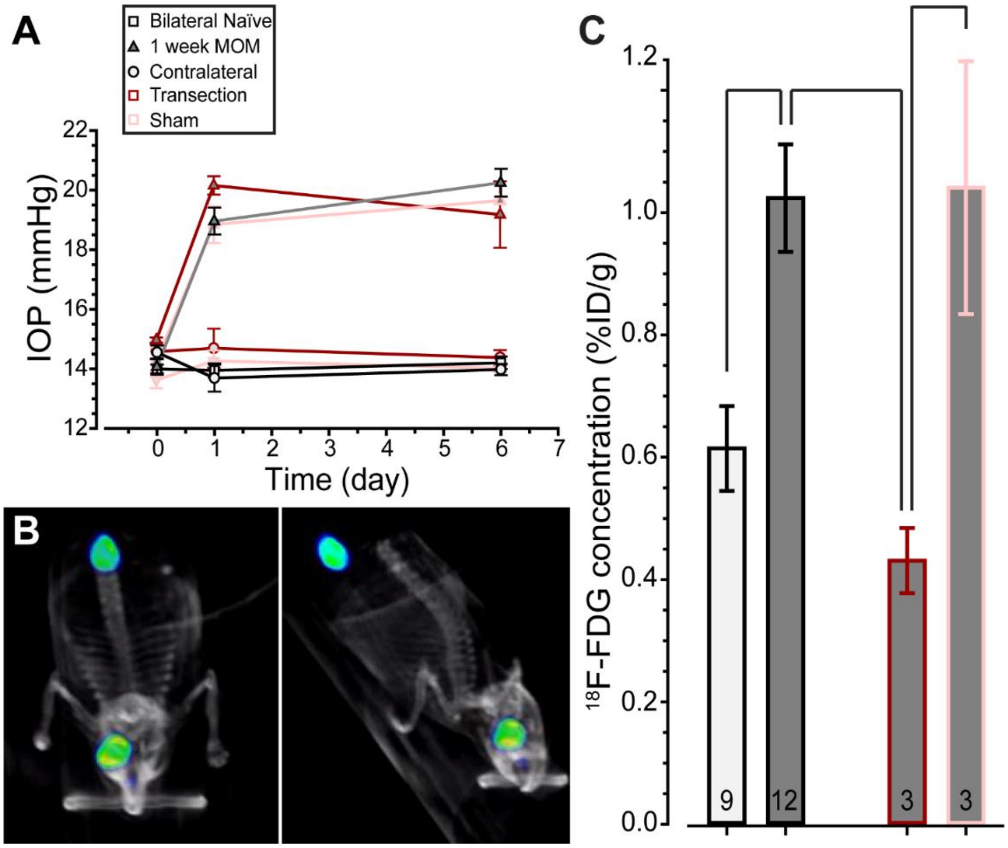

Figure 3.12 Energy transfer between normal and glaucomatous optic projections requires an intact optic nerve proper.

A. IOP was elevated in all 1-week MOM conditions (Δ). Transection, sham, and control cohorts did not exhibit significantly different elevations, but each was significantly elevated over bilateral naïve or contralateral cohorts ($p < 0.001$). **B.** After optic nerve transection, ^{18}F-FDG no longer flows to the IOP-exposed contralateral nerve. However, the signal remains within the bladder, demonstrating that the molecule was still metabolized and circulated through the bloodstream. **C.** Sham/MOM mice (pink outline) demonstrate contralateral ^{18}F-FDG signal similar to that of MOM mice (1.04 ± 0.21% vs 1.02 ± 0.09%; $p = 0.467$). Transection/MOM mice (red outline) demonstrate significantly less ^{18}F-FDG than mice that underwent sham procedure or microbead injection alone (0.43 ± 0.05%; $p = 0.023$, 0.003).

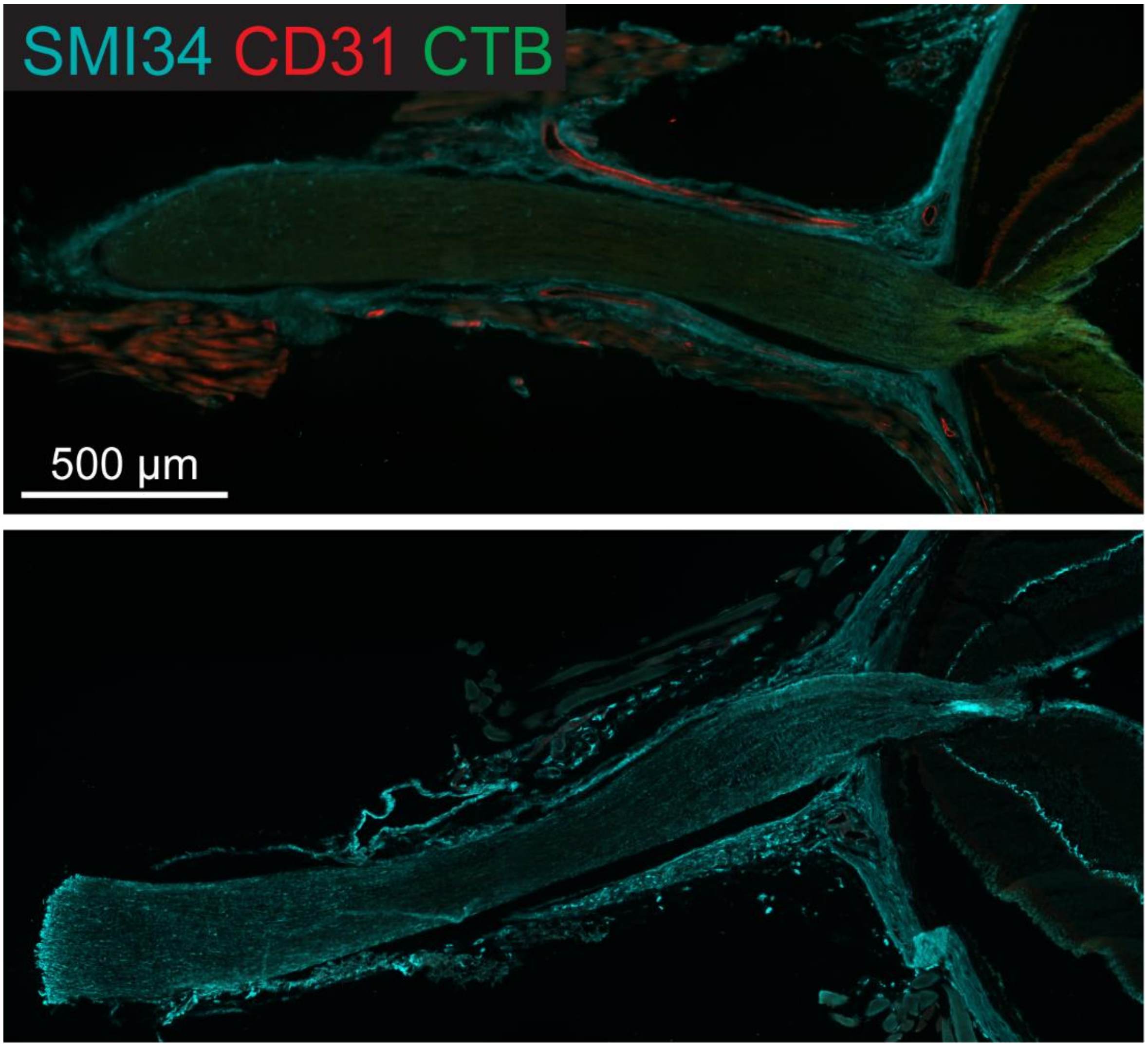

Figure 3.13 Optic nerves were transected beyond the entrance of the central retinal artery.

Top: Longitudinal optic nerve section from a transected optic nerve. SMI34 demarcates hyperphosphorylated neurofilaments; CD31 highlights vasculature in red; CTB is tagged with green fluorophores. The optic nerve shown here is intact for about 2 microns, and RGCs were capable of taking up and transporting CTB 3 days post-transection. **Bottom:** Longitudinal optic nerve section from a second transected optic nerve. The transected region is highlighted with bright SMI34 staining, indicating unhealthy RGC axons.

3.3.6 ENERGY TRANSFER DURING UNILATERAL GLAUCOMATOUS STRESS INVOLVES ASTROCYTE CONNEXINS

After establishing that an intact optic nerve proper is necessary for glucose redistribution during localized neurodegenerative stress, our next experiments aimed to establish the mechanism through which astrocyte glycogen could be redistributed. As astrocytes contain gap junctions, the simplest possible pathway through which metabolites can redistribute, the number of gap junctions between astrocytes increases during glaucomatous stress[64], and prior experiments have established the capability for metabolite redistribution through astrocyte gap junctions[276], we focused our attention on this mechanism.

We utilized our conditional astrocyte gap junction knockout, *GFAP-Cre-ER*^{t2} *x Cx43*$^{flox/flox}$, with *Cx43*$^{flox/flox}$ mice serving as control. Both groups received three consecutive tamoxifen gavages one week prior to any experimental manipulation. All *Cx43*$^{flox/flox}$ mice and a cohort of *GFAP-Cre-ER*^{t2} *x Cx43*$^{flox/flox}$ mice were intracamerally injected with microbeads to unilaterally elevate IOP. One week following this injection, the contralateral eye was injected with ^{18}F-FDG. After one hour of uptake, mice were anesthetized and PET scanned to determine the degree of glucose redistribution to the injured optic nerve.

KO control mice, or *Cx43*$^{flox/flox}$ mice with tamoxifen administered, exhibited glucose redistribution after unilateral IOP elevation similar to that of C57 mice that experienced IOP elevation for the same period of time (0.905 ± 0.111% vs 1.024 ± 0.087%; p=0.208; Figure 3.14). KO mice, however, exhibit a trend toward less glucose redistribution than WT mice even when IOP has not been elevated in either group (0.488 ± 0.018% vs 0.614 ± 0.069%; p = 0.087).

Further, 1 week of IOP elevation in KO mice results in a statistically significant 47% reduction in glucose redistribution compared to KO control (0.431 ± 0.057% vs 0.905 ± 0.111; $p < 0.001$).

Intriguingly, results from KO mice in all conditions more closely resemble transection levels of transport than even those of naïve WT mice. This hints that perhaps the metabolic networks formed through astrocyte gap junctions are important for normal function as well as during early neurodegenerative stress. This idea will be explored further in subsequent sections.

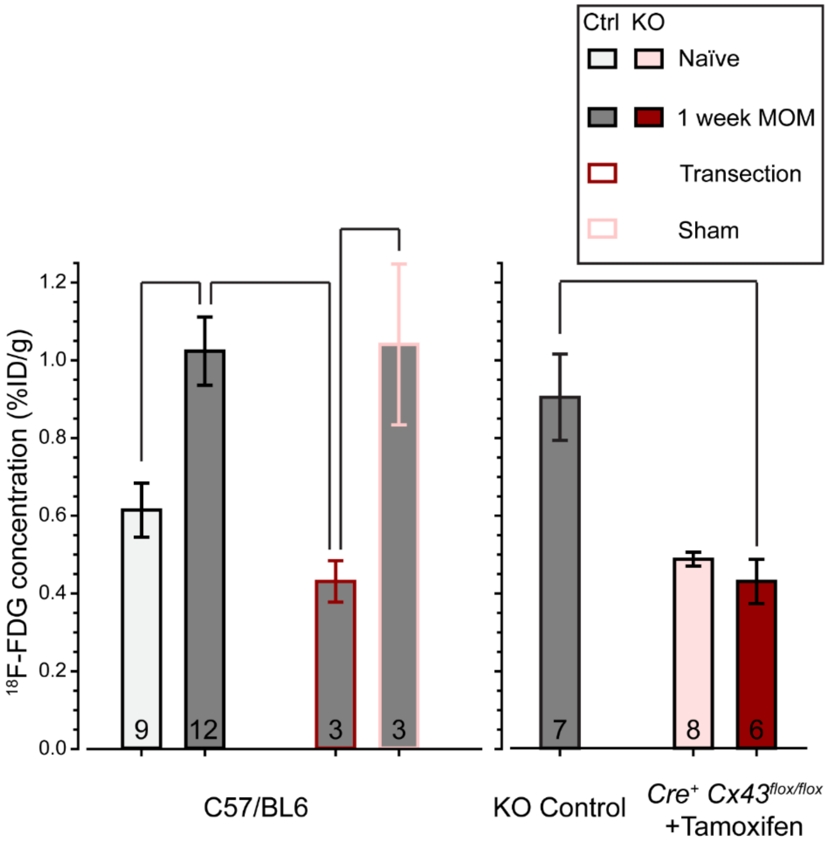

Figure 3.14 Energy transfer during unilateral glaucomatous stress involves astrocyte connexins.

In wild-type (C57/BL6) mice, contralateral nerves in naïve mice received 0.614 ± 0.070% of the injected dose while contralateral microbead-stressed nerves received 1.023 ± 0.088%, a 41% increase in glucose transfer ($p = 0.001$). Sham/MOM mice (pink outline) demonstrate contralateral ^{18}F-FDG signal similar to that of MOM mice (1.04 ± 0.21% vs 1.02 ± 0.09%; $p = 0.467$). Transection/MOM mice (red outline) demonstrate significantly less ^{18}F-FDG than mice that underwent sham procedure or microbead injection alone (0.43 ± 0.05%; $p = 0.023, 0.003$). KO control mice exhibited glucose redistribution after unilateral IOP elevation similar to that of C57 (0.905 ± 0.111% vs 1.024 ± 0.087%; $p=0.208$). One week of IOP elevation in KO mice results in a statistically significant 47% reduction in glucose redistribution compared to KO control (0.431 ± 0.057% vs 0.905 ± 0.111; $p < 0.001$).

3.3.7 ENERGY TRANSFER BETWEEN OPTIC PROJECTIONS CAUSES FUNCTIONAL DEFICITS IN OPTIC NERVE SIGNALING DURING METABOLIC STRESS

In the final experimental set of this aim we examined the functional consequences of energy transfer between optic projections. We measured the optic nerve compound action potential (CAP) in bilateral naïve, 1-week unilateral MOM, and 2-week unilateral MOM conditions. IOP was significantly elevated above baseline and contralateral eyes in both 1 week unilateral MOM and 2 week unilateral MOM conditions (Figure 3.15A; $p < 0.001$)

Optic nerves were initially placed in a bath of aCSF and baseline measurements were obtained over 15 minutes. For the following hour the bath was replaced with aCSF containing L-glucose, an enantiomer of D-glucose that cannot be digested by mammalian cells. For the final 30 minutes of the experiment, the bath returned to typical aCSF and the nerves' ability to recover from glucose depletion was determined. All measurements are presented as a percentage of the maximal baseline response for that nerve to normalize for any alterations in resistance.

In bilateral naïve mice, optic nerves exposed to aCSF containing L-glucose exhibited an initial increase in CAP area over the first 5 minutes of glucose depletion (to about 108%) and subsequently declined over the following 60 minutes to about 24% (Figure 3.15B). Nerves recovered to about 55% of baseline after 30 minutes of recovery. Nerves directly exposed to 1 week of elevated IOP exhibited the same response, with no point statistically differing from baseline values (Figure 3.15B). Intriguingly, the nerve contralateral to 1 week of elevated IOP did not exhibit as strong a signal. Contralateral 1-week nerves exhibited no initial increase in CAP area upon glucose depletion and fell to a mere 7% of their initial signal over the subsequent hour. Further, contralateral 1-week nerves only recovered about 45% of their initial CAP area. These values are significantly reduced from 1 week MOM values at each point from minute 0 through minute 90 apart from minutes 10, 15, and 20 (*, $p<0.039$) and are significantly reduced from naïve levels at minute 0, 40, 55, and 60 (#, $p<0.049$).

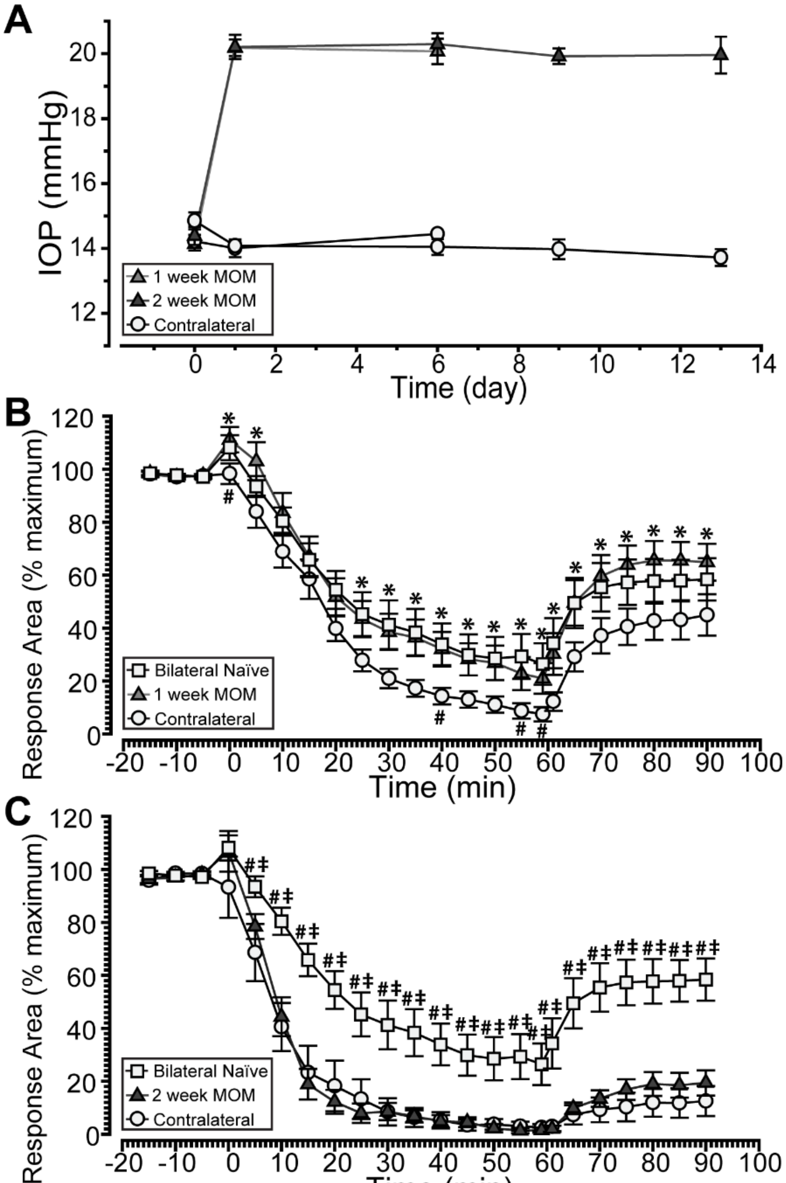

Figure 3.15 Unilateral IOP elevation causes bilateral functional deficits in CAP response during glucose depletion.

A. IOP was significantly elevated above contralateral values in both 1 week (20.07 ± 0.39 vs 14.45 ± 0.11; $p < 0.001$) and 2 week (19.96 ± 0.57 vs 13.72 ± 0.26; $p < 0.001$) unilateral conditions. **B.** Bilateral naïve optic nerves exposed to aCSF containing L-glucose exhibited an initial increase in CAP area (108.54 ± 4.01%), subsequently declined over the following 60 minutes (23.96 ± 8.36%),and recovered over the following 30 minutes in aCSF (54.87 ± 8.78%). Unilateral 1 week MOM nerves were not significantly different from bilateral naïve nerves at any point. Contralateral 1 week nerves exhibited no initial increase in CAP area (98.33 ± 3.90%), declined to a greater extent over the following 60 minutes of glucose depletion (7.45 ± 2.70%), and did not recover as well (44.97 ± 7.80%) as bilateral naïve (#, $p<0.049$) or 1 week MOM (*, $p<0.039$) nerves. **C.** Unilateral 2 week nerves and their contralatateral fellows exhibit diminished CAP response compared to bilateral naïve nerves both during 60 minutes of glucose depletion (1.55 ± 0.99%; 2.54 ± 1.26%) and 30 minutes of recovery (19.39 ± 4.77%; 12.53 ± 5.65%). Statistical significance was reached at every point 5 minutes and beyond for both 2 week MOM (‡, $p<0.031$) and contralateral groups (*, $p<0.026$).

Two weeks of unilateral IOP elevation resulted in diminished ability to survive glucose depletion bilaterally (Figure 3.15C). For every time point from 5 minutes post glucose depletion and beyond, both the 2 week MOM nerves (‡) and the contralateral 2 week MOM nerves (#) were significantly reduced from naïve values (p<0.031). At no point did contralateral nerves demonstrate a value significantly different from their fellow MOM cohort after 2 weeks of unilateral elevation.

3.3.8 ASTROCYTE-SPECIFIC CX43 KNOCKOUT RESCUES FUNCTIONAL DEFICITS IN OPTIC NERVE SIGNALING DURING METABOLIC STRESS

We next examined how our conditional Cx43 knockout would respond to the same experimental paradigm. IOP was unilaterally elevated for 1 week in KO mice to levels significantly greater than contralateral (18.81 ± 0.38 vs 14.05 ± 0.29; p <0.001; Figure 3.15). KO nerves were compared to C57 nerves exposed to the same elevation paradigm.

Naïve KO nerves did not statistically differ from naïve C57 nerves at any point throughout baseline, glucose depletion, or recovery measurements (Figure 3.16A). KO nerves

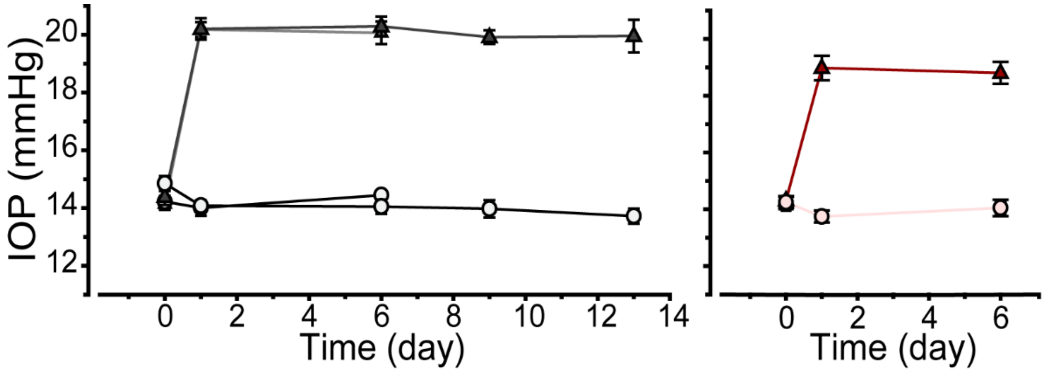

Figure 3.16 IOP elevation in C57 and KO mice for CAP experiments.

In C57 mice (left), IOP was significantly elevated above contralateral values in both 1 week (20.07 ± 0.39 vs 14.45 ± 0.11; p < 0.001) and 2 week (19.96 ± 0.57 vs 13.72 ± 0.26; p < 0.001) unilateral conditions. In KO mice (right, red), IOP was significantly elevated above contralateral levels for 1 week (18.81 ± 0.38 vs 14.05 ± 0.29; p <0.001).

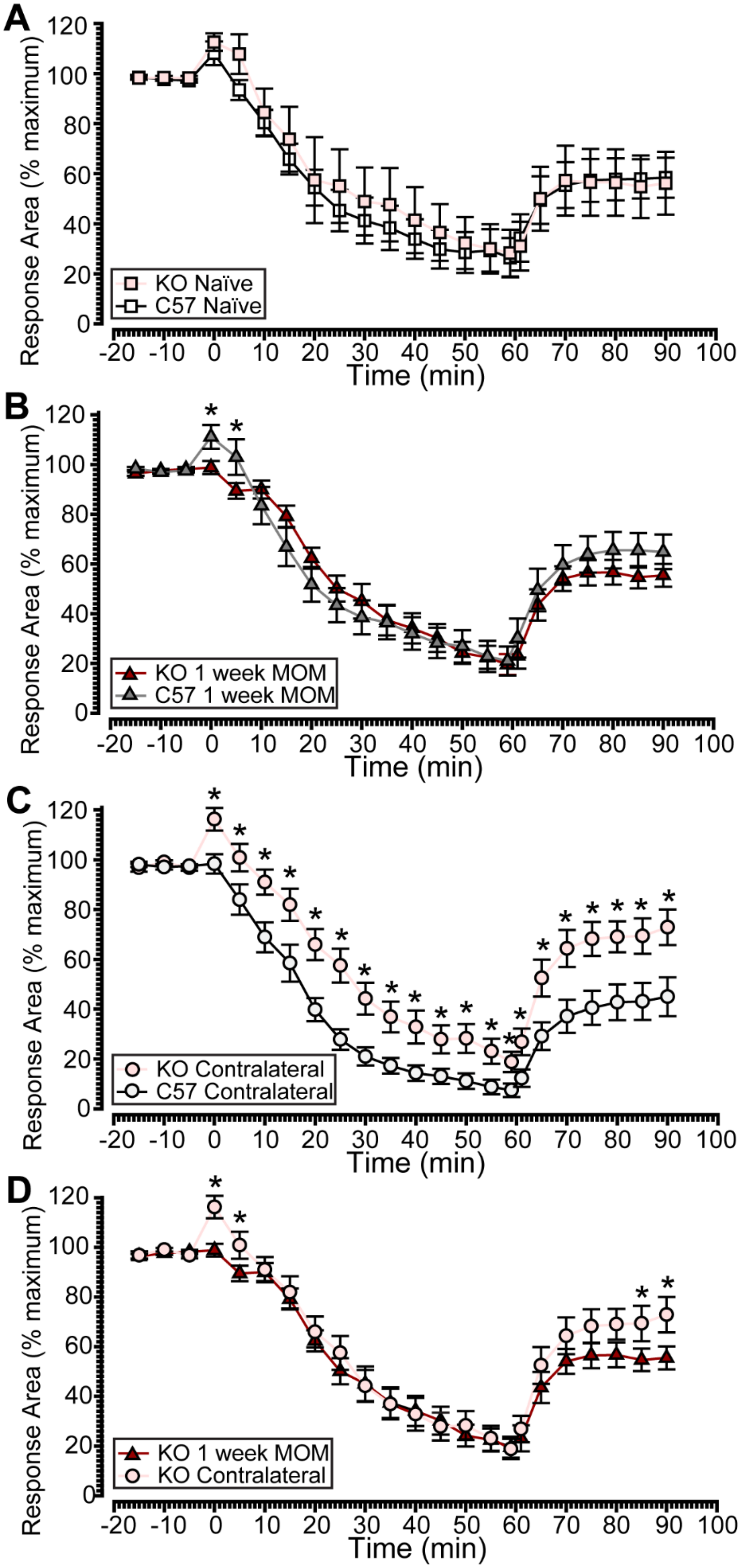

Figure 3.17 Cx43 KO rescues deficits in CAP response during glucose depletion after unilateral IOP elevation.

A. Naïve KO nerves did not statistically differ from naïve C57 nerves at any point measured. **B.** KO nerves exposed to 1 week of IOP elevation exhibit a diminished response compared to corresponding C57 nerves for the 5 minutes immediately following glucose depletion (*; p<0.049). **C.** KO 1 week contralateral nerves exhibit elevated CAP area compared to corresponding C57 nerves at every time point aside from baseline measures (*; p<0.027). **D.** The KO contralateral response is statistically greater than corresponding contralateral responses at minutes 0, 5, 85, and 90 (*; p<0.043).

exposed to 1 week of IOP elevation exhibit a diminished response compared to corresponding C57 nerves for the 5 minutes immediately following the initiation of glucose depletion ($p<0.049$), but closely resemble the C57 response for each subsequent timepoint (Figure 3.16B). However, KO nerves contralateral to 1 week of IOP elevation exhibit elevated CAP area compared to corresponding C57 nerves at every time point from glucose depletion onward (Figure 3.16C; $p<0.027$). Remarkably, the KO contralateral response is not statistically different from the naïve KO response at any time point. Additionally, the KO contralateral response is statistically greater than the fellow KO 1 week response immediately following the initiation of glucose depletion (minutes 0 and 5; $p<0.037$) and in the final measurements of the recovery phase (minutes 85 and 90; $p<0.043$). Certainly, KO rescues the contralateral signaling deficit in response to glucose depletion; however, it appears that this may occur at the sacrifice of the MOM nerve's signaling ability at a few key points in the timecourse.

3.4 DISCUSSION

The aim of Chapter 3 was to determine the molecular mechanism through which astrocytes redistribute resources from healthy regions of the brain to areas actively undergoing stress. To do so, we generated a locally and temporally controlled knockout of Cx43 in astrocytes expressing GFAP. Although this knockout did not eliminate every puncta of Cx43 within astrocytes, the vast majority of the protein was eliminated (Figure 3.6). In each experiment, we not only compared KO results to the appropriate controls but also compared our results to wild type (C57/BL6) mice.

We initially investigated the pattern of glycogen distribution between optic nerves in WT mice exposed to a timecourse of unilateral IOP elevation. Four days of unilateral IOP elevation resulted in the pattern we expected; in the nerve impacted by the stress of elevated IOP, glycogen is significantly diminished compared both to the contralateral nerve and to naïve nerves. At this time point, the nerve contralateral to IOP elevation did not exhibit any alterations in glycogen content.

Counterintuitively, this pattern did not continue for the remainder of the timecourse. After 1, 2, and 4 weeks of unilaterally elevated IOP in WT mice, nerves both ipsi- and contralateral to the IOP elevation exhibited diminished glycogen compared to naïve levels. Further, after 1 and 2 weeks of unilateral IOP elevation the microbead nerve contains significantly more glycogen than the contralateral, theoretically unstressed nerve. From these data, we hypothesized that the stressor of elevated IOP does not merely influence the brain locally, and perhaps there was an endogenously protective mechanism through which astrocytes were able to redistribute their energy stores to those regions most in need of assistance.

To directly test this, we repeated this experiment in *GFAP-Cre-ET^{t2} x Cx43$^{flox/flox}$* mice with *Cx43$^{flox/flox}$* mice serving as control. Both groups were given three tamoxifen gavages one week prior to IOP elevation, thus controlling for the effects of tamoxifen. IOP was elevated for either 4 days or 1 week, the timepoints our experiments in C57 mice demonstrated as nearest the tipping point for contralateral glycogen depletion. Control mice exhibited a pattern similar to that of WT mice at all time points examined; 4 days of elevation causes glycogen to diminish in the ipsilateral optic nerve while 1 week of elevation causes glycogen to diminish in both nerves compared to control values. Four days of IOP elevation in KO mice repeated the same pattern as control and WT mice. At this timepoint, glycogen diminished in the microbead nerve compared to contralateral and naïve values. However, KO reversed the pattern of glycogen distribution after 1 week of unilateral IOP elevation. Although glycogen levels diminished in both microbead and contralateral nerves, glycogen is significantly lower in the microbead nerve compared to the contralateral nerve.

From these data, we know Cx43 is a component of the normal energetic redistribution that occurs after localized neurodegenerative stress. However, glycogen levels still diminished in the contralateral nerve. There are multiple explanations for this phenomenon, each of which should be investigated in future experiments. There is likely redundancy in the system of energetic redistribution during localized neurodegenerative stress, perhaps involving other connexins within astrocytes[60]. However, this is unlikely to be the only explanation, as previously published data demonstrates that elimination of Cx43 from astrocytes results in elimination of 95% of gap junctions *in vitro*[60]. Perhaps, then, the regions of the brain that receive bilateral innervation are capable of altering signaling patterns in the contralateral eye in ways that consume more resources. There is evidence in humans for CNS control of glaucomatous progression, as the full visual field appears to be preserved by sacrificing regions in one eye and preserving the corresponding regions in the other[352]. Although the mouse visual system is markedly dissimilar from that of humans and a unilateral insult is additionally different from the glaucoma most humans experience, CNS control of degeneration is likely preserved. Perhaps these binocular regions require similar signals from both visual streams, and that would necessitate some remodeling in the contralateral eye that would likely consume energy reserves. One final hypothesis is that perhaps upon losing Cx43 mediated gap junctions astrocytes attempt to compensate by remodeling to a greater extent than would typically occur 1 week after unilateral IOP elevation, thus consuming additional resources. This would depend largely on the mechanism through which those astrocytes that reside in the contralateral stream would sense the stress in the other eye; this should be the next mechanism investigated in this line of work.

Upon establishing that glycogen was mobilized into glucose in both visual streams, we hypothesized that these energy reserves were not merely utilized locally; rather, glucose is drawn from the healthy projection to the actively stressed projection to help maintain RGC function. To test this, we devised an experiment where we elevated IOP unilaterally for one week and then injected ^{18}F-FDG, a radioactive glucose analogue[345], into the contralateral eye. After the mice were awake for one hour to allow for uptake, we imaged for 40 minutes in a PET scanner in static mode. The cumulative amount of radiation detected in the stressed optic nerve, ipsilateral to IOP elevation and contralateral to ^{18}F-FDG injection, was measured and compared between naïve and microbead-injected animals.

In wild-type mice 41% more glucose is transferred between the projections if the contralateral projection has been stressed through IOP elevation. The brain has a remarkable capacity to transport glucose between optic projections quickly when one is damaged. Most PET studies allow 40 minutes for ^{18}F-FDG uptake[58], which means that the transfer itself may have occurred in as few as 20 minutes. The majority of FDG was detected in the injected eye, with a maximum of about 1% of the injected dose making its way into the contralateral eye in the time allotted. A small amount of ^{18}F-FDG was additionally detected above the mouse's shoulder blades; there is a brown fat pad at this location, which would store ^{18}F-FDG that had made its way into the bloodstream from the eye. The majority of metabolites still available for energetic processing within the bloodstream would be absorbed here[345], while the energetically spent byproducts eventually make their way to the bladder.

The most logical avenue for these metabolites to utilize is through the astrocytes within which glycogen resides[93]. These astrocytes already contain the machinery to mobilize and utilize these stores, as well as transfer the metabolites to nearby cells[276]. However, the eye still contains a vascular network equipped with glucose transporters through which FDG could be, and likely is, absorbed into the bloodstream. FDG absorbed in this manner would immediately be diluted in the entire blood flow and need to travel through the majority of the body before making its way to the contralateral eye, as the vasculature within the two eyes is not a dual capillary system[351]. Thus, any ^{18}F-FDG absorbed in this manner would create a pattern of radiation far greater in any fat repositories than in the contralateral eye itself[345], a pattern we did not observe.

Although unlikely, we still investigated whether the blood flow could be responsible for ^{18}F-FDG transport by performing PET experiments on mice that each underwent a unilateral microbead injection to elevate IOP 7 days prior to scanning. The day before PET scans occurred, three mice underwent a unilateral optic nerve transection in the projection contralateral to IOP elevation while an additional three mice underwent a sham surgery. Transection resulted in a statistically significant 61% loss in ^{18}F-FDG transport to the contralateral eye compared to sham values. After the experiment, we determined that the optic nerves were intact at the location of entry for the central retinal artery, and determined that RGCs were still living and functional by injecting each eye with CTB. CTB uptake and transport was detected in RGCs 3 days after transection occurred. From these data, we inferred that glucose transfer must have necessitated an intact optic nerve proper.

We next utilized *GFAP-Cre-ET*^{t2} *x Cx43*$^{flox/flox}$ mice in our PET experiments to determine whether astrocyte connexins were involved in the transport of metabolites between optic projections. We chose to investigate this mechanism as it is the simplest possible pathway through which metabolites can redistribute, the number of gap junctions between astrocytes increases during glaucomatous stress[64], and prior experiments have established the capability for metabolite redistribution through gap junctions[276]. Further, we have already determined that astrocyte-derived energy stores diminish in the contralateral nerve during unilateral glaucomatous stress; therefore, it is likely a simple astrocyte-specific mechanism is involved, rather than a more convoluted mechanism involving other cell types. These cell types may be involved in addition to astrocytes, but astrocytes are the only cells we are certain contain metabolites that mobilize bilaterally after unilateral stress.

KO control mice, or *Cx43*$^{flox/flox}$ mice with tamoxifen administered[36], exhibited glucose redistribution after unilateral IOP elevation similar to that of C57 mice that experienced IOP elevation for the same period of time. From this, we know that tamoxifen itself and the genetic manipulations required to flox Cx43 did not impede glucose transfer between optic projections.

GFAP-Cre-ET^{t2} *x Cx43*$^{flox/flox}$ KO mice, however, exhibit a remarkable 47% reduction in glucose redistribution after IOP elevation compared to this control. We know, therefore, that astrocyte connexins are required for glucose redistribution between optic projections.

Intriguingly, KO mice additionally exhibit a trend toward less glucose redistribution than WT mice even when IOP has not been elevated in either group. In fact, results from KO mice in all conditions more closely resemble transection levels of transport than even those of naïve WT mice. This hints that perhaps the metabolic networks formed through astrocyte gap junctions are important for normal function as well as during early neurodegenerative stress. It is well established that normal neuronal signaling can require nearby astrocytes to mobilize their glycogen stores, especially within the visual system[52,338]. Retinal ganglion cells are particularly energetically demanding neurons; in addition to their extraordinary axonal length, they additionally possess a long unmyelinated portion within the retina and optic nerve head that cannot utilize saltatory conduction to conserve energy and preserve signal strength. In addition to these challenges, the optic nerve is isolated from the rest of the brain, which may result in particularly exaggerated energetic deficits. The optic nerve may rely upon astrocyte connexins to continually replenish glycogen stores from the brain's larger reserves.

Due to the optic nerve's relative isolation, energy transfer between optic projections may have consequences on neuronal function. This should be especially true during further metabolic stress. To determine the functional consequences of energy transfer between optic projections we measured the optic nerve compound action potential (CAP) in bilateral naïve, 1 week unilateral MOM and 2 week unilateral MOM conditions. We additionally probed each group's ability to cope with glucose deprivation by utilizing L-glucose, an enantiomer of table sugar that cannot be digested by mammalian cells[339]; further, we determined the ability to recover from this stress by replacing L-glucose with D-glucose, the typically occurring form.

Counterintuitively, nerves directly exposed to 1 week of elevated IOP exhibited the same response to glucose deprivation and recovery as nerves from bilateral naïve mice. However, the nerve contralateral to 1 week of elevated IOP did not exhibit as strong a signal. In fact, the contralateral nerve exhibited a diminished signal compared to the ipsilateral nerve at every time point beyond baseline, and that diminishment was significant at 17/20 time points measured. Thus, one week of IOP elevation results in a reduced ability for the contralateral nerve to cope with further metabolic stress. However, the ipsilateral nerve does not appear to be impacted by further metabolic stress. Perhaps this nerve has sufficient glycogen stores to survive the stressor, or has compensated in other ways for continuous metabolic stress.

Two weeks of IOP elevation, however, appear to impact both nerves' ability to cope with further glucose deprivation. For every time point from 5 minutes post glucose depletion and beyond, both the 2-week MOM nerves and the nerves contralateral to them were significantly reduced from naïve values. It appeared that contralateral nerves did not fare as well during recovery, but this trend did not reach significance at any time point. The bilateral weakness to metabolic stress after unilateral IOP elevation at only 2 weeks following induction speaks to the remarkable magnitude of this effect, and the isolation the optic nerve experiences.

We next examined how our conditional Cx43 knockout would respond to the same experimental paradigm. We hypothesized that metabolically isolating each nerve from the reserves of the other might rescue the weakness to metabolic stress in the contralateral nerve; this might, however, occur at the detriment of the initially stressed projection. Intriguingly, naïve KO nerve did not statistically differ from naïve C57 nerves at any point throughout baseline, glucose depletion, or recovery measurements. Whatever impact metabolic isolation has on these nerves does not appear to influence the normal functional ability of these projections without a neurodegenerative stressor present. This is particularly intriguing after our PET experiments, but the normal glycogen reserves did not appear to differ between *GFAP-Cre-ET*^{t2} *x Cx43*$^{flox/flox}$ mice, KO control mice, and C57/BL6 mice. Perhaps this is all that is necessary to maintain normal signaling without a neurodegenerative stressor present; or, perhaps, a more stringent test of signaling ability would reveal more deficits in the KO nerves. We were only evoking a signal once every 5 minutes after our initial calibration. Other studies evoke a signal as frequently as every 30 seconds[7,87,96]. This would be particularly interesting to look at in our KO mice, and should be investigated in future studies.

As hypothesized, KO nerves directly exposed to 1 week of IOP elevation exhibited a diminished response compared to corresponding C57 nerves. Surprisingly, this only occurred for the 5 minutes immediately following the initiation of glucose depletion, while the remainder of the timecourse closely resembled the C57 response. Even more remarkably, KO nerves contralateral to 1 week of IOP elevation exhibited elevated CAP area compared to corresponding C57 nerves at every time point from glucose depletion onward, and did not differ from the naïve KO response at any time point. Apparently, at 1 week of unilateral IOP elevation, Cx43 KO rescues the contralateral signaling deficit in response to glucose depletion. This does occur at the detriment of the MOM nerve's signaling ability early in glucose deprivation. *In vivo*, a depletion of glucose for any longer than 5 minutes would likely be the result of an acute ischemic event and beyond the scope of normal degeneration[129,353,354], so perhaps this inability to cope with glucose deprivation at these early time points would have a greater impact on the intact system.

It might, additionally, correspond with an inability to mobilize glycogen stores due to their previous depletion. The signaling pattern at these early time points likely reflects the glycogen stores available to be mobilized in response to glucose depletion. This should be tested in future experiments; if an inhibitor of glycogen polymerase[96] were added to the bath at the moment it switched to L-glucose containing aCSF, the contribution of glycogen stores to each point in the timecourse could then be determined.

Although these CAP results occurred as we hypothesized, the extent to which the ipsilateral optic nerve was impacted by its metabolic isolation did not appear to be balanced by the degree of rescue in the contralateral nerve. In fact, the rescue in the contralateral nerve far surpassed the signaling deficit in the ipsilateral nerve. This led us to hypothesize (and investigate in the following chapter) that perhaps inhibition of Cx43 might be an intriguing way to preserve function in the contralateral projection. However, this was not the case; visual function in the contralateral projection was preserved at 1 week regardless of Cx43 KO, but the ipsilateral projection exhibited far greater loss of function due to KO. Further, if the contralateral eye then experienced IOP elevation 1 week following the initial ipsilateral stressor, visual function in this contralateral stream in KO mice only surpassed that of WT mice 2 days following induction. This underlies the critical importance of these metabolic networks to preservation of neuronal function during neurodegeneration, and is explored in greater detail in Chapter 4.

CHAPTER 4

GLUCOSE REDISTRIBUTION THROUGH THE OPTIC PROJECTION ENDOGENOUSLY PROTECTS STRESSED AXONS BUT RENDERS DONATING TISSUE VULNERABLE TO ADDITIONAL STRESS

If you go on with this nuclear arms race, all you are going to do is make
the rubble bounce.

Winston Churchill

4.1 INTRODUCTION

In glaucomatous optic neuropathy, as in many neurodegenerative diseases, a growing body of evidence supports the idea that the stressed region does not degenerate independently[46,353]. Many glaucoma patients present with a "jigsaw" pattern of visual field maintenance between the two eyes[352], meaning that regions of the visual field that degenerate in one eye appear to actively be preserved in the contralateral retina. This finding has resulted in a prevailing hypothesis that the central nervous system is deeply involved, and perhaps even dictates, the patterns of degeneration that occur after a neurodegenerative stressor is applied.

Indeed, chronic neurodegenerative stress is not a focal problem for long. In Alzheimer's disease, although the earliest impacted regions are the olfactory bulbs[355,356] and hippocampus[357], the disease eventually spreads throughout the central nervous system and impacts nearly every region of the brain[204]. The pattern is so repeatable that many scientists now examine neurodegenerative disease through network spread models, envisioning a focal disturbance that spreads throughout the regions most related to those initially impacted as the disease continually invades new regions of the brain[358]. Many even hypothesize that the connectivity of the brain, although critical for its function, can propagate “disease factors” rapidly between regions.

However, the interconnectivity of the brain may also allow beneficial factors, such as the glucose needed to sustain neuronal repair and function, to be quickly transmitted through the brain and rescue a stressed region[276]. We demonstrated this in chapter 3, as have other scientists in different model systems. The rapid transport of growth factors[250,307] as well as metabolites[276] between cells and regions of the brain are critical in maintaining neuronal function during stress. This is especially true during early phases of neurodegeneration, when neurons increase their rate of energy consumption[131,141]. The immune response, too, appears to activate throughout multiple interconnected regions of the CNS even during a focal event[262].

Neurodegenerative stress in the real world is unlikely to be an isolated event. Astrocyte-derived resources increase neuronal survival, but the extent to which the redistribution of resources from healthy to degenerating tissue can influence the brain’s ability to resist further neurodegenerative stress is unknown. Here, we investigated how glucose redistribution through the optic projection can endogenously protect stressed axons and preserve visual function in the damaged eye; however, this also renders donating tissue vulnerable to additional stress. We utilize a staggered paradigm of IOP elevation and conditional gap junction knockout mice to induce a series of neurodegenerative stressors and test this hypothesis.

4.2 MATERIALS AND METHODS

4.2.1 INDUCTION OF OCULAR HYPERTENSION BY MICROBEAD OCCLUSION IN STAGGERED AND BILATERAL PARADIGMS

Intraocular pressure was acutely elevated[252] in 2-month-old male and female C57, *GFAP-Cre-ER*^{t2} *x Cx43*$^{flox/flox}$, and *Cx43*$^{flox/flox}$ mice (see sections 3.2.1 – 3.2.3) as described in section 3.2.4. Briefly, prior to injections, mice were anesthetized with isoflurane (Minrad Inc., Bethlehem, PA) and efficacy of anesthesia was evaluated by gentle pinching of the tail and paw. Eyedrops containing 1% tropicamide were applied to dilate the iris, and eyedrops containing 0.5% proparacaine were applied as a local anesthetic. The proparacaine drops were applied as necessary to maintain eye moisture and provide pre- and post-operative analgesia. Drops of antibiotic tobramycin ophthalmic solution (0.3%, Akorn) were also applied prior to the injection to counter infection.

Microbeads were injected using a standard microinjection setup (World Precision Instruments) consisting of a microsyringe pump and micromanipulator. A borosilicate microneedle pulled to a final diameter of 100µm was attached to a syringe filled with mineral oil to prevent backflow of injected solution. The needle tip was sterilized with 100% EtOH before drawing sterile PBS through the needle and finally a solution of PBS containing inert polystyrene microbeads (15µm diameter, 1 x 10^6 microbeads/ml solution, 1.5 µl injected per eye; Life Technologies, Carlsbad, CA). Microbeads were injected unilaterally into the anterior chamber of one eye. In bilateral paradigms, the contralateral eye was injected with beads as well. Following the procedure, additional numbing drops containing 0.5% proparacaine were applied. In staggered paradigms, the contralateral eye was injected 1 week following the initial injection using the same procedure.

Intraocular pressure (IOP) was measured in anesthetized (2.5% isoflurane) mice using TonoPen XL (Medtronic Solan, Jacksonville, FL) rebound tonometry as previously described[235,252]. An IOP measurement was determined as the mean of 15 readings. IOPs were measured for 2 days prior to microbead procedures to determine a baseline value and twice weekly until the experimental endpoint. In staggered paradigms, IOPs were additionally obtained the day immediately prior to and the day immediately following the second injection of beads to ensure rapid IOP elevation.

4.2.2 TRACING ANTEROGRADE AXONAL TRANSPORT

Anterograde axonal transport function was determined as described in section 2.2.4; briefly, forty-eight hours prior to perfusion, animals were anesthetized with 2.5% isoflurane and bilaterally injected intravitreally with 2µl of 0.5mg cholera toxin subunit B (CTB) conjugated to Alexa Fluor 488 (Invitrogen) as previously described[153,315]. Two days post-injection, animals were transcardially perfused with PBS followed by 4% paraformaldehyde in PBS. Each retina was checked to ensure a quality injection, and any retina without detectable CTB excluded the corresponding projection from the study. Brains were cryoprotected in 30% sucrose/PBS overnight, and 50µm coronal midbrain sections were cut on a freezing sliding microtome. Serial superior colliculus sections were imaged using a Nikon Eclipse TI microscope (Nikon Instruments) and the intensity of the fluorescent CTB signal was quantified using ImagePro custom routines (Media Cybernetics) as previously described[153,256]. CTB signal was normalized to background and alternating sections were analyzed for intensity. Intensity from each section was calculated to reconstruct a retinotopic map of intact anterograde transport across the superior colliculus. Intact transport for each map was defined as any region with an intensity ≥70% of the maximum CTB signal for that tissue.

4.2.3 GLYCOGEN ASSAY

Glycogen content was determined as in section 3.2.5; briefly, we modified an assay developed by Abcam (ab65620). Unanesthetized mice were sacrificed via cervical dislocation and beheading. Both optic nerves were dissected within one minute of sacrifice, alternating the nerve dissected first to control for postmortem metabolism. Tissues were immediately placed in 5 ml tubes containing a solution of ice-cold 85% ethanol/15% 30mM HCl[87] to halt metabolism. The nerves in the ethanol/HCl solution were gradually warmed to room temperature and the tissue was agitated gently for several hours to permit egress of all glucose (glucose is soluble in this solution, but glycogen is not). Nerves were then washed in 1X PBS 3 times for 5 minutes each. Using a paintbrush, nerves were then carefully transferred into 150 µl molecular grade water in a 1.5 ml microcentrifuge tube and placed on ice. Each sample was then ground using a pestle and immediately placed in an 95°C dry bath for 10 minutes to denature any remaining functional enzymes, then transferred immediately back to ice.

Using a NanoDrop 8000 (Thermo Scientific, Wilmington, DE) an A280 protein analysis was performed 3x on each sample, and the average value was determined to normalize to the amount of nerve obtained. From this point, Abcam’s fluorescent protocol was utilized. Briefly, samples and a standard curve were pipetted into a 96 well plate. A hydrolysis enzyme mix (mainly glucoamylases) was added to each well apart from glucose background control wells, and the plate was incubated with gentle agitation for 30 minutes at room temperature. A reaction mix containing the OxiRed probe and a development enzyme mix was added to each well and the plate was incubated again with gentle agitation for 30 minutes at room temperature while protected from light. The plate was immediately analyzed using a SpectraMax M2 Microplate Reader (Molecular Devices, San Jose, CA) to determine fluorescence (Ex 535/ Em 587) to detect the amount of hydrolyzed glycogen. The assay detects glycogen 0.0004 – 2 mg/ml, which is sensitive enough to assay a single mouse optic nerve in duplicate.

4.2.4 PSYCHOPHYSICAL VISUAL TESTING: OPTOMOTOR RESPONSE

The optomotor response (OMR) is a naturally occurring reflex that serves as a functional tool for quantitative analyses of visual system function in mice[359,360]. This reflex is evoked when a mouse can detect movement from the periphery to the central visual field; due to the minimal overlap of the two eyes' visual fields in mice, this allows for independent analysis of visual function in each eye in freely moving, awake, behaving mice.

Each mouse was placed on a platform surrounded by four LCD computer monitors. A sinusoidal grating of alternating white and black bars at 100% contrast rotating in either a clock-wise or counter clock-wise fashion was projected on all monitors. Mice able to perceive the moving stimulus produced a reflexive movement of the head in the direction of the stimulus. The visual acuity of each mouse was measured by altering the spatial frequency projected. The visual acuity threshold was determined as the highest spatial frequency for which reflexive tracking was noted. The presence of the reflexive head movement was recorded by an observer using a camera mounted above the mouse. Mice were tested for each eye's baseline acuity threshold three times in the week preceding any IOP elevation, and twice a week until CTB injection or the experimental endpoint.

4.2.5 STATISTICAL ANALYSIS

Data for are presented as mean ± standard error of the mean (SEM) for each treatment. Statistical analysis and p-values for comparing means were obtained using Kruskal-Wallis one-way ANOVA or two-sided t-tests for all data that met criteria for normality as confirmed using the Shapiro-Wilk normality test. For data that did not pass Shapiro-Wilk normality, non-parametric Mann-Whitney Rank Sum tests were used. Statistical tests were considered significant if $p < 0.05$. All statistical tests were performed with SigmaPlot 12.5 (Systat Software Inc., San Jose, CA). Numbers of samples and measurements along with actual *p* values of significance are indicated where appropriate in the text or figure legends.

4.3 RESULTS

4.3.1 IOP ELEVATION IN THE STAGGERED PARADIGM

The following experiments utilized a staggered paradigm of IOP elevation, with two cohorts of unilaterally elevated mice serving as controls. Mice were aged normally until 8 weeks, when a set of three tamoxifen gavages was used to induce Cx43 KO with corn oil gavages serving as control (see section 3.2.3). One week following gavage, IOP was elevated unilaterally. After an additional week, our 1-week unilateral cohort was sacrificed, while our 2-1 staggered cohort received unilateral microbead injections in the contralateral eye. After a final week, both the 2 week unilateral and 2-1 staggered cohorts were sacrificed (Figure 4.1A). IOP was significantly elevated above baseline and above contralateral naïve eyes in all conditions (p<0.001, Figures 4.1B,C,D). Two days prior to sacrifice, CTB conjugated to alexa fluor 488 was bilaterally injected intravitreally.

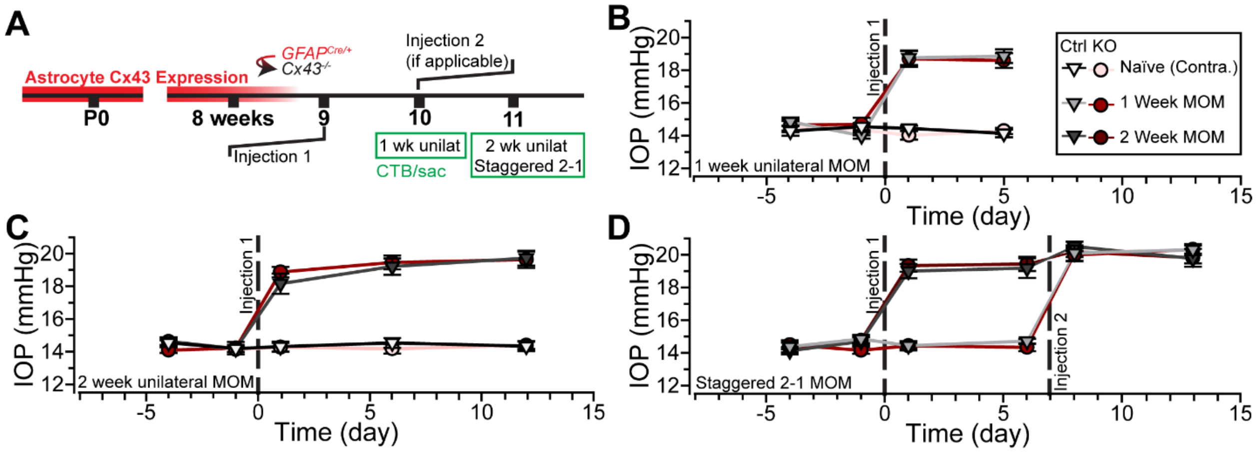

Figure 4.1 Microbead injection elevated IOP in staggered and control mice.

A. All mice were aged to 8 weeks, when the KO was induced. IOP was unilaterally elevated via intracameral injection of microbeads on week 9 in all cohorts. In the staggered cohort, a second microbead injection was performed on week 10 in the contralalteral eye. In all cohorts, CTB was intravitreally injected two days prior to sacrifice. The 1 week unilateral group was sacrificed on week 10, while the 2 week unilateral and staggered groups were sacrificed on week 11. IOP was significantly elevated unilaterally in microbead (Δ) compared to contralateral (o) eyes in the 1 week unilateral (**B**, p<0.001), 2 week unilateral (**C**, p<0.001), and staggered 2-1 (**D**, p<0.001) cohorts after all microbead injections.

4.3.2 GLYCOGEN DOES NOT REDISTRIBUTE AFTER STAGGERED IOP ELEVATION

Earlier, we established that glycogen diminishes in optic nerves bilaterally after unilateral IOP elevation, and that glycogen levels are particularly low in the optic nerve contralateral to the elevation 1 and two weeks after IOP elevation is induced (see Figure 3.7).

Here, we aimed to examine the impact a second contralateral elevation would have on glycogen distribution between the optic nerves in WT mice.

Naïve, unilateral 2 week, and unilateral 1 week results reflected the patterns we determined previously (Figure 4.2). Both 1 and 2 weeks of unilateral IOP elevation resulted in bilaterally diminished glycogen stores compared to naïve levels (naïve 9.19 ± 0.64 µg/mg protein; 1 week 7.08 ± 0.69, contralateral 5.00 ± 0.21; 2 week 6.75 ± 0.36, contralateral 4.81 ± 0.23; p = 0.028, 0.0002, 0.010, 0.0002). Further, in both 1 and 2 week unilateral conditions

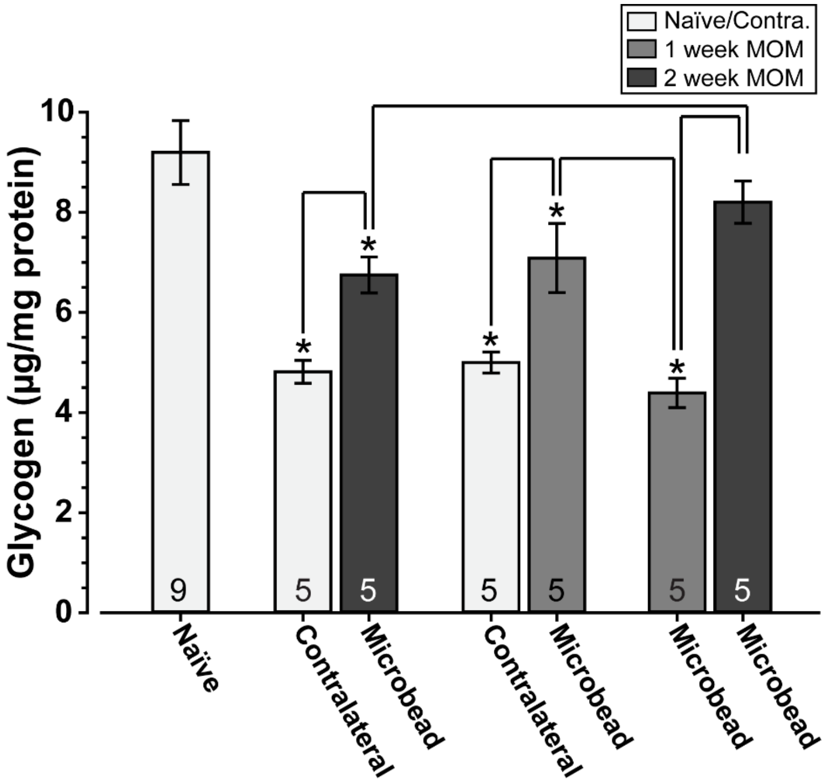

Figure 4.2 Staggered IOP elevation does not cause glycogen to redistributed to newly injured tissue.

Both 1 and 2 weeks of unilateral IOP elevation resulted in bilaterally diminished glycogen stores compared to naïve levels (*), with contralateral nerves exhibiting less glycogen than nerves ipsilateral to IOP elevation (p<0.05). In the staggered 2-1 paradigm, only the nerve exposed to 1 week of IOP elevation contained less glycogen than bilateral naïve nerves. The staggered 1 week group additionally contained significantly less glycogen than the staggered 2 week group (p<0.05), as well as significantly less than the unilateral 1 week nerves. Further, nerves in the staggered paradigm exposed to 2 weeks of IOP elevation contained significantly more glycogen than their unilateral counterparts (p<0.05).

contralateral nerves contained diminished glycogen compared to nerves ipsilateral to IOP elevation (p = 0.048, 0.0006).

Intriguingly, in mice that underwent the staggered paradigm of IOP elevation only the nerves exposed to 1 week of IOP contained glycogen significantly diminished from naïve levels (4.39 ± 0.29; $p < 0.001$). The nerves exposed to a full 2 weeks of IOP elevation exhibited glycogen levels that were not significantly different from those from naïve mice (8.20 ± 0.42; p = 0.15). Further, nerves in the staggered paradigm exposed to 1 week of IOP elevation contained significantly less glycogen than unilateral 1 week nerves (p = 0.004), and the nerves in the staggered paradigm exposed to two weeks of elevation contained significantly more glycogen than unilateral 2 week nerves (p = 0.015). This demonstrates that contralateral glycogen stores are not replaced after contralateral IOP elevation; rather, it appears contralateral IOP elevation exaggerates the disparity of energy stores between the nerves.

4.3.3 ANTEROGRADE AXONAL TRANSPORT FUNCTION IS DIFFERENTIALLY IMPACTED IN KO AND CONTROL MICE EXPOSED TO STAGGERED IOP ELEVATION

Anterograde axonal transport function was assessed in three different cohorts of mice, all of whom received bilateral intravitreal injections of CTB conjugated to alexa fluor 488 two days prior to perfusion. The first cohort had unilaterally elevated IOP for one week, the second for two weeks, and the third for two weeks in one eye and one week in the contralateral eye (Figure 4.3). One week of unilateral IOP elevation did not significantly reduce anterograde transport function in control mice (Figure 4.4; microbead 77.9 ± 7.8% topography density vs contralateral 82.0 ± 7.2%; p=0.35). In *GFAP-Cre-ER*^{t2} *x Cx43*$^{flox/flox}$ knockout mice, one week of unilateral IOP elevation reduced anterograde transport function by a remarkable 40.9% in the stressed optic projections (50.6 ± 10.9%), a significant reduction both from the contralateral naïve projections (91.5 ± 3.6%; p=0.002) and corresponding control projections (p=0.029).

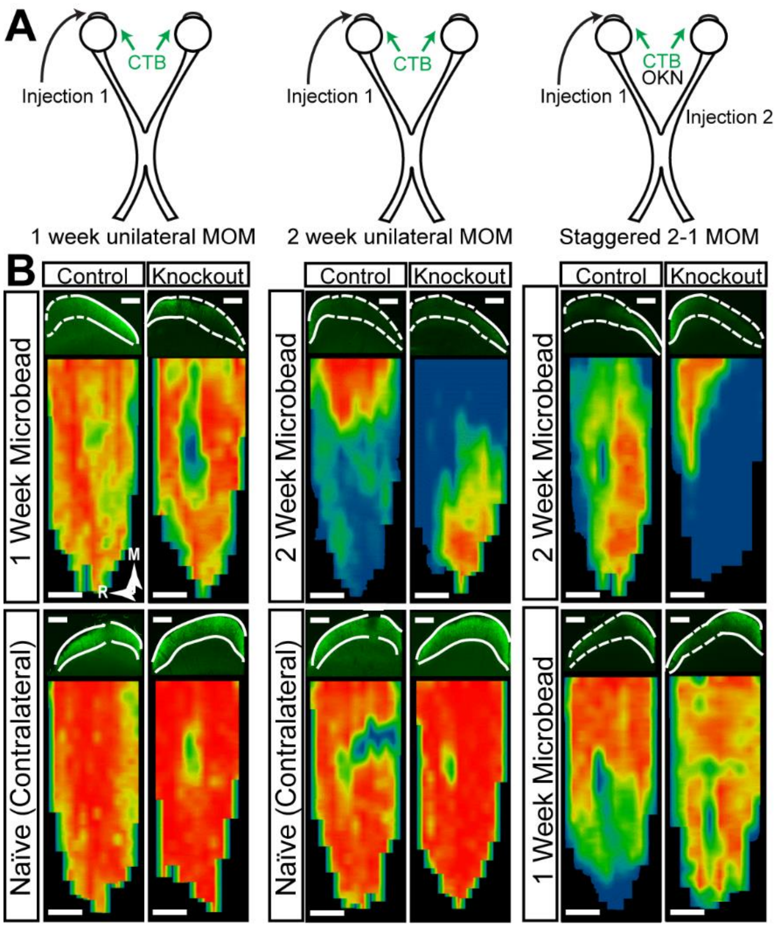

Figure 4.3 Representation of anterograde transport function in each elevation paradigm.

A. Diagrams of the three experimental paradigms to elevate IOP. 1 week and 2 week unilateral MOM groups received a single injection in one eye, and CTB two days prior to sacrifice. Staggered 2-1 MOM involved a unilateral IOP elevation in one eye followed by a contralateral IOP elevation one week later. This group additionally received CTB two days prior to sacrifice, but were additionally utilized for OKT experiments. **B.** Representative images for each optic projection. For each projection, the top image is a coronal section through the superior colliculus (SC; white outline) demonstrating intact (solid lines) and insufficient (dashed lines) anterograde transport function. The bottom image is a retinotopic map reconstructed from serial sections of SC. Density of signal from transported CTB ranges from 0% (blue) to 50% (green) to 100% (red). Medial (M) and rostral (R) orientations indicated.

Two weeks of unilaterally elevated IOP resulted in a statistically significant 24.3% loss in anterograde transport function between microbead and naïve optic projections in control mice (87.9 ± 5.3% vs 63.6 ± 9.4%; p=0.020). *GFAP-Cre-ER*^{t2} *x Cx43*$^{flox/flox}$ knockout mice exhibited more severe pathology; two weeks of elevated IOP caused a 45.6% loss in anterograde transport function compared to the contralateral naïve projections (92.8 ± 1.9% vs 47.2 ± 9.1%; p<0.001). This loss was greater than the loss exhibited by control mice, although the difference did not reach statistical significance (45.6 ± 8.9% vs 24.3 ± 8.1%; p=0.052).

The 2-1 staggered paradigm produced intriguing results in both control and KO mice. In control mice, the 2 week and 1 week projections both exhibited roughly 50% intact transport (1 week 50.3 ± 8.4%, 2 week 47.6 ± 8.2%; p=0.411). Remarkably, despite the fact that one eye was exposed to elevated IOP for double the length of time, the two projections do not exhibit a significant difference in transport ability between one another. However, the projections exposed to 1 week of elevated IOP demonstrate significantly diminished anterograde transport function compared to the corresponding unilaterally injected 1 week control projections (50.3 ± 8.4% vs 77.9 ± 7.8%; p=0.016). This demonstrates the impact localized neurodegeneration can have on nearby regions; certainly, the degenerative program was accelerated because the contralateral eye had already been exposed to stress.

The same staggered paradigm in KO mice, however, did result in a statistically significant difference in anterograde transport function between the two projections (1 week 51.1 ± 7.3% vs 2 week 31.7 ± 7.8%; p=0.0427). The KO projections exposed to 1 week of elevation in the staggered paradigm demonstrated a nearly identical percentage of intact anterograde transport to the unilateral KO 1 week exposed projections (51.1 ± 7.3% vs 50.6 ± 10.9%). Further, transport ability between the KO projections exposed to 2 weeks of elevation in the staggered paradigm and the unilateral KO 2 week projections was not statistically significant (31.7 ± 7.8% vs 47.2 ± 9.1%; p=0.106). However, the trend toward increased transport loss in the 2-1 paradigm may reveal other mechanisms involved in regulating degeneration between the two optic tracts.

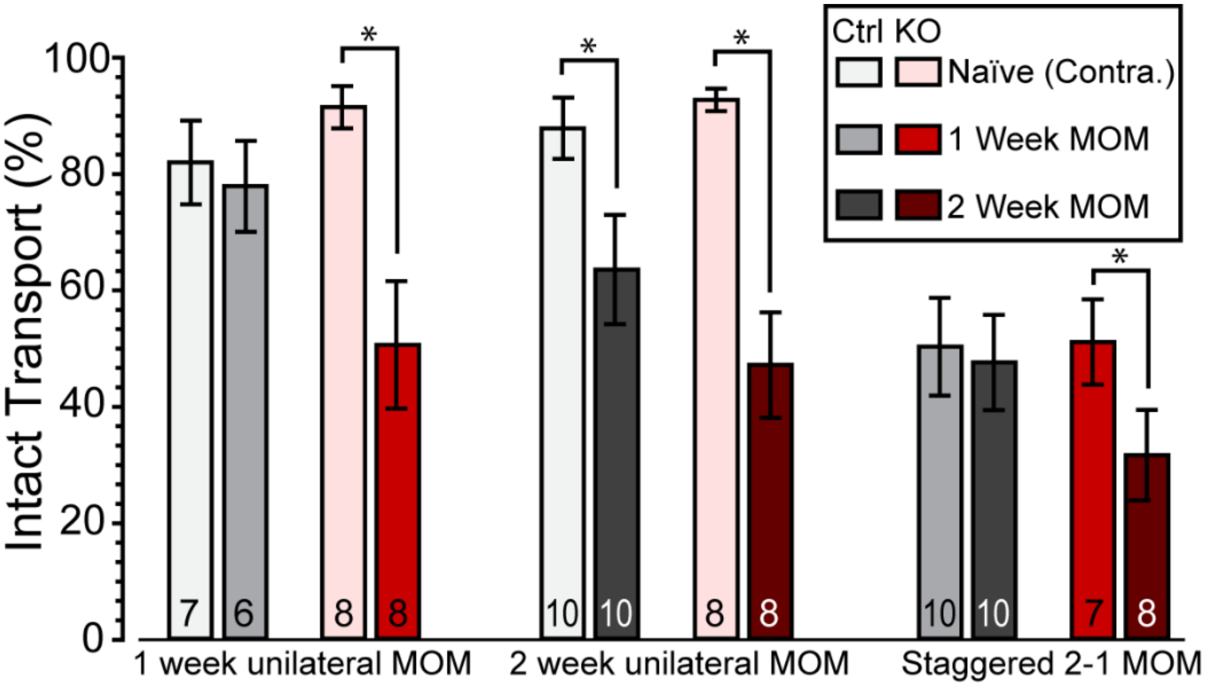

Figure 4.4 KO mice exhibit greater deficits in anterograde transport function after staggered IOP elevation.

One week of unilateral IOP elevation (left bars) did not significantly reduce anterograde transport function vs the contralateral projections in control mice (82.0 ± 7.2% vs 77.9 ± 7.8%; p=0.35); it did reduce function in KO mice (91.5 ± 3.6% vs 50.6 ± 10.9%) significantly both versus the contralateral projections (p=0.002) and the corresponding control projections (p=0.029). Two weeks of unilaterally elevated IOP (middle bars) resulted in a significant loss in anterograde transport function in control (87.9 ± 5.3% vs 63.6 ± 9.4%; p=0.020) and KO mice (92.8 ± 1.9% vs 47.2 ± 9.1%; p<0.001). Staggered 2-1 IOP elevation (right bars) resulted in roughly 50% intact transport in both the 2 and 1 week exposed projections in control mice (1 week 50.3 ± 8.4%, 2 week 47.6 ± 8.2%; p=0.411). The 1 week projections in the staggered paradigm exhibited significantly reduced transport function compared to the 1 week projections in the unilateral paradigm (50.3 ± 8.4% vs 77.9 ± 7.8%; p=0.016). In KO mice, the staggered paradigm resulted in significantly diminished transport in the 2 week compared to the 1 week projections (31.7 ± 7.8% vs 51.1 ± 7.3%; p=0.0427). KO projections exposed to 1 week of elevation in the staggered paradigm and in the unilateral paradigm both exhibited about 51% intact transport function (51.1 ± 7.3% vs 50.6 ± 10.9%), and the corresponding 2 week projections did not show a significant difference (31.7 ± 7.8% vs 47.2 ± 9.1%; p=0.106).

4.3.4 VISUAL FUNCTION IS DIFFERENTIALLY IMPACTED IN KO AND CONTROL MICE EXPOSED TO STAGGERED IOP ELEVATION

Visual function was assessed via optomotor response in the staggered 2-1 cohort in section 4.3.3 for anterograde transport function (Figure 4.5). Mice in both the control and KO cohort were initially tested and trained during three baseline measurements the week prior to any IOP elevation with no significant differences between groups or time points detected. On day 0, IOP was unilaterally elevated in all mice. OKT assessed 2 days following initial IOP elevation did not detect any differences amongst groups or between these measurements and the average baseline measurements for each group. From this result, we know that microbead injection does not impact visual function.

Six days following IOP elevation we detected diminished visual function in stressed visual streams compared to contralateral visual streams in both control and KO mice; however, visual function loss was exaggerated in KO mice. Control mice exhibited a loss of about 0.05 cycles/degree from both baseline and contralateral values (baseline 0.508 ± 0.011; 6 day contralateral 0.498 ± 0.008; 6 day MOM 0.449 ± 0.011; $p<0.001$, $p<0.001$). KO mice exhibited a loss of a full 0.11 cycles/degree from respective baseline and contralateral values (baseline 0.497 ± 0.007; 6 day contralateral 0.498 ± 0.008; 6 day MOM 0.387 ± 0.10). After 6 days of IOP elevation, knockouts exhibited a significantly lower value than the control outcome ($p<0.001$), demonstrating the impact of astrocyte connexins on visual function maintenance during neurodegenerative stress.

On day 7, the contralateral eye was injected with microbeads in all mice. Two days following this second microbead injection, control mice exhibited moderate visual function loss in both visual streams compared to respective baseline values (day 9 MOM 0.432 ± 0.007 vs baseline 0.508 ± 0.011; contralateral day 2 MOM 0.456 ± 0.006 vs baseline 0.505 ± 0.011; $p<0.001$, $p<0.001$). The previously stressed visual stream still exhibited significantly greater visual acuity loss than its contralateral partner that had been stressed for 7 fewer days ($p=0.007$); however, this gap in visual acuity loss is rapidly closing. In knockout mice, the previously stressed visual stream continued to rapidly decline in visual acuity compared to baseline (day 9 MOM 0.345 ± 0.011 vs baseline 0.497 ± 0.007; $p<0.001$), a significant change from the levels exhibited on day 6 ($p=0.008$). Intriguingly, the newly stressed visual stream did not exhibit any alteration from baseline values (contralateral day 2 MOM 0.502 ± 0.016 vs baseline 0.497 ± 0.010; $p=0.409$). This stream exhibits significantly elevated visual acuity levels compared to the control contralateral 2 day nerve ($p=0.009$). For this brief period of time after the second IOP elevation, it appears that the contralateral nerve is protected from immediate visual acuity loss in KO mice.

However, the contralateral nerve is only protected transiently. Thirteen days after the first IOP elevation and 6 days after the second, control visual streams do not exhibit any differences in functional visual acuity from one another (day 13 MOM 0.407 ± 0.013 vs contralateral day 6 MOM 0.398 ± 0.010; $p=0.331$), but both are diminished from their respective baseline values ($p<0.001$, $p<0.001$). This likely reflects the loss of glycogen initially from the contralateral visual stream; the contralateral stream now progresses through the degenerative program more quickly. However, KO no longer protects against visual acuity loss in the contralateral stream while the initially stressed stream continues to rapidly decline. Thirteen days after the initial injection, the initially stressed KO visual stream has diminished nearly 0.2 cycles per degree from baseline levels, a 39% loss in visual function over a mere two

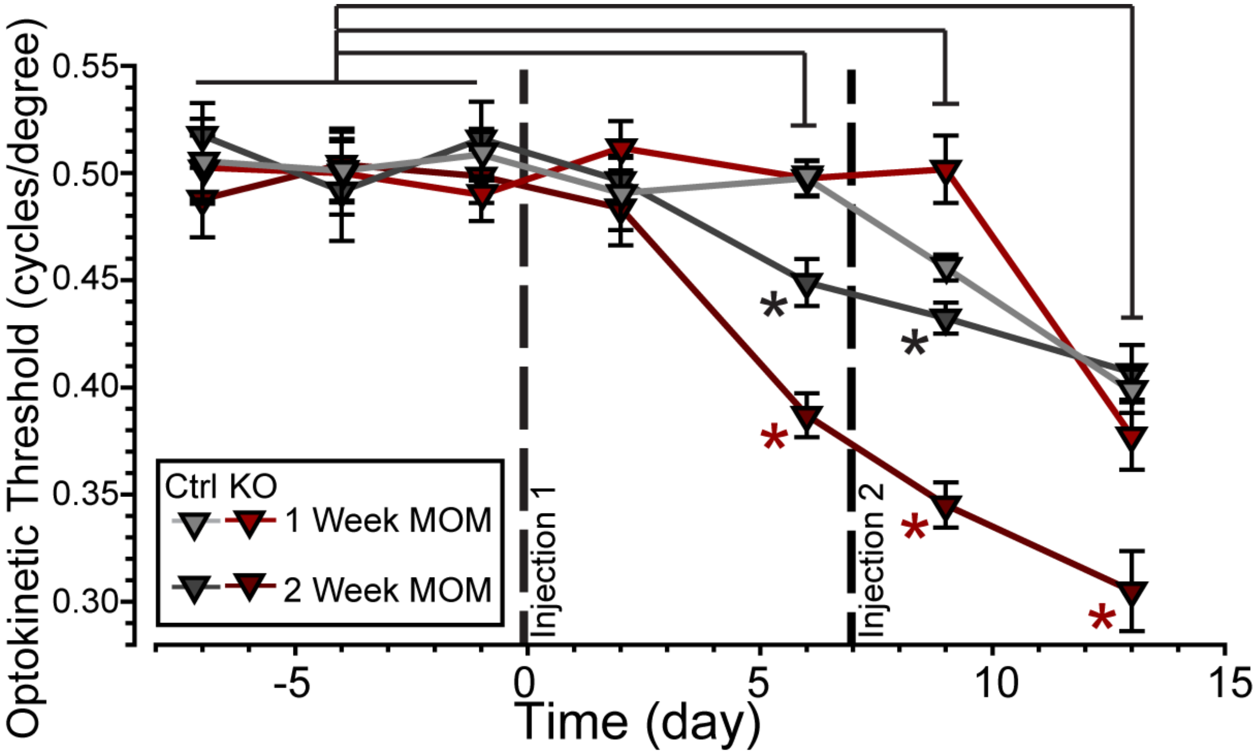

Figure 4.5 Visual function is differentially impacted in KO and control mice exposed to staggered IOP elevation.

Control (n = 10) and KO (n = 8) mice did not exhibit any differences in visual acuity during three baseline measurements (days -7, -4, and -1). On day 2 no group was significantly different from any other or from respective baseline levels. By day 6, visual acuity had diminished compared to baseline and contralateral levels in both control ((baseline 0.508 ± 0.011; 6 day contralateral 0.498 ± 0.008; 6 day MOM 0.449 ± 0.011; p<0.001, p<0.001) and KO mice (baseline 0.497 ± 0.007; 6 day contralateral 0.498 ± 0.008; 6 day MOM 0.387 ± 0.10). In stressed visual streams, KO mice exhibited visual acuity levels significantly below those of control mice (p<0.001). Two days following the second (contralateral) injection (day 9), visual acuity significantly diminished compared to baseline in both control visual streams (day 9 MOM 0.432 ± 0.007 vs baseline 0.508 ± 0.011; contralateral day 2 MOM 0.456 ± 0.006 vs baseline 0.505 ± 0.011; p<0.001, p<0.001). The previously stressed visual stream was still significantly more impacted compared to the newly stressed contralateral stream (p=0.007). In KO mice, the previously stressed visual stream continued to rapidly decline (day 9 MOM 0.345 ± 0.011; p=0.008 vs day 6, p<0.001 vs baseline) while the contralateral stream did not exhibit any significant change compared to any previous value (contralateral day 2 MOM 0.502 ± 0.016). On day 13, control visual streams are no longer significantly different from one another (day 13 MOM 0.407 ± 0.013 vs contralateral day 6 MOM 0.398 ± 0.010; p=0.331), but both are diminished from their respective baseline values (p<0.001, p<0.001). In KO mice, the initially stressed stream exhibits a significant loss compared both to baseline and day 9 (day 13 MOM 0.305 ± 0.019; p<0.001, p=0.032). The contralateral stream now exhibits a significant loss compared to baseline as well (contralateral day 6 MOM 0.377 ± 0.016 vs baseline 0.497 ± 0.010; p<0.001) weeks (day 13 MOM 0.305 ± 0.019 vs baseline 0.497 ± 0.007; p<0.001) and a significant loss from day 9 (p=0.032). This is a significantly greater loss compared to baseline than that exhibited by respective control visual streams (p<0.001). At this time point, the contralateral KO stream has now lost 25% of its visual acuity (contralateral day 6 MOM 0.377 ± 0.016 vs baseline 0.497 ± 0.010; p<0.001) and is no longer significantly different from the respective control visual stream (p=0.146). Thus, although KO protected the contralateral optic nerve transiently, this occurred at the detriment of the initially stressed stream and did not exhibit any long-lasting effects. Presumably, as the contralateral stream at 6 days post injection exhibited nearly the same level of visual acuity as the ipsilateral stream at 6 days post injection, visual function in both streams would continue to rapidly decline at a much greater rate than in control mice.

4.4 DISCUSSION

The neurodegenerative stressors one encounters in the world are not isolated, but most often an isolated stressor is the clearest to study. Once we established how the interconnectivity of the brain contributes to the broad impact of neurodegeneration, we then needed to establish how this paradigm would impact an individual impacted by multiple stressors. If resources are drawn away from one region of the brain to support another, does that then render the originating tissue vulnerable?

We utilized multiple paradigms of IOP elevation to assess this hypothesis. We compared mice with unilaterally elevated IOP 1 and 2 weeks after the stressor was induced to mice that underwent a sequence of injections. The first injection elevated IOP unilaterally; after a week, the contralateral eye was injected to elevate its IOP as well. Although the initially injected eye experienced IOP elevation for twice the period of time, the eye injected second was often impacted to the same degree or worse in many of our outcome measures.

We preliminarily examined glycogen distribution in C57 mice to determine whether the pattern of energetic distribution we previously noted was repeated in this experiment. Naïve, unilateral 2 week, and unilateral 1-week results reflected the patterns we determined previously (Figure 4.2). Both 1 and 2 weeks of unilateral IOP elevation resulted in bilaterally diminished glycogen stores compared to naïve levels ($p<0.05$). Further, in both conditions contralateral nerves contained diminished glycogen compared to nerves ipsilateral to IOP elevation ($p<0.05$).

Intriguingly, in mice that underwent the staggered paradigm of IOP elevation only the nerves exposed to 1 week of IOP contained glycogen significantly diminished from naïve levels. The nerves exposed to a full 2 weeks of IOP elevation exhibited glycogen levels that were not significantly different from those from naïve mice. Further, nerves in the staggered paradigm exposed to 1 week of IOP elevation contained significantly less glycogen than unilateral 1 week nerves, and the nerves in the staggered paradigm exposed to 2 weeks of elevation contained significantly more glycogen than unilateral 2 week nerves. This demonstrates that contralateral glycogen stores are not replaced after contralateral IOP elevation; rather, it appears contralateral IOP elevation exaggerates the disparity of energy stores between the nerves. Perhaps any glycogen mobilized by the second IOP elevation would continue moving along the concentration gradient established by the first injection. The exact mechanism of this exaggerated disparity in energy stores should be investigated in future studies. For our purposes, we continued to see diminished glycogen levels in the eye contralateral to the initial elevation.

For the remainder of these experiments, we utilized KO and KO control mice to address directly how astrocyte connexins serve to maintain or diminish neuronal function in each paradigm. One established measure of axonal health is anterograde transport function. Neurons utilize different machinery to transport molecules anterograde or retrograde at differing speeds; here, we examine active anterograde transport function, one of the earliest functional deficits established in our model[153]. To do so, we inject a fluorescently conjugated cholera toxin subunit β (CTB) intravitreally. CTB is then taken up by retinal ganglion cells and transported to their distal regions as their functional ability allows. We examine the amount of fluorescence in the most distal, and main, target reached in mice: the superior colliculus (SC). The percentage of regions exhibiting at least 70% of the maximal fluorescence represents the anterograde transport ability for that visual stream.

One week of unilateral IOP elevation did not significantly reduce anterograde transport function in control mice in either visual stream (Figure 4.4). In KO mice, one week of unilateral IOP elevation reduced anterograde transport function by a remarkable 40.9% in the stressed optic projections, a significant reduction both from the contralateral naïve projections and corresponding control projections. Certainly, astrocyte connexins play a role in the maintenance of neuronal function at this early stage of neurodegeneration.

Two weeks of unilaterally elevated IOP resulted in a statistically significant 24.3% loss in anterograde transport function between microbead and naïve optic projections in control mice. KO mice exhibited more severe pathology; two weeks of elevated IOP caused a 45.6% loss in anterograde transport function compared to the contralateral naïve. This loss was greater than the loss exhibited by control mice, although the difference did not reach statistical significance.

The 2-1 staggered paradigm produced intriguing results in both control and KO mice. In control mice, the 2-week and 1 week projections both exhibited roughly 50% intact transport. Remarkably, despite the fact that one eye was exposed to elevated IOP for double the length of time, the two projections do not exhibit a significant difference in transport ability between one another. However, the projections exposed to 1 week of elevated IOP demonstrate significantly diminished anterograde transport function compared to the corresponding unilaterally injected 1 week control projections. This demonstrates the impact localized neurodegeneration can have on nearby regions; certainly, the degenerative program was accelerated because the contralateral eye had already been exposed to stress.

The same staggered paradigm in KO mice, however, did result in a statistically significant difference in anterograde transport function between the two projections. Remarkably, the KO projections exposed to 1 week of elevation in the staggered paradigm demonstrated a nearly identical percentage of intact anterograde transport to the unilateral KO 1 week exposed, demonstrating how isolated these neurons become after astrocyte communication through connexins is limited. Additionally, transport ability between the KO projections exposed to 2 weeks of elevation in the staggered paradigm and the unilateral KO 2 week projections was not statistically significant. However, the trend toward increased transport loss in the 2-1 paradigm may reveal other mechanisms involved in regulating degeneration between the two optic tracts. These additional mechanisms may include other astrocyte connexins or remodeling patterns that may be differentially impacted by a bilateral model; these factors should be examined in future experiments.

Finally, we examined the functional ability of the visual system as a whole, and how visual function during neurodegeneration is differentially impacted in control and KO mice exposed to the staggered paradigm of neurodegeneration. Mice in both the control and KO cohort were initially assessed and trained during three baseline measurements the week prior to any IOP elevation with no significant differences between groups or time points detected. Further, OKT assessed 2 days following initial IOP elevation did not detect any differences amongst groups or between these measurements and the average baseline measurements for each group. From this result, we know that microbead injection, the microbeads themselves, and any chromatic aberrations that could have occurred from the IOP elevation do not impact visual function.

Six days following IOP elevation we detected diminished visual function in stressed visual streams compared to contralateral visual streams in both control and KO mice; however, visual function loss was exaggerated in KO mice. Intriguingly, this pattern of loss in control mice appears to precede the loss of active anterograde transport function, meaning that there is likely another earlier component to neurodegeneration. KO mice still exhibit remarkably exaggerated deficits compared to control mice at this timepoint, further underlining the critical importance of astrocyte connexins in maintaining visual function. Intriguingly, neither group exhibits altered visual function in the contralateral visual stream. Likely, the loss of astrocyte glycogen stores without a second stressor does not stress the system in any way significant enough to impede functional ability; thus, in the event that a single stressor occurs without any further stressors, metabolite redistribution serves to protect the stressed region at no functional cost at this early timepoint.

On the seventh day, the contralateral eye was injected with microbeads in all mice. This significantly elevated IOP to a level similar to the fellow eye. Two days following this second microbead injection, control mice exhibited moderate visual function loss in both visual streams compared to respective baseline values. Thus, functional loss is accelerated in the fellow eye due to the initial injection. Two days following the initial injection, no functional loss was detected in any group. The previously stressed visual stream still exhibited significantly greater visual acuity loss than its contralateral partner that has been stressed for seven fewer days; however, at this time point the gap in visual acuity loss is rapidly closing. In knockout mice, the previously stressed visual stream continued to rapidly decline in visual acuity compared to baseline and the levels exhibited on day 6. Intriguingly, the newly stressed visual stream did not exhibit any alteration from baseline values, just as two days after the initial injection no functional loss could be detected. This stream exhibits significantly elevated visual acuity levels compared to the control contralateral 2 day nerve (p=0.009). For this brief period of time after the second IOP elevation, it appears that the relative isolation inflicted upon the contralateral KO nerve protects it from immediate visual acuity loss in KO mice.

However, the contralateral nerve is only protected transiently. Thirteen days after the first IOP elevation and 6 days after the second, control visual streams do not exhibit any differences in functional visual acuity from one another, but both are diminished from their respective baseline values. This likely reflects the loss of glycogen initially from the contralateral visual stream; the contralateral stream now progresses through the degenerative program more quickly. However, both nerves still retain visual acuity of roughly 0.4 cycles per degree, a level within the normal visual acuity range demonstrated for mice in some studies[361]. Further, the similarities in visual acuity are reminiscent of the visual field maintenance demonstrated in human patients[352]. Perhaps maintaining the same visual acuity between affected visual streams assists the brain in constructing a coherent unified visual field for the mouse to explore.

Six days following the second injection, KO no longer protects against visual acuity loss in the contralateral stream while the initially stressed stream continues to rapidly decline. Thirteen days after the initial injection, the initially stressed KO visual stream has diminished nearly 0.2 cycles per degree from baseline levels, a 39% loss in visual function over a mere two weeks and a significant loss from day 9. This is a significantly greater loss compared to baseline than that exhibited by respective control visual streams. At this time point, the contralateral KO stream has now lost 25% of its visual acuity, a greater loss than either control visual stream exhibits. Intriguingly, this is nearly the exact visual acuity demonstrated by the initially stressed KO stream at the same timepoint.

Although KO protected the contralateral optic nerve transiently, this occurred at the detriment of the initially stressed stream and did not exhibit any long-lasting effects.

Remarkably, by the end of the experiment both experimental streams exhibited visual acuity below the levels of *both* control streams. Presumably, as the contralateral stream at 6 days post injection exhibited nearly the same level of visual acuity as the ipsilateral stream at 6 days post injection, visual function in both streams would continue to rapidly decline at a much greater rate than in control mice.

Isolating the degenerating region from the greater astrocyte network, therefore, does not appear to be a viable treatment if the initially stressed region is not to be completely sacrificed. The connectivity of astrocytes likely contributed to the overall health of the brain and renders minor stressors to any one region that would otherwise impact function inconsequential. Here, we demonstrate that the metabolites distributed through this network are functionally important to degenerating regions; however, this does not exclude the impact of the other factors that may be distributed through this network. Other positive factors, such as growth factors[250,270,307] and perhaps even neurotransmitters[21,24,34], would be an intriguing topic for future study.

CHAPTER 5

DISCUSSION AND CONCLUSIONS

It is the mark of an educated mind to be able to entertain a thought
without accepting it.

- Aristotle

5.1 SIGNIFICANCE

The brain is a disproportionately metabolically demanding organ. Despite comprising only 2% of human body mass, the brain accounts for roughly 30% of the resting rate of energy consumption[75,104,114]. Neurons rely primarily on glucose as an energy substrate, which is depleted quickly during periods of stress or high demand[18,52]. To maintain normal function, neurons rely upon astrocyte glia that create and store glycogen, which serves as the brain's largest energy reserve and a safeguard against periods of stress[1,52]. This metabolic collaboration between neurons and astrocytes is exceptionally important in degenerative disease, which taxes normal energy utilization and increases reliance on alternative sources[56,58].

As the brain ages its metabolic processes become less efficient, rendering the nervous system more susceptible to metabolic stress[169]. In preclinical neurodegeneration, hypometabolism and oxidative stress become increasingly apparent[131]. At this early stage of pathology, astrocytes remodel and utilize glycogen stores to preserve axonal function through chronic stress[74,96]. This endogenous protection likely occurs through multiple mechanisms, but some of the earliest occur due to a deficit of metabolites and metabolic resources[338]. What these mechanisms involve, however, is not fully established and could elucidate new protective therapies for those individuals in the early stages of pathology.

To address this, we utilized models of glaucomatous optic neuropathy, or glaucoma. Glaucoma is the world's leading cause of irreversible blindness, projected to impact 80 million people by the year 2020[211]. Retinal ganglion cell (RGC) axons contain an energetically demanding unmyelinated segment that travels through the retina and optic nerve head. This means that RGC axons must fire without energy-conserving saltatory conduction for much of their initial length. Additionally, the optic nerve head, the region through which unmyelinated RGC axons travel, is the location impacted most directly through intraocular pressure (IOP). IOP is one of the key risk factors for glaucoma[362] and a critical component of the disease that makes it particularly approachable for study of early neurodegeneration.

However, despite IOP being a risk factor, glaucoma itself is diagnosed through measures of optic nerve health, where deficits are first noted during the disease[229]. Functional and structural deficits emerge within the optic nerve early in progression, even as the cell body and axon segment in the retina persist[153,190]. Prior to axonal changes, astrocytes redistribute their processes near those axons that likely receive the most stress[16,190]. Therefore, not only is the optic nerve a prime model for studying the interactions between astrocytes and axons in response to stress, but it is also the key target for protective therapies in glaucoma.

Astrocytes form plastic networks of interconnected cells, and constantly remodel these networks to monitor and protect the tissue they reside within. They form these networks through gap junctions, a unique modality of specialized synapses that form a direct pathway for cell-to-cell communication between cytoplasm. Astrocytes utilize gap junctions, primarily composed of connexin 43 (Cx43), to couple with neighboring cells, share signals pertaining to the health of their domain, and redistribute resources[276]. Cx43 is permeable to molecules up to 1-1.2 KDa, much larger than the metabolic resources primarily utilized by the brain: glucose (180 Da), pyruvate (88 Da) and lactate (90 Da) [265].

The lifetime of connexins is only about 2 hours, meaning the networks they form are constantly modulated[275]. Intriguingly, astrocyte Cx43 is elevated in human glaucomatous optic nerve head[64]. However, the majority of studies on Cx43 in neurodegeneration pertain to the late stages of the disease, where inflammatory cytokines are dispersed through these membrane pores[130,278]. Here, we are interested in the early stages of neurodegeneration, where astrocyte gap junctions may modulate an endogenously protective mechanism wherein they remodel to redistribute resources from healthy regions of the brain to areas actively undergoing stress.

Our investigations revolved around the central hypothesis that early in neurodegeneration, astrocytes increase connectivity through cx43 to endogenously protect neuronal function by utilizing network-wide energy stores. Through our first aim we characterized astrocyte morphological remodeling during neurodegeneration, and noted the alterations in mitochondrial density that simultaneously occurred. Our second aim focused on metabolite redistribution through astrocytes from healthy to degenerating regions of the central nervous system, where we determined that astrocytes utilize gap junctions to redistribute resources. In our final aim, we investigated the impact metabolite redistribution had on the neurons within the originating tissue, and whether they were now more susceptible to neurodegenerative stressors due to resource depletion.

5.2 AIM 1

5.2.1 OUTCOMES

Hypertrophy of glial process in the optic nerve, particularly of astrocyte processes, is a prominent characteristic of a nerve experiencing substantial axon loss in glaucoma[328,193,308,309]. Our results demonstrate that as axons expand early prior to frank loss, the ramification of astrocyte processes in the inter-axonal space actually diminishes (Figures 2.1, 2.3) while the center of mass for glial ramification changed from an even distribution across the nerve to one skewed towards the edge of the nerve (Figures 2.4, 2.5). As axons continued to expand beyond the threshold for overt loss, the center of mass returned to an even distribution (Figure 2.5, right panel). Further, cross-sections of healthy DBA/2J optic nerve demonstrate organization along a common axis (Figure 2.6, left panel), exhibiting a high degree of parallelism as indicated by our metric (Figures 2.7, 2.8). As axon pathology increases with a commensurate increase in glial coverage of the nerve, parallelism diminishes and astrocytes distribute more evenly across the nerve (Figure 2.9). Accordingly, axon density, total number of axons, and axon expansion all predict changes in astrocyte parallelism more accurately than independent measures of glaucoma progression in the DBA/2J (i.e., IOP and age; Figure 2.10). As the mean axon area increases toward the threshold for loss, astrocyte parallelism increases without a change in overall glial coverage of the nerve (Figure 2.11). Once axon loss begins and density diminishes, parallelism decreases in kind (Figure 2.9E), presumably as astrocyte processes re-invade axon bundles.

In total, these results from the DBA/2J model indicate that astrocytes remodel biphasically. During early axon expansion prior to axonal loss, astrocyte processes increase in parallelism as CoM diminishes *independent from gliosis* (Figure 2.11). Once axons are lost, gliosis involves diminished parallelism and uniform astrocyte distribution across the nerve (Figure 2.9). It appears, then, that the astrocyte population as a whole remodels, altering its pattern of redistribution as the neurodegenerative state of the tissue alters. The population must, therefore, have a mechanism of communication that allows for rapid, concordant remodeling across great distances. A mechanism available for such rapid communication – at very little energetic cost – is readily available to astrocytes. We hypothesized that this population must be communicating through their gap junctions to coordinate remodeling throughout the tissue.

In longitudinal sections of nerve, we found that both GFAP and Cx43 are higher in proximal vs distal segments (Figures 2.12C, 2.13D). This is consistent with a more even distribution of astrocytes, as indicated by the higher CoM in the proximal vs the distal segment (Figure 2.12E). Previous work has demonstrated anterograde axonal transport from retina to brain is an early harbinger of axon pathology in the DBA/2J and degrades in distal-to-proximal fashion[153]. Here, we found that parallelism of GFAP-labeled astrocyte processes was higher in distal segments of our 10-month old DBA/2J nerves. (Figure 2.12F). As parallelism increased in the distal segment, astrocytes redistributed towards the nerve edge, as indicated by a lower

CoM (Figure 2.12G). This pattern of remodeling reflects that seen in early stages of axonal pathology, indicating that astrocytes in the distal nerve may be reacting to pathology prior to those in the proximal nerve.

In the distal segment, nerves containing elevated Cx43 also demonstrated higher levels of intact transport but did not show a relationship with parallelism (Figure 2.14B). In contrast, levels of Cx43 in the proximal segment predicted parallelism with no clear relationship to transport (Figure 2.14A). Thus, these results indicate that in the distal segment, where axonopathy has already begun, Cx43 in astrocytes better reflects axon function than astrocyte organization. This is consistent with findings demonstrating gap-junction coupling of the astrocyte network is tightly modulated by axonal function and neuronal activity[319]. Similarly, increased parallelism in the distal vs proximal segment is reminiscent of our results from cross-sections of proximal nerve, where increased parallelism correlated with early expansion of axons prior to overt loss (Figure 2.11B). Through gap-junction coupling, astrocytes may be able to more evenly distribute resources to those axons undergoing the highest degree of stress[230,231,312,331].

Our results suggest that early progression in the optic nerve involves remodeling of astrocyte processes, first to a higher state of organization with increased parallelism (Figure 2.11) and gap-junction coupling (Figure 2.14), then to gradual deterioration of organization as coverage increases and axons are lost (Figures 2.9, 2.10). Perhaps well-organized astrocyte processes lend structural stability to the nerve. In the optic nerve head, astrocytes form a continuously remodeling network that adapts to IOP exposure [332], with astrocyte actin and tubulin filaments gradually re-orienting as IOP increases[333]. With short exposures to elevated IOP, astrocyte processes retract towards the cell body[300]; astrocyte processes also may also fortify the edge of the nerve, as coverage in the center diminishes (Figure 3 of Sun et al., 2013). As astrocyte processes re-invade the nerve center with longer IOP exposure, their organization diminishes[300]. With acute injury (nerve crush), astrocyte processes appear to detach from the edge[16], but this likely reflects the more severe nature of the injury. Similar to our results in the myelinated nerve, astrocyte remodeling following induced short-term elevations in pressure is most extensive distal from the sclera[334]. Portions of the optic nerve beyond the sclera itself are unlikely to be impacted directly by elevated IOP, and secondary changes could involve different structural mechanisms. This may be why we did not note a simple linear relationship between IOP and loss of parallelism (Figure 2.10B), but did find strong correlations between measures of axonal degeneration and loss of parallelism (Figures 2.10, 2.11).

Perhaps the most important question is whether early astrocyte remodeling is protective or pathogenic. Cx43 is elevated in the optic nerve head and the retina in human glaucomatous tissue[64], and here we find that astrocyte remodeling is associated with increased Cx43 (Figure 2.14). Intriguingly, we additionally find that elevated Cx43 is also associated with intact axonal anterograde transport (Figure 2.14D). This suggest that the early phases of astrocyte remodeling involving increased connectivity may be a component of an endogenously protective mechanism, wherein these alterations within astrocytes positively influence the health of axons within the optic nerve. In late stages of neurodegeneration, Cx43-mediated coupling helps disperse inflammatory cytokines through gap junctions[278,335]. The data presented herein leads us to believe that Cx43 exhibits a multitude of functions, like astrocytes themselves. In these early stages of pathology, gap junctions allow astrocytes to couple with neighboring cells and share signals that may contribute to the redistribution of resources to those regions most at risk.

Concurrently, the degenerating optic nerve undergoes significant diminishment in its mitochondrial capacity. These two findings are not as disparate as they initially appear. Astrocytes are directly responsible for the mitochondrial health of the optic nerve; as mitochondria age and begin to degenerate themselves, they are shuttled from axons into nearby astrocytes that degrade them[336]. This maintains the structural stability of axons, whose neurofilaments are particularly susceptible to the increased reactive oxygen species produced by aging mitochondria[118,167]. We found that nerves exhibiting axon expansion prior to frank loss demonstrated diminished numbers of mitochondria per unit area of tissue with increasing axon size (Figure 2.15). If axons are not transporting fresh mitochondria to distal regions of the nerve, those mitochondria that are degraded as they age will not be replaced. As anterograde transport fails more and more proximally, this phenotype will become more severe. This renders axons increasingly reliant on astrocytes and their energy stores (Figure 2.16). Astrocytes depleting their resources then increase their connectivity – perhaps to obtain resources from nearby regions. This, however, may drastically affect the functionality of the system as a whole.

5.2.2 FUTURE DIRECTIONS

In subsequent aims, we investigated the metabolic aspects of astrocyte remodeling and resource distribution in great detail. There are, however, many open avenues still worth investigating that are revealed by this preliminary observational data. What are the triggers of astrocyte remodeling? In our model, there is a direct physical strain on the tissue and mechanoreceptors capable of sensing this strain. Many mechanoreceptors reside upon astrocytes and utilize calcium flux to cause downstream effects. Could these calcium waves generate enough of a stimulus to dictate both the necessity and directionality of remodeling needed to maintain the integrity of the optic nerve?

Metabolic stress itself is directly sensed by a protein cascade centered around the enzyme adenosine 5’ monophosphate-activated protein kinase, or AMPK. AMPK activation relates directly to the energetic state of a cell, and its downstream signaling partners include many factors directly involved in remodeling. Could AMPK activation in one region of tissue cause a cascade that would impact nearby tissue and propagate a response through astrocyte gap junctions? Which downstream partners are activated at different distances from the initial stressor?

Finally, the mechanism of remodeling itself could be an intriguing topic of study. We know that the cytoskeletal protein GFAP is upregulated in activated astrocytes; is it differentially activated in astrocytes activated in different manners, such as A1 versus A2 astrocytes? Will A2 astrocytes eventually demonstrate an activation pattern more similar to an A1 astrocyte after a stressor becomes chronic? How do other cytoskeletal proteins react and remodel in individual astrocytes as the population alters as a whole?

Any of these investigations would reveal critically important information about the brain’s response to neurodegenerative stress, and how that stress alters the brain once it becomes chronic. Further, a greater understanding of the astrocyte response in particular may provide avenues for protective therapies for those in the early stages of pathology.

5.3 AIM 2

5.3.1 OUTCOMES

The aim of Chapter 3 was to investigate the early stages of neurodegeneration, and determine the molecular mechanism through which astrocytes redistribute resources from healthy regions of the brain to areas actively undergoing stress. To do so, we generated a locally and temporally controlled knockout of Cx43 in astrocytes expressing GFAP. Although this knockout did not eliminate every puncta of Cx43 within astrocytes, the vast majority of the protein was eliminated (Figure 3.6). In each experiment, we not only compared KO results to the appropriate controls but additionally compared our results to wild type (C57/BL6) mice.

We initially investigated the pattern of glycogen distribution between optic nerves in WT mice exposed to a timecourse of unilateral IOP elevation. While a short four-day exposure to unilateral IOP elevation resulted in reduced glycogen in the nerve ipsilateral to the stressor, any longer exposure resulted in bilateral diminishment in glycogen. There appears to be particular importance to 1 week of exposure compared to earlier timepoints. In our model, this may be the inflection point between chronic and acute exposure. From these data, we hypothesized that the stressor of chronically elevated IOP does not merely impact the brain locally. Perhaps there was an endogenously protective mechanism through which astrocytes were able to redistribute their energy stores to those regions most in need of assistance.

To directly test this, we repeated this experiment in *GFAP-Cre-ET^{t2} x Cx43$^{flox/flox}$* mice with *Cx43$^{flox/flox}$* littermates serving as control for both tamoxifen exposure and the genetic manipulation required to generate our model. IOP was elevated for either 4 days or 1 week, the timepoints our experiments in C57 mice demonstrated as nearest the tipping point for contralateral glycogen depletion. Control mice exhibited a pattern similar to that of WT mice at all time points examined, and four days of IOP elevation in KO mice repeated the same pattern as control and WT mice. However, KO reversed the pattern of glycogen distribution after 1 week of unilateral IOP elevation. Although glycogen levels diminished in both microbead and contralateral nerves, glycogen is significantly lower in the microbead nerve compared to the contralateral nerve. From these data, we know Cx43 is a component of the normal energetic redistribution that occurs after localized neurodegenerative stress. However, glycogen levels still diminished in the contralateral nerve. There are multiple explanations for this phenomenon, each of which should be investigated in future experiments as detailed below.

Upon establishing that glycogen was mobilized into glucose in both visual streams, we hypothesized that these energy reserves were not merely utilized locally; rather, glucose was drawn from the healthy projection to the actively stressed projection to help maintain RGC function. To test this, we devised an experiment where we elevated IOP unilaterally for one week and then injected ^{18}F-FDG, a radioactive glucose analogue, into the contralateral eye. After the mice were awake for one hour to allow for uptake, we imaged for 40 minutes in a PET scanner in static mode. The cumulative amount of radiation detected in the stressed optic nerve, ipsilateral to IOP elevation and contralateral to ^{18}F-FDG injection, was measured and compared between naïve and microbead-injected animals.

In wild-type mice 41% more glucose is transferred between the projections if the contralateral projection has been stressed through IOP elevation. The brain has a remarkable capacity to transport glucose between optic projections quickly when one is damaged. Most PET studies allow 40 minutes for ^{18}F-FDG uptake[58], which means that the transfer itself may have occurred in as few as 20 minutes. The majority of FDG was detected in the injected eye, with a maximum of about 1% of the injected dose making its way into the contralateral eye in the time allotted. A small amount of ^{18}F-FDG was additionally detected above the mouse's shoulder blades; there is a brown fat pad at this location, which would store ^{18}F-FDG that had made its way into the bloodstream from the eye. The majority of metabolites still available for energetic processing within the bloodstream would be absorbed here[345], while the energetically spent byproducts eventually make their way to the bladder.

The most logical avenue for these metabolites to utilize is through the astrocytes within which glycogen resides. These astrocytes already contain the machinery to mobilize and utilize these stores, as well as transfer the metabolites to nearby cells[276]. However, the eye still contains a vascular network equipped with glucose transporters through which FDG could be, and likely is, absorbed into the bloodstream. FDG absorbed in this manner would immediately be diluted in the entire blood flow and need to travel through the majority of the body before making its way to the contralateral eye, as the vasculature within the two eyes is not a dual capillary system. Thus, any ^{18}F-FDG absorbed in this manner would create a pattern of radiation far greater in any fat repositories than in the contralateral eye itself, a pattern we did not observe.

Although unlikely, we still investigated whether the blood flow could be responsible for ^{18}F-FDG transport by performing PET experiments on mice that each underwent a unilateral microbead injection and optic nerve transection in the contralateral projection. Transection resulted in a statistically significant 61% loss in ^{18}F-FDG transport to the contralateral eye compared to sham values. After the experiment, we determined that the optic nerves were intact at the location of entry for the central retinal artery, and determined that RGCs were still living and functional. From these data, we inferred that glucose transfer must have necessitated an intact optic nerve proper.

We next utilized *GFAP-Cre-ET^{t2} x Cx43$^{flox/flox}$* mice in our PET experiments to determine whether astrocyte connexins were involved in the transport of metabolites between optic projections. We chose to investigate this mechanism as it is the simplest possible pathway through which metabolites can redistribute, the number of gap junctions between astrocytes increases during glaucomatous stress[64], and prior experiments have established the capability for metabolite redistribution through gap junctions[276]. Further, we have already determined that astrocyte-derived energy stores diminish in the contralateral nerve during unilateral glaucomatous stress; therefore, it is likely a simple astrocyte-specific mechanism is involved, rather than a more convoluted mechanism involving other cell types. These cell types may be involved in addition to astrocytes, but astrocytes are the only cells we are certain contain metabolites that mobilize bilaterally after unilateral stress.

KO control mice exhibited glucose redistribution after unilateral IOP elevation similar to that of C57 mice that experienced IOP elevation for the same period of time, so we know that tamoxifen itself and the genetic manipulations required to flox Cx43 did not impede glucose transfer between optic projections. *GFAP-Cre-ET*^{t2} *x Cx43*$^{flox/flox}$ KO mice, however, exhibit a remarkable 47% reduction in glucose redistribution after IOP elevation compared to this control. We know, therefore, that astrocyte connexins are required for glucose redistribution between optic projections.

Intriguingly, KO mice additionally exhibit a trend toward less glucose redistribution than WT mice even when IOP has not been elevated in either group. In fact, results from KO mice in all conditions more closely resemble transection levels of transport than even those of naïve WT mice. This hints that perhaps the metabolic networks formed through astrocyte gap junctions are important for normal function as well as during early neurodegenerative stress. It is well established that normal neuronal signaling can require nearby astrocytes to mobilize their glycogen stores, especially within the visual system[52,338]. Retinal ganglion cells are particularly energetically demanding neurons; in addition to their extraordinary axonal length, they additionally possess a long unmyelinated portion within the retina and optic nerve head that cannot utilize saltatory conduction to conserve energy and preserve signal strength. In addition to these challenges, the optic nerve is isolated from the rest of the brain, which may result in particularly exaggerated energetic deficits. The optic nerve may rely upon astrocyte connexins to continually replenish glycogen stores from the brain's larger reserves.

Due to the optic nerve's relative isolation, energy transfer between optic projections may have consequences on neuronal function. This should be especially true during further metabolic stress. To determine the functional consequences of energy transfer between optic projections we measured the optic nerve compound action potential (CAP) in bilateral naïve, 1 week unilateral MOM and 2 week unilateral MOM conditions. We additionally probed each group's ability to cope with glucose deprivation by utilizing L-glucose, an enantiomer of table sugar that cannot be digested by mammalian cells; further, we determined the ability to recover from this stress by replacing L-glucose with D-glucose, the typically occurring form.

Counterintuitively, nerves directly exposed to 1 week of elevated IOP exhibited the same response to glucose deprivation and recovery as nerves from bilateral naïve mice. However, the nerve contralateral to 1 week of elevated IOP did not exhibit as strong a signal. In fact, the contralateral nerve exhibited a diminished signal compared to the ipsilateral nerve at every time point beyond baseline, and that diminishment was significant at 17/20 time points measured. Thus, one week of IOP elevation results in a reduced ability for the contralateral nerve to cope with further metabolic stress. However, the ipsilateral nerve does not appear to be impacted by further metabolic stress. Perhaps this nerve has sufficient glycogen stores to survive the stressor or has compensated in other ways for continuous metabolic stress. These other ways may include redistribution of Nodes of Ranvier, or the energetically demanding ion channels expressed at nodes, to reduce the energetic demand of signaling, a phenomenon previously detected in the ipsilateral nerve in models of glaucoma[188]. Concurrently, hypermyelination by oligodendrocytes may increase the nerve's insulation and allow it to more efficiently conduct signals[189]. Each of these hypotheses involves remodeling and thus increased energetic demand; further, how this remodeling will impact the system long-term has yet to be determined. Myelin sheaths are involved in providing energetic support to the axons they surround[5] and gap junctions have not been found between layers of myelin[288], meaning that any metabolites may be more diluted or have a longer distance to traverse as the number of myelin layers increases. At one week of chronic neurodegenerative stress, this does not appear to be an issue yet; the impact of hypermyelination on energy dynamics as the disease progresses through longer periods of chronic stress has yet to be determined. Certainly by 2 weeks of unilaterally elevated IOP there exists bilateral weakness to metabolic stress. This speaks to the critical importance of glycogen stores and the buffer they confer against metabolic stress, and the isolation the optic nerve experiences from the reserves throughout the brain. It additionally hints that any remodeling that occurs within the nerve to protect it one week following IOP elevation is no longer effective, and may be detrimental, two weeks following induction.

We next examined how our conditional Cx43 knockout would respond to the same experimental paradigm. We hypothesized that metabolically isolating each nerve from the reserves of the other might rescue the weakness to metabolic stress in the contralateral nerve; this might, however, occur at the detriment of the initially stressed projection. Intriguingly, naïve KO nerve did not statistically differ from naïve C57 nerves at any point throughout baseline, glucose depletion, or recovery measurements. Whatever impact metabolic isolation has on these nerves does not appear to impact the normal functional ability of these projections without a neurodegenerative stressor present. This is particularly intriguing after our PET experiments, but the normal glycogen reserves did not appear to differ between *GFAP-Cre-ET*^{t2} *x Cx43*$^{flox/flox}$ mice, KO control mice, and C57/BL6 mice. Perhaps this is all that is necessary to maintain normal signaling without a neurodegenerative stressor present; or, perhaps, a more stringent test of signaling ability would reveal more deficits in the KO nerves.

We were only evoking a signal once every 5 minutes after our initial calibration. Other studies evoke a signal as frequently as every 30 seconds.

As hypothesized, KO nerves directly exposed to 1 week of IOP elevation exhibited a diminished response compared to corresponding C57 nerves. Surprisingly, this only occurred for the 5 minutes immediately following the initiation of glucose depletion, while the remainder of the timecourse closely resembled the C57 response. Even more remarkably, KO nerves contralateral to 1 week of IOP elevation exhibited elevated CAP area compared to corresponding C57 nerves at every time point from glucose depletion onward, and did not differ from the naïve KO response at any time point. Apparently, at 1 week of unilateral IOP elevation, Cx43 KO rescues the contralateral signaling deficit in response to glucose depletion. This does occur at the detriment of the MOM nerve's signaling ability early in glucose deprivation. *In vivo*, a depletion of glucose for any longer than 5 minutes would likely be the result of an acute ischemic event and beyond the scope of normal degeneration, so perhaps this inability to cope with glucose deprivation at these early time points would have a greater impact on the intact system.

Although these CAP results occurred as we hypothesized, the extent to which the ipsilateral optic nerve was impacted by its metabolic isolation did not appear to be balanced by the degree of rescue in the contralateral nerve. In fact, the rescue in the contralateral nerve far surpassed the signaling deficit in the ipsilateral nerve. This led us to hypothesize (and investigate in the following chapter) that perhaps inhibition of Cx43 might be an intriguing way to preserve function in the contralateral projection. However, this was not the case; visual function in the contralateral projection was preserved at 1 week regardless of Cx43 KO, but the ipsilateral projection exhibited far greater loss of function due to KO. Further, if the contralateral eye then experienced IOP elevation 1 week following the initial ipsilateral stressor, visual function in this contralateral stream in KO mice only surpassed that of WT mice 2 days following induction. This underlies the critical importance of these metabolic networks to preservation of neuronal function during neurodegeneration and is explored in greater detail in Aim 3.

5.3.2 FUTURE DIRECTIONS

From these data, we know Cx43 is a component of the normal energetic redistribution that occurs after localized neurodegenerative stress. However, glycogen levels still diminished in the contralateral nerve. There are multiple explanations for this phenomenon, each of which should be investigated in future experiments. There is likely redundancy in the system of energetic redistribution during localized neurodegenerative stress, perhaps involving other connexins within astrocytes. However, this is unlikely to be the only explanation, as previously published data demonstrates that elimination of Cx43 from astrocytes results in elimination of 95% of gap junctions *in vitro*[60]. Perhaps, then, the regions of the brain that receive bilateral innervation are capable of altering signaling patterns in the contralateral eye in ways that consume more resources. There is evidence in humans for CNS control of glaucomatous progression, as the full visual field appears to be preserved by sacrificing regions in one eye and preserving the corresponding regions in the other[352]. Although the mouse visual system is markedly dissimilar from that of humans and a unilateral insult is additionally different from the glaucoma most humans experience, CNS control of degeneration is likely preserved. Perhaps these binocular regions require similar signals from both visual streams, and that would necessitate some remodeling in the contralateral eye that would likely consume energy reserves. One final hypothesis is that perhaps upon losing Cx43 mediated gap junctions astrocytes attempt to compensate by remodeling to a greater extent than would typically occur 1 week after unilateral IOP elevation, thus consuming additional resources. This would depend largely on the mechanism through which those astrocytes that reside in the contralateral stream would sense the stress in the other eye; this should be the next mechanism investigated in this line of work.

These experiments focused mainly on the contributions the fellow optic nerve makes to support its partner. Although the brain is farther removed from the stressor than the contralateral optic nerve, astrocyte networks could still theoretically expand from the optic nerve through the brain itself. We did see radioactivity in the brain after ^{18}F-FDG injection into an eye in WT mice. This indicates that metabolic networks extend beyond the scope of the optic projections alone. An interesting future experiment to determine the contribution the metabolic networks in the brain have on metabolic redistribution would be to transect the optic chiasm sagitally, maintaining two intact and distinct optic projections that no longer cross. Each would still reach their target brain regions, and any astrocyte connectivity to the brain should then be maintained.

There are multiple intriguing future directions involving CAP recording as well. We were only evoking a signal once every 5 minutes after our initial calibration, while other studies evoke a signal as frequently as every 30 seconds. More frequent stimulation may increase the metabolic stress each nerve experiences and thus reveal greater differences between experimental conditions. This would be particularly interesting to look at in our KO mice, and should be investigated in future studies.

A moment of particular interest in our CAP experimental timeline is the first 5 minutes following L-glucose aCSF within the bath. In groups that contain normal glycogen stores, the signaling at this moment is elevated above baseline levels. However, groups with reduced glycogen do not exhibit increased CAP signaling above baseline at these points. Therefore, the signaling pattern at these early time points likely reflects the glycogen stores available to be mobilized in response to glucose depletion. This should be tested in future experiments; if an inhibitor of glycogen polymerase were added to the bath at the moment it switched to L-glucose containing aCSF, the contribution of glycogen stores to each point in the timecourse could then be determined. As these time points are most relevant to the timescale involved in short ischemic events or local increases in metabolic demand, each of which is involved in neurodegenerative stress, information on signaling at this location could be particularly relevant to understanding the local contribution of astrocyte metabolic networks to neurodegenerative disease.

5.4 AIM 3

5.4.1 OUTCOMES

The neurodegenerative stressors one encounters in the world are not isolated, but most often an isolated stressor is the clearest to study. Once we established how the interconnectivity of the brain contributes to the broad impact of neurodegeneration, we then needed to establish how this paradigm would impact an individual impacted by multiple stressors. If resources are drawn away from one region of the brain to support another, does that then render the originating tissue vulnerable? To investigate this, we utilized a staggered pattern of IOP elevation at the precise timepoint we previously determined to be the inflection point for resource redistribution.

We utilized KO and KO control mice to address directly how astrocyte connexins serve to maintain or diminish neuronal function in each paradigm. Here, we examined active anterograde transport function, one of the earliest neuronal functional deficits established in our model[153]. One week of unilateral IOP elevation did not significantly reduce anterograde transport function in control mice in either visual stream, and two weeks resulted in a 24.3% functional loss (Figure 4.4). In KO mice, one week of unilateral IOP elevation reduced anterograde transport function by a remarkable 40.9% in the stressed optic projections, a significant reduction both from the contralateral naïve projections and corresponding control projections. Two weeks of IOP elevation in KO mice caused a 45.6% loss in anterograde transport function compared to the contralateral naïve nerve. Certainly, astrocyte connexins play a role in the maintenance of neuronal function at this early stage of neurodegeneration.

The 2-1 staggered paradigm produced intriguing results in both control and KO mice. In control mice, the 2-week and 1 week projections both exhibited roughly 50% intact transport. Remarkably, despite the fact that one eye was exposed to elevated IOP for double the length of time, the two projections do not exhibit a significant difference in transport ability between one another. However, the projections exposed to 1 week of elevated IOP demonstrate significantly diminished anterograde transport function compared to the corresponding unilaterally injected 1 week control projections. This demonstrates the impact localized neurodegeneration can have on nearby regions; certainly, the degenerative program was accelerated because the contralateral eye had already been exposed to stress.

The same staggered paradigm in KO mice, however, did result in a statistically significant difference in anterograde transport function between the two projections. Remarkably, the KO projections exposed to 1 week of elevation in the staggered paradigm demonstrated a nearly identical percentage of intact anterograde transport to the unilateral KO 1 week exposed, demonstrating how isolated these neurons become after astrocyte communication through connexins is limited. Additionally, transport ability between the KO projections exposed to 2 weeks of elevation in the staggered paradigm and the unilateral KO 2 week projections was not statistically significant. However, the trend toward increased transport loss in the 2-1 paradigm may reveal other mechanisms involved in regulating degeneration between the two optic tracts. These additional mechanisms may include other astrocyte connexins or remodeling patterns that may be differentially impacted by a bilateral model; these factors should be examined in future experiments.

Finally, we examined the functional ability of the visual system as a whole, and how visual function during neurodegeneration is differentially impacted in control and KO mice exposed to the staggered paradigm of neurodegeneration. Six days following IOP elevation we detected diminished visual function in stressed visual streams compared to contralateral visual streams in both control and KO mice; however, visual function loss was exaggerated in KO mice.

Intriguingly, this pattern of loss in control mice appears to precede the loss of active anterograde transport function, meaning that there is likely another earlier component to neurodegeneration. KO mice still exhibit remarkably exaggerated deficits compared to control mice at this timepoint, further underlining the critical importance of astrocyte connexins in maintaining visual function. Intriguingly, neither group exhibits altered visual function in the contralateral visual stream. Likely, the loss of astrocyte glycogen stores without a second stressor does not stress the system in any way significant enough to impede functional ability; thus, in the event that a single stressor occurs without any further stressors, metabolite redistribution serves to protect the stressed region at no functional cost at this early timepoint.

On the seventh day, the contralateral eye was injected with microbeads in all mice. Two days following this second microbead injection, control mice exhibited moderate visual function loss in both visual streams compared to respective baseline values. Thus, functional loss is accelerated in the fellow eye due to the initial injection. Two days following the initial injection, no functional loss was detected in any group. The previously stressed visual stream still exhibited significantly greater visual acuity loss than its contralateral partner that has been stressed for seven fewer days; however, at this time point the gap in visual acuity loss is rapidly closing. In knockout mice, the previously stressed visual stream continued to rapidly decline in visual acuity compared to baseline and the levels exhibited on day 6. Intriguingly, the newly stressed visual stream did not exhibit any alteration from baseline values, just as two days after the initial injection no functional loss could be detected. For this brief period of time after the second IOP elevation, it appears that the relative isolation inflicted upon the contralateral KO nerve protects it from immediate visual acuity loss in KO mice.

However, the contralateral nerve is only protected transiently. Thirteen days after the first IOP elevation and 6 days after the second, control visual streams do not exhibit any differences in functional visual acuity from one another, but both are diminished from their respective baseline values. This likely reflects the loss of glycogen initially from the contralateral visual stream; the contralateral stream now progresses through the degenerative program more quickly. However, both nerves still retain visual acuity of roughly 0.4 cycles per degree, a level within the normal visual acuity range demonstrated for mice in some studies[361]. Further, the similarities in visual acuity are reminiscent of the visual field maintenance demonstrated in human patients[352]. Perhaps maintaining the same visual acuity between affected visual streams assists the brain in constructing a coherent unified visual field for the mouse to explore.

Six days following the second injection, KO no longer protects against visual acuity loss in the contralateral stream while the initially stressed stream continues to rapidly decline. Thirteen days after the initial injection, the initially stressed KO visual stream has diminished nearly 0.2 cycles per degree from baseline levels, a 39% loss in visual function over a mere two weeks and a significant loss from day 9. This is a significantly greater loss compared to baseline than that exhibited by respective control visual streams. At this time point, the contralateral KO stream has now lost 25% of its visual acuity, a greater loss than either control visual stream exhibits. Intriguingly, this is nearly the exact visual acuity demonstrated by the initially stressed KO stream at the same timepoint. Therefore, although KO protected the contralateral optic nerve transiently, this occurred at the detriment of the initially stressed stream and did not exhibit any long-lasting effects. Remarkably, by the end of the experiment both experimental streams exhibited visual acuity below the levels of *both* control streams. Presumably, as the contralateral stream at 6 days post injection exhibited nearly the same level of visual acuity as the ipsilateral stream at 6 days post injection, visual function in both streams would continue to rapidly decline at a much greater rate than in control mice.

Isolating the degenerating region from the greater astrocyte network, therefore, does not appear to be a viable treatment if the initially stressed region is not to be completely sacrificed. The connectivity of astrocytes likely contributed to the overall health of the brain and renders minor stressors to any one region that would otherwise impact function inconsequential. Here, we demonstrate that the metabolites distributed through this network are functionally important to degenerating regions; however, this does not exclude the impact of the other factors that may be distributed through this network. Other positive factors, such as growth factors and perhaps even neurotransmitters, would be an intriguing topic for future study.

5.4.2 FUTURE DIRECTIONS

Intriguingly, in mice that underwent the staggered paradigm of IOP elevation only the nerves exposed to 1 week of IOP contained glycogen significantly diminished from naïve levels. The nerves exposed to a full 2 weeks of IOP elevation exhibited glycogen levels that were not significantly different from those from naïve mice. Further, nerves in the staggered paradigm exposed to 1 week of IOP elevation contained significantly less glycogen than unilateral 1 week nerves, and the nerves in the staggered paradigm exposed to 2 weeks of elevation contained significantly more glycogen than unilateral 2 week nerves. This demonstrates that contralateral glycogen stores are not replaced after contralateral IOP elevation; rather, it appears contralateral IOP elevation exaggerates the disparity of energy stores between the nerves. Perhaps any glycogen mobilized by the second IOP elevation would continue moving along the concentration gradient established by the first injection. The exact mechanism of this exaggerated disparity in energy stores should be investigated in future studies.

The KO projections exposed to 1 week of elevation in the staggered paradigm demonstrated a nearly identical percentage of intact anterograde transport to the unilateral KO 1 week exposed, demonstrating how isolated the injured region became after astrocyte communication through connexins was limited. Additionally, transport ability between the KO projections exposed to 2 weeks of elevation in the staggered paradigm and the unilateral KO 2 week projections was not statistically significant. However, the trend toward increased transport loss in the 2-1 paradigm may reveal other mechanisms involved in regulating degeneration between the two optic tracts. These additional mechanisms may include other astrocyte connexins or remodeling patterns that may be differentially impacted by a bilateral model; these factors should be examined in future experiments.

Surprisingly, the pattern of visual function loss in control mice appears to precede the loss of active anterograde transport function, meaning that there is likely another earlier component to neurodegeneration than anterograde transport loss that directly impacts visual ability, or at least the visuomotor response. An unlikely explanation is that this might even include the anterograde segment of the eye, although any chromatic aberrations should have been detected on the sessions immediately following IOP elevation. Perhaps neuronal remodeling directly needs to be accommodated for by the brain, as signaling patterns likely are altered as ion channels and dendritic fields reorganize. Findings involving any earlier neurodegenerative components would be critical for the advancement of the field of neurodegeneration in general, as an earlier hallmark of damage could help identify etiology in diseases that still lack it.

Metabolite redistribution through the astrocyte network is critically important in maintaining function in degenerating regions; however, this does not exclude the impact of the other factors that may be distributed through this network. Other positive factors, such as growth factors and perhaps even neurotransmitters, would be an intriguing topic for future study. Each newly identified positive factor provides another avenue to supplement as we attempt to prolong neuronal function in those suffering from the early stages of neurodegenerative decline.

CONCLUSION

Historically, reactive astrocytes have been largely considered harbingers of neurodegenerative progression[53,54,305]. However, a purely detrimental response would not be evolutionarily conserved. The remodeling populations of astrocytes undergo in the early stages of pathology may in fact be endogenously protective[36,299], and is certainly more complex than early models of glial scarring imply[42,43]. In this study, we have found that astrocytes in the optic nerve remodel as a population, responding to neurodegenerative stress by altering their morphology prior to any axonal loss[190]. As astrocytes orient in parallel, they increase their expression of connexin 43 (Cx43)[64,74]. Increased Cx43 is directly correlated with axonal anterograde transport function, indicating that astrocyte connectivity is important in regulating neuronal health through neurodegenerative stress[74,274].

Astrocyte connectivity through gap junctions is critically important for neuronal health during both normal function[61,276,297,319] and neurodegenerative progression[37,274,354]. Through gap junctions, astrocytes form a metabolic network capable of sustaining function in hyperactive or metabolically deficient cells within their domain[6,276,319]. Here, we examine the remarkable extent and functional contribution of these astrocyte-mediated metabolic networks in the early stages of chronic neurodegenerative stress. During this stage of neurodegeneration, astrocytes locally deplete their metabolic stores and the number of neuronal mitochondria rapidly declines[190]. Together, these factors render tissue locally susceptible to metabolic stress. To compensate, astrocytes increase their connectivity and draw upon the resources of nearby healthy regions. In our model of unilateral glaucoma, 'nearby' regions extends through the optic nerve to the contralateral eye, a remarkable distance of 10mm.

Without Cx43, astrocytes retain only 5% of their gap junction mediated connectivity[60]. This isolates degenerating regions from the full astrocyte network, causing rapid loss of local neuronal function. Without the resources available from the full metabolic network, neurons lose anterograde transport ability and visual function in corresponding regions of the visual field suffer. However, when astrocyte connectivity is reduced the regions that typically donate their resources are able to better sustain their function when they also encounter neurodegenerative stressors – at least temporarily. Once the second stressor too becomes chronic, the newly stressed region rapidly declines in functionality as well.

Isolating the degenerating region from the greater astrocyte network, therefore, is not a viable treatment for either sustaining function in that region or in the regions that donate their resources. In fact, this isolation renders any region exposed to a neurodegenerative stressor particularly susceptible to that stress. This speaks to the critical importance of astrocyte-mediated metabolic networks in buffering against the stressors we encounter throughout the world. These dynamic networks are capable of rapidly altering in response to neuronal signaling and external stressors to endogenously protect the brain. Future studies should leverage this information to supplement and sustain the metabolic network, which may lead to preventative treatments that further protect the brain against neurodegenerative stressors.

REFERENCES

1 Brown, A. M. & Ransom, B. R. Astrocyte glycogen and brain energy metabolism. *Glia* **55**, 1263-1271, doi:10.1002/glia.20557 (2007).

2 Allen, N. J. & Barres, B. A. NEUROSCIENCE Glia - more than just brain glue. *Nature* **457**, 675-677, doi:10.1038/457675a (2009).

3 Castellano, B. *et al.* A Double Staining Technique for Simultaneous Demonstration of Astrocytes and Microglia in Brain Sections and Astroglial Cell-Cultures. *Journal of Histochemistry & Cytochemistry* **39**, 561-568 (1991).

4 Kim, W. G. *et al.* Regional difference in susceptibility to lipopolysaccharide-induced neurotoxicity in the rat brain: role of microglia. *J Neurosci* **20**, 6309-6316 (2000).

5 Morrison, B. M., Lee, Y. & Rothstein, J. D. Oligodendroglia: metabolic supporters of axons. *Trends Cell Biol* **23**, 644-651, doi:10.1016/j.tcb.2013.07.007 (2013).

6 Meyer, N. *et al.* Oligodendrocytes in the Mouse Corpus Callosum Maintain Axonal Function by Delivery of Glucose. *Cell Rep* **22**, 2383-2394, doi:10.1016/j.celrep.2018.02.022 (2018).

7 Tekkok, S. B., Brown, A. M., Westenbroek, R., Pellerin, L. & Ransom, B. R. Transfer of glycogen-derived lactate from astrocytes to axons via specific monocarboxylate transporters supports mouse optic nerve activity. *J Neurosci Res* **81**, 644-652, doi:10.1002/jnr.20573 (2005).

8 Nishiyama, A., Komitova, M., Suzuki, R. & Zhu, X. Polydendrocytes (NG2 cells): multifunctional cells with lineage plasticity. *Nat Rev Neurosci* **10**, 9-22, doi:10.1038/nrn2495 (2009).

9 Tower, D. B. & Young, O. M. THE ACTIVITIES OF BUTYRYLCHOLINESTERASE AND CARBONIC ANHYDRASE, THE RATE OF ANAEROBIC GLYCOLYSTS, AND THE QUESTION OF A CONSTANT DENSITY OF GLIAL CELLS IN CEREBRAL CORTICES OF VARIOUS MAMMALIAN SPECIES FROM MOUSE TO WHALE. *J Neurochem* **20**, 269-278 (1973).

10 Formichella, C. R., Abella, S. K., Sims, S. M., Cathcart, H. M. & Sappington, R. M. Astrocyte Reactivity: A Biomarker for Retinal Ganglion Cell Health in Retinal Neurodegeneration. *J Clin Cell Immunol* **5**, doi:10.4172/2155-9899.1000188 (2014).

11 Lovatt, D. *et al.* The transcriptome and metabolic gene signature of protoplasmic astrocytes in the adult murine cortex. *J Neurosci* **27**, 12255-12266, doi:10.1523/JNEUROSCI.3404-07.2007 (2007).

12 Sun, D. & Jakobs, T. C. Structural Remodeling of Astrocytes in the Injured CNS. *Neuroscientist* **18**, 567-588, doi:10.1177/1073858411423441 (2012).

13 Oberheim, N. A., Wang, X., Goldman, S. & Nedergaard, M. Astrocytic complexity distinguishes the human brain. *Trends Neurosci* **29**, 547-553, doi:10.1016/j.tins.2006.08.004 (2006).

14 Miller, R. H. & Raff, M. C. Fibrous and protoplasmic astrocytes are biochemically and developmentally distinct. *J Neurosci* **4**, 585-592 (1984).

15 Sosunov, A. A. *et al.* Phenotypic heterogeneity and plasticity of isocortical and hippocampal astrocytes in the human brain. *J Neurosci* **34**, 2285-2298, doi:10.1523/JNEUROSCI.4037-13.2014 (2014).

16 Sun, D., Lye-Barthel, M., Masland, R. H. & Jakobs, T. C. Structural remodeling of fibrous astrocytes after axonal injury. *J Neurosci* **30**, 14008-14019, doi:10.1523/JNEUROSCI.3605-10.2010 (2010).

17 Oberheim, N. A. *et al.* Uniquely hominid features of adult human astrocytes. *J Neurosci* **29**, 3276-3287, doi:10.1523/JNEUROSCI.4707-08.2009 (2009).

18 Swanson, R. A., Morton, M. M., Sagar, S. M. & Sharp, F. R. Sensory stimulation induces local cerebral glycogenolysis: demonstration by autoradiography. *Neuroscience* **51**, 451-461 (1992).

19 Zonta, M. *et al.* Neuron-to-astrocyte signaling is central to the dynamic control of brain microcirculation. *Nat Neurosci* **6**, 43-50, doi:10.1038/nn980 (2003).

20 Abbott, N. J., Ronnback, L. & Hansson, E. Astrocyte-endothelial interactions at the blood-brain barrier. *Nat Rev Neurosci* **7**, 41-53, doi:10.1038/nrn1824 (2006).

21 Montero, T. D. & Orellana, J. A. Hemichannels: new pathways for gliotransmitter release. *Neuroscience* **286**, 45-59, doi:10.1016/j.neuroscience.2014.11.048 (2015).

22 Hipp, J. F. & Siegel, M. BOLD fMRI Correlation Reflects Frequency-Specific Neuronal Correlation. *Curr Biol* **25**, 1368-1374, doi:10.1016/j.cub.2015.03.049 (2015).

23 Mulligan, S. J. & MacVicar, B. A. Calcium transients in astrocyte endfeet cause cerebrovascular constrictions. *Nature* **431**, 195-199, doi:10.1038/nature02827 (2004).

24 Bazargani, N. & Attwell, D. Astrocyte calcium signaling: the third wave. *Nat Neurosci* **19**, 182-189, doi:10.1038/nn.4201 (2016).

25 Loaiza, A., Porras, O. H. & Barros, L. F. Glutamate triggers rapid glucose transport stimulation in astrocytes as evidenced by real-time confocal microscopy. *Journal of Neuroscience* **23**, 7337-7342 (2003).

26 Gourine, A. V. *et al.* Astrocytes control breathing through pH-dependent release of ATP. *Science* **329**, 571-575, doi:10.1126/science.1190721 (2010).

27 Han, X. *et al.* Forebrain engraftment by human glial progenitor cells enhances synaptic plasticity and learning in adult mice. *Cell Stem Cell* **12**, 342-353, doi:10.1016/j.stem.2012.12.015 (2013).

28 Cahoy, J. D. *et al.* A transcriptome database for astrocytes, neurons, and oligodendrocytes: a new resource for understanding brain development and function. *J Neurosci* **28**, 264-278, doi:10.1523/JNEUROSCI.4178-07.2008 (2008).

29 Chung, W. S. *et al.* Astrocytes mediate synapse elimination through MEGF10 and MERTK pathways. *Nature* **504**, 394-+, doi:10.1038/nature12776 (2013).

30 Tasdemir-Yilmaz, O. E. & Freeman, M. R. Astrocytes engage unique molecular programs to engulf pruned neuronal debris from distinct subsets of neurons. *Genes Dev* **28**, 20-33, doi:10.1101/gad.229518.113 (2014).

31 Carmignoto, G. & Haydon, P. G. Astrocyte calcium signaling and epilepsy. *Glia* **60**, 1227-1233, doi:10.1002/glia.22318 (2012).

32 Hamby, M. E. *et al.* Inflammatory mediators alter the astrocyte transcriptome and calcium signaling elicited by multiple G-protein-coupled receptors. *J Neurosci* **32**, 14489-14510, doi:10.1523/JNEUROSCI.1256-12.2012 (2012).

33 Rossi, D. *et al.* Defective tumor necrosis factor-alpha-dependent control of astrocyte glutamate release in a transgenic mouse model of Alzheimer disease. *J Biol Chem* **280**, 42088-42096, doi:10.1074/jbc.M504124200 (2005).

34 Lee, W. *et al.* Enhanced Ca^{2+}-dependent glutamate release from astrocytes of the BACHD Huntington's disease mouse model. *Neurobiology of Disease* **58**, 192-199, doi:10.1016/j.nbd.2013.06.002 (2013).

35 Bezzi, P. *et al.* CXCR4-activated astrocyte glutamate release via TNFa: amplification by microglia triggers neurotoxicity. *Nature Neuroscience* **4**, 702-710, doi:Doi 10.1038/89490 (2001).

36 Sun, D., Moore, S. & Jakobs, T. C. Optic nerve astrocyte reactivity protects function in experimental glaucoma and other nerve injuries. *J Exp Med* **214**, 1411-1430, doi:10.1084/jem.20160412 (2017).

37 Shinotsuka, T., Yasui, M. & Nuriya, M. Astrocytic gap junctional networks suppress cellular damage in an in vitro model of ischemia. *Biochem Biophys Res Commun* **444**, 171-176, doi:10.1016/j.bbrc.2014.01.035 (2014).

38 Li, L. *et al.* Protective role of reactive astrocytes in brain ischemia. *J Cereb Blood Flow Metab* **28**, 468-481, doi:10.1038/sj.jcbfm.9600546 (2008).

39 Zhou, X. H. *et al.* Involvement of inflammation, degradation, and apoptosis in a mouse model of glaucoma. *Journal of Biological Chemistry* **280**, 31240-31248, doi:10.1074/jbc.M502641200 (2005).

40 Colombo, E. & Farina, C. Astrocytes: Key Regulators of Neuroinflammation. *Trends Immunol* **37**, 608-620, doi:10.1016/j.it.2016.06.006 (2016).

41 Jang, E. *et al.* Phenotypic polarization of activated astrocytes: the critical role of lipocalin-2 in the classical inflammatory activation of astrocytes. *J Immunol* **191**, 5204-5219, doi:10.4049/jimmunol.1301637 (2013).

42 Sofroniew, M. V. Molecular dissection of reactive astrogliosis and glial scar formation. *Trends Neurosci* **32**, 638-647, doi:10.1016/j.tins.2009.08.002 (2009).

43 Yuan, Y. M. & He, C. The glial scar in spinal cord injury and repair. *Neurosci Bull* **29**, 421-435, doi:10.1007/s12264-013-1358-3 (2013).

44 Goritz, C. *et al.* A pericyte origin of spinal cord scar tissue. *Science* **333**, 238-242, doi:10.1126/science.1203165 (2011).

45 Park, K. K. *et al.* Promoting axon regeneration in the adult CNS by modulation of the PTEN/mTOR pathway. *Science* **322**, 963-966, doi:10.1126/science.1161566 (2008).

46 Liddelow, S. A. *et al.* Neurotoxic reactive astrocytes are induced by activated microglia. *Nature* **541**, 481-487, doi:10.1038/nature21029 (2017).

47 Sofroniew, M. V. & Vinters, H. V. Astrocytes: biology and pathology. *Acta Neuropathol* **119**, 7-35, doi:10.1007/s00401-009-0619-8 (2010).

48 Braak, H. & Braak, E. Neuropathological stageing of Alzheimer-related changes. *Acta Neuropathol* **82**, 239-259 (1991).

49 Goedert, M. & Spillantini, M. G. A century of Alzheimer's disease. *Science* **314**, 777-781, doi:10.1126/science.1132814 (2006).

50 Sidoryk-Wegrzynowicz, M. *et al.* Astrocytes in mouse models of tauopathies acquire early deficits and lose neurosupportive functions. *Acta Neuropathol Commun* **5**, 89, doi:10.1186/s40478-017-0478-9 (2017).

51 Hampton, D. W. *et al.* Cell-mediated neuroprotection in a mouse model of human tauopathy. *J Neurosci* **30**, 9973-9983, doi:10.1523/JNEUROSCI.0834-10.2010 (2010).

52 Falkowska, A. *et al.* Energy Metabolism of the Brain, Including the Cooperation between Astrocytes and Neurons, Especially in the Context of Glycogen Metabolism. *International Journal of Molecular Sciences* **16**, 25959-25981, doi:10.3390/ijms161125939 (2015).

53 Braak, H., Sastre, M. & Del Tredici, K. Development of alpha-synuclein immunoreactive astrocytes in the forebrain parallels stages of intraneuronal pathology in sporadic Parkinson's disease. *Acta Neuropathol* **114**, 231-241, doi:10.1007/s00401-007-0244-3 (2007).

54 Wakabayashi, K., Hayashi, S., Yoshimoto, M., Kudo, H. & Takahashi, H. NACP/alpha-synuclein-positive filamentous inclusions in astrocytes and oligodendrocytes of Parkinson's disease brains. *Acta Neuropathol* **99**, 14-20 (2000).

55 Emsley, J. G. & Macklis, J. D. Astroglial heterogeneity closely reflects the neuronal-defined anatomy of the adult murine CNS. *Neuron Glia Biol* **2**, 175-186, doi:10.1017/S1740925X06000202 (2006).

56 Elstner, M. *et al.* Expression analysis of dopaminergic neurons in Parkinson's disease and aging links transcriptional dysregulation of energy metabolism to cell death. *Acta Neuropathol* **122**, 75-86, doi:10.1007/s00401-011-0828-9 (2011).

57 Dienel, G. A. & Cruz, N. F. Astrocyte activation in working brain: energy supplied by minor substrates. *Neurochem Int* **48**, 586-595, doi:10.1016/j.neuint.2006.01.004 (2006).

58 Ding, F., Yao, J., Rettberg, J. R., Chen, S. & Brinton, R. D. Early decline in glucose transport and metabolism precedes shift to ketogenic system in female aging and Alzheimer's mouse brain: implication for bioenergetic intervention. *PLoS One* **8**, e79977, doi:10.1371/journal.pone.0079977 (2013).

59 Giaume, C. & Theis, M. Pharmacological and genetic approaches to study connexin-mediated channels in glial cells of the central nervous system. *Brain Res Rev* **63**, 160-176, doi:10.1016/j.brainresrev.2009.11.005 (2010).

60 Dermietzel, R. *et al.* Connexin43 null mice reveal that astrocytes express multiple connexins. *Brain Research Reviews* **32**, 45-56, doi:Doi 10.1016/S0165-0173(99)00067-3 (2000).

61 Giaume, C. & Naus, C. C. Connexins, gap junctions, and glia. *Wiley Interdisciplinary Reviews: Membrane Transport and Signaling* **2**, 133-142, doi:10.1002/wmts.87 (2013).

62 Koulakoff, A., Ezan, P. & Giaume, C. Neurons control the expression of connexin 30 and connexin 43 in mouse cortical astrocytes. *Glia* **56**, 1299-1311, doi:10.1002/glia.20698 (2008).

63 Reaume, A. G. *et al.* Cardiac malformation in neonatal mice lacking connexin43. *Science* **267**, 1831-1834 (1995).

64 Kerr, N. M., Johnson, C. S., Green, C. R. & Danesh-Meyer, H. V. Gap junction protein connexin43 (GJA1) in the human glaucomatous optic nerve head and retina. *J Clin Neurosci* **18**, 102-108, doi:10.1016/j.jocn.2010.06.002 (2011).

65 Frisch, C. *et al.* Mice with astrocyte-directed inactivation of connexin43 exhibit increased exploratory behaviour, impaired motor capacities, and changes in brain acetylcholine levels. *Eur J Neurosci* **18**, 2313-2318 (2003).

66 Nagy, J. I. *et al.* Connexin26 in adult rodent central nervous system: Demonstration at astrocytic gap junctions and colocalization with connexin30 and connexin43. *Journal of Comparative Neurology* **441**, 302-323, doi:DOI 10.1002/cne.1414 (2001).

67 Nagy, J. I., Patel, D., Ochalski, P. A. Y. & Stelmack, G. L. Connexin30 in rodent, cat and human brain: Selective expression in gray matter astrocytes, co-localization with connexin43 at gap junctions and late developmental appearance. *Neuroscience* **88**, 447-468, doi:Doi 10.1016/S0306-4522(98)00191-2 (1999).

68 Froes, M. M. *et al.* Gap-junctional coupling between neurons and astrocytes in primary central nervous system cultures. *Proceedings of the National Academy of Sciences of the United States of America* **96**, 7541-7546, doi:DOI 10.1073/pnas.96.13.7541 (1999).

69 Alvarez-Maubecin, V., Garcia-Hernandez, F., Williams, J. T. & Van Bocksaele, E. J. Functional coupling between neurons and glia. *Journal of Neuroscience* **20**, 4091-4098 (2000).

70 Bittman, K., Becker, D. L., Cicirata, F. & Parnavelas, J. G. Connexin expression in homotypic and heterotypic cell coupling in the developing cerebral cortex. *J Comp Neurol* **443**, 201-212 (2002).

71 Tress, O. *et al.* Panglial gap junctional communication is essential for maintenance of myelin in the CNS. *J Neurosci* **32**, 7499-7518, doi:10.1523/JNEUROSCI.0392-12.2012 (2012).

72 Nagy, J. I., Dudek, F. E. & Rash, J. E. Update on connexins and gap junctions in neurons and glia in the mammalian nervous system. *Brain Res Brain Res Rev* **47**, 191-215, doi:10.1016/j.brainresrev.2004.05.005 (2004).

73 Orthmann-Murphy, J. L., Freidin, M., Fischer, E., Scherer, S. S. & Abrams, C. K. Two distinct heterotypic channels mediate gap junction coupling between astrocyte and oligodendrocyte connexins. *Journal of Neuroscience* **27**, 13949-13957, doi:10.1523/Jneurosci.3395-07.2007 (2007).

74 Cooper, M. L., Collyer, J. W. & Calkins, D. J. Astrocyte remodeling without gliosis precedes optic nerve Axonopathy. *Acta Neuropathologica Communications* **6**, doi:ARTN 38

10.1186/s40478-018-0542-0 (2018).

75 Wang, Z. *et al.* Specific metabolic rates of major organs and tissues across adulthood: evaluation by mechanistic model of resting energy expenditure. *Am J Clin Nutr* **92**, 1369-1377, doi:10.3945/ajcn.2010.29885 (2010).

76 Kety, S. S. & Schmidt, C. F. The Nitrous Oxide Method for the Quantitative Determination of Cerebral Blood Flow in Man: Theory, Procedure and Normal Values. *J Clin Invest* **27**, 476-483, doi:10.1172/JCI101994 (1948).

77 Sokoloff, L. Localization of functional activity in the central nervous system by measurement of glucose utilization with radioactive deoxyglucose. *J Cereb Blood Flow Metab* **1**, 7-36, doi:10.1038/jcbfm.1981.4 (1981).

78 Petit, J., Burlet-Godinot, S., Dunant, E., Lengacher, S. & Magistretti, P. J. Expression of genes related to brain energy metabolism following pharmacological and instrumental short sleep deprivation. *Sleep* **31**, A137-A138 (2008).

79 Nehlig, A. Brain uptake and metabolism of ketone bodies in animal models. *Prostaglandins Leukot Essent Fatty Acids* **70**, 265-275, doi:10.1016/j.plefa.2003.07.006 (2004).

80 Zielke, H. R., Zielke, C. L. & Baab, P. J. Direct measurement of oxidative metabolism in the living brain by microdialysis: a review. *J Neurochem* **109 Suppl 1**, 24-29, doi:10.1111/j.1471-4159.2009.05941.x (2009).

81 van Hall, G. *et al.* Blood lactate is an important energy source for the human brain. *Journal of Cerebral Blood Flow and Metabolism* **29**, 1121-1129, doi:10.1038/jcbfm.2009.35 (2009).

82 Attwell, D. *et al.* Glial and neuronal control of brain blood flow. *Nature* **468**, 232-243, doi:10.1038/nature09613 (2010).

83 Iadecola, C. & Nedergaard, M. Glial regulation of the cerebral microvasculature. *Nat Neurosci* **10**, 1369-1376, doi:10.1038/nn2003 (2007).

84 Bernardinelli, Y., Magistretti, P. J. & Chatton, J. Y. Astrocytes generate Na+-mediated metabolic waves. *Proc Natl Acad Sci U S A* **101**, 14937-14942, doi:10.1073/pnas.0405315101 (2004).

85 Brown, A. M. Brain glycogen re-awakened. *J Neurochem* **89**, 537-552, doi:10.1111/j.1471-4159.2004.02421.x (2004).

86 Pelletier, J., Bellot, G., Pouyssegur, J. & Mazure, N. M. Biochemical titration of glycogen in vitro. *J Vis Exp*, e50465, doi:10.3791/50465 (2013).

87 Wender, R. *et al.* Astrocytic glycogen influences axon function and survival during glucose deprivation in central white matter. *J Neurosci* **20**, 6804-6810 (2000).

88 Louzao, M. C. *et al.* "Fluorescent glycogen" formation with sensibility for in vivo and in vitro detection. *Glycoconj J* **25**, 503-510, doi:10.1007/s10719-007-9075-7 (2008).

89 Hertz, L., Peng, L. & Dienel, G. A. Energy metabolism in astrocytes: high rate of oxidative metabolism and spatiotemporal dependence on glycolysis/glycogenolysis. *J Cereb Blood Flow Metab* **27**, 219-249, doi:10.1038/sj.jcbfm.9600343 (2007).

90 Vilchez, D. *et al.* Mechanism suppressing glycogen synthesis in neurons and its demise in progressive myoclonus epilepsy. *Nat Neurosci* **10**, 1407-1413, doi:10.1038/nn1998 (2007).

91 Cruz, N. F. & Dienel, G. A. High glycogen levels in brains of rats with minimal environmental stimuli: implications for metabolic contributions of working astrocytes. *J Cereb Blood Flow Metab* **22**, 1476-1489, doi:10.1097/01.WCB.0000034362.37277.C0 (2002).

92 Rennie, M. J., Winder, W. W. & Holloszy, J. O. A sparing effect of increased plasma fatty acids on muscle and liver glycogen content in the exercising rat. *Biochemical Journal* **156**, 647-655, doi:10.1042/bj1560647 (1976).

93 Phelps, C. H. Barbiturate-induced glycogen accumulation in brain. An electron microscopic study. *Brain Res* **39**, 225-234 (1972).

94 Magistretti, P. J., Morrison, J. H., Shoemaker, W. J., Sapin, V. & Bloom, F. E. Vasoactive intestinal polypeptide induces glycogenolysis in mouse cortical slices: a possible regulatory mechanism for the local control of energy metabolism. *Proc Natl Acad Sci U S A* **78**, 6535-6539 (1981).

95 Magistretti, P. J., Manthorpe, M., Bloom, F. E. & Varon, S. Functional receptors for vasoactive intestinal polypeptide in cultured astroglia from neonatal rat brain. *Regulatory Peptides* **6**, 71-80, doi:10.1016/0167-0115(83)90136-2 (1983).

96 Brown, A. M. *et al.* Astrocyte glycogen metabolism is required for neural activity during aglycemia or intense stimulation in mouse white matter. *J Neurosci Res* **79**, 74-80, doi:10.1002/jnr.20335 (2005).

97 Gibbs, M. E., Anderson, D. G. & Hertz, L. Inhibition of glycogenolysis in astrocytes interrupts memory consolidation in young chickens. *Glia* **54**, 214-222, doi:10.1002/glia.20377 (2006).

98 Suzuki, A. *et al.* Astrocyte-neuron lactate transport is required for long-term memory formation. *Cell* **144**, 810-823, doi:10.1016/j.cell.2011.02.018 (2011).

99 Alberini, C. M., Cruz, E., Descalzi, G., Bessieres, B. & Gao, V. Astrocyte glycogen and lactate: New insights into learning and memory mechanisms. *Glia* **66**, 1244-1262, doi:10.1002/glia.23250 (2018).

100 Prats, C. *et al.* An optimized histochemical method to assess skeletal muscle glycogen and lipid stores reveals two metabolically distinct populations of type I muscle fibers. *PLoS One* **8**, e77774, doi:10.1371/journal.pone.0077774 (2013).

101 Hashimoto, T., Hussien, R., Cho, H. S., Kaufer, D. & Brooks, G. A. Evidence for the mitochondrial lactate oxidation complex in rat neurons: demonstration of an essential component of brain lactate shuttles. *PLoS One* **3**, e2915, doi:10.1371/journal.pone.0002915 (2008).

102 Coughlin, L., Morrison, R. S., Horner, P. J. & Inman, D. M. Mitochondrial morphology differences and mitophagy deficit in murine glaucomatous optic nerve. *Invest Ophthalmol Vis Sci* **56**, 1437-1446, doi:10.1167/iovs.14-16126 (2015).

103 Yan, M. H., Wang, X. & Zhu, X. Mitochondrial defects and oxidative stress in Alzheimer disease and Parkinson disease. *Free Radic Biol Med* **62**, 90-101, doi:10.1016/j.freeradbiomed.2012.11.014 (2013).

104 Duarte, J. M., Girault, F. M. & Gruetter, R. Brain energy metabolism measured by (13)C magnetic resonance spectroscopy in vivo upon infusion of [3-(13)C]lactate. *J Neurosci Res* **93**, 1009-1018, doi:10.1002/jnr.23531 (2015).

105 Schurr, A., Miller, J. J., Payne, R. S. & Rigor, B. M. An increase in lactate output by brain tissue serves to meet the energy needs of glutamate-activated neurons. *J Neurosci* **19**, 34-39 (1999).

106 Boumezbeur, F. *et al.* The contribution of blood lactate to brain energy metabolism in humans measured by dynamic 13C nuclear magnetic resonance spectroscopy. *J Neurosci* **30**, 13983-13991, doi:10.1523/JNEUROSCI.2040-10.2010 (2010).

107 Gallagher, C. N. *et al.* The human brain utilizes lactate via the tricarboxylic acid cycle: a 13C-labelled microdialysis and high-resolution nuclear magnetic resonance study. *Brain* **132**, 2839-2849, doi:10.1093/brain/awp202 (2009).

108 Schurr, A. & Payne, R. S. Lactate, not pyruvate, is neuronal aerobic glycolysis end product: an in vitro electrophysiological study. *Neuroscience* **147**, 613-619, doi:10.1016/j.neuroscience.2007.05.002 (2007).

109 Volkenhoff, A. *et al.* Glial Glycolysis Is Essential for Neuronal Survival in Drosophila. *Cell Metab* **22**, 437-447, doi:10.1016/j.cmet.2015.07.006 (2015).

110 Liu, L., MacKenzie, K. R., Putluri, N., Maletic-Savatic, M. & Bellen, H. J. The Glia-Neuron Lactate Shuttle and Elevated ROS Promote Lipid Synthesis in Neurons and Lipid Droplet Accumulation in Glia via APOE/D. *Cell Metab* **26**, 719-737 e716, doi:10.1016/j.cmet.2017.08.024 (2017).

111 Perge, J. A., Koch, K., Miller, R., Sterling, P. & Balasubramanian, V. How the Optic Nerve Allocates Space, Energy Capacity, and Information. *Journal of Neuroscience* **29**, 7917-7928, doi:10.1523/Jneurosci.5200-08.2009 (2009).

112 Herrero-Mendez, A. *et al.* The bioenergetic and antioxidant status of neurons is controlled by continuous degradation of a key glycolytic enzyme by APC/C-Cdh1. *Nat Cell Biol* **11**, 747-752, doi:10.1038/ncb1881 (2009).

113 Boumezbeur, F. *et al.* Altered brain mitochondrial metabolism in healthy aging as assessed by in vivo magnetic resonance spectroscopy. *J Cereb Blood Flow Metab* **30**, 211-221, doi:10.1038/jcbfm.2009.197 (2010).

114 Lebon, V. *et al.* Astroglial contribution to brain energy metabolism in humans revealed by 13C nuclear magnetic resonance spectroscopy: elucidation of the dominant pathway for neurotransmitter glutamate repletion and measurement of astrocytic oxidative metabolism. *J Neurosci* **22**, 1523-1531 (2002).

115 Itoh, Y. *et al.* Dichloroacetate effects on glucose and lactate oxidation by neurons and astroglia in vitro and on glucose utilization by brain in vivo. *Proc Natl Acad Sci U S A* **100**, 4879-4884, doi:10.1073/pnas.0831078100 (2003).

116 Bouzier-Sore, A. K. *et al.* Competition between glucose and lactate as oxidative energy substrates in both neurons and astrocytes: a comparative NMR study. *Eur J Neurosci* **24**, 1687-1694, doi:10.1111/j.1460-9568.2006.05056.x (2006).

117 Almeida, A., Moncada, S. & Bolanos, J. P. Nitric oxide switches on glycolysis through the AMP protein kinase and 6-phosphofructo-2-kinase pathway. *Nature Cell Biology* **6**, 45-U49, doi:10.1038/ncb1080 (2004).

118 Lopez-Fabuel, I. *et al.* Complex I assembly into supercomplexes determines differential mitochondrial ROS production in neurons and astrocytes. *Proc Natl Acad Sci U S A* **113**, 13063-13068, doi:10.1073/pnas.1613701113 (2016).

119 Attwell, D. & Laughlin, S. B. An energy budget for signaling in the grey matter of the brain. *J Cereb Blood Flow Metab* **21**, 1133-1145, doi:10.1097/00004647-200110000-00001 (2001).

120 Barros, L. F. *et al.* Preferential transport and metabolism of glucose in Bergmann glia over Purkinje cells: a multiphoton study of cerebellar slices. *Glia* **57**, 962-970, doi:10.1002/glia.20820 (2009).

121 Nehlig, A., Wittendorp-Rechenmann, E. & Lam, C. D. Selective uptake of [14C]2-deoxyglucose by neurons and astrocytes: high-resolution microautoradiographic imaging by cellular 14C-trajectography combined with immunohistochemistry. *J Cereb Blood Flow Metab* **24**, 1004-1014, doi:10.1097/01.WCB.0000128533.84196.D8 (2004).

122 Chuquet, J., Quilichini, P., Nimchinsky, E. A. & Buzsaki, G. Predominant enhancement of glucose uptake in astrocytes versus neurons during activation of the somatosensory cortex. *J Neurosci* **30**, 15298-15303, doi:10.1523/JNEUROSCI.0762-10.2010 (2010).

123 Pellerin, L. & Magistretti, P. J. Glutamate Uptake into Astrocytes Stimulates Aerobic Glycolysis - a Mechanism Coupling Neuronal-Activity to Glucose-Utilization. *Proceedings of the National Academy of Sciences of the United States of America* **91**, 10625-10629, doi:DOI 10.1073/pnas.91.22.10625 (1994).

124 Schmidt, S. *et al.* Neuronal functions, feeding behavior, and energy balance in Slc2a3+/- mice. *Am J Physiol Endocrinol Metab* **295**, E1084-1094, doi:10.1152/ajpendo.90491.2008 (2008).

125 Stuart, C. A. *et al.* Brain glucose transporter (Glut3) haploinsufficiency does not impair mouse brain glucose uptake. *Brain Res* **1384**, 15-22, doi:10.1016/j.brainres.2011.02.014 (2011).

126 Wang, D. *et al.* A mouse model for Glut-1 haploinsufficiency. *Hum Mol Genet* **15**, 1169-1179, doi:10.1093/hmg/ddl032 (2006).

127 Rinholm, J. E. *et al.* Regulation of oligodendrocyte development and myelination by glucose and lactate. *J Neurosci* **31**, 538-548, doi:10.1523/JNEUROSCI.3516-10.2011 (2011).

128 Funfschilling, U. *et al.* Glycolytic oligodendrocytes maintain myelin and long-term axonal integrity. *Nature* **485**, 517-521, doi:10.1038/nature11007 (2012).

129 Liu, Y. *et al.* Ubiquilin-1 protects cells from oxidative stress and ischemic stroke caused tissue injury in mice. *J Neurosci* **34**, 2813-2821, doi:10.1523/JNEUROSCI.3541-13.2014 (2014).

130 Abdul-Muneer, P. M., Chandra, N. & Haorah, J. Interactions of oxidative stress and neurovascular inflammation in the pathogenesis of traumatic brain injury. *Mol Neurobiol* **51**, 966-979, doi:10.1007/s12035-014-8752-3 (2015).

131 Mosconi, L., Pupi, A. & De Leon, M. J. Brain glucose hypometabolism and oxidative stress in preclinical Alzheimer's disease. *Ann N Y Acad Sci* **1147**, 180-195, doi:10.1196/annals.1427.007 (2008).

132 Wilson, J. X. Antioxidant defense of the brain: a role for astrocytes. *Can J Physiol Pharmacol* **75**, 1149-1163 (1997).

133 Anderson, G. & Maes, M. Neurodegeneration in Parkinson's disease: interactions of oxidative stress, tryptophan catabolites and depression with mitochondria and sirtuins. *Mol Neurobiol* **49**, 771-783, doi:10.1007/s12035-013-8554-z (2014).

134 Payne, S. C., Bartlett, C. A., Harvey, A. R., Dunlop, S. A. & Fitzgerald, M. Myelin Sheath Decompaction, Axon Swelling, and Functional Loss during Chronic Secondary Degeneration in Rat Optic Nerve. *Investigative Ophthalmology & Visual Science* **53**, 6093-6101, doi:10.1167/iovs.12-10080 (2012).

135 Shih, A. Y. *et al.* Coordinate regulation of glutathione biosynthesis and release by Nrf2-expressing glia potently protects neurons from oxidative stress. *J Neurosci* **23**, 3394-3406 (2003).

136 Fernandez-Fernandez, S., Almeida, A. & Bolanos, J. P. Antioxidant and bioenergetic coupling between neurons and astrocytes. *Biochem J* **443**, 3-11, doi:10.1042/BJ20111943 (2012).

137 Parfenova, H., Leffler, C. W., Basuroy, S., Liu, J. & Fedinec, A. L. Antioxidant roles of heme oxygenase, carbon monoxide, and bilirubin in cerebral circulation during seizures. *J Cereb Blood Flow Metab* **32**, 1024-1034, doi:10.1038/jcbfm.2012.13 (2012).

138 Almeida, A., Almeida, J., Bolanos, J. P. & Moncada, S. Different responses of astrocytes and neurons to nitric oxide: the role of glycolytically generated ATP in astrocyte protection. *Proc Natl Acad Sci U S A* **98**, 15294-15299, doi:10.1073/pnas.261560998 (2001).

139 Vargas, M. R. & Johnson, J. A. The Nrf2-ARE cytoprotective pathway in astrocytes. *Expert Rev Mol Med* **11**, e17, doi:10.1017/S1462399409001094 (2009).

140 Sancheti, H. *et al.* Hypermetabolic state in the 7-month-old triple transgenic mouse model of Alzheimer's disease and the effect of lipoic acid: a 13C-NMR study. *J Cereb Blood Flow Metab* **34**, 1749-1760, doi:10.1038/jcbfm.2014.137 (2014).

141 Mosconi, L. *et al.* Declining brain glucose metabolism in normal individuals with a maternal history of Alzheimer disease. *Neurology* **72**, 513-520, doi:10.1212/01.wnl.0000333247.51383.43 (2009).

142 Dringen, R. Metabolism and functions of glutathione in brain. *Progress in Neurobiology* **62**, 649-671, doi:10.1016/s0301-0082(99)00060-x (2000).

143 Ben-Yoseph, O., Boxer, P. A. & Ross, B. D. Assessment of the role of the glutathione and pentose phosphate pathways in the protection of primary cerebrocortical cultures from oxidative stress. *J Neurochem* **66**, 2329-2337 (1996).

144 Allaman, I. *et al.* Amyloid-beta aggregates cause alterations of astrocytic metabolic phenotype: impact on neuronal viability. *J Neurosci* **30**, 3326-3338, doi:10.1523/JNEUROSCI.5098-09.2010 (2010).

145 Stokin, G. B. *et al.* Axonopathy and transport deficits early in the pathogenesis of Alzheimer's disease. *Science* **307**, 1282-1288, doi:10.1126/science.1105681 (2005).

146 Terry, R. D. The Pathogenesis of Alzheimer Disease: An Alternative to the Amyloid Hypothesis. *Journal of Neuropathology and Experimental Neurology* **55**, 1023-1025, doi:10.1097/00005072-199655100-00001 (1996).

147 Williamson, T. L. & Cleveland, D. W. Slowing of axonal transport is a very early event in the toxicity of ALS–linked SOD1 mutants to motor neurons. *Nature Neuroscience* **2**, 50-56, doi:10.1038/4553 (1999).

148 Kawamura, Y. *et al.* Morphometric Comparison of the Vulnerability of Peripheral Motor and Sensory Neurons in Amyotrophic Lateral Sclerosis. *Journal of Neuropathology & Experimental Neurology* **40**, 667-675, doi:10.1097/00005072-198111000-00008 (1981).

149 Bruijn, L. I. *et al.* ALS-Linked SOD1 Mutant G85R Mediates Damage to Astrocytes and Promotes Rapidly Progressive Disease with SOD1-Containing Inclusions. *Neuron* **18**, 327-338, doi:10.1016/s0896-6273(00)80272-x (1997).

150 George, S., Rey, N. L., Reichenbach, N., Steiner, J. A. & Brundin, P. alpha-Synuclein: the long distance runner. *Brain Pathol* **23**, 350-357, doi:10.1111/bpa.12046 (2013).

151 Ubeda-Banon, I., Saiz-Sanchez, D., de la Rosa-Prieto, C. & Martinez-Marcos, A. alpha-Synuclein in the olfactory system in Parkinson's disease: role of neural connections on spreading pathology. *Brain Struct Funct* **219**, 1513-1526, doi:10.1007/s00429-013-0651-2 (2014).

152 Szebenyi, G. *et al.* Neuropathogenic Forms of Huntingtin and Androgen Receptor Inhibit Fast Axonal Transport. *Neuron* **40**, 41-52, doi:10.1016/s0896-6273(03)00569-5 (2003).

153 Crish, S. D., Sappington, R. M., Inman, D. M., Horner, P. J. & Calkins, D. J. Distal axonopathy with structural persistence in glaucomatous neurodegeneration. *Proceedings of the National Academy of Sciences of the United States of America* **107**, 5196-5201, doi:10.1073/pnas.0913141107 (2010).

154 De Vos, K. J., Grierson, A. J., Ackerley, S. & Miller, C. C. Role of axonal transport in neurodegenerative diseases. *Annu Rev Neurosci* **31**, 151-173, doi:10.1146/annurev.neuro.31.061307.090711 (2008).

155 Puls, I. *et al.* Mutant dynactin in motor neuron disease. *Nat Genet* **33**, 455-456, doi:10.1038/ng1123 (2003).

156 Zhao, C. *et al.* Charcot-Marie-Tooth Disease Type 2A Caused by Mutation in a Microtubule Motor KIF1Bβ. *Cell* **105**, 587-597, doi:10.1016/s0092-8674(01)00363-4 (2001).

157 Chang, D. T., Rintoul, G. L., Pandipati, S. & Reynolds, I. J. Mutant huntingtin aggregates impair mitochondrial movement and trafficking in cortical neurons. *Neurobiol Dis* **22**, 388-400, doi:10.1016/j.nbd.2005.12.007 (2006).

158 Ackerley, S. *et al.* p38alpha stress-activated protein kinase phosphorylates neurofilaments and is associated with neurofilament pathology in amyotrophic lateral sclerosis. *Mol Cell Neurosci* **26**, 354-364, doi:10.1016/j.mcn.2004.02.009 (2004).

159 Miller, K. E. & Sheetz, M. P. Axonal mitochondrial transport and potential are correlated. *J Cell Sci* **117**, 2791-2804, doi:10.1242/jcs.01130 (2004).

160 De Vos, K. J. *et al.* Familial amyotrophic lateral sclerosis-linked SOD1 mutants perturb fast axonal transport to reduce axonal mitochondria content. *Hum Mol Genet* **16**, 2720-2728, doi:10.1093/hmg/ddm226 (2007).

161 Prokop, A. The intricate relationship between microtubules and their associated motor proteins during axon growth and maintenance. *Neural Dev* **8**, 17, doi:10.1186/1749-8104-8-17 (2013).

162 Westphal, D., Dewson, G., Czabotar, P. E. & Kluck, R. M. Molecular biology of Bax and Bak activation and action. *Biochimica et Biophysica Acta (BBA) - Molecular Cell Research* **1813**, 521-531, doi:10.1016/j.bbamcr.2010.12.019 (2011).

163 Wang, C. & Youle, R. J. The role of mitochondria in apoptosis*. *Annu Rev Genet* **43**, 95-118, doi:10.1146/annurev-genet-102108-134850 (2009).

164 Pavlov, P. F. *et al.* Mitochondrial gamma-secretase participates in the metabolism of mitochondria-associated amyloid precursor protein. *FASEB J* **25**, 78-88, doi:10.1096/fj.10-157230 (2011).

165 Zampese, E. *et al.* Presenilin 2 modulates endoplasmic reticulum (ER)-mitochondria interactions and Ca2+ cross-talk. *Proc Natl Acad Sci U S A* **108**, 2777-2782, doi:10.1073/pnas.1100735108 (2011).

166 Narendra, D., Tanaka, A., Suen, D. F. & Youle, R. J. Parkin is recruited selectively to impaired mitochondria and promotes their autophagy. *J Cell Biol* **183**, 795-803, doi:10.1083/jcb.200809125 (2008).

167 Ordonez, D. G., Lee, M. K. & Feany, M. B. alpha-synuclein Induces Mitochondrial Dysfunction through Spectrin and the Actin Cytoskeleton. *Neuron* **97**, 108-124 e106, doi:10.1016/j.neuron.2017.11.036 (2018).

168 Yano, H. *et al.* Inhibition of mitochondrial protein import by mutant huntingtin. *Nat Neurosci* **17**, 822-831, doi:10.1038/nn.3721 (2014).

169 Kujoth, G. C. *et al.* Mitochondrial DNA mutations, oxidative stress, and apoptosis in mammalian aging. *Science* **309**, 481-484, doi:10.1126/science.1112125 (2005).

170 Smigrodzki, R., Parks, J. & Parker, W. D. High frequency of mitochondrial complex I mutations in Parkinson's disease and aging. *Neurobiol Aging* **25**, 1273-1281, doi:10.1016/j.neurobiolaging.2004.02.020 (2004).

171 Cottrell, D. A. *et al.* Cytochrome c oxidase deficient cells accumulate in the hippocampus and choroid plexus with age. *Neurobiology of Aging* **22**, 265-272, doi:10.1016/s0197-4580(00)00234-7 (2001).

172 Anderson, S. *et al.* Sequence and organization of the human mitochondrial genome. *Nature* **290**, 457-465, doi:10.1038/290457a0 (1981).

173 Taylor, R. W. & Turnbull, D. M. Mitochondrial DNA mutations in human disease. *Nat Rev Genet* **6**, 389-402, doi:10.1038/nrg1606 (2005).

174 Simon, D. K. *et al.* Low mutational burden of individual acquired mitochondrial DNA mutations in brain. *Genomics* **73**, 113-116, doi:10.1006/geno.2001.6515 (2001).

175 Chinnery, P. F. *et al.* Point Mutations of the mtDNA Control Region in Normal and Neurodegenerative Human Brains. *The American Journal of Human Genetics* **68**, 529-532, doi:10.1086/318204 (2001).

176 Jazin, E. E., Cavelier, L., Eriksson, I., Oreland, L. & Gyllensten, U. Human brain contains high levels of heteroplasmy in the noncoding regions of mitochondrial DNA. *Proceedings*

of the National Academy of Sciences **93**, 12382-12387, doi:10.1073/pnas.93.22.12382 (1996).

177 Tzoulis, C. *et al.* Molecular pathogenesis of polymerase gamma-related neurodegeneration. *Ann Neurol* **76**, 66-81, doi:10.1002/ana.24185 (2014).

178 Luoma, P. *et al.* Parkinsonism, premature menopause, and mitochondrial DNA polymerase γ mutations: clinical and molecular genetic study. *The Lancet* **364**, 875-882, doi:10.1016/s0140-6736(04)16983-3 (2004).

179 Schriner, S. E. *et al.* Extension of murine life span by overexpression of catalase targeted to mitochondria. *Science* **308**, 1909-1911, doi:10.1126/science.1106653 (2005).

180 Lu, T. *et al.* Gene regulation and DNA damage in the ageing human brain. *Nature* **429**, 883-891, doi:10.1038/nature02661 (2004).

181 Dorostkar, M. M., Zou, C., Blazquez-Llorca, L. & Herms, J. Analyzing dendritic spine pathology in Alzheimer's disease: problems and opportunities. *Acta Neuropathol* **130**, 1-19, doi:10.1007/s00401-015-1449-5 (2015).

182 El-Danaf, R. N. & Huberman, A. D. Characteristic patterns of dendritic remodeling in early-stage glaucoma: evidence from genetically identified retinal ganglion cell types. *J Neurosci* **35**, 2329-2343, doi:10.1523/JNEUROSCI.1419-14.2015 (2015).

183 Risner, M. L., Pasini, S., Cooper, M. L., Lambert, W. S. & Calkins, D. J. Axogenic mechanism enhances retinal ganglion cell excitability during early progression in glaucoma. *Proc Natl Acad Sci U S A* **115**, E2393-E2402, doi:10.1073/pnas.1714888115 (2018).

184 Williams, P. A. *et al.* Inhibition of the classical pathway of the complement cascade prevents early dendritic and synaptic degeneration in glaucoma. *Mol Neurodegener* **11**, 26, doi:10.1186/s13024-016-0091-6 (2016).

185 Mukai, R. *et al.* The Complement System Is Critical in Maintaining Retinal Integrity during Aging. *Front Aging Neurosci* **10**, 15, doi:10.3389/fnagi.2018.00015 (2018).

186 Arancibia-Carcamo, I. L. & Attwell, D. The node of Ranvier in CNS pathology. *Acta Neuropathol* **128**, 161-175, doi:10.1007/s00401-014-1305-z (2014).

187 Nave, K. A. Myelination and support of axonal integrity by glia. *Nature* **468**, 244-252, doi:10.1038/nature09614 (2010).

188 Smith, M. A., Plyler, E. S., Dengler-Crish, C. M., Meier, J. & Crish, S. D. Nodes of Ranvier in Glaucoma. *Neuroscience* **390**, 104-118, doi:10.1016/j.neuroscience.2018.08.016 (2018).

189 Cercignani, M. *et al.* Characterizing axonal myelination within the healthy population: a tract-by-tract mapping of effects of age and gender on the fiber g-ratio. *Neurobiol Aging* **49**, 109-118, doi:10.1016/j.neurobiolaging.2016.09.016 (2017).

190 Cooper, M. L., Crish, S. D., Inman, D. M., Horner, P. J. & Calkins, D. J. Early astrocyte redistribution in the optic nerve precedes axonopathy in the DBA/2J mouse model of glaucoma. *Exp Eye Res* **150**, 22-33, doi:10.1016/j.exer.2015.11.016 (2016).

191 Agathocleous, M. & Harris, W. A. From progenitors to differentiated cells in the vertebrate retina. *Annu Rev Cell Dev Biol* **25**, 45-69, doi:10.1146/annurev.cellbio.042308.113259 (2009).

192 Reese, B. E. Development of the retina and optic pethway. *Vision Res* (2012).

193 Bosco, A. *et al.* Reduced retina microglial activation and improved optic nerve integrity with minocycline treatment in the DBA/2J mouse model of glaucoma. *Invest Ophthalmol Vis Sci* **49**, 1437-1446, doi:10.1167/iovs.07-1337 (2008).

194 Perry, V. H. & Cowey, A. Retinal ganglion cells that project to the superior colliculus and pretectum in the macaque monkey. *Neuroscience* **12**, 1125-1137, doi:10.1016/0306-4522(84)90007-1 (1984).

195 Perry, V. H., Oehler, R. & Cowey, A. Retinal ganglion cells that project to the dorsal lateral geniculate nucleus in the macaque monkey. *Neuroscience* **12**, 1101-1123, doi:10.1016/0306-4522(84)90006-x (1984).

196 Bunt, A. H., Hendrickson, A. E., Lund, J. S., Lund, R. D. & Fuchs, A. F. Monkey retinal ganglion cells: morphometric analysis and tracing of axonal projections, with a consideration of the peroxidase technique. *J Comp Neurol* **164**, 265-285, doi:10.1002/cne.901640302 (1975).

197 Livingstone, M. & Hubel, D. Segregation of form, color, movement, and depth: anatomy, physiology, and perception. *Science* **240**, 740-749, doi:10.1126/science.3283936 (1988).

198 Dreher, B., Sefton, A. J., Ni, S. Y. & Nisbett, G. The morphology, number, distribution and central projections of Class I retinal ganglion cells in albino and hooded rats. *Brain Behav Evol* **26**, 10-48, doi:10.1159/000118764 (1985).

199 Ellis, E. M., Gauvain, G., Sivyer, B. & Murphy, G. J. Shared and distinct retinal input to the mouse superior colliculus and dorsal lateral geniculate nucleus. *J Neurophysiol* **116**, 602-610, doi:10.1152/jn.00227.2016 (2016).

200 Calkins, D. J. *et al.* The challenge of regenerative therapies for the optic nerve in glaucoma. *Exp Eye Res* **157**, 28-33, doi:10.1016/j.exer.2017.01.007 (2017).

201 Laha, B., Stafford, B. K. & Huberman, A. D. Regenerating optic pathways from the eye to the brain. *Science* **356**, 1031-1034, doi:10.1126/science.aal5060 (2017).

202 Lim, J. H. *et al.* Neural activity promotes long-distance, target-specific regeneration of adult retinal axons. *Nat Neurosci* **19**, 1073-1084, doi:10.1038/nn.4340 (2016).

203 Nicholls, J. & Saunders, N. Regeneration of immature mammalian spinal cord after injury. *Trends in Neurosciences* **19**, 229-234, doi:10.1016/0166-2236(96)10021-7 (1996).

204 Kadir, A. *et al.* Dynamic changes in PET amyloid and FDG imaging at different stages of Alzheimer's disease. *Neurobiol Aging* **33**, 198 e191-114, doi:10.1016/j.neurobiolaging.2010.06.015 (2012).

205 Koronyo-Hamaoui, M. *et al.* Identification of amyloid plaques in retinas from Alzheimer's patients and noninvasive in vivo optical imaging of retinal plaques in a mouse model. *Neuroimage* **54 Suppl 1**, S204-217, doi:10.1016/j.neuroimage.2010.06.020 (2011).

206 Ning, A., Cui, J., To, E., Ashe, K. H. & Matsubara, J. Amyloid-beta deposits lead to retinal degeneration in a mouse model of Alzheimer disease. *Invest Ophthalmol Vis Sci* **49**, 5136-5143, doi:10.1167/iovs.08-1849 (2008).

207 Hinton, D. R., Sadun, A. A., Blanks, J. C. & Miller, C. A. Optic-nerve degeneration in Alzheimer's disease. *N Engl J Med* **315**, 485-487, doi:10.1056/NEJM198608213150804 (1986).

208 Sadun, A. A. & Bassi, C. J. Optic Nerve Damage in Alzheimer's Disease. *Ophthalmology* **97**, 9-17, doi:10.1016/s0161-6420(90)32621-0 (1990).

209 Ghezzi, A. *et al.* Prospective study of multiple sclerosis with early onset. *Mult Scler* **8**, 115-118, doi:10.1191/1352458502ms786oa (2002).

210 Tham, Y. C. *et al.* Global prevalence of glaucoma and projections of glaucoma burden through 2040: a systematic review and meta-analysis. *Ophthalmology* **121**, 2081-2090, doi:10.1016/j.ophtha.2014.05.013 (2014).

211 Quigley, H. A. & Broman, A. T. The number of people with glaucoma worldwide in 2010 and 2020. *Br J Ophthalmol* **90**, 262-267, doi:10.1136/bjo.2005.081224 (2006).

212 Calkins, D. J. Critical pathogenic events underlying progression of neurodegeneration in glaucoma. *Prog Retin Eye Res* **31**, 702-719, doi:10.1016/j.preteyeres.2012.07.001 (2012).

213 Gordon, M. O. *et al.* The Ocular Hypertension Treatment Study - Baseline factors that predict the onset of primary open-angle glaucoma. *Archives of Ophthalmology* **120**, 714-720 (2002).

214 Nongpiur, M. E., Ku, J. Y. & Aung, T. Angle closure glaucoma: a mechanistic review. *Curr Opin Ophthalmol* **22**, 96-101, doi:10.1097/ICU.0b013e32834372b9 (2011).

215 Nesher, R., Mimouni, M. D., Khoury, S., Nesher, G. & Segal, O. Delayed diagnosis of subacute angle closure glaucoma in patients presenting with headaches. *Acta Neurol Belg* **114**, 269-272, doi:10.1007/s13760-014-0290-2 (2014).

216 Koz, O. G., Turkcu, M. F., Yarangumeli, A., Koz, C. & Kural, G. Normotensive glaucoma and risk factors in normotensive eyes with pseudoexfoliation syndrome. *J Glaucoma* **18**, 684-688, doi:10.1097/IJG.0b013e31819c4311 (2009).

217 Trick, G. L. Visual dysfunction in normotensive glaucoma. *Doc Ophthalmol* **85**, 125-133 (1993).

218 Jeong, J. H., Park, K. H., Jeoung, J. W. & Kim, D. M. Preperimetric normal tension glaucoma study: long-term clinical course and effect of therapeutic lowering of intraocular pressure. *Acta Ophthalmol* **92**, e185-193, doi:10.1111/aos.12277 (2014).

219 Heijl, A. *et al.* Reduction of intraocular pressure and glaucoma progression: results from the Early Manifest Glaucoma Trial. *Arch Ophthalmol* **120**, 1268-1279 (2002).

220 Leske, M. C. *et al.* Factors for glaucoma progression and the effect of treatment - The Early Manifest Glaucoma Trial. *Archives of Ophthalmology* **121**, 48-56 (2003).

221 Mamikonian, V. R. [The upper limit of individual normal range of intraocular pressure--a personalized criterion for IOP evaluation]. *Vestn Oftalmol* **130**, 71-78 (2014).

222 Yusuf, I. H., Ratnarajan, G., Kerr, R. S. & Salmon, J. F. Juvenile-onset Normal Tension Glaucoma From Chronic, Recurrent Low Cerebrospinal Fluid Pressure. *J Glaucoma* **25**, e738-740, doi:10.1097/IJG.0000000000000455 (2016).

223 Berdahl, J. P., Allingham, R. R. & Johnson, D. H. Cerebrospinal fluid pressure is decreased in primary open-angle glaucoma. *Ophthalmology* **115**, 763-768, doi:10.1016/j.ophtha.2008.01.013 (2008).

224 Burgoyne, C. F. A biomechanical paradigm for axonal insult within the optic nerve head in aging and glaucoma. *Exp Eye Res* **93**, 120-132, doi:10.1016/j.exer.2010.09.005 (2011).

225 Hood, D. C. *et al.* Initial arcuate defects within the central 10 degrees in glaucoma. *Invest Ophthalmol Vis Sci* **52**, 940-946, doi:10.1167/iovs.10-5803 (2011).

226 Sponsel, W. E. *et al.* Pattern Electroretinography and Visual Evoked Potentials Provide Clinical Evidence of CNS Modulation of High- and Low-Contrast VEP Latency in Glaucoma. *Transl Vis Sci Technol* **6**, 6, doi:10.1167/tvst.6.6.6 (2017).

227 Reilly, M. A., Villarreal, A., Maddess, T. & Sponsel, W. E. Refined Frequency Doubling Perimetry Analysis Reaffirms Central Nervous System Control of Chronic Glaucomatous Neurodegeneration. *Transl Vis Sci Technol* **4**, 7, doi:10.1167/tvst.4.3.7 (2015).

228 Carbonaro, F., Hysi, P. G., Fahy, S. J., Nag, A. & Hammond, C. J. Optic disc planimetry, corneal hysteresis, central corneal thickness, and intraocular pressure as risk factors for glaucoma. *Am J Ophthalmol* **157**, 441-446, doi:10.1016/j.ajo.2013.10.017 (2014).

229 Piette, S. D. & Sergott, R. C. Pathological optic-disc cupping. *Curr Opin Ophthalmol* **17**, 1-6, doi:10.1097/01.icu.0000193072.17122.f3 (2006).

230 Grytz, R., Sigal, I. A., Ruberti, J. W., Meschke, G. & Downs, J. C. Lamina Cribrosa Thickening in Early Glaucoma Predicted by a Microstructure Motivated Growth and Remodeling Approach. *Mech Mater* **44**, 99-109, doi:10.1016/j.mechmat.2011.07.004 (2012).

231 Fazio, M. A. *et al.* Regional variations in mechanical strain in the posterior human sclera. *Invest Ophthalmol Vis Sci* **53**, 5326-5333, doi:10.1167/iovs.12-9668 (2012).

232 Howell, G. R. *et al.* Axons of retinal ganglion cells are insulted in the optic nerve early in DBA/2J glaucoma. *J Cell Biol* **179**, 1523-1537, doi:10.1083/jcb.200706181 (2007).

233 Beirowski, B., Babetto, E., Coleman, M. P. & Martin, K. R. The WldS gene delays axonal but not somatic degeneration in a rat glaucoma model. *Eur J Neurosci* **28**, 1166-1179, doi:10.1111/j.1460-9568.2008.06426.x (2008).

234 Anderson, M. G. *et al.* Mutations in genes encoding melanosomal proteins cause pigmentary glaucoma in DBA/2J mice. *Nature Genetics* **30**, 81-85, doi:10.1038/ng794 (2002).

235 Inman, D. M., Sappington, R. M., Horner, P. J. & Calkins, D. J. Quantitative correlation of optic nerve pathology with ocular pressure and corneal thickness in the DBA/2 mouse

model of glaucoma. *Invest Ophthalmol Vis Sci* **47**, 986-996, doi:10.1167/iovs.05-0925 (2006).

236 John, S. W. *et al.* Essential iris atrophy, pigment dispersion, and glaucoma in DBA/2J mice. *Invest Ophthalmol Vis Sci* **39**, 951-962 (1998).

237 McKinnon, S. J., Schlamp, C. L. & Nickells, R. W. Mouse models of retinal ganglion cell death and glaucoma. *Exp Eye Res* **88**, 816-824, doi:10.1016/j.exer.2008.12.002 (2009).

238 Morrison, J. C. *et al.* A rat model of chronic pressure-induced optic nerve damage. *Exp Eye Res* **64**, 85-96, doi:10.1006/exer.1996.0184 (1997).

239 Nissirios, N. *et al.* Comparison of anterior segment structures in two rat glaucoma models: an ultrasound biomicroscopic study. *Invest Ophthalmol Vis Sci* **49**, 2478-2482, doi:10.1167/iovs.07-0965 (2008).

240 Ueda, J. *et al.* Experimental glaucoma model in the rat induced by laser trabecular photocoagulation after an intracameral injection of India ink. *Jpn J Ophthalmol* **42**, 337-344 (1998).

241 Levkovitch-Verbin, H. *et al.* Translimbal laser photocoagulation to the trabecular meshwork as a model of glaucoma in rats. *Investigative Ophthalmology & Visual Science* **43**, 402-410 (2002).

242 Aihara, M., Lindsey, J. D. & Weinreb, R. N. Experimental mouse ocular hypertension: establishment of the model. *Invest Ophthalmol Vis Sci* **44**, 4314-4320 (2003).

243 Grozdanic, S. D. *et al.* Laser-induced mouse model of chronic ocular hypertension. *Invest Ophthalmol Vis Sci* **44**, 4337-4346 (2003).

244 Nakatani, Y., Higashide, T., Ohkubo, S. & Sugiyama, K. Influences of the inner retinal sublayers and analytical areas in macular scans by spectral-domain OCT on the diagnostic ability of early glaucoma. *Invest Ophthalmol Vis Sci* **55**, 7479-7485, doi:10.1167/iovs.14-15530 (2014).

245 Grozdanic, S. D., Kwon, Y. H., Sakaguchi, D. S., Kardon, R. H. & Sonea, I. M. Functional evaluation of retina and optic nerve in the rat model of chronic ocular hypertension. *Exp Eye Res* **79**, 75-83, doi:10.1016/j.exer.2004.02.011 (2004).

246 Mittag, T. W. *et al.* Retinal damage after 3 to 4 months of elevated intraocular pressure in a rat glaucoma model. *Invest Ophthalmol Vis Sci* **41**, 3451-3459 (2000).

247 Sawada, A. & Neufeld, A. H. Confirmation of the rat model of chronic, moderately elevated intraocular pressure. *Exp Eye Res* **69**, 525-531, doi:10.1006/exer.1999.0732 (1999).

248 Garcia-Valenzuela, E., Shareef, S., Walsh, J. & Sharma, S. C. Programmed cell death of retinal ganglion cells during experimental glaucoma. *Exp Eye Res* **61**, 33-44 (1995).

249 Grozdanic, S. D. *et al.* Temporary elevation of the intraocular pressure by cauterization of vortex and episcleral veins in rats causes functional deficits in the retina and optic nerve. *Exp Eye Res* **77**, 27-33 (2003).

250 Ko, M. L., Hu, D. N., Ritch, R. & Sharma, S. C. The combined effect of brain-derived neurotrophic factor and a free radical scavenger in experimental glaucoma. *Invest Ophthalmol Vis Sci* **41**, 2967-2971 (2000).

251 Goldblum, D. & Mittag, T. Prospects for relevant glaucoma models with retinal ganglion cell damage in the rodent eye. *Vision Res* **42**, 471-478 (2002).

252 Sappington, R. M., Carlson, B. J., Crish, S. D. & Calkins, D. J. The microbead occlusion model: a paradigm for induced ocular hypertension in rats and mice. *Invest Ophthalmol Vis Sci* **51**, 207-216, doi:10.1167/iovs.09-3947 (2010).

253 Weber, A. J. & Zelenak, D. Experimental glaucoma in the primate induced by latex microspheres. *J Neurosci Methods* **111**, 39-48 (2001).

254 Urcola, J. H., Hernandez, M. & Vecino, E. Three experimental glaucoma models in rats: comparison of the effects of intraocular pressure elevation on retinal ganglion cell size and death. *Exp Eye Res* **83**, 429-437, doi:10.1016/j.exer.2006.01.025 (2006).

255 Ngumah, Q. C., Buchthal, S. D. & Dacheux, R. F. Longitudinal non-invasive proton NMR spectroscopy measurement of vitreous lactate in a rabbit model of ocular hypertension. *Exp Eye Res* **83**, 390-400, doi:10.1016/j.exer.2006.01.015 (2006).

256 Ward, N. J., Ho, K. W., Lambert, W. S., Weitlauf, C. & Calkins, D. J. Absence of transient receptor potential vanilloid-1 accelerates stress-induced axonopathy in the optic projection. *J Neurosci* **34**, 3161-3170, doi:10.1523/JNEUROSCI.4089-13.2014 (2014).

257 Ito, Y. A., Belforte, N., Cueva Vargas, J. L. & Di Polo, A. A Magnetic Microbead Occlusion Model to Induce Ocular Hypertension-Dependent Glaucoma in Mice. *J Vis Exp*, e53731, doi:10.3791/53731 (2016).

258 Williams, A. L. *et al.* Evidence for widespread structural brain changes in glaucoma: a preliminary voxel-based MRI study. *Invest Ophthalmol Vis Sci* **54**, 5880-5887, doi:10.1167/iovs.13-11776 (2013).

259 Rojas, B. *et al.* Microglia in mouse retina contralateral to experimental glaucoma exhibit multiple signs of activation in all retinal layers. *J Neuroinflammation* **11**, 133, doi:10.1186/1742-2094-11-133 (2014).

260 Gallego, B. I. *et al.* IOP induces upregulation of GFAP and MHC-II and microglia reactivity in mice retina contralateral to experimental glaucoma. *J Neuroinflammation* **9**, 92, doi:10.1186/1742-2094-9-92 (2012).

261 Kanamori, A., Nakamura, M., Nakanishi, Y., Yamada, Y. & Negi, A. Long-term glial reactivity in rat retinas ipsilateral and contralateral to experimental glaucoma. *Exp Eye Res* **81**, 48-56, doi:10.1016/j.exer.2005.01.012 (2005).

262 Cen, L. P. *et al.* Bilateral retinal microglial response to unilateral optic nerve transection in rats. *Neuroscience* **311**, 56-66, doi:10.1016/j.neuroscience.2015.09.067 (2015).

263 Kipfer-Kauer, A., McKinnon, S. J., Frueh, B. E. & Goldblum, D. Distribution of amyloid precursor protein and amyloid-beta in ocular hypertensive C57BL/6 mouse eyes. *Curr Eye Res* **35**, 828-834, doi:10.3109/02713683.2010.494240 (2010).

264 Willecke, K. *et al.* Structural and functional diversity of connexin genes in the mouse and human genome. *Biol Chem* **383**, 725-737, doi:10.1515/BC.2002.076 (2002).

265 Cao, F. *et al.* A quantitative analysis of connexin-specific permeability differences of gap junctions expressed in HeLa transfectants and Xenopus oocytes. *J Cell Sci* **111 (Pt 1)**, 31-43 (1998).

266 L. Harris, A. Emerging issues of connexin channels: biophysics fills the gap. *Quarterly Reviews of Biophysics* **34**, doi:10.1017/s0033583501003705 (2002).

267 Das Sarma, J. *et al.* Multimeric connexin interactions prior to the trans-Golgi network. *J Cell Sci* **114**, 4013-4024 (2001).

268 Laird, D. W. Life cycle of connexins in health and disease. *Biochem J* **394**, 527-543, doi:10.1042/BJ20051922 (2006).

269 Jordan, K., Chodock, R., Hand, A. R. & Laird, D. W. The origin of annular junctions: a mechanism of gap junction internalization. *J Cell Sci* **114**, 763-773 (2001).

270 Leithe, E. & Rivedal, E. Epidermal growth factor regulates ubiquitination, internalization and proteasome-dependent degradation of connexin43. *J Cell Sci* **117**, 1211-1220, doi:10.1242/jcs.00951 (2004).

271 Schubert, A. L., Schubert, W., Spray, D. C. & Lisanti, M. P. Connexin family members target to lipid raft domains and interact with caveolin-1. *Biochemistry* **41**, 5754-5764 (2002).

272 Beardslee, M. A., Laing, J. G., Beyer, E. C. & Saffitz, J. E. Rapid Turnover of Connexin43 in the Adult Rat Heart. *Circulation Research* **83**, 629-635, doi:10.1161/01.res.83.6.629 (1998).

273 Laird, D. W., Puranam, K. L. & Revel, J. P. Turnover and phosphorylation dynamics of connexin43 gap junction protein in cultured cardiac myocytes. *Biochemical Journal* **273**, 67-72, doi:10.1042/bj2730067 (1991).

274 Le, H. T. *et al.* Gap Junction Intercellular Communication Mediated by Connexin43 in Astrocytes Is Essential for Their Resistance to Oxidative Stress. *Journal of Biological Chemistry* **289**, 1345-1354, doi:10.1074/jbc.M113.508390 (2014).

275 Solan, J. L. & Lampe, P. D. Specific Cx43 phosphorylation events regulate gap junction turnover in vivo. *FEBS Lett* **588**, 1423-1429, doi:10.1016/j.febslet.2014.01.049 (2014).

276 Rouach, N., Koulakoff, A., Abudara, V., Willecke, K. & Giaume, C. Astroglial metabolic networks sustain hippocampal synaptic transmission. *Science* **322**, 1551-1555, doi:10.1126/science.1164022 (2008).

277 Giardina, S. F., Mikami, M., Goubaeva, F. & Yang, J. Connexin 43 confers resistance to hydrogen peroxide-mediated apoptosis. *Biochem Biophys Res Commun* **362**, 747-752, doi:10.1016/j.bbrc.2007.08.066 (2007).

278 Chen, Y. S., Green, C. R., Danesh-Meyer, H. V. & Rupenthal, I. D. Neuroprotection in the treatment of glaucoma--A focus on connexin43 gap junction channel blockers. *Eur J Pharm Biopharm* **95**, 182-193, doi:10.1016/j.ejpb.2015.01.031 (2015).

279 Ramachandran, S., Xie, L. H., John, S. A., Subramaniam, S. & Lal, R. A novel role for connexin hemichannel in oxidative stress and smoking-induced cell injury. *PLoS One* **2**, e712, doi:10.1371/journal.pone.0000712 (2007).

280 Hutnik, C. M., Pocrnich, C. E., Liu, H., Laird, D. W. & Shao, Q. The protective effect of functional connexin43 channels on a human epithelial cell line exposed to oxidative stress. *Invest Ophthalmol Vis Sci* **49**, 800-806, doi:10.1167/iovs.07-0717 (2008).

281 Kar, R., Riquelme, M. A., Werner, S. & Jiang, J. X. Connexin 43 channels protect osteocytes against oxidative stress-induced cell death. *J Bone Miner Res* **28**, 1611-1621, doi:10.1002/jbmr.1917 (2013).

282 Rouach, N. *et al.* Gap junctions and connexin expression in the normal and pathological central nervous system. *Biology of the Cell* **94**, 457-475, doi:10.1016/s0248-4900(02)00016-3 (2002).

283 Dermietzel, R. *et al.* Oligodendrocytes express gap junction proteins connexin32 and connexin45. *Glia* **20**, 101-114, doi:10.1002/(sici)1098-1136(199706)20:2<101::Aid-glia2>3.0.Co;2-c (1997).

284 Kunzelmann, P., Blumcke, I., Traub, O., Dermietzel, R. & Willecke, K. *Journal of Neurocytology* **26**, 17-22, doi:10.1023/a:1018555207379 (1997).

285 Altevogt, B. M., Kleopa, K. A., Postma, F. R., Scherer, S. S. & Paul, D. L. Connexin29 Is Uniquely Distributed within Myelinating Glial Cells of the Central and Peripheral Nervous Systems. *The Journal of Neuroscience* **22**, 6458-6470, doi:10.1523/jneurosci.22-15-06458.2002 (2002).

286 Rash, J. E. *et al.* Grid-mapped freeze-fracture analysis of gap junctions in gray and white matter of adult rat central nervous system, with evidence for a “panglial syncytium” that is not coupled to neurons. *Journal of Comparitive Neurology* **388**, doi:10.1002/(SICI)1096-9861(19971117)388:2<265::AID-CNE6>3.0.CO;2-%23 (1998).

287 Pastor, A., Kremer, M., Möller, T., Kettenmann, H. & Dermietzel, R. Dye coupling between spinal cord oligodendrocytes: Differences in coupling efficiency between gray and white matter. *Glia* **24**, 108-120, doi:10.1002/(sici)1098-1136(199809)24:1<108::Aid-glia11>3.0.Co;2-v (1998).

288 Maglione, M. *et al.* Oligodendrocytes in mouse corpus callosum are coupled via gap junction channels formed by connexin47 and connexin32. *Glia* **58**, 1104-1117, doi:10.1002/glia.20991 (2010).

289 Saez, P. J. *et al.* ATP is required and advances cytokine-induced gap junction formation in microglia in vitro. *Mediators Inflamm* **2013**, 216402, doi:10.1155/2013/216402 (2013).

290 Dobrenis, K. *et al.* Human and mouse microglia express connexin36, and functional gap junctions are formed between rodent microglia and neurons. *J Neurosci Res* **82**, 306-315, doi:10.1002/jnr.20650 (2005).

291 Eugenin, E. A. *et al.* Microglia at brain stab wounds express connexin 43 and in vitro form functional gap junctions after treatment with interferon-gamma and tumor necrosis factor-alpha. *Proc Natl Acad Sci U S A* **98**, 4190-4195, doi:10.1073/pnas.051634298 (2001).

292 Wasseff, S. K. & Scherer, S. S. Activated microglia do not form functional gap junctions in vivo. *J Neuroimmunol* **269**, 90-93, doi:10.1016/j.jneuroim.2014.02.005 (2014).

293 Dermietzel, R., Hertberg, E. L., Kessler, J. A. & Spray, D. C. Gap junctions between cultured astrocytes: immunocytochemical, molecular, and electrophysiological analysis. *The Journal of Neuroscience* **11**, 1421-1432, doi:10.1523/jneurosci.11-05-01421.1991 (1991).

294 Batter, D. K. *et al.* Heterogeneity in gap junction expression in astrocytes cultured from different brain regions. *Glia* **6**, 213-221, doi:10.1002/glia.440060309 (1992).

295 Rash, J. E., Yasumura, T., Dudek, F. E. & Nagy, J. I. Cell-Specific Expression of Connexins and Evidence of Restricted Gap Junctional Coupling between Glial Cells and between Neurons. *The Journal of Neuroscience* **21**, 1983-2000, doi:10.1523/jneurosci.21-06-01983.2001 (2001).

296 Alvarez-Maubecin, V., García-Hernández, F., Williams, J. T. & Van Bockstaele, E. J. Functional Coupling between Neurons and Glia. *The Journal of Neuroscience* **20**, 4091-4098, doi:10.1523/jneurosci.20-11-04091.2000 (2000).

297 Lundgaard, I., Osorio, M. J., Kress, B. T., Sanggaard, S. & Nedergaard, M. White matter astrocytes in health and disease. *Neuroscience* **276**, 161-173, doi:10.1016/j.neuroscience.2013.10.050 (2014).

298 Okada, S. *et al.* Conditional ablation of Stat3 or Socs3 discloses a dual role for reactive astrocytes after spinal cord injury. *Nat Med* **12**, 829-834, doi:10.1038/nm1425 (2006).

299 Sofroniew, M. V. Reactive astrocytes in neural repair and protection. *Neuroscientist* **11**, 400-407, doi:10.1177/1073858405278321 (2005).

300 Sun, D., Qu, J. & Jakobs, T. C. Reversible reactivity by optic nerve astrocytes. *Glia* **61**, 1218-1235, doi:10.1002/glia.22507 (2013).

301 Myer, D. J., Gurkoff, G. G., Lee, S. M., Hovda, D. A. & Sofroniew, M. V. Essential protective roles of reactive astrocytes in traumatic brain injury. *Brain* **129**, 2761-2772, doi:10.1093/brain/awl165 (2006).

302 Tuck, M. W. & Crick, R. P. The age distribution of primary open angle glaucoma. *Ophthalmic Epidemiol* **5**, 173-183 (1998).

303 Baltan, S. *et al.* Metabolic vulnerability disposes retinal ganglion cell axons to dysfunction in a model of glaucomatous degeneration. *J Neurosci* **30**, 5644-5652, doi:10.1523/JNEUROSCI.5956-09.2010 (2010).

304 Calkins, D. J. Age-related changes in the visual pathways: blame it on the axon. *Invest Ophthalmol Vis Sci* **54**, ORSF37-41, doi:10.1167/iovs.13-12784 (2013).

305 Cavallotti, C., Pacella, E., Pescosolido, N., Tranquilli-Leali, F. M. & Feher, J. Age-related changes in the human optic nerve. *Can J Ophthalmol* **37**, 389-394 (2002).

306 Sandell, J. H. & Peters, A. Effects of age on the glial cells in the rhesus monkey optic nerve. *J Comp Neurol* **445**, 13-28 (2002).

307 Crish, S. D. *et al.* Failure of Axonal Transport Induces a Spatially Coincident Increase in Astrocyte Bdnf Prior to Synapse Loss in a Central Target. *Neuroscience* **229**, 55-70, doi:10.1016/j.neuroscience.2012.10.069 (2013).

308 Bosco, A. *et al.* Glial coverage in the optic nerve expands in proportion to optic axon loss in chronic mouse glaucoma. *Exp Eye Res* **150**, 34-43, doi:10.1016/j.exer.2016.01.014 (2016).

309 Jakobs, T. C., Libby, R. T., Ben, Y., John, S. W. & Masland, R. H. Retinal ganglion cell degeneration is topological but not cell type specific in DBA/2J mice. *J Cell Biol* **171**, 313-325, doi:10.1083/jcb.200506099 (2005).

310 Lye-Barthel, M., Sun, D. & Jakobs, T. C. Morphology of astrocytes in a glaucomatous optic nerve. *Invest Ophthalmol Vis Sci* **54**, 909-917, doi:10.1167/iovs.12-10109 (2013).

311 Schuettauf, F. *et al.* Retinal neurodegeneration in the DBA/2J mouse-a model for ocular hypertension. *Acta Neuropathol* **107**, 352-358, doi:10.1007/s00401-003-0816-9 (2004).

312 Pazos, M. *et al.* Expansions of the neurovascular scleral canal and contained optic nerve occur early in the hypertonic saline rat experimental glaucoma model. *Exp Eye Res* **145**, 173-186, doi:10.1016/j.exer.2015.10.014 (2016).

313 Buckingham, B. P. *et al.* Progressive ganglion cell degeneration precedes neuronal loss in a mouse model of glaucoma. *J Neurosci* **28**, 2735-2744, doi:10.1523/JNEUROSCI.4443-07.2008 (2008).

314 Sappington, R. M., Pearce, D. A. & Calkins, D. J. Optic nerve degeneration in a murine model of juvenile ceroid lipofuscinosis. *Invest Ophthalmol Vis Sci* **44**, 3725-3731 (2003).

315 Dapper, J. D., Crish, S. D., Pang, I. H. & Calkins, D. J. Proximal inhibition of p38 MAPK stress signaling prevents distal axonopathy. *Neurobiol Dis* **59**, 26-37, doi:10.1016/j.nbd.2013.07.001 (2013).

316 Lambert, W. S., Ruiz, L., Crish, S. D., Wheeler, L. A. & Calkins, D. J. Brimonidine prevents axonal and somatic degeneration of retinal ganglion cell neurons. *Mol Neurodegener* **6**, 4, doi:10.1186/1750-1326-6-4 (2011).

317 Liuzzi, F. J. & Miller, R. H. Radially Oriented Astrocytes in the Normal Adult-Rat Spinal-Cord. *Brain Research* **403**, 385-388, doi:Doi 10.1016/0006-8993(87)90081-3 (1987).

318 Miller, J. P. & Liuzzi, F. J. Regional specialization of the radial glial cells of the adult frog spinal cord. *Journal of Neurocytology* **15**, 187-196, doi:10.1007/bf01611655 (1986).

319 Rouach, N., Glowinski, J. & Giaume, C. Activity-dependent neuronal control of gap-junctional communication in astrocytes. *J Cell Biol* **149**, 1513-1526 (2000).

320 Libby, R. T. *et al.* Inherited glaucoma in DBA/2J mice: pertinent disease features for studying the neurodegeneration. *Vis Neurosci* **22**, 637-648, doi:10.1017/S0952523805225130 (2005).

321 Schlamp, C. L., Li, Y., Dietz, J. A., Janssen, K. T. & Nickells, R. W. Progressive ganglion cell loss and optic nerve degeneration in DBA/2J mice is variable and asymmetric. *BMC Neurosci* **7**, 66, doi:10.1186/1471-2202-7-66 (2006).

322 Saleh, M., Nagaraju, M. & Porciatti, V. Longitudinal evaluation of retinal ganglion cell function and IOP in the DBA/2J mouse model of glaucoma. *Invest Ophthalmol Vis Sci* **48**, 4564-4572, doi:10.1167/iovs.07-0483 (2007).

323 Scholz, M. *et al.* Dependency of intraocular pressure elevation and glaucomatous changes in DBA/2J and DBA/2J-Rj mice. *Invest Ophthalmol Vis Sci* **49**, 613-621, doi:10.1167/iovs.07-0745 (2008).

324 Williams, R. W., Strom, R. C., Rice, D. S. & Goldowitz, D. Genetic and environmental control of variation in retinal ganglion cell number in mice. *Journal of Neuroscience* **16**, 7193-7205 (1996).

325 Goldstein, M. E. *et al.* Phosphorylation of Neurofilament Proteins and Chromatolysis Following Transection of Rat Sciatic-Nerve. *Journal of Neuroscience* **7**, 1586-1594 (1987).

326 Shea, T. B. & Chan, W. K. H. Regulation of neurofilament dynamics by phosphorylation. *European Journal of Neuroscience* **27**, 1893-1901, doi:10.1111/j.1460-9568.2008.06165.x (2008).

327 Soto, I. *et al.* Retinal ganglion cells downregulate gene expression and lose their Axons within the optic nerve head in a mouse glaucoma model. *Journal of Neuroscience* **28**, 548-561, doi:10.1523/Jneurosci.3714-07.2008 (2008).

328 Hernandez, M. R. The optic nerve head in glaucoma: role of astrocytes in tissue remodeling. *Prog Retin Eye Res* **19**, 297-321 (2000).

329 Johnson, E. C., Deppmeier, L. M. H., Wentzien, S. K. F., Hsu, I. & Morrison, J. C. Chronology of optic nerve head and retinal responses to elevated intraocular pressure. *Investigative Ophthalmology & Visual Science* **41**, 431-442 (2000).

330 Dai, C. *et al.* Structural basis of glaucoma: the fortified astrocytes of the optic nerve head are the target of raised intraocular pressure. *Glia* **60**, 13-28, doi:10.1002/glia.21242 (2012).

331 Strouthidis, N. G., Yang, H., Downs, J. C. & Burgoyne, C. F. Comparison of clinical and three-dimensional histomorphometric optic disc margin anatomy. *Invest Ophthalmol Vis Sci* **50**, 2165-2174, doi:10.1167/iovs.08-2786 (2009).

332 Sigal, I. A. *et al.* IOP-induced lamina cribrosa deformation and scleral canal expansion: independent or related? *Invest Ophthalmol Vis Sci* **52**, 9023-9032, doi:10.1167/iovs.11-8183 (2011).

333 Tehrani, S., Johnson, E. C., Cepurna, W. O. & Morrison, J. C. Astrocyte processes label for filamentous actin and reorient early within the optic nerve head in a rat glaucoma model. *Invest Ophthalmol Vis Sci* **55**, 6945-6952, doi:10.1167/iovs.14-14969 (2014).

334 Wang, R., Seifert, P. & Jakobs, T. C. Astrocytes in the Optic Nerve Head of Glaucomatous Mice Display a Characteristic Reactive Phenotype. *Invest Ophthalmol Vis Sci* **58**, 924-932, doi:10.1167/iovs.16-20571 (2017).

335 Decrock, E. *et al.* Connexin 43 hemichannels contribute to the propagation of apoptotic cell death in a rat C6 glioma cell model. *Cell Death Differ* **16**, 151-163, doi:10.1038/cdd.2008.138 (2009).

336 Davis, C. H. *et al.* Transcellular degradation of axonal mitochondria. *Proc Natl Acad Sci U S A* **111**, 9633-9638, doi:10.1073/pnas.1404651111 (2014).

337 Bittner, C. X. *et al.* High resolution measurement of the glycolytic rate. *Front Neuroenergetics* **2**, doi:10.3389/fnene.2010.00026 (2010).

338 Belanger, M., Allaman, I. & Magistretti, P. J. Brain energy metabolism: focus on astrocyte-neuron metabolic cooperation. *Cell Metab* **14**, 724-738, doi:10.1016/j.cmet.2011.08.016 (2011).

339 Tabernero, A., Giaume, C. & Medina, J. M. Endothelin-1 regulates glucose utilization in cultured astrocytes by controlling intercellular communication through gap junctions. *Glia* **16**, 187-195, doi:Doi 10.1002/(Sici)1098-1136(199603)16:3<187::Aid-Glia1>3.0.Co;2-# (1996).

340 Simon, A. M., McWhorter, A. R., Dones, J. A., Jackson, C. L. & Chen, H. Heart and head defects in mice lacking pairs of connexins. *Dev Biol* **265**, 369-383 (2004).

341 Ganat, Y. M. *et al.* Early postnatal astroglial cells produce multilineage precursors and neural stem cells in vivo. *J Neurosci* **26**, 8609-8621, doi:10.1523/JNEUROSCI.2532-06.2006 (2006).

342 Calera, M. R. *et al.* Connexin43 is required for production of the aqueous humor in the murine eye. *J Cell Sci* **119**, 4510-4519, doi:10.1242/jcs.03202 (2006).

343 Liao, Y., Day, K. H., Damon, D. N. & Duling, B. R. Endothelial cell-specific knockout of connexin 43 causes hypotension and bradycardia in mice. *Proc Natl Acad Sci U S A* **98**, 9989-9994, doi:10.1073/pnas.171305298 (2001).

344 Tragardh, M., Moller, N. & Sorensen, M. Methodologic Considerations for Quantitative 18F-FDG PET/CT Studies of Hepatic Glucose Metabolism in Healthy Subjects. *J Nucl Med* **56**, 1366-1371, doi:10.2967/jnumed.115.154211 (2015).

345 Chakraborty, D., Bhattacharya, A. & Mittal, B. R. Patterns of brown fat uptake of 18F-fluorodeoxyglucose in positron emission tomography/computed tomography scan. *Indian J Nucl Med* **30**, 320-322, doi:10.4103/0972-3919.164147 (2015).

346 Kanamori, A., Catrinescu, M. M., Traistaru, M., Beaubien, R. & Levin, L. A. In vivo imaging of retinal ganglion cell axons within the nerve fiber layer. *Invest Ophthalmol Vis Sci* **51**, 2011-2018, doi:10.1167/iovs.09-4021 (2010).

347 Lazarov-Spiegler, O., Solomon, A. S. & Schwartz, M. Link between optic nerve regrowth failure and macrophage stimulation in mammals. *Vision Research* **39**, 169-175, doi:10.1016/s0042-6989(98)00089-3 (1999).

348 McInnes, G. & Howes, D. W. Lateral canthotomy and cantholysis: a simple, vision-saving procedure. *Cjem* **4**, 49-52, doi:10.1017/s1481803500006060 (2015).

349 Stys, P. K., Ransom, B. R. & Waxman, S. G. Compound action potential of nerve recorded by suction electrode: a theoretical and experimental analysis. *Brain Res* **546**, 18-32, doi:10.1016/0006-8993(91)91154-S (1991).

350 Jahn, H. M. *et al.* Refined protocols of tamoxifen injection for inducible DNA recombination in mouse astroglia. *Sci Rep* **8**, 5913, doi:10.1038/s41598-018-24085-9 (2018).

351 May, C. A. & Lutjen-Drecoll, E. Morphology of the murine optic nerve. *Invest Ophthalmol Vis Sci* **43**, 2206-2212 (2002).

352 Sponsel, W. E., Groth, S. L., Satsangi, N., Maddess, T. & Reilly, M. A. Refined Data Analysis Provides Clinical Evidence for Central Nervous System Control of Chronic Glaucomatous Neurodegeneration. *Transl Vis Sci Technol* **3**, 1, doi:10.1167/tvst.3.3.1 (2014).

353 Nakase, T., Yoshida, Y. & Nagata, K. Enhanced connexin 43 immunoreactivity in penumbral areas in the human brain following ischemia. *Glia* **54**, 369-375, doi:10.1002/glia.20399 (2006).

354 Nakase, T., Söhl, G., Theis, M., Willecke, K. & Naus, C. C. G. Increased Apoptosis and Inflammation after Focal Brain Ischemia in Mice Lacking Connexin43 in Astrocytes. *The American Journal of Pathology* **164**, 2067-2075, doi:10.1016/s0002-9440(10)63765-0 (2004).

355 Murphy, C. Loss of Olfactory Function in Dementing Disease. *Physiology & Behavior* **66**, 177-182, doi:10.1016/s0031-9384(98)00262-5 (1999).

356 McCaffrey, R. J., Duff, K. & Solomon, G. S. Olfactory dysfunction discriminates probable Alzheimer's dementia from major depression: a cross-validation and extension. *J Neuropsychiatry Clin Neurosci* **12**, 29-33, doi:10.1176/jnp.12.1.29 (2000).

357 Hyman, B., Van Hoesen, G., Damasio, A. & Barnes, C. Alzheimer's disease: cell-specific pathology isolates the hippocampal formation. *Science* **225**, 1168-1170, doi:10.1126/science.6474172 (1984).

358 Raj, A. & Iturria-Medina, Y. Editorial: Network Spread Models of Neurodegenerative Diseases. *Front Neurol* **9**, 1159, doi:10.3389/fneur.2018.01159 (2018).

359 Douglas, R. M. *et al.* Independent visual threshold measurements in the two eyes of freely moving rats and mice using a virtual-reality optokinetic system. *Vis Neurosci* **22**, 677-684, doi:10.1017/S0952523805225166 (2005).

360 Prusky, G. T., Alam, N. M., Beekman, S. & Douglas, R. M. Rapid quantification of adult and developing mouse spatial vision using a virtual optomotor system. *Invest Ophthalmol Vis Sci* **45**, 4611-4616, doi:10.1167/iovs.04-0541 (2004).

361 Cahill, H. & Nathans, J. The optokinetic reflex as a tool for quantitative analyses of nervous system function in mice: application to genetic and drug-induced variation. *PLoS One* **3**, e2055, doi:10.1371/journal.pone.0002055 (2008).

362 Quigley, H. A. Neuronal death in glaucoma. *Prog Retin Eye Res* **18**, 39-57 (1999).